Developing Analysis, Modeling, and Simulation Tools for Connected and Automated Vehicle Applications

PUBLICATION NO. FHWA-HRT-21-077

SEPTEMBER 2021

U.S. Department of Transportation
Federal Highway Administration

Research, Development, and Technology
Turner-Fairbank Highway Research Center
6300 Georgetown Pike
McLean, VA 22101-2296

FOREWORD

Connected and automated vehicles (CAVs) are expected to produce significant mobility, safety, and environmental benefits to the traveling public. State and local departments of transportation will be seeking to implement new transportation solutions that are enabled by CAV capabilities. However, traffic analysis, modeling, and simulation (AMS) tools, typically used to evaluate transportation improvement projects, are not well suited for evaluating emerging technologies such as CAVs. This project seeks to develop AMS models for the most prominent CAV applications and incorporate these models into existing AMS simulation tools to improve the state of the practice.

This report focuses on specific CAV application models related to cooperative adaptive cruise control, automated lane changing, speed harmonization, and merge coordination and their respective implementation into AMS simulation tools. This report will be of interest to researchers, model developers, and State and local departments of transportation that are interested in better AMS tools for estimating the potential impacts of CAV technology.

Brian P. Cronin, P.E.
Director of Safety and Operations
Research and Development

Recommended citation: Federal Highway Administration, *Developing Analysis, Modeling, and Simulation Tools for Connected and Automated Vehicle Applications Report* (Washington, DC: 2021) https://doi.org/10.21949/1521664.

TECHNICAL REPORT DOCUMENTATION PAGE

1. Report No. FHWA-HRT-21-077	2. Government Accession No.	3. Recipient's Catalog No.
4. Title and Subtitle Developing Analysis, Modeling, and Simulation Tools for Connected and Automated Vehicle Applications		5. Report Date September 2021 6. Performing Organization Code
7. Author(s) Chapter 1: Zhitong Huang (ORCID: 0000-0003-2871-6302), David K. Hale (ORCID: 0000-0001-5486-9367), Steven E. Shladover (ORCID: 0000-0002-3207-0084), and Xiaoyun Lu (ORCID: 0000-0001-6491-3990) Chapter 2: Zhitong Huang, David K. Hale, and Steven E. Shladover Chapter 3: Hao Liu (ORCID: 0000-0001-5585-6576), Xiaoyun Lu, and Steven E. Shladover Chapter 4: Qianwen Li and Xiaopeng Li Chapter 5: Hani Mahmassani, Alireza Talebpour, Moein Hosseini, Amr Elfar Chapter 6: Zhitong Huang, David K. Hale, Steven E. Shladover, Xiaoyun Lu, Xiaopeng Li, Hani Mahmassani, Alireza Talebpour		8. Performing Organization Report No.
9. Performing Organization Name and Address Leidos Inc. 11251 Roger Bacon Drive Reston, VA 20190		10. Work Unit No. 11. Contract or Grant No. DTFH61-12-D-00030, TO 22
12. Sponsoring Agency Name and Address Office of Operations Research and Development Federal Highway Administration 6300 Georgetown Pike McLean, VA 22101		13. Type of Report and Period Covered Final Report; September 2017–September 2020 14. Sponsoring Agency Code HRDO-20
15. Supplementary Notes The Government Task Managers were John Halkias (HOTM-1) and Gene McHale (HRDO-20; ORCID: 0000-0003-1031-6538).		
16. Abstract Connected and automated vehicle (CAV) technologies offer potentially transformative societal impacts, including significant mobility, safety, and environmental benefits. Traffic analysis, modeling, and simulation (AMS) tools provide an efficient means to evaluate transportation improvement projects before deployment. However, current AMS tools are not well suited for evaluating CAV applications due to their inability to represent vehicle connectivity, communication, and automated driving features. Many independent researchers have developed models of CAV systems based on a divergent array of underlying assumptions. As a result, there is little consensus in the literature about the most likely impacts of CAV technologies. Thus, a consistent set of models based on the best available data and most accurate possible representations of the behaviors of drivers of conventional vehicles and CAVs can produce realistic and believable predictions of CAV impacts. The Federal Highway Administration sponsored this project to develop AMS models for the most prominent CAV applications, incorporate these models into existing AMS simulation tools to improve the state of the practice, and conduct real-world case studies for the most prominent CAV applications to better understand their impact and deployment strategies and methods.		
17. Key Words Connected and automated vehicle, traffic simulation, microsimulation, cooperative adaptive cruise control, coordinated merging, speed harmonization, market penetration rate, variable speed advisory	18. Distribution Statement No restrictions. This document is available to the public through the National Technical Information Service, Springfield, VA 22161. http://www.ntis.gov	

19. Security Classif. (of this report) Unclassified	20. Security Classif. (of this page) Unclassified	21. No. of Pages 192	22. Price N/A

Form DOT F 1700.7 (8-72) Reproduction of completed page authorized.

SI* (MODERN METRIC) CONVERSION FACTORS

APPROXIMATE CONVERSIONS TO SI UNITS

Symbol	When You Know	Multiply By	To Find	Symbol
		LENGTH		
in	inches	25.4	millimeters	mm
ft	feet	0.305	meters	m
yd	yards	0.914	meters	m
mi	miles	1.61	kilometers	km
		AREA		
in^2	square inches	645.2	square millimeters	mm^2
ft^2	square feet	0.093	square meters	m^2
yd^2	square yard	0.836	square meters	m^2
ac	acres	0.405	hectares	ha
mi^2	square miles	2.59	square kilometers	km^2
		VOLUME		
fl oz	fluid ounces	29.57	milliliters	mL
gal	gallons	3.785	liters	L
ft^3	cubic feet	0.028	cubic meters	m^3
yd^3	cubic yards	0.765	cubic meters	m^3
	NOTE: volumes greater than 1,000 L shall be shown in m^3			
		MASS		
oz	ounces	28.35	grams	g
lb	pounds	0.454	kilograms	kg
T	short tons (2,000 lb)	0.907	megagrams (or "metric ton")	Mg (or "t")
		TEMPERATURE (exact degrees)		
°F	Fahrenheit	5 (F-32)/9 or (F-32)/1.8	Celsius	°C
		ILLUMINATION		
fc	foot-candles	10.76	lux	lx
fl	foot-Lamberts	3.426	$candela/m^2$	cd/m^2
		FORCE and PRESSURE or STRESS		
lbf	poundforce	4.45	newtons	N
lbf/in^2	poundforce per square inch	6.89	kilopascals	kPa

APPROXIMATE CONVERSIONS FROM SI UNITS

Symbol	When You Know	Multiply By	To Find	Symbol
		LENGTH		
mm	millimeters	0.039	inches	in
m	meters	3.28	feet	ft
m	meters	1.09	yards	yd
km	kilometers	0.621	miles	mi
		AREA		
mm^2	square millimeters	0.0016	square inches	in^2
m^2	square meters	10.764	square feet	ft^2
m^2	square meters	1.195	square yards	yd^2
ha	hectares	2.47	acres	ac
km^2	square kilometers	0.386	square miles	mi^2
		VOLUME		
mL	milliliters	0.034	fluid ounces	fl oz
L	liters	0.264	gallons	gal
m^3	cubic meters	35.314	cubic feet	ft^3
m^3	cubic meters	1.307	cubic yards	yd^3
		MASS		
g	grams	0.035	ounces	oz
kg	kilograms	2.202	pounds	lb
Mg (or "t")	megagrams (or "metric ton")	1.103	short tons (2,000 lb)	T
		TEMPERATURE (exact degrees)		
°C	Celsius	1.8C+32	Fahrenheit	°F
		ILLUMINATION		
lx	lux	0.0929	foot-candles	fc
cd/m^2	candela/m2	0.2919	foot-Lamberts	fl
		FORCE and PRESSURE or STRESS		
N	newtons	2.225	poundforce	lbf
kPa	kilopascals	0.145	poundforce per square inch	lbf/in^2

*SI is the symbol for International System of Units. Appropriate rounding should be made to comply with Section 4 of ASTM E380. (Revised March 2003)

TABLE OF CONTENTS

LIST OF FIGURES

LIST OF TABLES

LIST OF ABBREVIATIONS

2D	two-dimensional
ACC	adaptive cruise control
ADAS	advanced driving assistant system
AMS	analysis, modeling, and simulation
API	application programming interface
AV	autonomous vehicle
BM	behavior model
CACC	cooperative adaptive cruise control
CAV	connected and automated vehicle
CF	car following
CM	coordinated merging
CMDV	connected manually driven vehicle
CMS	changeable message sign
CTH	constant time headway
CV	connected vehicle
DLC	discretionary lane change
DOT	department of transportation
ECDF	empirical cumulative distribution function
FHWA	Federal Highway Administration
HOV	high-occupancy vehicle
HV	human-driven vehicle
I2V	infrastructure-to-vehicle
ID	identity
IDM	intelligent driver model
KS	Kolmogorov–Smirnov
LC	lane changing
LV	lane-changing vehicle
microSDK	Microscopic Simulator Software Development Kit
MOVES	MOtor Vehicle Emission Simulator
MPC	model predictive control
MPR	market penetration rate
NGSIM	Next Generation Simulation
RM	ramp metering
RMSE	root mean square error
SAE	Society of Automotive Engineers
SPDHRM	speed harmonization
SV	simulated vehicle
TMC	traffic management center
TOSCo	Traffic Optimization for Signalized Corridors
TTI	travel time index
UAV	unmanned aerial vehicle
V2I	vehicle-to-infrastructure
V2V	vehicle-to-vehicle
vehicle/h	vehicle per hour

VSA	variable speed advisory
VSL	variable speed limit
VT	Virginia Tech

EXECUTIVE SUMMARY

Connected and automated vehicle (CAV) technologies offer potentially transformative societal impacts, including significant mobility, safety, and environmental benefits. State and local agencies are interested in harnessing the potential benefits of CAVs. However, for agencies to be able to plan beneficial deployments of infrastructure-to-vehicle (I2V) and vehicle-to-vehicle (V2V) technology, it is helpful to be able to robustly predict the impacts of such deployments and identify which applications best address their unique transportation problems. Traffic analysis, modeling, and simulation (AMS) tools provide an efficient means to evaluate transportation improvement projects before deployment.

Current AMS tools are not well-suited for evaluating CAV applications due to their inability to represent vehicle connectivity and automated driving features. The development of a new generation of tools involves spending a lot of resources and time to develop, calibrate, and validate them. This option may not meet current preferences. However, agencies cannot reliably use existing AMS tools to evaluate CAV alternatives unless modeling and simulation frameworks incorporate representations of automation and connectivity capabilities. Many independent researchers have developed models of CAV systems based on a divergent array of underlying assumptions. As a result, there is little consensus in the literature regarding the most likely impacts of CAV technologies.

There is a desire for a consistent set of models to produce realistic and believable predictions of CAV impacts. These models can be based on the best available data and include the most accurate possible representations of the behaviors of drivers of conventional vehicles and CAVs. Deployment concepts, strategies, and guidelines are also key for allowing State and local agencies to understand how and where to deploy CAV technologies.

To meet these goals, the Federal Highway Administration (FHWA) sponsored this project with three primary objectives:

- Develop AMS models for the most prominent CAV applications.
- Incorporate these models into existing AMS simulation tools.
- Conduct real-world case studies (e.g., practical implementation scenarios and real-world transportation networks) for the most prominent CAV applications in order to better understand their impacts and deployment strategies and methods.

This report focuses on the first two objectives. Separately published case-study reports contain the technical details of the case-study results (Ma et al. 2021; Huang et al. [forthcoming]; Liu et al. 2021). For readers' convenience, this report contains some high-level details on the case studies.

To identify stakeholder needs, the research team hosted several webinars and a face-to-face meeting to elicit feedback and input from transportation modelers, CAV application developers/deployers, and potential CAV deployment test sites. This project selected three CAV applications and three real-world case studies to model. The applications and case studies were selected based on feedback from the industry, selection criteria defined by FHWA, and available

resources for this project. The CAV applications are a lane-changing (LC) model for light-duty CAVs, a combined application that integrates speed harmonization (SPDHRM) and coordinated merging (CM), and an improved cooperative adaptive cruise control (CACC) model for light-duty vehicles. The two freeway case studies are I‑66 in Northern Virginia applying CACC, SPDHRM, and CM and SR 99 in Sacramento, CA, applying CACC and coordinated ramp metering. The arterial case study applies Traffic Optimization for Signalized Corridors (TOSCo) to the Plymouth corridor in Ann Arbor, MI, (a low-speed arterial) and SH 105 in Conroe, TX (a high-speed arterial). The research team worked with the corresponding case-study agencies, namely the Virginia Department of Transportation (DOT), the California DOT, the City of Ann Arbor, MI, and the City of Conroe, TX, for input and feedback on the case-study scenarios.

MODEL DEVELOPMENT OUTCOMES

CACC is a popular CAV application in longitudinal vehicle following because it can increase highway capacity and traffic-flow stability without requiring construction of new infrastructure. Many transportation agencies have started to assess this application for potential future implementation. To effectively evaluate the benefits of the CACC application, an analyst can use a mixed-traffic environment to represent different market implementation stages of CAV technology. To this end, this project developed an improved CACC model that considers four different types of vehicle behaviors: human-driven vehicles (HV), connected manually driven vehicles (CMDV), autonomous vehicles (AVs), and CAVs. This model aims to create an analysis platform that depicts the interactions of the HV, CMDV, AV, and CAV in real-world infrastructure settings with variations of traffic demand and traffic management strategies. To evaluate the accuracy of this model, the developers implemented the model in Aimsun®. A Kolmogorov–Smirnov (KS) test indicated that calibration and validation were successful. The researchers also conducted a sensitivity study to evaluate the impacts of the increased compliance rate enabled by CMDV-based variable speed advisory (VSA) over the entire traffic stream. The sensitivity analysis results indicated that the VSA control could have significant effects on the freeway corridor when the CMDV market penetration is 10 percent.

LC is one of the fundamental behaviors modeled in traffic-simulation tools. The accuracy of lane-change modeling profoundly affects the confidence level of simulation results generated by traffic-simulation tools. Because most CAV LC models are developed without field data, they are forced to rely on assumptions and may not correctly replicate actual CAV behaviors. To cover this gap, a field data-based light-duty CAV LC model was developed. To support the assessment of CAV technology, the researchers developed a new mixed-traffic simulation framework that combines vehicle car-following (CF) and LC movements and fully considers the dynamics of surrounding vehicles and different mixed-traffic scenarios. This model includes three crucial components: a CF component, an LC decisionmaking component, and an LC/LC abortion path-generation and following component. To evaluate the accuracy of the proposed model, the team implemented the model in the Vissim® microsimulation software (PTV Group 2018). The team leveraged field data collected during previous field experiments for calibration and validation. The interior-point method was used for calibration. The validation root mean square error values suggested a successful calibration. According to calibration and validation results, this model replicated field CAV LC behaviors well in simulation.

CM and SPDHRM are two additional CAV freeway applications that could reduce congestion and improve mobility. To help the CAV community assess these applications, the researchers developed a joint application model that integrates SPDHRM and CM. These algorithms also utilize various methods of communicating the updated speed limits to the connected vehicles (CVs) (automated or human-driven) and non-CVs (automated or human-driven). The team developed a set of novel SPDHRM algorithms that utilize machine learning to predict the onset of congestion and to activate the SPDHRM in a highway segment. The CM model jointly optimizes the lateral trajectory of an LC vehicle and the longitudinal control of the vehicle(s) in the target lane. This method uses two approaches to optimize the trajectory. The first method minimizes the disturbance caused by the LC maneuver for a platoon of vehicles. In contrast, the second method designs a gap-generation methodology that utilizes a forward-moving shock wave to create enough gap for the LC vehicle. The developers implemented SPDHRM and CM in the same simulation platform. Future users of the platform can evaluate the benefits of SPDHRM and CM as independent applications; they can also assess the combined benefits of these two applications. The team used field data collected from Austin, TX, to calibrate and validate interactions of HVs with Level 1 automation to improve the fidelity of the developed models. To evaluate the benefits of the proposed application, the research team conducted a proof-of-concept case study. Simulation results indicate that utilizing both strategies increases the average speed while decreasing the average travel time, the speed standard deviation, and the travel time standard deviation. Moreover, applying the applications jointly can reduce the number and intensity of the shock waves that occur at the merging point of the road segment.

This report provides key information for the applications, including model development and logic, model calibration and validation, and examples of how to implement developed models into a simulation tool. This information will enable the CAV modeling community to adapt the logic developed and documented in this report to interface with their simulation software of choice.

CASE STUDY OUTCOMES

The major objective of the three case studies was to investigate SAE Level 1 automation technology for mitigating or solving existing transportation problems related to congestion, fuel consumption, and emissions at various freeway and arterial corridors. To better understand impacts and deployment strategies of CAV technologies, the most popular Level 1 CAV applications were implemented and evaluated. To effectively simulate impacts of CAV deployment, the case studies utilized real-world transportation networks and selected practical implementation scenarios by interviewing representatives of State or local transportation agencies from the case-study locations.

The I–66 case study evaluated the effectiveness of three CAV applications: CACC, SPDHRM, and CM on a 13-mi freeway segment of I–66 outside the I–495 Beltway. Both infrastructure and CAV technological strategies were simulated and discussed. The case study evaluated the potential benefits of dedicated ramps and a realistic managed lane concept—a high-occupancy vehicle (HOV) lane that CVs, CAVs, and HOVs (human-driven or CV/CAV) can all access. The simulation results showed that all three CAV applications, when applied individually or bundled together, improved system performance. CACC platooning (i.e., V2V operations) generated the

most benefits, but SPDHRM and CM further improved these benefits when market penetration rates were low-to-medium.

The TOSCo case study examined the mobility and environmental impacts of using I2V communication to optimize speed for strings of equipped vehicles, thus reducing the need for equipped vehicles to stop at intersections. The Crash Avoidance Metrics Partners research team developed a traffic-simulation environment to evaluate the effectiveness and potential mobility and environmental benefits generated through the application of the TOSCo system in both low- and high-speed corridor environments. Although TOSCo produced substantial reductions in stop delay and the number of stops in both corridors, TOSCo did not significantly affect corridorwide total delay, travel time, travel speed, vehicle emissions, or fuel consumption.

The SR 99 case study investigated the effectiveness of CACC on corridorwide traffic mobility performance and fuel consumption. Researchers evaluated the performance of the busy urban corridor under various CACC market penetration scenarios, traffic demand inputs, and CACC management strategies. The case study revealed that the average speed of the SR 99 corridor increases linearly with CACC market penetration. The CACC string operation improved vehicle fuel efficiency in the low-to-medium CACC market penetration scenarios because it mitigated traffic congestion. When CACC market penetration exceeded 40 percent, traffic flow ran at higher speed, which might not produce the optimal vehicle fuel economy. When CACC market penetration reached 100 percent, the corridor allowed about 30 percent more traffic to enter the network without experiencing reduced travel time. The strategy of directing all CAV vehicles to use a managed-lane degraded corridor performance when implemented alone, because it induced additional unnecessary CACC vehicle lane changes that impeded the traffic flow in the general-purpose lanes.

The detailed reports for these case studies were published separately from this report. Readers interested in technical details of the case studies can review the case-study reports (Ma et al. 2021; Huang et al. [forthcoming]; Liu et al. 2021).

CHAPTER 1. INTRODUCTION

Connected and automated vehicle (CAV) technologies offer potentially transformative societal impacts, including significant mobility, safety, and environmental benefits. State and local agencies are interested in harnessing the potential benefits of CAVs. However, for agencies to be able to plan beneficial deployments of infrastructure-to-vehicle (I2V) and vehicle-to-vehicle (V2V) technology, it is important to be able to robustly predict the impacts of such deployments and identify which applications best address their unique transportation problems. Traffic analysis, modeling, and simulation (AMS) tools provide an efficient means to evaluate transportation improvement projects before deployment.

However, current AMS tools are not well suited for evaluating CAV applications due to their inability to represent vehicle connectivity and automated driving features. The development of a new generation of tools involves spending a lot of resources and time to develop, calibrate, and validate them. This option may not meet current preferences. However, agencies cannot reliably use existing AMS tools to evaluate CAV alternatives unless modeling and simulation frameworks incorporate representations of automation and connectivity capabilities. Many independent researchers have developed models of CAV systems based on a divergent array of underlying assumptions. As a result, there is little consensus in the literature regarding the most likely impacts of CAV technologies.

There is a need for a consistent set of models to produce realistic and believable predictions of CAV impacts. These models can be based on the best available data and include the most accurate possible representations of driver behaviors of conventional vehicles and CAVs. Deployment concepts, strategies, and guidelines are also key for allowing State and local agencies to understand how and where to deploy CAV technologies.

To meet these goals, the Federal Highway Administration (FHWA) sponsored this project to develop AMS models for the most prominent CAV applications and to incorporate these models into existing AMS simulation tools.

FHWA'S CAV ANALYSIS, MODELING, AND SIMULATION PROJECTS

This project builds on a previous FHWA project, *Development of an AMS Framework for V2I and Connected/Automated Vehicle Environment* (Mahmassani et al. 2018), referred to as the CAV AMS Phase I project. As such, this project is often referred to as the CAV AMS Phase II project.

The Phase I project developed a conceptual framework for an AMS system for evaluating the impacts of CAV technologies on transportation system performance at the strategic, tactical, and operational levels. This framework provides the basis for future development of CAV-enabled evaluation tools. The proposed framework included four main components, which provided the core for an envisioned CAV AMS system for evaluating strategic, tactical, and operational impacts of CAVs: demand changes, supply changes, operational performance, and network integration.

Upon completion of the Phase I framework project, the Phase II project's research team discussed the ramifications of this completed work. The team endeavored to keep the foundational framework principles in mind when formulating the model development plans. There were three specific objectives of the Phase II project:

- Develop AMS models for the most prominent CAV applications.
- Incorporate these models into existing AMS modeling tools.
- Conduct real-world case studies (e.g., practical implementation scenarios and real-world transportation networks) for the most prominent CAV applications to better understand their impacts and deployment strategies and methods.

This report covers the first two objectives. The detailed reports for the case studies were published separately from this report (Ma et al. 2021; Huang et al. [forthcoming]; Liu et al. 2021).

REPORT OVERVIEW

Chapter 2 of the report describes the stakeholder interaction process, leading to a final selection of top-priority case studies and CAV applications for development. Chapters 3–5 describe the model development, calibration, validation, implementation, and sensitivity analysis process for three selected applications, respectively. Chapter 6 provides a set of conclusions for the overall project.

CHAPTER 2. IDENTIFICATION OF CAV SIMULATION COMMUNITY'S NEEDS

In the initial stages of the project, the research team performed brainstorming and down-selection exercises to prioritize CAV applications for subsequent intensive research and development. The team selected and identified CAV applications to model and case studies to analyze.

To make these key decisions, the team sought stakeholder input. The team drafted a list of candidates using stakeholder rosters from analogous projects, plus suggestions from FHWA team members and contracting team members. Candidate stakeholders included representatives from State and local governments, research institutions, tool developers, and the U.S. Department of Transportation. The team invited stakeholders by email to participate in the project activities or to opt out. They grouped the final stakeholder roster into approximately 25 CAV application experts, 25 CAV host site representatives, and 50 simulation modeling experts, for a total of approximately 100 stakeholders, not including members of the project team organizations.

The team held a stakeholder face-to-face meeting at the Turner-Fairbank Highway Research Center on February 6, 2018. The stakeholders provided useful input to assist in the down-selection process of the most promising potential CAV applications and case studies. The research team studied the stakeholder comments and combined them with the perspectives of the project team and FHWA project sponsors to narrow down the selection of potential applications and case studies. The team made recommendations based on the respective evaluation criteria defined for each category and described in the next section.

REVIEW OF CANDIDATE CAV APPLICATIONS

The research team selected the CAV applications for modeling based on the following criteria, ranked in approximate order of importance:

- Scope and timing of transportation system impacts.
- Importance to stakeholder groups.
- Availability of some models to represent performance as a starting point (i.e., not starting from scratch).
- Preliminary data requirements to represent system performance or user acceptance.

In the course of the discussion on February 6, the stakeholders raised a couple of additional considerations. First, it is helpful to consider both the importance of CAV application modeling for deployment decisions by State and local government agencies and the importance of Federal government policy decisions regarding topics such as how strongly to emphasize cooperative systems as compared to autonomous systems. Second, it is helpful to not only treat the CAV applications as independent systems, but also to consider how to model the way they would function when deployed in combinations.

The team presented and discussed 10 CAV applications in the stakeholder meeting. Participants were invited to suggest additional applications for the list, though none were proposed. The team asked the participants to express their level of support for each application on a scale from one to five. Table 1 shows ratings of 10 CAV applications according to stakeholders' votes.

The top-rated applications (i.e., the mean rating is not less than 3.6) include both freeway and signalized arterial applications; one of the options includes no vehicle automation. One application covers heavy trucks. However, none of these applications include public transit services. These applications would all be modeled at the microscopic traffic operations level so that multiple applications could be combined for assessment of their joint impacts in their respective operating environments (either freeway or signalized arterials).

Table 1. Stakeholder ratings for CAV applications.

Application	Mean Rating
V2V highway merge coordination	4.0
I2V highway speed harmonization	3.9
Truck CACC/platooning	3.9
Light-vehicle highway CACC	3.8
Eco traffic signal control (no vehicle automation)	3.6
Arterial eco-CACC vehicle speed control	3.6
Low-speed driverless urban shuttle vehicles for first-mile/last-mile access to line-haul transit	3.2
Low-speed urban transit network company services using highly automated vehicles	3.0
Automated bus rapid transit on busways	2.8
Automated small package delivery	2.4

CACC = cooperative adaptive cruise control.

The team aimed to down select to five CAV applications for continued consideration for AMS tool development. Toward this goal, the team decided to combine the two arterial applications into one, with integrated consideration of the adjustments to both the traffic signal control timing and the speed control of the vehicles approaching the traffic signal. The logical approach to the development and evaluation of these applications would be to design them as part of an integrated system from the start. The team recommended the following five CAV applications for further consideration:

Freeway applications:

- V2V freeway merge coordination.
- I2V freeway speed harmonization (SPDHRM) (i.e., variable speed advisories or limits that could be applied to support safety, throughput, or traffic smoothing goals).
- Freeway cooperative adaptive cruise control (CACC) driving for light-duty vehicles.
- Freeway CACC or platooning for heavy trucks.

Arterial applications:

1. Traffic signal control integrated with I2V vehicle speed control to support smoothing arterial traffic and reducing energy consumption.

FINAL SELECTION OF CAV APPLICATIONS

The project team discussed the selection of CAV applications with the FHWA team according to resources of this project, existing field data, the starting point and required resources of each application, and other considerations. Together they decided on the following two applications for model development under this project:

- CACC for light-duty vehicles, with heavy truck CACC modeling as an optional future add-on if additional resources are received.

- Joint application that integrates SPDHRM and merge coordination on the same simulation platform.

The team presented these two applications to project stakeholders at a stakeholder webinar on September 14, 2018, to solicit their suggestions. No objection was received. Therefore, the team decided to pursue developing models for these two applications under this project.

During the model development of CACC for light-duty vehicles, the team found that it was not feasible to add heavy-truck CACC modeling due to resource limitations. The project team started to investigate the possibility of developing the third application under this project and to determine which application to develop.

During model development, the team also observed that most CAV lane-changing (LC) models were developed without field data to calibrate and validate the behaviors. Thus, these models rely on assumptions and may not correctly replicate actual CAV behaviors. To cover this gap, the team selected a third application, a field data-based light-duty CAV LC model.

REVIEW OF CANDIDATE CAV CASE STUDIES

The research team aimed to select the case studies based on the following criteria, ranked in approximate order of importance:

1. Importance to the stakeholder group.
2. Support from relevant State and local agencies.
3. Availability of existing high-fidelity transportation network data and coded and well-calibrated models.
4. Ability to draw broader conclusions of national applicability.
5. Compatibility with selected CAV applications.

The team presented 14 potential case-study locations to the participants in the February 6 workshop. During that meeting, the participants suggested several additional locations (e.g., Chicago, IL, Orlando, FL, and an expansion of the I–66 Virginia corridor to include adjacent arterials). The discussion also highlighted the importance of connecting the case-study sites to the CAV applications that would be evaluated by case studies to make sure the target applications are suitable for implementing in the case-study sites. Other key considerations in down-selecting the case-study sites included:

- Retaining at least one of the freeway, arterial, and combined corridor environments to have the flexibility to model any of the CAV applications.

- Including sites where different simulation tools have been used.

- Minimizing the additional calibration burden on this project by considering the accuracy of the previously calibrated network.

The stakeholders were asked to rank the possible networks for the case studies. Table 2 documents the highest ratings.

Table 2. Stakeholder ratings for CAV case studies.

Case Study Site	Mean Rating	Type (Notes)
Anthem, AZ	3.9	Arterial
I–66 and privately managed lanes on I–395, Virginia	3.9	Freeway
I–15, San Diego, CA	3.7	Combined corridors
Redwood Road, Salt Lake City, UT	3.7	Arterial
US 101, San Mateo County, CA	3.6	Combined corridors
SR 99, Sacramento, CA	3.5	Freeway

It was not always clear whether the stakeholders were voting on the merits of these sites as testbeds for physical experimentation with the CAV applications or as simulation evaluation sites. The team ultimately decided to eliminate the Anthem, AZ, site from consideration because of its small size and very specialized local character (closed suburban community), which would tend to limit the applicability of any modeling results derived there for other more typical sites. In addition, the privately managed lanes on the I–395 network were considered not well calibrated, so the project team decided to eliminate this network for consideration in this project.

Initially, the team recommended retention of the following case-study sites for further study:

- Freeway sites:
  - I–66 outside the I–495 Beltway, Northern Virginia.
  - SR 99, Sacramento, CA.
- Arterial site: Redwood Road, Salt Lake City, UT.
- Combined freeway and arterial corridor networks:
  - I–15, San Diego, CA.
  - US 101 and El Camino Real, San Mateo County, CA.

The sites provided a good diversity of choices, with both the freeway and combined corridor alternatives. Furthermore, the combined corridor networks included one relatively simple network (i.e., US 101 and El Camino Real) and one more complicated network (i.e., I–15 San Diego).

FINAL SELECTION OF CASE STUDIES

To identify the final case-study candidate sites, the project team discussed the selection of case studies with the FHWA team and made the selections based on resources and the availability of an existing high-fidelity transportation network. The project team selected the following two freeway sites for the first case studies under this project:

- I–66 outside the Beltway in Northern Virginia, featuring the following CAV applications: CACC, SPDHRM, and coordinated merging (CM).

- SR 99 in Sacramento, CA, featuring the following CAV applications: CACC and coordinated ramp metering (RM).

After the selection of the first two freeway case studies, the available resources for the third case study were very limited. However, it was important to include a case study for signalized arterials to evaluate the benefits of Level 1 automation for improving the performance of arterials. To cover this gap, the project team worked with the FHWA team to identity potential arterial case-study sites. According to the FHWA team's suggestions, Traffic Optimization for Signalized Corridors—which studies strings of CAV vehicles on signalized corridors at the Plymouth corridor in Ann Arbor, MI, and SH 105 in Conroe, TX—was selected as the arterial case study, since an existing FHWA project could be leveraged to meet the limitation of available resources.

Results and analysis of these three case studies were published in separate reports (Ma et al. 2021; Huang et al. [forthcoming]; Liu et al. 2021).

CHAPTER 3. CACC FOR LIGHT-DUTY VEHICLES

LIST OF VARIABLES

This section lists all variables used in this chapter along with their definitions. The variables only apply to models described in this chapter. The same notation might represent different variables in other chapters of the report.

a_{CV} = acceleration of connected manually driven vehicles.
a_F = free acceleration, which describes the driver's acceleration when the speed choice is not constrained by the preceding vehicles.
a_G = Gipps' acceleration term, which provides a safety constraint for crash avoidance (Ciuffo et al. 2012).
a_{Max} = driver's maximum acceptable acceleration.
a_N = Newell acceleration term, which represents the driver's acceleration when following the preceding vehicle (Newell 2002).
$\hat{b}$ = subject driver's estimate of the preceding vehicle's most severe braking capabilities.
b_f = most severe braking the subject driver wishes to undertake.
d_{jam} = jam gap.
$D_{n,m}$ = KS test statistic that represents the largest difference between the two curves $F_{c,n}(\varepsilon)$ and $F_{v,n}(\varepsilon)$.
$d(t)$ = clearance gap with regard to the leader at time t.
ε = random parameter that represents the subject driver's response (compliance) to the advisory speed control.
ε_{low} and ε_{high} = data samples in the low- and high-calibration dataset, respectively.
$F_{c,n,low}(\varepsilon)$ = empirical cumulative distribution function of the low-calibration dataset, respectively.
$F_{c,n}(\varepsilon)$ = empirical cumulative distribution function (ECDF) of the calibration dataset of size n.
$F_{v,m}(\varepsilon)$ = ECDF of the validation dataset of size m.
$F_{v,n,high}(\varepsilon)$ = empirical cumulative distribution function of the high-calibration dataset.
θ = increase of the compliance level.
i = identity (ID) of the data aggregation section.
j = link ID.
k = ID of the speed-limit update interval.
M = number of connected manually driven vehicles that have traveled in section i during the update interval k.
N_c = number of data aggregation sections in each speed-control segment.
N_l = number of speed aggregation sections in a merge, diverge, or weaving link.
N_m = number of speed data samples that vehicle m has sent to the speed controller while it was in section i.
O_c = critical occupancy.
O_j = measured bottleneck occupancy.
p = section number in a merge, diverge, and weaving link list.
ρ_1, ρ_2, and ρ_3 = weights.

γ = model coefficient.
σ = parameter that represents the random speed fluctuation around a target speed.
ς_{o1}, ς_{o2} = unitless control gains.
τ_h = desired headway.
τ_r = reaction time.
u = nth speed sample of vehicle m.
V^* = variable speed limit (VSL)/variable speed advisory (VSA) of the current road section.
$\overline{v}$ = speed of the traffic flow.
V_f^d = advisory speed computed for the downstream link.
V_0 = driver's desired speed.
V_f = free-flow speed.
V_S = step speed that limits the spatial and temporal change of the VSA.
V_{safe} = safe car-following speed.
v_l = speed of the preceding vehicle.
V_T = threshold speed for identifying the congested section.
$v(t)$ = current vehicle speed.
V_f^u = advisory speed computed for the upstream link.
$v(t+\tau_r)$ = speed of the subject vehicle after reaction time.

PURPOSE OF THE MODEL

In the next few decades, the traffic stream is likely to be mixed with human-driven vehicles (HVs), connected manually driven vehicles (CMDVs), autonomous vehicles (AVs), and CAVs all operating simultaneously. The interaction of various types of vehicle fleets may induce complex traffic-flow patterns that do not exist in the current transportation system. Such complex traffic is difficult to model using existing traffic simulation and evaluation approaches, thus bringing about significant uncertainty as transportation stakeholders attempt to improve the system performance via the new technologies. This lack of understanding of future traffic-flow patterns leads to difficulties in the development of active traffic management strategies. To address the challenge, the project team developed a CMDV model and integrated the model into its existing AMS framework. Because connected vehicle (CV), in a general sense, would include manually driven vehicles and automatically driven vehicles, such as CAV, the research team used CMDV to specifically represent the connected but manually driven vehicle.

To test the CMDV model, the project team adopted a previously developed simulation framework for modeling mixed traffic: the California Partners for Advanced Transportation Technology simulation framework (referred to as the simulation framework or model framework in the remainder of this chapter). This existing framework contained an HV model developed based on the Next Generation Simulation (NGSIM) oversaturated flow model (Yeo et al. 2008), an AV model developed based on field tests of adaptive cruise control (ACC) vehicles (Milanés and Shladover 2014), and a CAV model developed based on field tests of CACC vehicles (Milanés and Shladover 2014). The existing models were calibrated based on field data (Kan et al. 2019). The detailed algorithms of the HV, ACC, and CACC models are open source and documented in an existing report (Liu et al. 2018). One limitation of the existing framework is that it is incapable of capturing the behavior of CMDVs. Thus, the objective of this study was to accurately model CMDV behavior and to implement it in the existing modeling framework. Figure 1 shows the major components of the modeling framework.

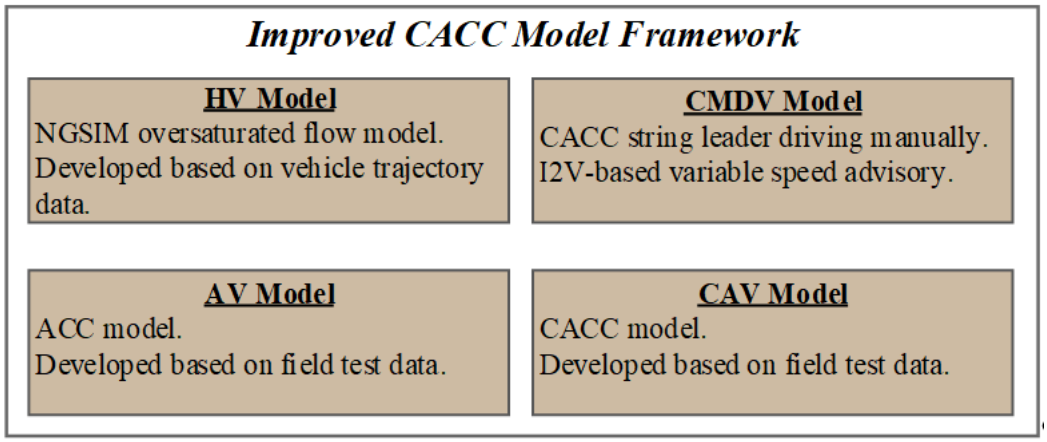

Source: FHWA.

Figure 1. Diagram. Components of the modeling framework.

A CMDV is a manually driven vehicle. It differs from a conventional HV in two aspects. In this modeling framework, the CMDV model depicts the differences via two major functionalities:

- Serving as the leader of CACC strings while driving manually.
- Affecting human drivers' speed behavior via onboard message display of limit (VSL) or variable speed advisory (VSA) broadcast via I2V communication by traffic management centers (TMC).

The research team developed the first function in a previous effort; for details on the function algorithm, see Liu et al. (2018).

The remainder of this chapter gives a detailed description of the second function. The proposed CMDV model intended to depict the speed adaptation of connected drivers due to the I2V-based speed control and the quantification of the effects of such behavior changes on the mixed traffic. Studies of VSA/VSL compliance confirm that only a small portion of drivers choose to modulate their driving behavior as requested by the system. This decision may be intentional (e.g., a driver can overlook the speed information from roadside signs) or unintentional (e.g., a driver fails to check the current speed against the posted speed limit). However, the research team hypothesized that the CMDV system may help avoid these human errors by sending warning messages via onboard devices to better motivate drivers to follow the VSL or VSA. For example, in the study of Farah et al. (2012), drivers equipped with CMDV received warning messages when they drove faster than the speed limit. Test results showed that the average speed of the equipped drivers was significantly lower than the nonequipped drivers. The measured free-flow speed of the equipped drivers was almost equal to the speed limit. The same trend was observed in Spyropoulou et al. (2014), where the intelligent speed adaptation system was adopted to promote a uniform speed among drivers in the concerned road segment.

Incorporating the CMDV model into the modeling framework enables users to assess a wide variety of traffic scenarios. Those scenarios reflect the effects of the latest technological advances in vehicle automation and connectively, such as isolated ACC operation, CACC strings, and CV speed management. Simulating those scenarios in mixed traffic may generate

useful insights into the transportation system, thus benefiting the development of future traffic management strategies and infrastructure upgrades. Since the components in the modeling framework have been calibrated and validated with the field data, the modeling outputs reasonably emulate the traffic-flow dynamics expected in the real-world system. The research team also provided basic information on the model implementation. With this information, readers can easily adopt the developed models to their studies or transfer the models to different simulation environments.

MODEL DEVELOPMENT AND LOGIC

Descriptions of Model Logic

A CMDV is a manually driven vehicle; the infrastructure influences the human driver's behavior by displaying an I2V advisory speed from a TMC. This research adopts the stimulus-response paradigm to model the behavior adaptation of the CMDV drivers in the traffic stream (Liu et al. 2017). This modeling approach quantifies the reaction of drivers (i.e., the response) due to the change of the surrounding traffic conditions (i.e., the stimuli). In traditional traffic-flow models, the stimulus can be traffic stimuli, such as the speed change of the preceding vehicles and the variation of the space gap between a subject vehicle and the leading vehicles. In the CMDV environment, additional stimuli can come from the onboard system that gives advisory speeds generated by the VSA/VSL control. This research incorporated the I2V-affected speed behavior parameter into a state-of-the-art microscopic car-following (CF) model as factors impacting drivers' response sensitivity to traffic stimuli. Liu et al. (2018) details the models adopted to depict human drivers' CF and LC in various traffic conditions. The human-driver model uses the desired speed parameter to describe drivers' speed choice when there is no constraint from other road users (Yeo et al. 2008). For a conventional human driver, the desired speed is a constant value drawn from a predetermined desired speed distribution. This study, on the other hand, developed a stochastic model that quantifies CMDV drivers' speed behavior under the influence of the advisory speed. This model was incorporated into the human-driver model to replace the desired speed parameter originally used for conventional human drivers.

The CMDV systems can assist drivers such that the drivers' responses would become quicker and more consistent, possibly resulting in fewer traffic disturbances and a more stable traffic stream. The CMDV system effectiveness, however, relies on drivers' compliance with the CMDV information. The CMDV system cannot affect the traffic flow unless the driver follows its instructions. The ability and willingness to follow instructions varies from driver to driver. In this study, the driver speed compliance and its variation were determined based on empirical datasets reported by existing studies (Lu et al. 2019).

Model Development

Speed Adaptation of Connected Drivers

In this study, the research team assumes that a TMC sends VSA instead of VSL to CMDVs. The VSA data samples were used because most U.S. transportation agencies adopt VSA instead of VSL for traffic management due to institutional issues. The research team also assumes that the communication between the TMC and CMDVs takes place in a perfect communication

environment in this study. The modeling framework does not capture the communication delay and message packet loss. This assumption is not unreasonable since the VSA was updated every 30 s. One could send the VSA several times to guarantee it is received. After receiving the VSA via I2V communications from the TMC, the CMDV drivers will adjust their speed behaviors accordingly. Because the drivers' reactions to the VSA are naturally inconsistent, their speed adjustments can follow a random distribution instead of a constant level. For this reason, this study developed an empirical stochastic CMDV model that captured drivers' speed patterns under the VSA influence. The CMDV CF model was developed based on the NGSIM oversaturated flow human-driver model calibrated in Kan et al. (2019). Within the model framework, the same CF and LC logic for human drivers was used for the CMDV drivers because the CMDV drivers still operate their vehicles manually. This study revised the original human-driver acceleration model to capture CMDV drivers' speeds under the influence of VSA. Particularly, the model uses the equation in figure 2 to represent a CMDV driver's acceleration:

$$a_{CV} = \min(a_F, a_N, a_G)$$

Figure 2. Equation. Acceleration of a CMDV.

$$a_F = a_{Max}\left[1 - \left(\frac{v(t)}{V_0}\right)^{\gamma}\right]$$

Figure 3. Equation. Free acceleration term used for calculating the acceleration of a manually driven CV.

$$a_N(t) = \frac{\left(d(t) - d_{jam}\right)/\tau_h - v(t)}{\tau_h/2}$$

Figure 4. Equation. CF acceleration term used for calculating the acceleration of a CMDV.

$$a_G(t) = \frac{v_{safe}(t + \tau_r) - v(t)}{\tau_r}$$

Figure 5. Equation. Safety acceleration term used for calculating the acceleration of a CMDV.

$$v_{safe}(t + \tau_r) = A(t) + \sqrt{A(t)^2 - C(t)}$$

Figure 6. Equation. Safe speed for calculating the safety acceleration.

$$A(t) = -b_f \tau_r$$

Figure 7. Equation. Reaction related term in the safe speed calculation.

$$C(t) = b_f\left[2\left(d(t) - d_{jam}\right) - v(t)\tau_r - v_l(t)^2/(-\hat{b})\right]$$

Figure 8. Equation. Deceleration prediction term in the safe speed calculation.

The three terms in figure 2 reflect different aspects of the driver behavior. The free acceleration term a_F (figure 3) is affected by a driver's maximum acceptable acceleration and desired speed;

the CF term a_N (figure 4) is affected by the desired headway and jam gap; and the safety term a_G (figure 5) is affected by the safe CF speed (figure 6), reaction time, and jam gap (figure 3). The safe CF speed is affected by both reaction-related term (figure 7) and deceleration-prediction term (figure 8). The VSA is expected to affect drivers' desired speed, while other behavior parameters, such as the reaction time and desired gap, receive little influence from the connected speed control. For this reason, the VSA algorithm can only change a CMDV driver's free acceleration term. The other two acceleration terms remain the same as the terms used in the human-driver model. For this reason, V_0 for a connected driver becomes a variable, as shown in figure 9.

For a normal (i.e., nonconnected) human driver, the desired speed V_0 is a constant parameter that is determined based on the (fixed) speed limit of the road segment and the driver's compliance level to the speed limit. For a connected human driver (i.e., a CMDV), V_0 for time t is a variable calculated using figure 9:

$$V_0(t) = V_j^*(t) + \sigma + \varepsilon$$

Figure 9. Equation. Desired speed of a CMDV.

A human driver is not capable of tracking a target speed perfectly. Even if the driver completely complies with the VSL/VSA, the driver cannot always maintain the vehicle speed exactly at the VSL/VSA level. The vehicle speed is expected to fluctuate around the target speed and to be subject to the limit of the front vehicle speed and relative distance. To capture those factors, the equation adopts a stochastic parameter σ that follows a normal distribution with a 0 mean and a standard deviation of 6.3 mph. This result is identical to human drivers' speed fluctuation around the posted speed limit observed at the test cite (see the Model Calibration and Validation section of this report). The parameter ε is the major parameter that influences the effectiveness of the CMDV. A value of 0 indicates that the driver completely complies with the VSA/VSL from the onboard speed display. In this case, the traffic system functions most effectively because of the high CMDV compliance rate. As the parameter deviates from 0, the effectiveness of the CMDV at smoothing traffic flow will reduce. In this study, the distribution of ε was obtained from the field data. The calibration and validation of ε is discussed later in this chapter.

Traffic Data for Connected Speed Management

The CMDV affects drivers' speed behavior via VSA/VSL. This study uses a VSA algorithm based on the study in Lu et al. (2018). The algorithm can provide VSA displayed as an advisory speed on roadside variable message signs or directly fed to drivers in CMDVs. In the proposed model, the algorithm generates tailored speed advisories for individual CMDVs based on their distance from the bottlenecks and the traffic congestion conditions of the bottlenecks. To generate such VSAs, it continuously monitors the aggregated speed and traffic occupancy patterns of the freeway corridor to identify if there are active bottlenecks. If there is no bottleneck, the algorithm intends to harmonize the traffic. If an active bottleneck is found, the algorithm adaptively determines the appropriate advisory speed for vehicles in the subjective section to alleviate the traffic congestion. When multiple bottlenecks are pinpointed, the VSA algorithm handles each bottleneck sequentially from the most upstream one to the most downstream one. It allows the advisory speed derived from a downstream bottleneck to override

the advisory speed for the upstream bottlenecks if the downstream advisory speed is lower than the upstream one. This process will give priority to downstream bottlenecks when their congestion level is higher than their upstream counterparts, thus increasing the corridor throughput.

The VSA algorithm calls for aggregated freeway speed and occupancy data as the input for the variable advisory speed computation. Occupancy indicates the percentage of time a traffic detector is occupied by vehicles. To obtain the speed dataset, it first segregates the concerned freeway corridor into consecutive data aggregation sections (figure 10). The speed data from individual CMDVs are averaged within a section over an update interval (e.g., 30 s in this study). The resulting mean speed is a temporal average of CMDVs' space mean speed, which represents the traffic condition for the section over a concerned period. The computation of the average speed is shown in figure 11. In low CMDV market penetration cases, there might not be any CMDVs in a speed aggregation section during an update interval. In this case, the speed estimations for sections immediately upstream and downstream from this section are used to linearly interpolate the speed of this section. Fixed-traffic monitoring stations, such as loop detector stations, provide the occupancy datasets along a concerned freeway corridor. Since the VSA algorithm adopts the critical occupancy as the control reference, the measured occupancy can be used to calculate the error between the control output and the reference. Since the measured occupancy is obtained via point-loop sensors, the data collection device might not cover all data aggregation sections within the study freeway corridor. To address the problem, the linear interpolation approach is also adopted to calculate the occupancy of a section based on the occupancy measurements from the closest two loop-detector stations.

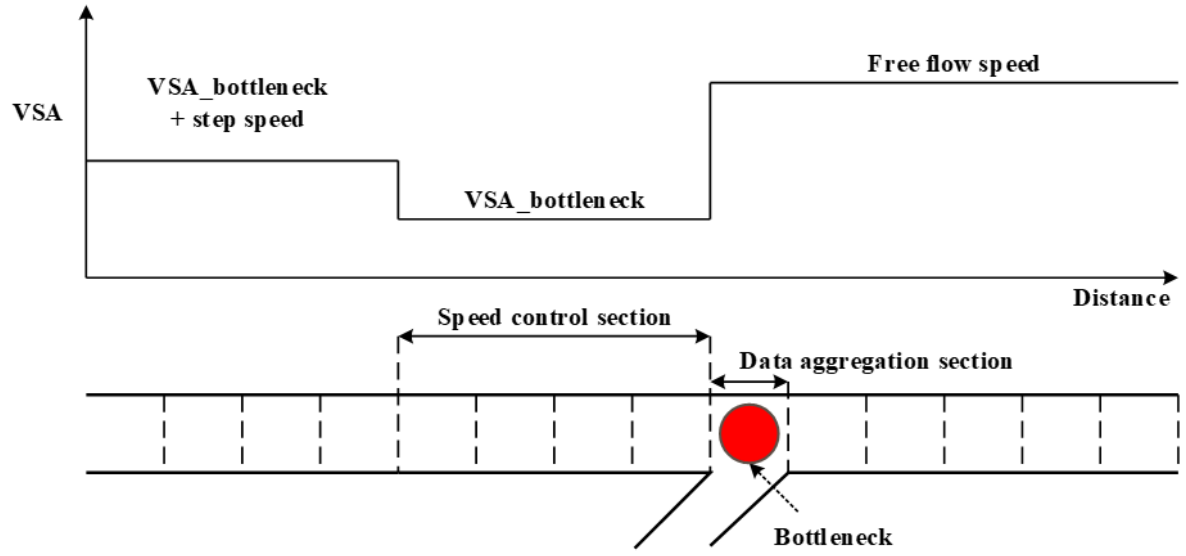

Source: FHWA.

Figure 10. Plot. Segregation of a freeway corridor.

$$\bar{v}_i(k) = \frac{1}{\sum_{m=1}^{M} N_m} \sum_{m=1}^{M} \sum_{n=1}^{N_m} u_{mn}$$

Figure 11. Equation. Computation of the aggregated speed for a section.

A data aggregation section can be short (e.g., less than 0.3 mi) compared with the length of the freeway corridor. This short section ensures that speed data from each section represent variations of the local congestion pattern. When implementing the advisory speed control, on the other hand, it is desirable to combine multiple data aggregation sections (e.g., 1.5 mi) such that they share the same advisory speed. Otherwise, drivers would need to change the speed frequently as they pass each section. This speed change will reduce traffic stability and driving comfort. The combined section is called the speed-control section (figure 10). Each speed-control section contains multiple data aggregation sections. The VSA algorithm gradually decreases the advisory speed for vehicles upstream from a bottleneck (see the VSA bottleneck + step speed in figure 10). The advisory speed reduction takes place discretely at the end point of each speed-control section.

Variable Advisory Speed Computation for Isolated Bottlenecks

The VSA algorithm decreases the input traffic flow to the bottleneck by recommending a reduced speed for upstream CMDVs to reduce or eliminate traffic congestion at an isolated bottleneck. In the mixed-traffic stream, the scattered CMDVs can still act as actuators of the speed control, leading to the speed reduction of the entire traffic flow. Such a speed change lowers the traffic load to the bottleneck, thus helping the congested area recover from the breakdown state, eventually bringing the bottleneck flow to the maximum capacity rate. In addition, the VSA algorithm reduces the advisory speed gradually for freeway segments upstream from the bottleneck. This can suppress the development of traffic disturbances that originated from the bottleneck.

If a data aggregation section i is an active bottleneck, the advisory speed for the bottleneck section and its downstream sections (i.e., $\forall\, j \in j \geq i$) is the original posted speed limit V_f. The advisory speed for the speed-control sections immediately upstream from the bottleneck (i.e., $\forall j \in \lfloor (i-j)/N_c \rfloor = 1$) is V_j, as shown in figure 12:

$$V_j(k) = \bar{v}_j(k-1) + \begin{cases} \varsigma_{o1} \cdot \left(O_c - O_j(k)\right) & O_j(k) < O_c \\ \varsigma_{o2} \cdot \left(O_c - O_j(k)\right) & O_j(k) \geq O_c \end{cases}$$

Figure 12. Equation. Variable advisory speed for sections upstream from the bottleneck.

The equation in figure 12 also provides VSA for sections further upstream from the bottleneck (i.e., $\forall j \in \lfloor (i-j)/N_c \rfloor > 1$), with the exception that the measured bottleneck occupancy O_j is replaced by a weighted occupancy calculated by a semiglobally looking ahead algorithm, as shown in figure 13:

$$O_j(k) = \rho_1 \cdot o_j(k) + \rho_2 \cdot o_{j+N_c}(k) + \rho_3 \cdot o_{j+2N_c}(k)$$

Figure 13. Equation. Weighted occupancy computation.

The weight is selected such that it has lower value when it is farther away in the downstream from the subject section.

The advisory speed of all sections is bounded by the spatial and temporal limits and the maximum and minimum limits, as shown in figure 14:

$$\left|V_j(k) - V_{j+1}(k)\right| \leq V_S$$

$$\left|V_j(k) - V_j(k-1)\right| \leq V_S$$

$$V_{min} \leq V_j(k) \leq V_{max}$$

Figure 14. Equation. Spatial, temporal, and maximum/minimum bounds for the advisory speed.

In the implementation, the value of V_s (ft/s) could be different from section to section depending on the length. The VSA algorithm has the following effects:

- Vehicles at the bottleneck section and its downstream sections (i.e., $j \geq i$) can travel at the original posted speed limit. This process allows queued vehicles to leave the congestion area as fast as possible.

- Vehicles in the speed-control section upstream from the bottleneck section have the advisory speed reduced from the posted speed limit to regulate the traffic flow entering the bottleneck section. A feedback controller is adopted to achieve a stable change of the advisory speed.

- Sections further upstream from the bottleneck adopt a semiglobally looking ahead algorithm to compute the advisory speed. This algorithm allows the traffic stream in upstream sections to also respond to the bottleneck traffic condition, thus improving the overall freeway performance.

- Advisory speed changes between two consecutive update intervals and two consecutive speed-control segments is less than the step speed V_s. With this constraint, the advisory speed changes gradually over time and space. Especially when the VSA algorithm first becomes active, this prevents the controller from suddenly reducing the advisory speed to a level much lower than the posted speed limit.

- Advisory speed is bounded by the minimum speed limit V_{min} and maximum speed limit V_{max}. For traffic safety consideration, the maximum advisory speed should be no greater than the posted speed limit. The lower bound is associated with the smallest traffic flow the VSA algorithm can generate via the speed control.

Implementation of the Connected Speed Management in Freeway Corridors

For the corridor implementation, the VSA algorithm sequentially handles the bottlenecks from upstream to downstream using the method described in the previous section. The process starts with the identification of the bottleneck sections. Ideally, a bottleneck-searching algorithm considers all sections in a freeway corridor. Since the (recurrent) congestion usually takes place near the freeway merge, diverge, or weaving areas, considering sections outside those regions could increase the computation burden of the controllers. To this end, the algorithm may call for a list of data aggregation sections that contain the merge, diverge, and weaving links. In the list, all data aggregation sections that belong to the same merge, diverge, or weaving segment are mapped to a unique link ID. If a link contains N_l data aggregation sections, a data aggregation section p is identified as a bottleneck if the average speed meets the condition in figure 15:

$$\bar{v}_p(k) \leq V_T$$

Figure 15. Equation. Identification of bottleneck sections.

The bottleneck searching algorithm moves from section 1 to section N_l (i.e., from the upstream section to the downstream section). Once a section in a link is identified as congested, the upstream front of a congested area is located. The remaining data aggregation sections are then disregarded for increasing the computation efficiency. Afterward, the VSA algorithm uses equations in figure 12 through figure 14 to determine the speed limits for all data aggregation sections of the corridor.

The VSA algorithm applies the above bottleneck searching and speed-limit computation routine iteratively for each link in the merge, diverge, and weaving link list, from the most upstream link to the most downstream link. The final advisory speed of a data aggregation section j is determined as shown in figure 16:

$$V_j^* = \begin{cases} V_j^u, & V_j^u < V_j^d \\ V_j^d, & otherwise \end{cases}$$

Figure 16. Equation. Final advisory speed for a section.

Some upstream bottlenecks may no longer take the original posted speed limit as the advisory speed for output sections. Instead, the advisory speed is determined based on the traffic operation of the downstream bottleneck. If the downstream bottleneck is very congested, the algorithm can apply an advisory speed slower than the posted speed limit at the output section of the upstream bottleneck. As a result, the upstream bottleneck will generate a reduced input flow into the downstream bottleneck, helping the recovery of the traffic-flow operation at the downstream bottleneck first. This method then coordinates the operation of the upstream and downstream bottlenecks for systematic performance improvement.

MODEL CALIBRATION AND VALIDATION

Assumptions in Calibration and Validation

The parameter ε in figure 9 denotes the deviation of a driver's desired speed from a given advisory speed. It describes the driver's compliance level to the speed control. For this reason, the parameter could be calibrated and validated based on speed datasets that depict the behavior of real-world drivers under the influence of an active VSA/VSL control. To determine ε, the research adopts the following assumptions:

- The calibration and validation involve datasets that represent drivers' desired speed. While the desired speed represents the driver's personal preference, it is difficult to directly observe the speed choice with the field speed data. This study assumes that the desired speed pattern is reflected by drivers' speed choices when they have the freedom to select their speed levels. This usually happens on uncongested roads. In congested traffic, the vehicle movement is restricted by the preceding vehicles. The speed data in congested traffic thus cannot depict the desired speed distributions.

- There is no massively implemented VSA/VSL system that connects with drivers via I2V systems. Thus, it is impossible to obtain enough speed data for CMDVs for the model calibration and validation. To address the data limitation, the researchers assumed that the CMDV drivers' speed pattern is similar to normal human drivers' behaviors when those drivers are affected by the VSA/VSL displayed on the roadside changeable message signs (CMS). This assumption justifies the use of VSA field test data from San Diego, CA, for model calibration and validation.

Calibration and Validation Datasets

Once the CMDV model captured the desired speed preference of individual CMDV drivers, the research team integrated the model into microscopic simulation of mixed traffic. Applying the CMDV model in a microscopic simulation environment enables sensitivity analyses that reveal the impact of CMDV market penetration levels on traffic flow and vehicle energy efficiency. With these assumptions and discussions, the research team calibrated and validated ε with the field data that describe normal human drivers' free-speed choices under the influence of VSA. The calibration and validation data were collected under a California Department of Transportation project, which included an extensive traffic data collection (Lu et al. 2019). This field test was conducted on SR 78 eastbound from Vista Village Drive in Vista, CA, to the freeway interchange of SR 78 eastbound and I–15 in Escondido, CA, as shown in figure 17. The roadway segment is a three-lane freeway with a posted speed limit of 65 mph, with 10 onramps and 10 off-ramps. This freeway corridor contained high-traffic volume during both morning and evening peak hours. The data were collected for 5 w, from March 30 to May 4, 2018, with VSA activation.

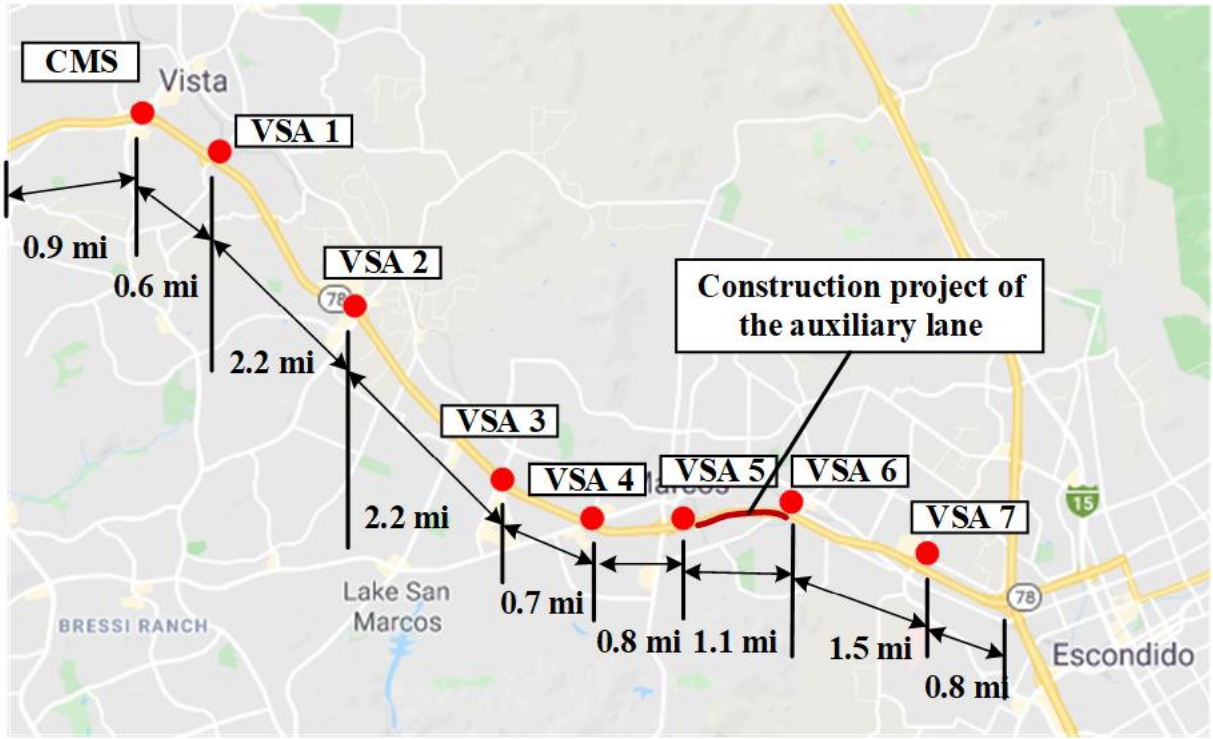

Figure 17. Map. Overview of system scope, VSA sign, CMS locations, and construction area (Lu et al. 2019).

Recurrent bottlenecks were observed daily on weekdays in the study road segment. The morning bottleneck occurred between 6 and 9 a.m. at two locations: one near San Marcos Boulevard (milepost 12.27) and another near interchange of SR 78 eastbound to I–15 (milepost 16.6). The evening bottleneck occurred between 2 and 7 p.m. near the interchange of SR 78 eastbound to I-15 northbound and I–15 southbound. Vehicle speeds dropped from 65 mph to as low as 15 mph after the onset of the congestion. There was a construction project on the new auxiliary lane in both directions of SR 78, between Twin Oaks Valley Road and Woodland Parkway. A speed limit of 65 mph was posted for that stretch of the roadway.

Seven VSA signs were located at the key locations determined from the analysis on the recurrent bottlenecks. Calculated VSA values were then rounded to multiples of 5 mph and displayed on the VSA signs. The VSA signs were located on the roadside to display the advisory speed, which was updated in real time every 30 s. A CMS displaying “Follow Advisory Speed” was placed at the starting point of the test site to instruct drivers to obey the speed posted by the downstream VSA. The posted speed on VSA during morning and evening peak hours was recommended to drivers but not enforced.

Traffic data were collected from two sources. The traffic flow, speed, and occupancy were collected from loop detectors in the study corridor at 30-s intervals. The data were then fused with real-time speed and speed advisory data, captured every 30 s by radar sensors mounted on the VSA display equipment, at seven different sites along the 10.8-mi section of SR 78 eastbound. These two sources of data were then processed to estimate the overall traffic state

along the corridor, which was in turn used to estimate the effectiveness of VSA on drivers' speed behaviors.

The entire dataset, including traffic volume, speed, occupancy, and VSA level, provides 5 w worth of data samples. Data samples of 4 w were used to determine the distribution of ε. The remaining data samples were adopted for model validation.

Calibration and Validation Methodology

The methodology adopted to calibrate and validate the random distribution of the drivers' response to the speed-limit control follows a three-step procedure.

Step 1: Data Preparation

Given data on the speed limit and the observed speed, it is possible to calculate ε. In the observed data, VSA levels ranged from 5 to 65 mph in increments of 5 mph. The initial data analysis indicated that the speed deviation ε is a variable with respect to the VSA levels. The deviation tended to grow larger as VSA decreased. Ideally, the distribution fitting of ε should be conducted at individual VSA levels; however, the sample size in the data was small for low VSA levels, especially those lower than 25 mph. The field data showed a similar bimodal pattern for lower VSA levels from 5 to 35 mph with a peak around the VSA level and another peak at a value substantially larger than the VSA level. The second peak depicted driver groups with poor compliance with the VSA. The field observation also showed a similar pattern for higher VSA levels from 35 to 65 mph with a peak near 65 mph, indicating good compliance. For this reason, the data samples were grouped into two VSA levels—low VSA level from 0 to 35 mph and high VSA level from 35 to 65 mph. The VSA feedback to the driver is a multiple of 5 mph. Therefore, such division does not lose the generality.

For each VSA level, the deviation data were divided randomly into a calibration set and a validation set. For each set of speed observation of low VSA level and high VSA level, 70 percent of the data were randomly selected for the calibration dataset. The other 30 percent of the data were selected for the validation dataset.

Step 2: Distribution Calibration

Since the deviation of the observed speed from the VSA does not follow an analytical distribution (e.g., normal distribution), an empirical distribution was used to describe the deviation distribution. An ECDF is a cumulative form of the probability distribution function of a given dataset. More formally, given the data points of sample size N, $Y_1, Y_2, \ldots Y_N$ are in order from smallest to largest. The ECDF is defined as $ECDF(i) = n(i) / N$, where $n(i)$ is the number of data points less than Y_i. Using the calibration set Y, the ECDFs of ε were found for the low VSA level from 0 to 35 mph and the high VSA level from 35 to 65 mph. The difference between the observed speed and VSA for low- and high-VSA levels are noted as ε_{low} and ε_{high}, respectively. A Python® package, statsmodels, provides statistical model estimation functions (Seabold and Perktold 2010). This package was used to determine the ECDFs of ε_{low} and ε_{high}, as $F_{c,n,low}(\varepsilon)$ and $F_{c,n,high}(\varepsilon)$, respectively, as shown in figure 18.

$$\varepsilon_{low} \sim F_{c,n,low}(\varepsilon)$$

$$\varepsilon_{high} \sim F_{c,n,high}(\varepsilon)$$

Figure 18. Equation. Empirical cumulative distribution functions for the low- and high-VSA levels.

Step 3: Distribution Validation

The two-sample Kolmogorov-Smirnov (KS) test is a statistical test to validate if two samples come from an empirical distribution of a continuous random variable (Massey 1951). In this work, a KS test is performed to validate the calibrated distribution $F_{c,n,low}(\varepsilon)$ and $F_{c,n,high}(\varepsilon)$. The two-sample KS test is a hypothesis test with the null hypothesis that two data samples for a random variable—in this case, the deviation ε—come from a common distribution. The test statistic $D_{n,m}$ is given as shown in figure 19:

$$D_{n,m} = \sup_{\varepsilon} \left| F_{c,n}(\varepsilon) - F_{v,m}(\varepsilon) \right|$$

Figure 19. Equation. KS test statistic.

The test statistic $D_{n,m}$ is the largest difference between the two curves $F_{c,n,low}(\varepsilon)$ and $F_{c,n,high}(\varepsilon)$, as shown in figure 20 and figure 21. The null hypothesis is rejected at a significance level α for large samples, if:

$$D_{n,m} > c(\alpha)\sqrt{\frac{n+m}{nm}}$$

Figure 20. Equation. Criterion for rejecting the null hypothesis.

Where the critical value is given as $c(\alpha = 0.05) = 1.36$. The statistician fails to reject the null hypothesis, otherwise.

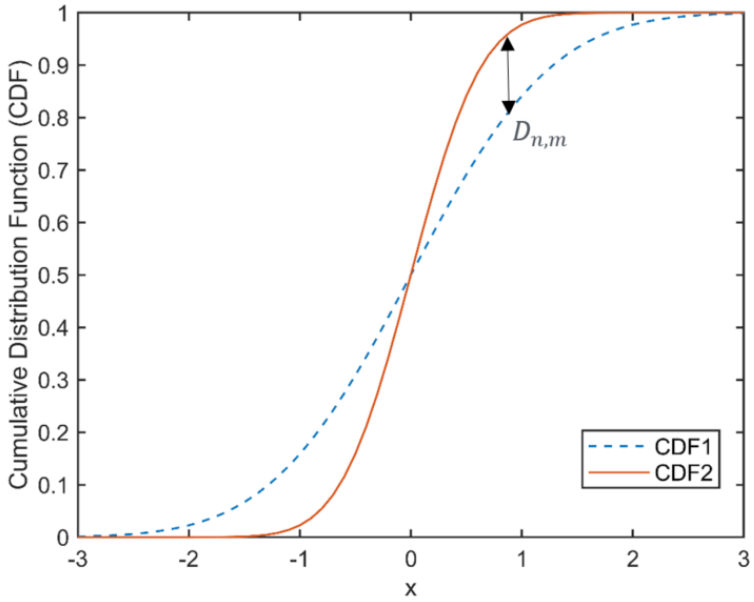

Source: FHWA.

Figure 21. Diagram. Visualization of the KS test statistic.

Calibration and Validation Results

The sample sizes for the calibration and validation datasets for low- and high-VSA levels are given in table 3. Since the data were gathered from a field observation of drivers' speed on the public road, the sample collection was not performed in a controlled experiment. Though generally a sufficient sample size for a statistical analysis is 30 for well-designed random experiments, this rule may not be suitable for this uncontrolled observation. In addition, ε for each 5 mph VSA level did not seem to have a smooth distribution function even with a sample size in a scale of hundreds. After adding data samples from multiple VSA levels, the deviation for the low VSA and the high VSA seemed to have smooth distribution functions with sample sizes in a scale of thousands.

Table 3. Sample sizes for the low- and high-VSA cases.

Sample Sizes	Low Variable Speed Advisory (0–35 mph)	High Variable Speed Advisory (35–65 mph)
Sample size of calibration dataset	5,380	73,706
Sample size of validation dataset	2,306	31,589
Total sample size	7,686	105,295

The calibration results of the empirical cumulative distribution functions for the low- and high-VSA levels are shown in figure 22. The *x*-axis is the deviation in mph. The *y*-axis is the cumulative probability. The mean and the standard deviation values are also given in the graphs. The calibrated distributions have been used in the sensitivity analyses to generate the random numbers that describe the baseline compliance level.

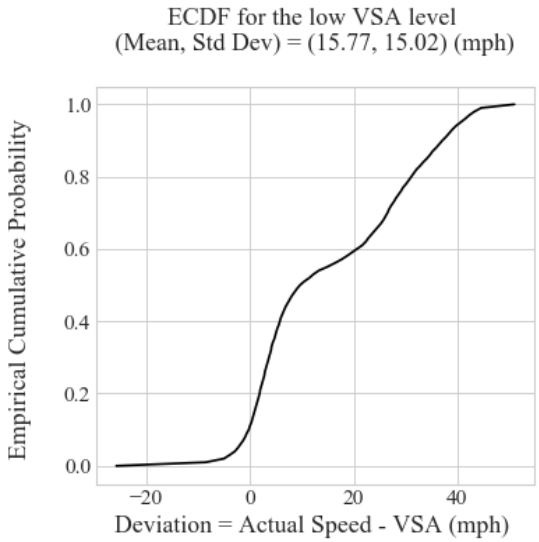

Source: FHWA.
Std Dev = standard deviation

A. Low VSA levels.

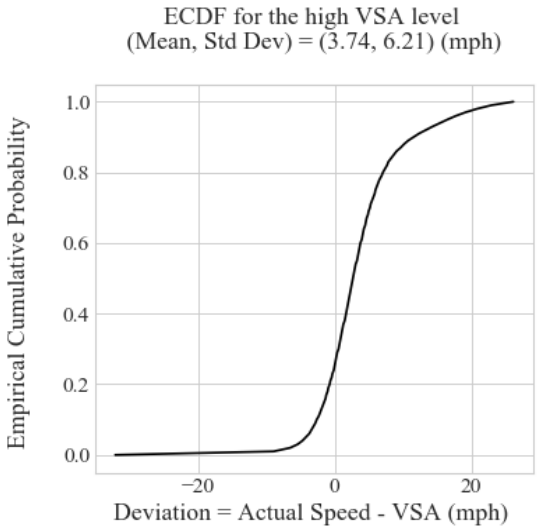

Source: FHWA.
Std Dev = standard deviation

B. High VSA levels.

Figure 22. Diagram. Calibrated empirical distributions of ε for the low and high VSA levels (mean and standard deviation in mph).

The results of the two-sample KS test for low and high VSA levels are given in table 4. In both cases, the researchers failed to reject the null hypotheses. In other words, the calibration and validation datasets follow a common distribution.

Table 4. Results of the two-sample KS test.

Validation Results	Low VSA (0–35 mph)	High VSA (35–65 mph)
Null hypothesis	Data samples 1 and 2 follow a common distribution	Data samples 1 and 2 follow a common distribution
Data sample 1	Calibration datasets	Calibration datasets
Data sample 2	Validation datasets	Validation datasets
Level of significance	0.05	0.05
D statistic	0.01168	0.00564
Critical *D* value	0.03385	0.00915
Test result	Since the *D* statistic is smaller than the critical *D* value, fail to reject the null hypothesis	Since the *D* statistic is smaller than the critical *D* value, fail to reject the null hypothesis

In addition, the probability density functions for the low and high VSA levels are given to visually inspect the KS test goodness of fit between the calibration and validation datasets in figure 23. The probability density function of the low VSA levels shows a bimodal distribution. The left peak around 0 mph represents driver populations that closely follow the VSA. The right peak is associated with drivers that do not comply with the VSA. This usually happened at freeway sections upstream from the bottleneck where the VSA was intentionally set to levels

lower than the traffic speed. In this case, vehicles entering the bottleneck would reduce the speed, thus creating a reduced input traffic flow to the congested area. This reduction could help lower the congestion intensity at the bottleneck. When the VSA was much lower than the traffic speed, some drivers may have ignored the VSA because they thought the advisory speed was not credible. Such behavior leads to the second peak in the probability density function.

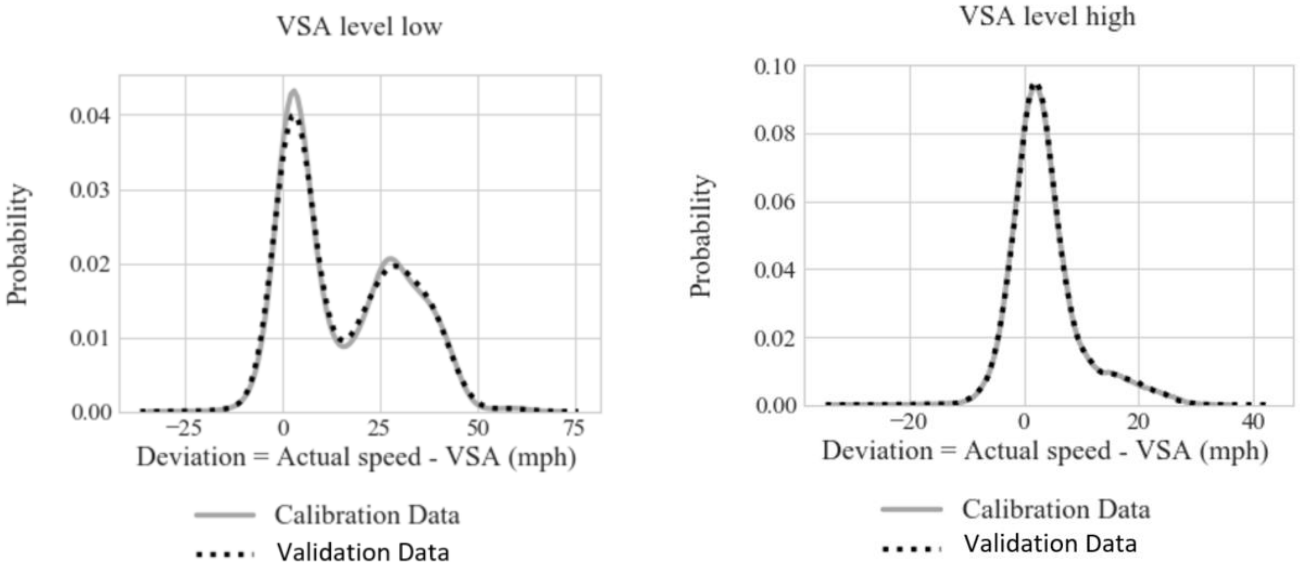

Source: FHWA.

A. Low VSA levels.

Source: FHWA.

B. High VSA levels.

Figure 23. Diagram. Probability density functions for the calibration and validation datasets.

BASIC INFORMATION ON MODEL IMPLEMENTATION

Understanding the update process of the simulation tool is important for implementing the proposed CMDV model in the simulation environment. A typical microscopic traffic-simulation tool updates the traffic-flow dynamics discretely—it computes the new location, speed, and acceleration of individual vehicles at the end of an update interval. While this is a simplification of the physical world, it gives computational advantage to the simulation tool, especially when the tool models thousands of vehicles in a network. In general, the computation process within an update interval can be divided into three stages:

Stage 1: Information Gathering

This stage takes place at the very beginning of an update interval. It allows the simulation tool to obtain the latest status of the modeled vehicles, traffic control and monitoring devices, and traffic management strategies. Those pieces of information are used to compute the new system status at the end of the update interval.

Stage 2: New System Status Computation

The simulation tool computes the new system status based on the information input in the previous stage. In this stage, the tool calculates the new position, speed, and acceleration for

individual modeled vehicles, the new state for the traffic signals, and the updated implementation scheme of traffic-management strategies (e.g., activate or deactivate a managed lane, calculate new advisory speeds, and turn ramp meters on or off). This stage only computes the new system status; it does not implement the updates. All computation processes in this stage are performed based on a common deterministic baseline (i.e., the system status of the previous update interval). In this case, the update of the modeled entities does not rely on the new status of other entities. Such an update method allows the simulation tool to execute the update process without following a specific order (from the most downstream section to the upstream section, for example). The new status computation for individual modeled entities can start simultaneously. This update method is ideal for applying parallel computing to increase the simulation speed.

Stage 3: System Status Update

Once the simulation tool has determined the new status of each modeled entity in the previous stage, it assigns the new status to each entity. The modeled vehicles move to a new position with an updated speed and acceleration. The signal lights change color. The new scheme of the traffic management strategies is executed, and the update interval ends.

The proposed CMDV algorithm can be easily implemented in the three-stage update framework:

- The algorithm uses CMDV speed and loop detector occupancy as the inputs. Those inputs are obtained in the first stage when the simulation tool gathers the current status of all simulated entities. Usually, a simulation tool with an application programming interface (API) would provide functions to access attributes of simulated entities. Those functions may be used to collect the inputs for the CMDV algorithm.

- The CMDV algorithm computes the advisory speed based on the CMDV speed and loop occupancy inputs. The computation process is implemented in the second stage. If the simulation tool allows the user to deploy the customized system update functions, the computation of the advisory speed can be integrated into the customized update functions.

- The computed advisory speed is sent to individual CMDVs in the traffic stream in the last stage. In this case, the user would develop a function to update the desired speed for only the CMDV type, while keeping the original desired speed for other vehicle types.

USE CASE AND SENSITIVITY STUDY

Implementation of the Developed Model into a Traffic-Simulation Tool

The project team implemented the CMDV model in the modeling framework by creating a new CMDV vehicle class, in addition to the existing HV, AV, and CAV classes. The logic of the CMDV model is not proprietary and can be implemented into the analyst's choice of microsimulation software. For the purpose of testing the model, the researchers implemented the CF and LC mechanisms for the four vehicle classes in a microscopic simulation tool via its Microscopic Simulator Software Development Kit (microSDK) and API programming tools (Aimsun 2020). The microSDK contains two key classes—a behavior model (BM) class and a

simulated vehicle (SV) class. The BM class configures the global parameters (e.g., simulation time, timestep, and origin-demand matrix) of the simulation environment. It controls the process of each simulation run (e.g., start/end of the simulation, creation of new vehicles, and update of vehicle movement). The SV class offers functions to access real-time vehicle data and compute the acceleration, speed, and location of individual vehicles at each update interval. By incorporating customized methods and functions in the two classes, the model framework reproduces the patterns of a traffic flow mixed with regular HVs, CMDVs, ACC vehicles, and CACC vehicles.

The BM class controls the implementation process of the simulation logic. The BM class used in the model is named *mybehavioralModel*. The logic flow of this class is illustrated in figure 24. In the figure, the bold notations indicate the model functions that correspond to the component in the logic flow. In the simulation algorithm, the new vehicle creation and LC/CF update rely on functions in the SV class. The SV class in the framework is named *myVehicleDef*. When a new vehicle is created, the framework first calls *SetPara4NewVeh* to specify the initial parameters (e.g., desired headway, desired speed, and reaction time) to the vehicle. Afterward, the simulation model determines its initial speed and location by calling *AdjustArrivalVehicle_New*. Once the initial parameters are determined, the simulation tool calls *evaluateLaneChanging* and *evaluateCarFollowing* to update the lateral and longitudinal speed and position of each modeled vehicle. The terminologies used in the CF and LC interactions are defined in figure 25. The overall logic flow of the CF and LC algorithms for vehicles in the manual driving mode is shown in figure 26.

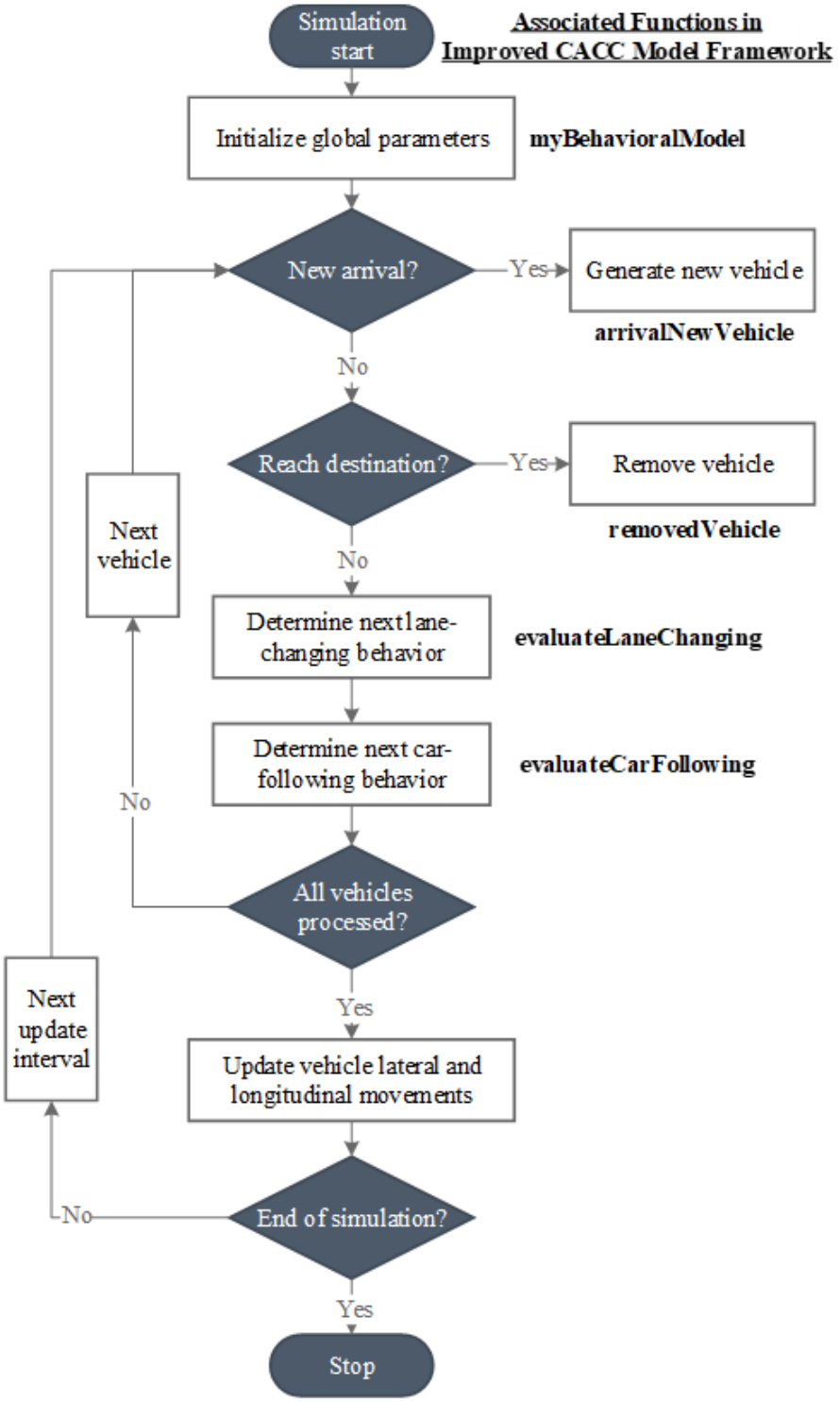

Source: FHWA.

Figure 24. Diagram. Logic flow of the simulation algorithm.

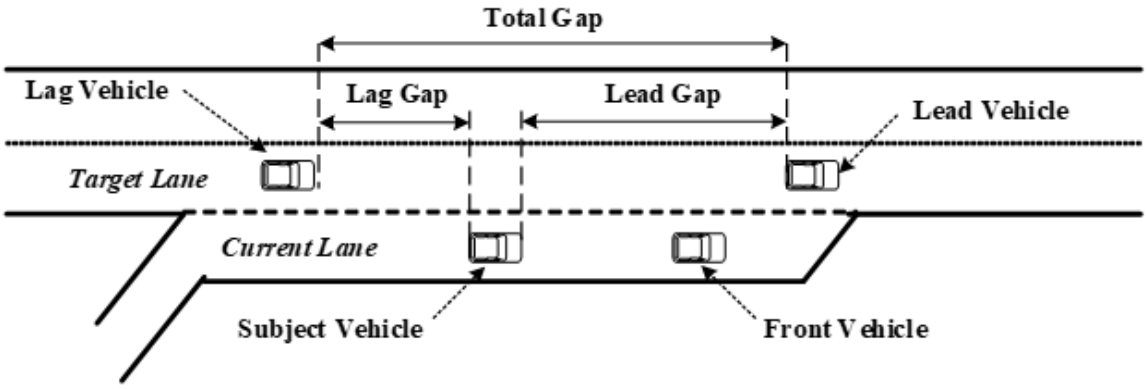

Source: FHWA.

Figure 25. Diagram. Terminology definitions in an LC process.

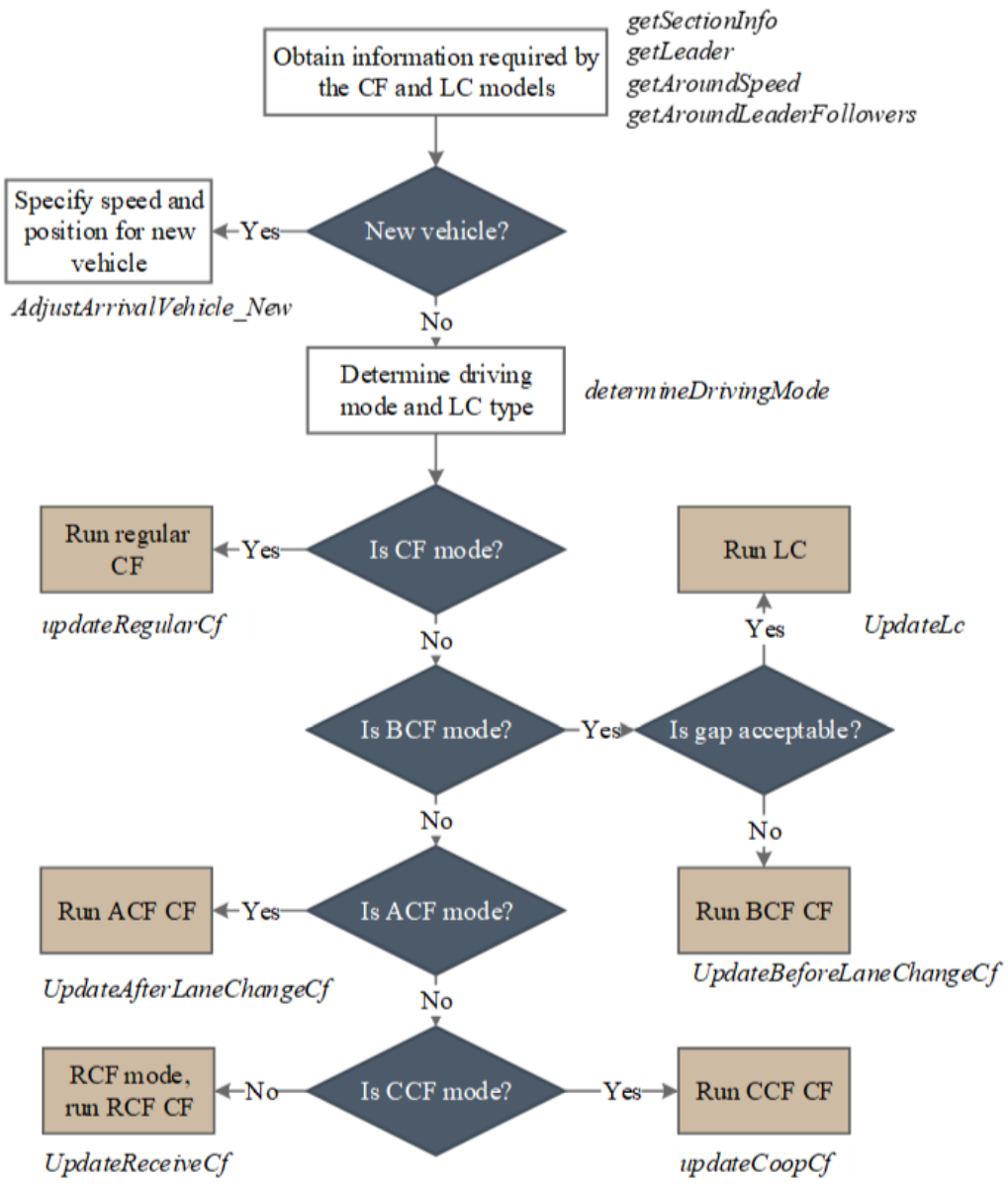

Source: FHWA.
ACF = after lane-changing car-following mode (a driver temporarily adopts a short gap after a lane-change maneuver); BCF = before lane-changing car-following mode (a driver speeds up or slows down to align with an acceptable gap in the target lane); CCF = cooperative car-following mode; LC includes discretionary lane change (DLC), active lane change (ALC), and mandatory lane change (MLC); RCF = receiving car-following mode (a driver temporarily adopts a short gap after a vehicle from the adjacent lane merges in front).

Figure 26. Diagram. CF and LC logic for manually driven vehicles.

In addition to the manual driving mode, the simulation framework also incorporates the ACC, CACC, and CMDV models. The logic flow of the ACC algorithm is shown in figure 27. All processes in the figure are embedded in an umbrella function named *NGSIMPlusACC*. For an ACC vehicle, the framework first determines the driving mode for the subject vehicle with the

function *determineDrivingModePlusACC*, which identifies the driving mode based on the vehicle status in the current step. The driving mode is associated with various CF models to be implemented in the system update stage to update the vehicle status. The driving mode identification process first checks if it needs to switch to the manually driven mode. The mode switch takes place if the subject vehicle is willing to yield to a lane-changing vehicle, if the vehicle attempts to make a lane change, or if there is a collision risk. Since the driver performs the yielding and LC maneuvers manually, the framework adopts the human-driver functions *NeedCoop* and *NeedLC* for ACC (and CACC and CMDV) as well. The collision risk is determined based on the *ACC_Manual_TakeOver_Check_CAMP* algorithm (Kiefer et al. 2003). When there is a collision risk, the ACC and CACC driver cut off the automated control and brake manually to avoid a crash. When there is no need for a mode switch, the ACC vehicle adopts the ACC controller to update the vehicle speed and position. This automated longitudinal movement update uses *Run_ACC* function.

The logic flow of the CACC algorithm is shown in figure 28. All processes in the figure are embedded in an umbrella function named *NGSIMPlusACC_CACC_V2VAHM*. For a CACC vehicle, the framework first determines the driving mode for the subject vehicle with the function *determineDrivingModePlusACC_CACC_V2XAHM*, which identifies the driving mode based on the vehicle status in the current step. The driving mode is associated with the CF models to be implemented to update the vehicle status. Similar to the ACC counterpart, the function first checks if it needs to switch to the manually driven mode. The mode switch takes place if the subject vehicle is willing to yield to an LC vehicle, if the vehicle attempts to make a lane change, or if there is a collision risk. When there is no need for a switch to the manual mode, the CACC vehicle adopts either the ACC controller or the CACC controller, depending on whether the preceding vehicle is a manually driven vehicle or a vehicle with connectivity. In the framework, both CACC vehicles and manually driven vehicles with vehicle awareness devices are counted as vehicles with connectivity. Those vehicles can serve as CACC string leaders, allowing the following CACC vehicle to adopt the CACC mode. The longitudinal movement update uses *Run_ACC* function if the CACC vehicle uses ACC mode, and *Run_CACC* function if the CACC mode is applied.

The CF and LC logics for CMDV are the same as the HV algorithms. The difference between a CMDV and an HV is that the CMDV can receive real-time VSA from the TMC. Once CMDV drivers receive the VSA/VSL, they change their desired speed based on the VSA level and the compliance level. The framework implements the modeling procedure in Aimsun® API instead of Aimsun microSDK to reduce the computation load. If the procedure were executed in microSDK, the framework would call the VSA functions repeatedly for all vehicles in the network. Since many of the calculations in these functions are identical for all vehicles, such an implementation scheme could induce much unnecessary computation demand.

On the other hand, the Aimsun API offers an *AAPIPostMagage* function that is automatically executed at the end of each simulation interval. As the VSA/VSL functions are embedded in *AAPIPostMagage*, the framework runs the VSA algorithm only once in every simulation interval to generate updated desired speed levels for all CMDVs. This process creates an efficient model implementation that is important for evaluating large road networks. The CMDV algorithm integrates the following functions into *AAPIPostMagage*:

- CollectSpeedAdvisoryData(), which collects section-based traffic data for calculating the VSA.
- DetermineAdvisorySpeed(), which computes the VSA for vehicles in different road sections.
- SetAdvisorySpeed(), which sets the desired speed of each CMDV based on its compliance and the real-time VSA level.

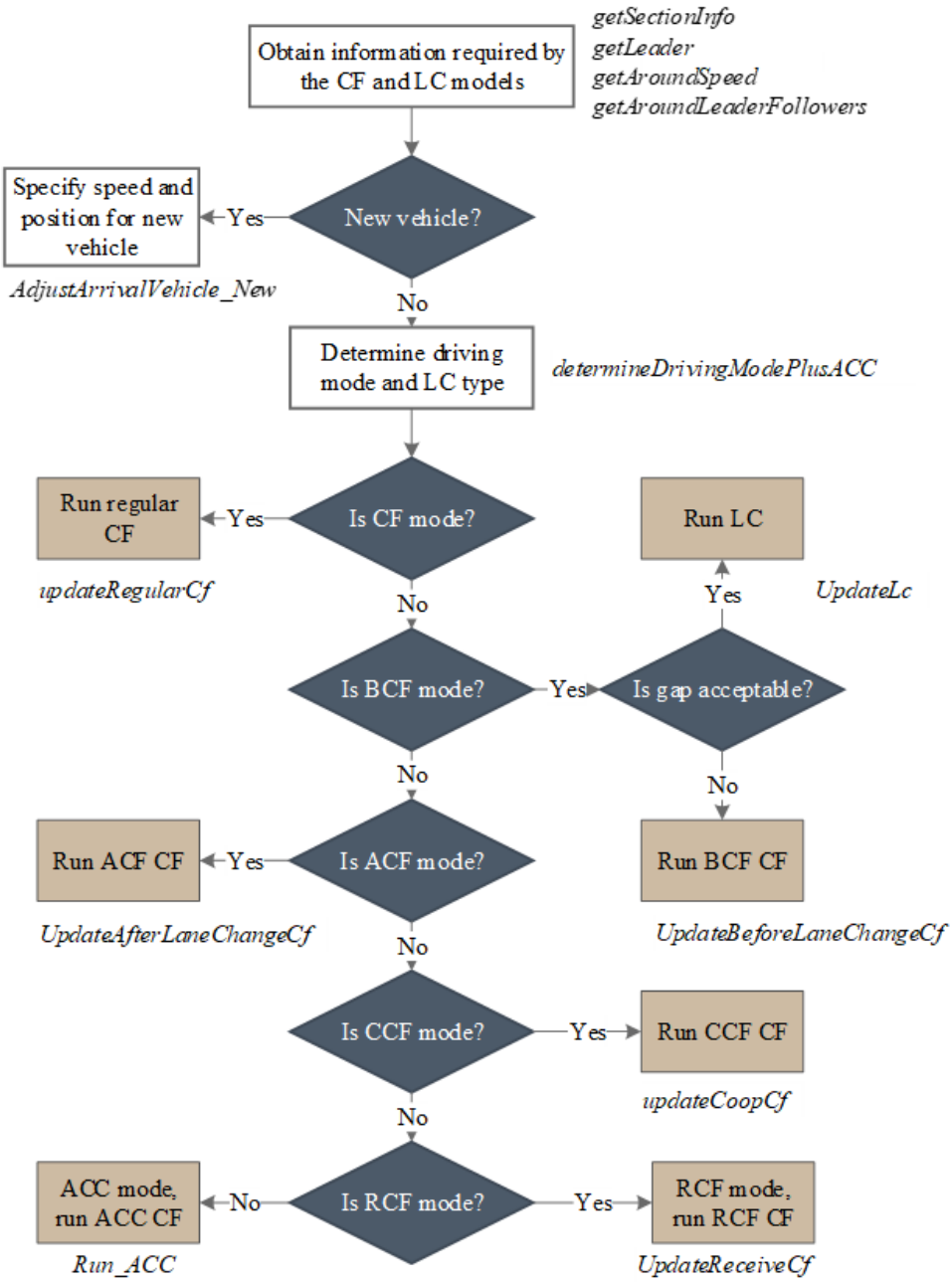

Source: FHWA.

ACF = after lane-changing car-following mode (a driver temporarily adopts a short gap after a lane-change maneuver); BCF = before lane-changing car-following mode (a driver speeds up or slows down to align with an acceptable gap in the target lane); CCF = cooperative car-following mode; LC includes discretionary lane change (DLC), active lane change (ALC), and mandatory lane change (MLC); RCF = receiving car-following mode (a driver temporarily adopts a short gap after a vehicle from the adjacent lane merges in front).

Figure 27. Diagram. Model logic flow for ACC vehicles.

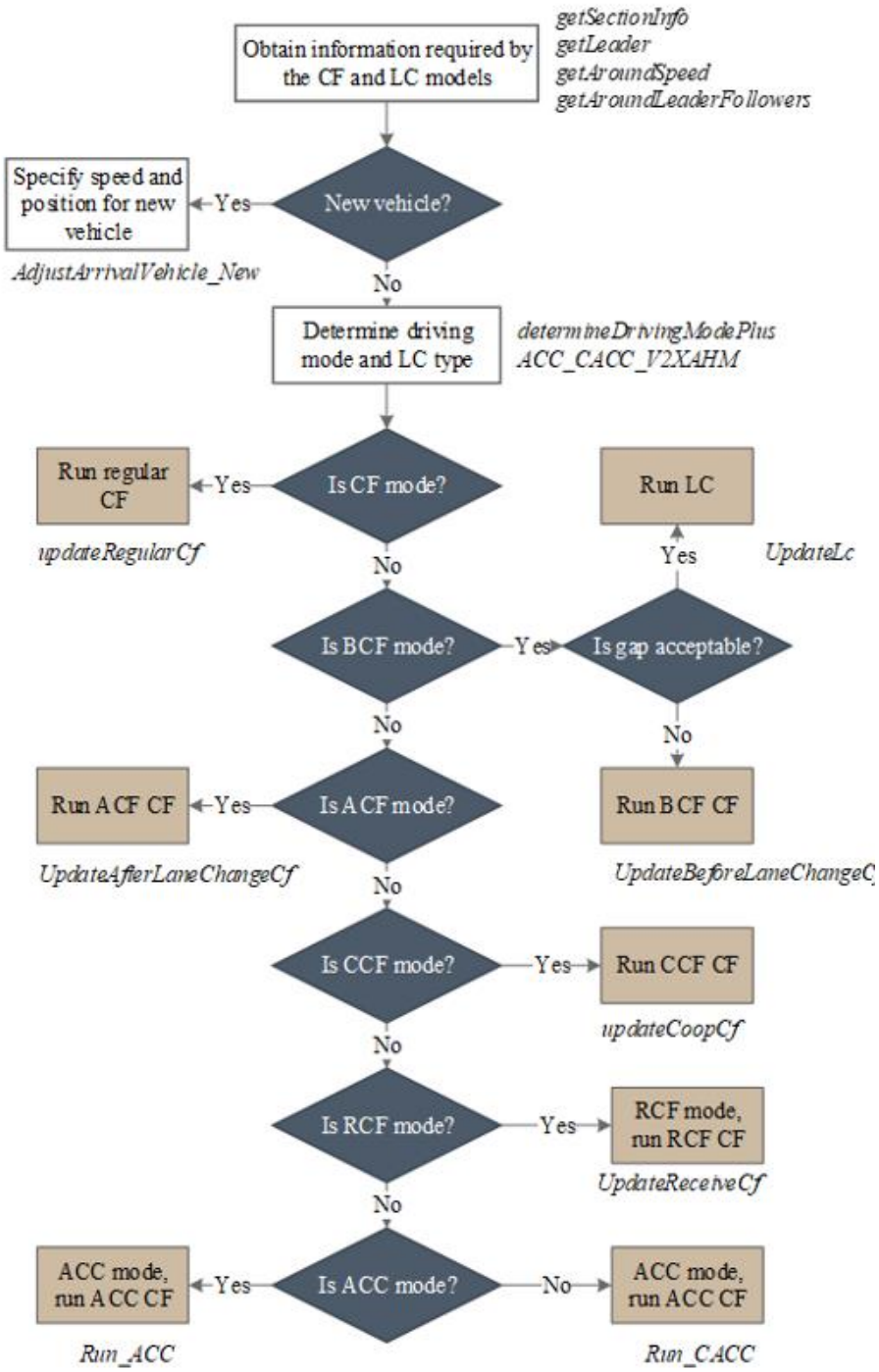

Source: FHWA.

ACF = after lane-changing car-following mode (a driver temporarily adopts a short gap after a lane-change maneuver); BCF = before lane-changing car-following mode (a driver speeds up or slows down to align with an acceptable gap in the target lane); CCF = cooperative car-following mode; LC includes discretionary lane change (DLC), active lane change (ALC), and mandatory lane change (MLC); RCF = receiving car-following mode (a driver temporarily adopts a short gap after a vehicle from the adjacent lane merges in front).

Figure 28. Diagram. Model logic flow for CACC vehicles.

Design of Simulation Experiments

The project team tested the developed CMDV model under various simulation scenarios. The scenarios tested the model sensitivity to assumptions of the CMDV market penetration rate (MPR) and the human drivers' compliance levels to the VSA from the I2V communication. The MPR increased from 0 to 100 percent, with a 10-percent step. The compliance level increased from the baseline compliance level to the full compliance level. The baseline compliance level was obtained based on the empirical data described in figure 22. A modeled driver's compliance (i.e., ε in figure 9) was determined using the following steps:

- Step 1: Generate a random real number, μ, that follows a uniform distribution between 0 and one.
- Step 2: Take μ as a cumulative probability, find its corresponding ε in figure 22.

Thus, the driver's speed deviation from the VSA follows the empirical distribution identified in the model calibration. In scenarios where drivers' compliance levels are increased, the random compliance ε changes based on the increased rate of compliance. If the compliance level increases by θ ($0 < \theta <= 1$), the new compliance is given as shown in figure 29:

$$\varepsilon' = \varepsilon \cdot (1 - \theta)$$

Figure 29. Equation. Determination of the increased compliance level.

When θ is equal to 1, it reaches the full compliance level (i.e., $\varepsilon' = 0$). The simulation scenarios are listed in table 5.

Table 5. Simulation scenarios for CMDV.

ID	CMDV MPR (Percent)	Compliance Increase (θ)
1	0	N/A
2	10	0 (baseline compliance)
3	20	0
4	30	0
5	40	0
6	50	0
7	60	0
8	70	0
9	80	0
10	90	0
11	100	0
12	10	0.05
13	10	0.10
14	10	0.15
15	10	0.20
16	10	0.25
17	10	0.30
18	10	1.00

ID	CMDV MPR (Percent)	Compliance Increase (θ)
19	20	0.05
20	20	0.10
21	20	0.15
22	20	0.20
23	20	0.25
24	20	0.30
25	20	1.00
26	100	0.05
27	100	0.10
28	100	0.15
29	100	0.20
30	100	0.25
31	100	0.30
32	100	1.00

ID = identity; N/A = not applicable.

In addition to the CMDVs, the proposed VSA algorithm was applied with the CACC vehicles such that the advisory speed was used as the reference speed of the CACC controller. When an advisory speed was sent to CACC vehicles, it was assumed that the CACC controller would perfectly adopt the advisory speed as the reference speed. There was no random variation in the reference speed. The resulting scenarios can depict the effects of automated controllers on the VSA performance. The CACC scenarios are defined in table 6 as the following:

Table 6. Simulation scenarios for CACC vehicles.

ID	CACC MPR (Percent)	VSA On or Off
33	10	Off
34	20	Off
35	30	Off
36	10	On
37	20	On
38	30	On

ID = identity.

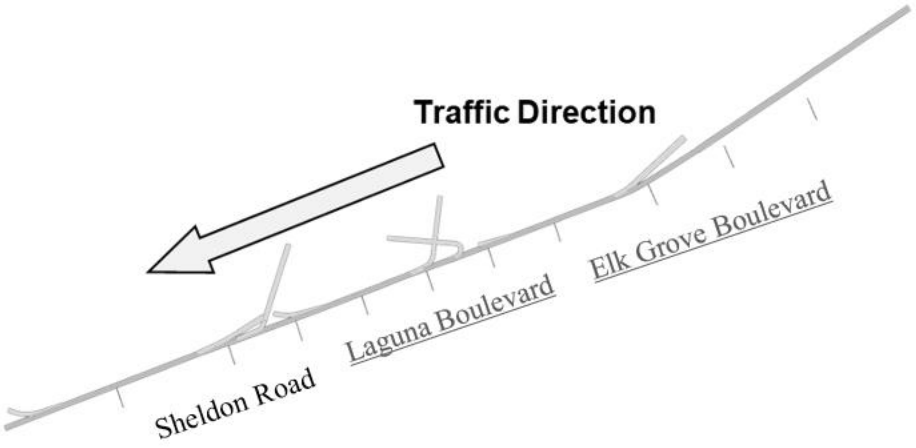

Source: FHWA.

Figure 30. Diagram. Simulated freeway corridor.

Simulation Results

The impacts of CMDV market penetration are depicted by the average traffic speed and vehicle fuel economy. The fuel results were computed using two models: the Virginia Tech (VT) comprehensive power-based fuel consumption model (Rakha et al. 2011) and the MOtor Vehicle Emission Simulator (MOVES) model (Ramezani et al. 2019). Results from the two models provide a comprehensive picture of the effectiveness of the CMDV speed adaptation. The parameters used in the two fuel models are listed in table 7 and table 8.

Table 7. Fuel model parameters of the MOVES model.

Parameter Name	Parameter Value
Rolling resistance (ft-lb/ft)	35.1
Rotational resistance (FPS/ft^2)	0.137
Aerodynamic drag coefficient (FPS^2/ft^3)	1.03E−2
Vehicle age distribution	California average vehicle age distribution in 2019
Fuel supply	MOVES default
Fuel formulation	MOVES default
Alternative vehicle and fuels technology	MOVES default
Temperature	Average July temperature measured in Sacramento, CA
Humidity	Average July humidity measured in Sacramento, CA

Table 8. Fuel model parameters of the VT comprehensive power-based fuel consumption model.

Parameter Name	Parameter Value
Alpha 0	5.92E−4
Alpha 1	4.24E−5
Alpha 2	1.00E−6
Vehicle mass (lb)	3203
Driveline efficiency	0.92
Density of air at sea level at a temperature of 15 °C (lb/ft^3)	7.68E−2
Vehicle drag coefficient	0.30
Correction factor for altitude	1.00
Vehicle frontal area (ft^2)	25.0
Rolling resistance parameters C_r, C_1, and C_2 used in the VT model	1.75, 3.28E−1, 4.58

As figure 31 shows, the average speed of the traffic flow has little change with the CMDV market penetration. However, this lack of speed change does not mean that the CMDV did not change the traffic-flow pattern. Essentially, the CMDV had two major effects on the traffic flow. First, the CMDVs upstream from the bottleneck adopted reduced speeds recommended by the VSA algorithm. As CMDVs started to slow down, they made the following vehicles reduce speed as well. This reduced speed eventually led to the slowdown of the traffic flow for freeway sections upstream from the bottleneck. On the other hand, the speed reduction helped the bottleneck recover from the congested status, which increased the queue discharging rate. As the queued vehicles could leave the congested region faster, vehicles spent less time in the low-speed status. For this reason, the average speed of the modeled vehicles in the congested bottleneck improved. As the two effects worked simultaneously, the average speed of the studied freeway corridor remained identical to the non-CMDV case.

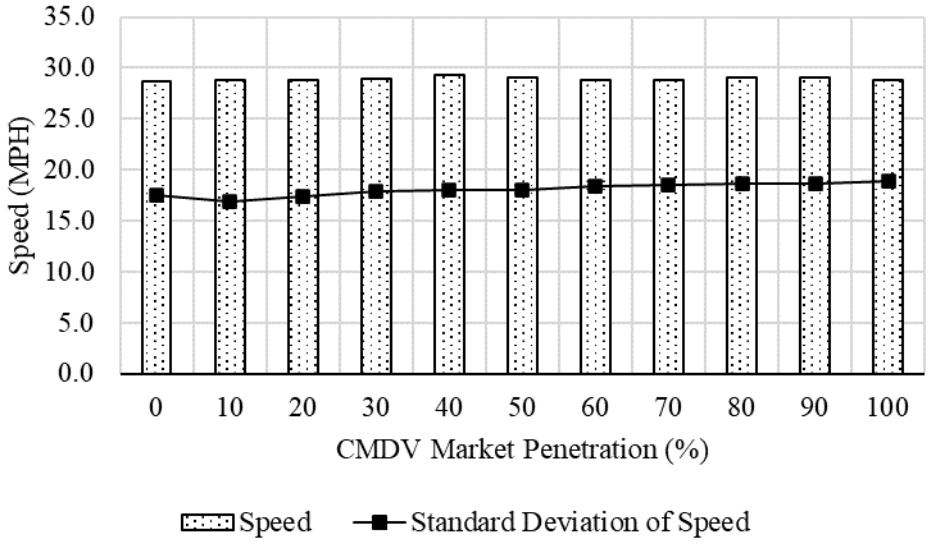

Source: FHWA.

Figure 31. Diagram. Average vehicle speed and the standard deviation of the speed under various CMDV market penetrations.

The two effects of CMDV led to the harmonization of vehicle speed and improvement of the bottleneck traffic flow, which resulted in improved vehicle fuel efficiency. As figure 32 shows, vehicle fuel efficiency increased with the CMDV market penetration. The project team observed the largest increase when the market penetration changed from 0 to 40 percent. When the CMDV market penetration was 40 percent or higher, the fuel efficiency increase became less rapid. This result indicates that 40 percent is a turning point for the CMDV performance when the driver compliance level follows the observed distribution. The speed adaptation of less than half of vehicles could already alter the speed of the traffic flow. Further increasing the CMDV market penetration could not generate additional vehicle energy benefits. The VT model gave a higher estimation than the MOVES model because the VT model used parameters of more recent vehicles than those in the MOVES model. The newer vehicles generally have higher energy performance than the older vehicles. Despite the difference in the magnitude of the results, the two models provide curves with a similar trend.

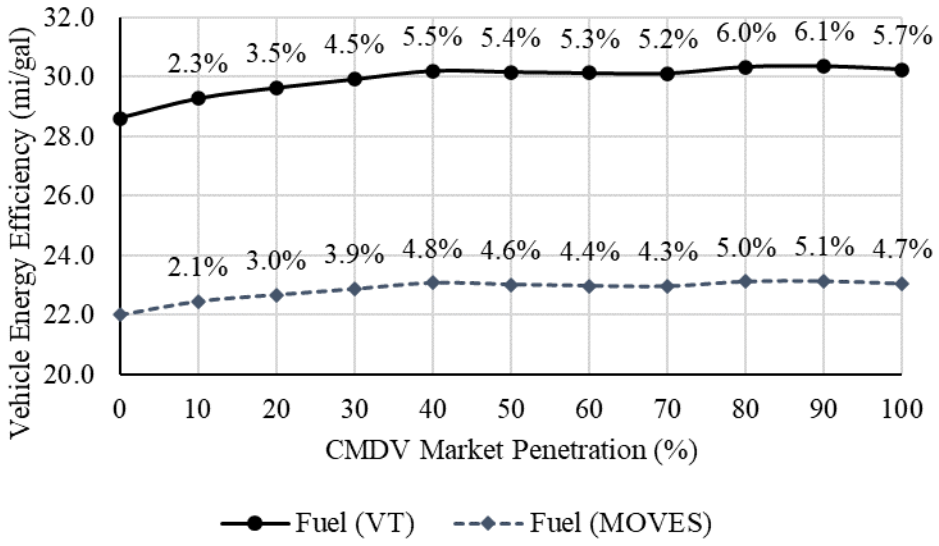

Source: FHWA.

Figure 32. Diagram. Average vehicle fuel efficiency under various CMDV market penetrations.

The effects of drivers' compliance are depicted in table 9, through table 11. The results indicate that a small change in the driver compliance level had little influence on both the average speed and fuel efficiency. The speed and fuel performance of the studied freeway corridor changed less than 2 percent as drivers' compliance level increased from 5 to 30 percent. This trend is consistent when the CMDV market penetration was 10, 20, or 100 percent. It implies that the performance of the VSA is not sensitive to the small increase of drivers' compliance, regardless of the CMDV market penetration levels. On the other hand, when all drivers fully complied with the CMDV, the vehicle energy efficiency became substantially better than the baseline compliance (see the final rows in table 9 through table 11). The standard deviation of vehicle speed significantly decreased as well. The results suggest that the effectiveness of CMDV also relies on how drivers react to the CMDV information. When drivers are willing to closely follow the CMDV instruction, the effects of CMDV can obtain an extra 2- to 3-percent improvement. Given that the energy efficiency improvement ranges from 2 to 6 percent under the baseline compliance (figure 32), the extra increase of the energy performance is significant.

Table 9. Effects of driver compliance level on the speed and vehicle fuel efficiency at 10-percent CMDV market penetration case.

Compliance Increase (%)	Fuel Efficiency from MOVES (mi/gal)	Fuel Efficiency from VT (mi/gal)	Vehicle Speed (mph)	Std Dev of Vehicle Speed (mph)
0	22.5	29.3	28.9	16.9
5	22.6	29.5	29.3	17.1
10	22.6	29.4	29.1	17.0
15	22.6	29.5	29.1	17.2
20	22.7	29.6	29.2	16.9
25	22.7	29.6	29.2	16.9
30	22.5	29.4	28.8	16.8
100	22.8	29.7	28.9	16.0

Std Dev = standard deviation.

Table 10. Effects of driver compliance level on the speed and vehicle fuel efficiency at 20-percent CMDV market penetration case.

Compliance Increase (%)	Fuel Efficiency from MOVES (mi/gal)	Fuel Efficiency from VT (mi/gal)	Vehicle Speed (mph)	Std Dev of Vehicle Speed (mph)
0	22.7	29.6	28.8	17.4
5	22.9	29.9	29.1	17.4
10	22.9	29.9	29.2	17.5
15	22.8	29.8	29.0	17.3
20	22.7	29.7	28.6	17.4
25	22.7	29.7	28.6	17.5
30	22.8	29.8	28.8	17.3
100	23.2	30.3	28.8	16.2

Std Dev = standard deviation.

Table 11. Effects of driver compliance level on the speed and vehicle fuel efficiency at 100-percent CMDV market penetration case.

Compliance Increase (%)	Fuel Efficiency from MOVES (mi/gal)	Fuel Efficiency from VT (mi/gal)	Vehicle Speed (mph)	Std Dev of Vehicle Speed (mph)
0	23.0	30.2	28.8	18.9
5	23.2	30.4	29.0	18.8
10	23.2	30.5	29.0	19.0
15	23.3	30.6	29.0	19.0
20	23.4	30.7	29.3	18.9
25	23.2	30.4	28.6	19.0
30	23.3	30.6	28.9	19.0
100	23.7	31.0	28.6	18.2

Std Dev = standard deviation.

As the compliance level was further increased to 100 percent, it substantially changed the traffic-flow patterns. Figure 33 and figure 34 show the fundamental diagrams of the bottleneck link when the CMDV market penetration was 100 percent. Table 12 shows a comparison of the averaged speed and vehicle fuel efficiency. Figure 33 depicts the results when the baseline compliance level was applied, whereas figure 34 illustrates the results with 100-percent improvement of the compliance level. Compared to figure 33, points in figure 34 shift left and up toward higher-flow regions. The CMDV speed compliance improved the traffic flow of the bottleneck.

The increased compliance level resulted in the CMDV's increased capability to regulate the traffic flow. Consequently, the CMDV speed adaptation could more effectively reduce the input flow to the bottleneck, leading to a decrease in the congestion level and the increase of the bottleneck traffic-flow rate. That explained the left and upward shift of the points in the fundamental diagram in figure 34. However, the VSA algorithm implemented in the analysis was a reactive algorithm. It reduced the input traffic flow to the bottleneck when the bottleneck traffic became congested, and it increased the input flow after the congestion disappeared. The delayed response of the VSA algorithm did not always benefit traffic flow. In some cases, the bottleneck was congested, while the onramp traffic would be light in the next few minutes. The congestion level should lessen due to the decrease of the onramp traffic disturbance. This situation naturally led to an increase in the bottleneck flow rate. However, the VSA algorithm would continue reducing the input flow to the bottleneck in this case because it still detected the congestion status of the bottleneck. This input flow reduction could overly reduce the input flow, making some of the bottleneck capacity underused (see points in the dashed box in figure 34, where the occupancy is in the middle range, but the flow rate is overly reduced by the VSA).

In other cases, the bottleneck congestion had been relieved, but the heavy onramp traffic would break down the bottleneck traffic again in the next few minutes. The VSA algorithm would increase the input flow because it only detected the light traffic condition of the bottleneck. This input flow increase could create much heavier congestion than in the no-control case (see points in the dotted box in figure 34, where the capacity reduction caused by the excessive traffic input is much higher than the rest of the points in the same occupancy range). As the increase of

drivers' compliance levels led to the enhanced VSA control capability, these undesirable control behaviors also happened more frequently. The negative effect of these behaviors could offset the benefit due to the bottleneck flow increase. This discussion indicates that a predicative algorithm is desired to generate VSAs that match the future traffic conditions. Such an algorithm is expected to enhance the performance of CMDV.

Table 12. Comparison of the baseline compliance and the full compliance level.

CMDV MPR (%)	Compliance Increase (%)	Fuel Efficiency from MOVES (mi/gal)	Fuel Efficiency from VT (mi/gal)	Vehicle Speed (mph)	Std Dev of Vehicle Speed (mph)
10	0	22.5	29.3	28.9	16.9
10	100	22.8	29.7	28.9	16.0
20	0	22.7	29.6	28.8	17.4
20	100	23.2	30.3	28.8	16.2
100	0	23.0	30.2	28.8	18.9
100	100	23.7	31.0	28.6	18.2

Std Dev = standard deviation.

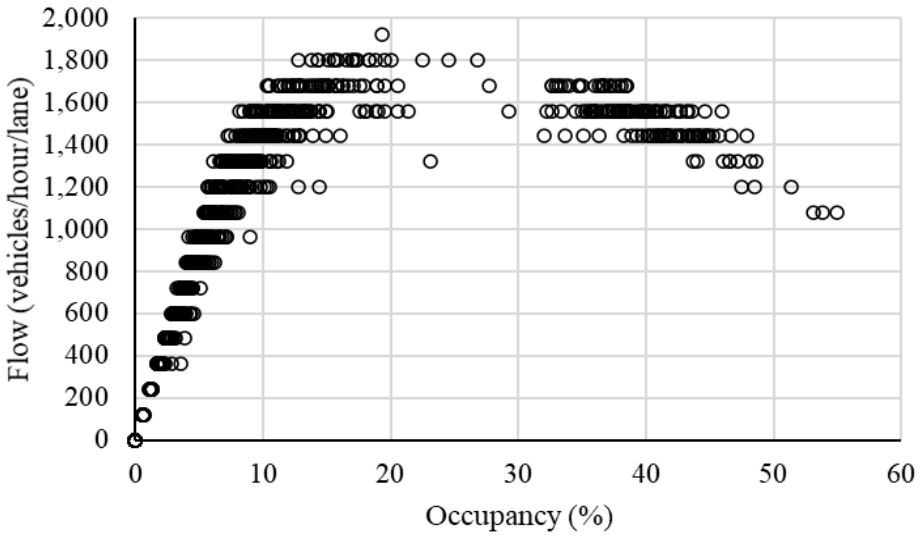

Source: FHWA.

Figure 33. Diagram. Fundamental diagram of 20-percent CMDV market penetration with the baseline compliance level.

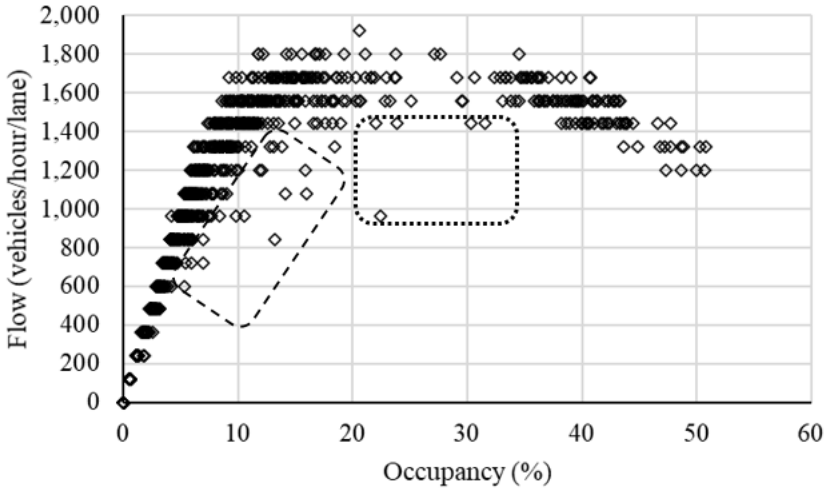

Source: FHWA.

Figure 34. Diagram. Fundamental diagram of 20-percent CMDV market penetration with the full compliance level.

When the VSA algorithm was applied with CACC vehicles, the vehicles perfectly adopted the advisory speed. As a result, the undesired control behavior became more prominent than in the CMDV case. For the 30-percent CACC market penetration case, the fundamental diagrams with and without the I2V advisory speed are displayed in figure 35 and figure 36. The comparison of the two plots shows that the congestion at the bottleneck was greatly improved by the VSA control. Nonetheless, there was also a great increase in the cases where the bottleneck capacity was underused (e.g., points in the dashed box in figure 36). In this case, the queued vehicles upstream from the bottleneck spent more time in the congested condition, reducing the speed and vehicle energy performance of the corridor. The comparison between the traffic speed and vehicle fuel economy with and without VSA is shown in table 13. The vehicle fuel efficiency was improved by 5–6 percent, while the speed remained the same with and without the VSA. The vehicle energy efficiency improvement was in the same range as the CMDV cases with 40 percent or higher market penetration. If the VSA algorithm can eliminate the capacity underuse condition, the performance of the VSA under the CAV condition may be much better.

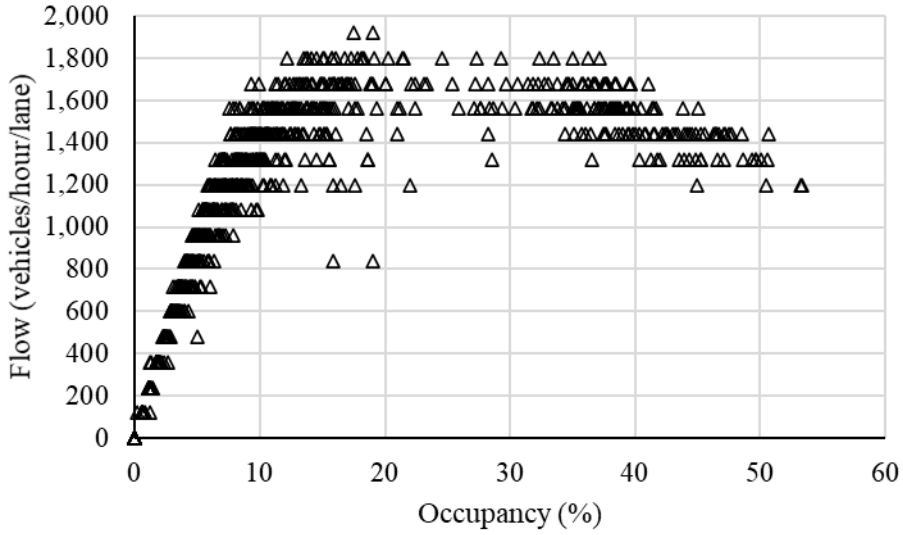

Source: FHWA.

Figure 35. Diagram. Fundamental diagram of 30-percent CACC vehicle market penetration without the VSA.

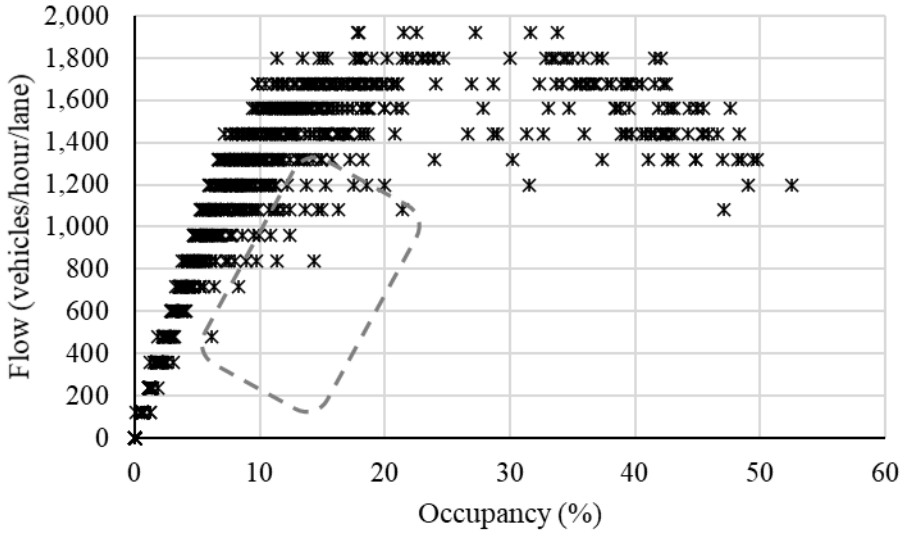

Source: FHWA.

Figure 36. Diagram. Fundamental diagram of 30-percent CACC vehicle market penetration with the VSA.

Table 13. Comparison of the baseline compliance and the full compliance level.

Comparison	Fuel Efficiency from MOVES (mi/gal)	Fuel Efficiency from VT (mi/gal)	Vehicle Speed (mph)	Std Dev of Vehicle Speed (mph)
No VSA	22.8	29.3	30.8	18.7
VSA	23.9	31.1	30.6	15.2
Percent change	5.1 percent	6.0 percent	-0.9 percent	-18.9 percent

Std Dev = standard deviation.

The results shown in table 13 indicate that the reactive nature of the VSA controller impedes the improvement of the SPDHRM and vehicle fuel efficiency, even when the CMDV drivers are willing to fully comply with the advisory speed or the CACC vehicles perfectly adopt the advisory speed. A possible direction for further improvement is to use a predictive VSA algorithm to generate advisory speeds. The predictive algorithm can estimate the short-term disturbances from the onramp traffic. It then computes the input flow to the bottleneck that matches the bottleneck traffic condition, leading to a more efficient bottleneck operation. However, the traffic flow changes rapidly within the bottleneck area; a fast and localized speed control is desired to create input flows that maximize the bottleneck throughput. Such speed control might be difficult for human drivers to implement. In this sense, the predictive VSA algorithm is expected to perform best with the automated speed controller, such as CACC. Another direction of improvement combines the onramp metering and VSA control. With the RM, the disturbance caused by the onramp traffic becomes controllable. The VSA algorithm can generate speed commands based on the metering rate. Since the combined implementation of VSA and RM does not require frequent change of a vehicle's reference speed in the bottleneck area, it is easier for human drivers to follow.

SUMMARY

This section presented the modeling approach the team used to depict the CMDV drivers' compliance behaviors in response to the I2V-based VSA in mixed traffic. The CMDV drivers' speed adaptation due to VSA was captured by a stimulus-response model, which allowed drivers' desired speed to change based on the VSA level. A random variable was used to model the fluctuation of the desired speed in the traffic flow. The field VSA test data were used for the model calibration and validation so that the CMDV drivers' speed adaptations represented real-world drivers' speed patterns under the influence of VSA control. The CMDV drivers' compliance was best modeled with empirical distributions of two speed groups: a low-speed group when the VSA was less than 35 mph and a high-speed group when the VSA was more than 35 mph. The calibration and validation process adopted distribution fitting and hypothesis test approaches to determine the parameters of the empirical distribution. The two-sample KS test was conducted to show the goodness of fit of those empirical cumulative distribution functions with the real-world data. The CMDV model then applied the validated compliance distribution to evaluate the effectiveness of CMDVs on the freeway corridor operations.

The model calibration and validation datasets represent drivers' responses to the VSA displayed on the roadside message sign instead of directly fed into the vehicle. Admittedly, such feedback will have less influence on the driver than in-vehicle displays. For this reason, this research designed a sensitivity analysis to explore the effectiveness of the CMDV speed adaptation under

various CMDV market penetrations and driver compliance levels. In addition, the sensitivity analysis identified the impact of using automated speed controllers with the I2V-based VSA algorithm.

The analysis results indicate that the I2V-based VSA control could have substantial effects on the freeway corridor when the CMDV market penetration is 10–40 percent. With the advisory speed, the average speed and variation of the speed remained similar to the no-control case, but the vehicle fuel efficiency increased 2–5 percent, depending on the results of different energy models. These results suggest that the speed adaptation of a few connected drivers could substantially change the traffic-flow pattern, leading to more energy-efficient traffic flow. As the CMDV market penetration further increased, the reduction of the speed variation and the improvement of the fuel efficiency stabilized. When the CMDV market penetration reached 100 percent, the average speed decreased by about 1 percent and the vehicle fuel economy increased 5–6 percent.

The performance of the VSA algorithm was not sensitive to small changes in the driver compliance level. However, the traffic- flow patterns changed significantly when the CMDV drivers fully complied with the VSA. The full compliance brought about 2–3 percent extra benefit on vehicle fuel efficiency. If the VSA algorithm could generate advisory speed based on the predicted traffic conditions, the effects of CMDV should become further increased. When the VSA was implemented with CACC, the CACC controller could perfectly adopt the advisory speed as the reference speed. Nonetheless, adding the VSA algorithm to the CACC vehicles did not bring notable benefits to the freeway corridor (e.g., 5- to 6-percent increase of the energy efficiency) because the VSA controller tended to underuse the bottleneck capacity due to its delayed response to the traffic variations. To address this shortcoming, the team recommends a predictive VSA algorithm or the combined application of VSA and RM.

This report details the implementation of the proposed CMDV model in a simulation framework that also has a calibrated HV, AV, and CAV model. The results detailed in this report were obtained using the Aimsun modeling platform. However, the model logics are open source, and the information in this document may be helpful for researchers and analysts to implement the modeling framework in their customized tools of choice.

CHAPTER 4. LC FOR LIGHT-DUTY CAVS

LIST OF VARIABLES

This section lists all variables used in this chapter along with their definitions. Those variables only apply to the CAV lane-change model described in this chapter. The same notation might represent different variables in other chapters of the report.

a_{bias} = asymmetry term with a positive value for left turn and negative value for right turn, guaranteeing the keep-right directive rule.
$\tilde{a}_{\mathrm{CAV}}(t)$ = target acceleration of the CAV in the current lane at time t.
$\hat{a}_{\mathrm{CAV}}(t)$ = target acceleration of the CAV in the target lane at time t.
$\hat{a}_f(t)$ = target acceleration of the following vehicle in the target lane at time t.
b_{CAV} = maximum deceleration of the CAV.
$\hat{b}_f$ = maximum deceleration of the following vehicle in the target lane.
$\hat{b}_l$ = maximum deceleration of the preceding vehicle in the target lane.
c = case index.
C = length of vehicle (same for CAVs and HVs).
D = test track lane width.
E_c^t = error between the simulated LC time point and field-observed LC time point in case c.
g_{CAV} = desired time gap of the CAV.
$\mathcal{J}$ = CAV set.
j = CAV index.
J = total number of CAVs.
$\mathcal{K}$ = HV set.
k = HV index.
K = total number of HVs.
K_1, K_2 = parameters of the linearized ACC CF model.
L = test track segment length.
$\mathcal{N}$ = vehicle set (including CAVs and HVs).
N = total number of vehicles.
n = vehicle index.
Q_c = total number of time points in case c.
q = time point index in calibration and validation.
q_{all} = total traffic throughput.
q_{CAV} = CAV throughput.
q_{HV} = HV throughput.
q_1 = mainline throughput.
q_2 = onramp throughput.
R = right-exiting vehicle.
$RMSE_c^x$ = root mean square error of the CAV longitudinal positions in case c.
$RMSE_c^v$ = root mean square error of the CAV speeds in case c.
$R^{\mathrm{X}}(t)$, $R^{\mathrm{Y}}(t)$ = longitudinal gap and the lateral offset between the CAV and vehicle 2 at time t.
r_1^{CAVdiv} = mainline CAV diverging rate.
r_2^{CAVdiv} = onramp CAV diverging rate.

r_1^{CAV} = mainline CAV penetration rate.
r_2^{CAV} = onramp CAV penetration rate.
r_1^{HVdiv} = mainline HV diverging rate.
r_2^{HVdiv} = onramp HV diverging rate.
r^{CAV} = CAV penetration rate in case study ($r^{CAV} = r_1^{CAV} = r_1^{CAV}$).
$S(t)$ = expected minimum safety distance calculated by Gipps' safe distance algorithm at time t.
s_0 = minimum gap.
$\mathrm{STD}v_{\mathrm{CAV}}$ = CAV speed standard deviation in the simulation period.
$\mathrm{STD}v_{\mathrm{HV}}$ = HV speed standard deviation in the simulation period.
$\mathrm{STD}v_{\mathrm{all}}$ = speed standard deviation across all vehicles in the simulation period.
t = current simulation time.
T = through vehicle.
τ_{CAV} = reaction time of the CAV.
t_c^{LCobs} = field-observed LC time point in case c.
t_c^{LCcal} = calibrated LC time point in case c.
t_c^{LCval} = validated LC time point in case c.
T_j = number of time points that CAV j was running in the simulation period.
T_k = number of time points that HV k was running in the simulation period.
$v_{\mathrm{CAV}}(t)$ = speed of the CAV at time t.
$\hat{v}_f(t)$ = speed of the following vehicle in the target lane at time t.
$v_l(t)$ = speed of the preceding vehicle in the current lane at time t.
$\hat{v}_l(t)$ = speed of the preceding vehicle in the target lane at time t.
$\hat{w}_f$ = maximum acceleration of the following vehicle in the target lane.
$x_{\mathrm{CAV}}(t)$ = longitudinal position of the CAV at time t.
$x_{c,q}^{obs}$ = field-observed longitudinal position of the CAV at time point q in case c.
$x_{c,q}^{cal}$ = calibrated longitudinal position of the CAV at time point q in case c.
$x_{c,q}^{val}$ = validated longitudinal position of the CAV at time point q in case c.
$\hat{x}_f(t)$ = longitudinal position of the following vehicle in the target lane at time t.
$\hat{x}_l(t)$ = longitudinal position of the preceding vehicle in the target lane at time t.
$x_l(t)$ = longitudinal position of the preceding vehicle in the current lane at time t.
$x_2(t)$, $y_2(t)$ = longitudinal and lateral positions of vehicle 2 at time t.
$(x'_{\mathrm{CAV}}, y'_{\mathrm{CAV}})$ = CAV LC trajectory.
$y_{\mathrm{CAV}}(t)$ = lateral position of the CAV at time t.
$v_{c,q}^{obs}$ = field-observed speed of the CAV at time point q in case c.
$v_{c,q}^{cal}$ = calibrated speed of the CAV at time point q in case c.
$v_{c,q}^{val}$ = validated speed of the CAV at time point q in case c.
$\bar{v}_{CAV}$ = all CAVs' average speed in the simulation period.
$\bar{v}_{HV}$ = all HVs' average speed in the simulation period.
$\bar{v}_{all}$ = average speed across all vehicles in the simulation period.
$v_j(t)$ = CAV j speed at time point t.
$v_k(t)$ = HV k speed at time point t.
$\hat{v}_j$ = average speed of CAV j in the simulation period.
$\hat{v}_k$ = average speed of HV k in the simulation period.

β = parameters set.
Δa = acceleration changing threshold, preventing LCs when the associated advantage is marginal.
Δt = simulation timestep.
ΔT = IDM time gap.
$\Delta v(t) = v_{CAV}(t) - \hat{v}_f(t)$ with unit ft/s.
δ = acceleration exponent.
φ = CAV cooperation rate.

PURPOSE OF THE MODEL

CAV technologies can significantly improve traffic safety and reduce traffic congestion. SAE defines six distinct levels of automated control; with each increasing level, the human driver cedes more control of the vehicle to the automated system (Smith 2013). Level 1 automation is defined as when the system can handle longitudinal control of the vehicle under certain conditions and is available in many vehicles today (e.g., ACC on freeways) (Xiao and Gao 2010; Gunter et al. 2019). LC control is a fundamental leap from Level 1 to higher levels of automation, i.e., SAE Levels 2–5 (Smith 2013). Thus, to robustly model the impacts of higher levels of automation, analysts and researchers desire accurate models of CAV LC.

Existing studies of LC control are limited to static-motion planning without considering surrounding HV dynamics in a mixed-traffic environment (B. Li et al. 2018; Xu et al. 2012). In addition, motion planning and LC decision are separately studied in a static setting. However, these two components are interdependent in real-world driving. Vehicle motions may change dynamically and affect the LC decision consequentially. More importantly, there lacks a comprehensive modeling framework that incorporates both longitudinal and lateral movements of CAVs across different cooperation classes in a mixed-traffic environment. Without such a framework, traffic operators and transportation planners may not fully understand or be well prepared for the impacts of CAV LC behaviors in near-future mixed traffic. Further, without this framework bridging an individual vehicle's behavior-to-system performance, there will remain a gap between automakers that purely focus on an individual vehicle's functions and transportation stakeholders concerned with transportation system performance.

Motivated by these research gaps, this study proposed a new mixed-traffic simulation framework that integrates vehicle CF and LC movements in mixed traffic with CAVs of different cooperation behaviors. This framework is centered at a CAV LC model integrated with CF dynamics in mixed traffic. The model includes three key components: a CF component, an LC decisionmaking component, and an LC/LC abortion path generation and following component. The research team formulated incentive and safety criteria to model both mandatory and incentive-based LC behaviors. An LC abortion module is activated whenever the safety criterion fails to be met before the CAV passes the lane marking to model this new CAV feature. Field data (Wang et al. 2020) were leveraged to demonstrate how to calibrate and validate the proposed CAV model in the mandatory LC context. According to the calibration and validation results, this model's results well-replicated the field observations. To demonstrate the applicability of the proposed model, the team further implemented a case study of a segment of the I–75 freeway in the Tampa Bay area on the Vissim microsimulation platform (PTV Group 2018). The case study also drew a set of managerial insights into how different parameter

settings impact the traffic performance, including mobility and traffic stability, accounting for uncertain and varying technologies in the process of following CAV deployment. For example, it is noted that the impacts of several key parameters (e.g., on CAV cooperation levels and their propensity to make discretionary LCs) on traffic performance are nonlinear (e.g., first improving and then degrading). These findings indicate that efforts may be taken to optimize these parameters from the perspective of transportation operators (e.g., facilities and policies to promote vehicle cooperation) and automakers (e.g., tuning parameters in their LC models) for the best traffic performance. These insights may help stakeholders better understand and prepare for near-future mixed-CAV traffic with different LC behaviors and suggest the optimal LC configurations for automakers to achieve the best overall traffic performance.

Considering uncertain technology developments and unknown behaviors in emerging mixed traffic, the proposed framework is meant to be adaptable to more general scenarios other than those presented in this study. For example, this study only used the linearized ACC CF model (i.e., Milanés and Shladover 2014), which can be easily replaced with other customized CF models (e.g., CACC, platooning) per application requirements. Further, this study uses the default HV behavior models obtained from the existing pure HV traffic, which may vary in emerging mixed traffic. For example, Zhao et al. (2020) showed that the behavior for an HV to follow a CAV may vary drastically from the existing HV CF behavior when the CAV has obvious features for the HV driver to identify, yet this behavior may remain unchanged if the HV cannot differentiate the vehicle type. In the cases that HV exhibit different driving behaviors, the new behavior models can be used instead of the default ones in this framework.

The next section describes the proposed simulation framework and the CAV LC model. Then, how to use field data to calibrate and validate this model is illustrated. Next, basic information is provided for model implementation. A case study with the I–75 section is presented to illustrate the applicability of the proposed framework and draw managerial insights. The final section summarizes this chapter.

MODEL DEVELOPMENT AND LOGIC

Description of Model Logic

This section briefly introduces the proposed mixed-traffic simulation framework and the CAV LC model, as illustrated in figure 37. The proposed framework can fully control HVs and CAVs in mixed traffic. A vehicle set $\mathcal{N}$ is defined containing N vehicles indexed by $n \in \mathcal{N} := \{1, 2, \ldots, N\}$. Each vehicle is initialized with its type (i.e., HV or CAV) and route (i.e., origin and destination). CAV cooperation rate is also defined, indicating the probability of a CAV being cooperative to CAV LCs on an adjacent lane(s). For the HV control component, customized HV, CF, and LC strategies can be implemented according to the application requirements. Please refer to recent studies on HVs' responses to AVs with and without a differentiable appearance for HV behavior modeling in mixed traffic (Zhao et al. 2020; Hamdar et al. 2019). This study mainly focused on the CAV LC model shown in boldface in figure 37.

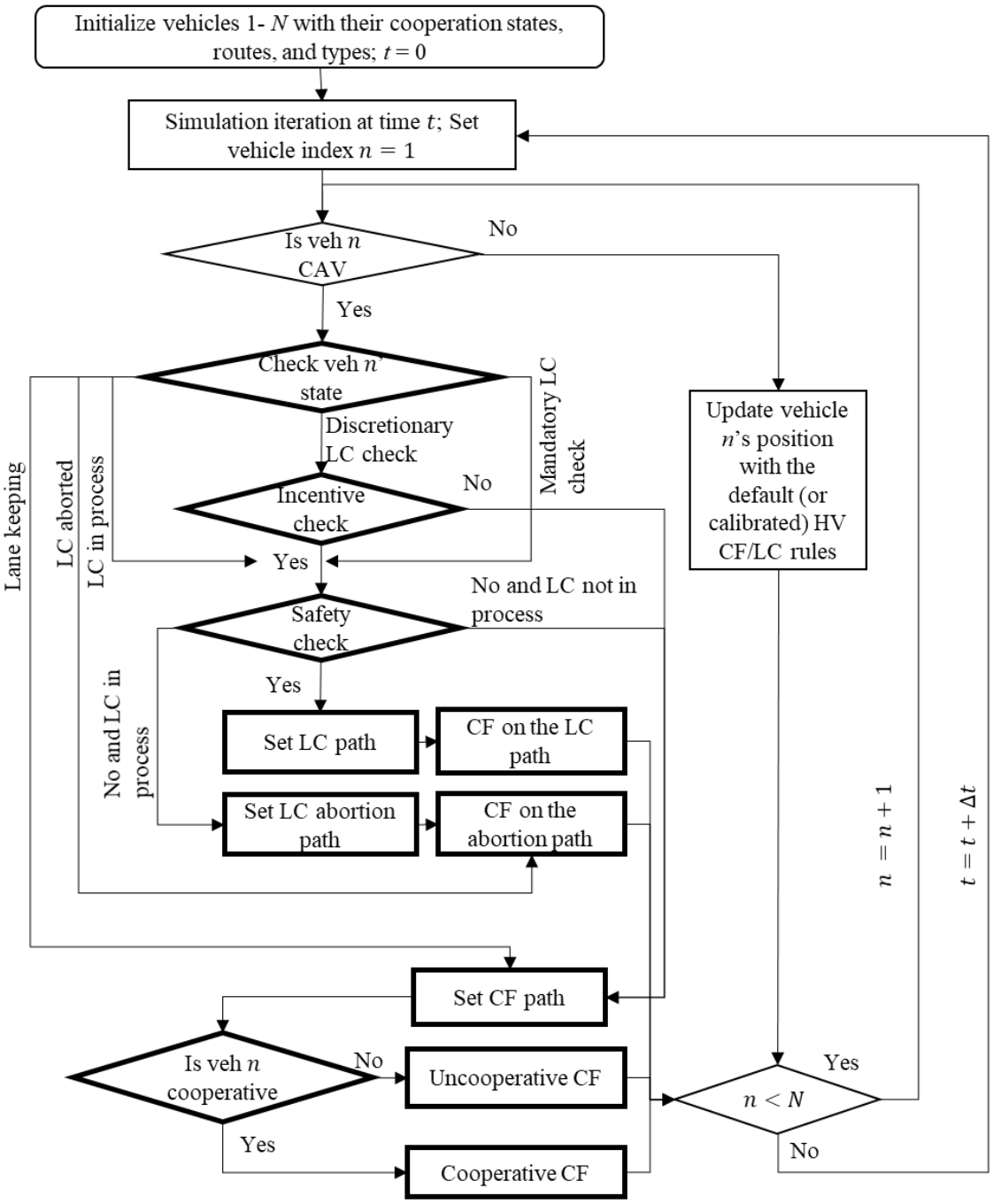

Source: FHWA.

Figure 37. Flowchart. The proposed mixed-traffic simulation framework.

CAV States

At simulation time *t*, CAV *n*'s possible states are listed as follows:

- Mandatory LC checking: CAV *n* changes to a specific lane to reach its destination. For example, CAVs "R" in the middle lane within the mandatory LC zone in figure 38.

- Discretionary LC checking: CAV *n* can stay on any one of multiple lanes. For example, CAV "R" outside of the mandatory LC zone and CAVs "T" in figure 38.
- Lane keeping: CAV *n* stays in the same lane to reach the destination or due to regulation (e.g., solid markings). For example, CAV "R" in the right lane within the mandatory LC zone.
- LC in process: CAV *n* has already initiated the LC movements. For example, the highlighted CAV "R" in the solid red circle in figure 38.
- LC abortion in process: CAV *n* just aborted the LC to come back to the current lane. For example, the highlighted CAV "T" in the red dashed ellipse in figure 38.

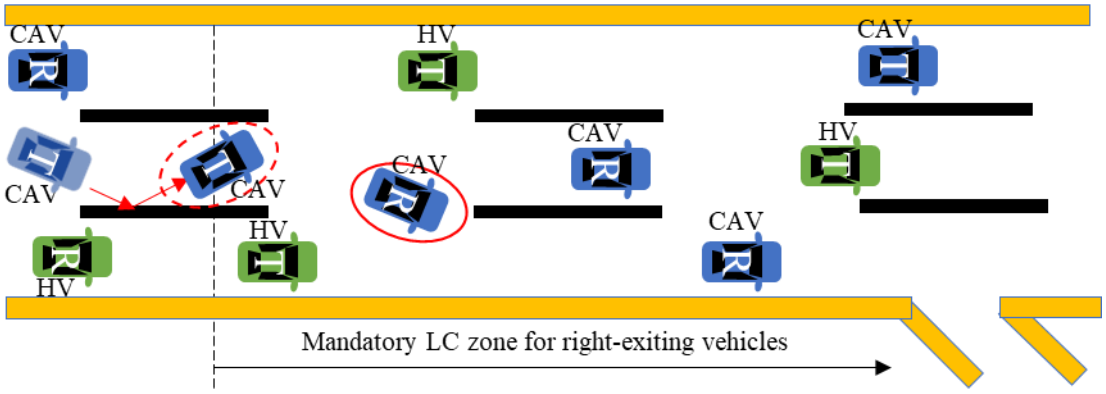

Source: FHWA.
R = right-exiting vehicle.
T = through vehicle.

Figure 38. Illustration. Vehicle states.

CAV CF

As shown in figure 39, the center line of the lane is set as CAV CF path (i.e., the red dashed line). At simulation time *t*, CAV *n*'s CF behavior is defined based on the cooperative state.

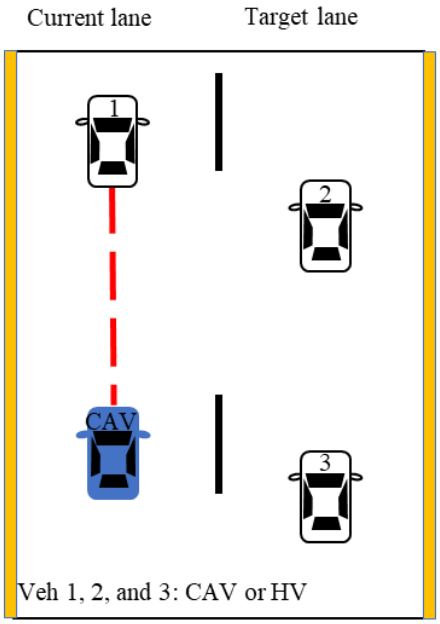

Source: FHWA.
Veh = vehicle.

Figure 39. CAV CF path.

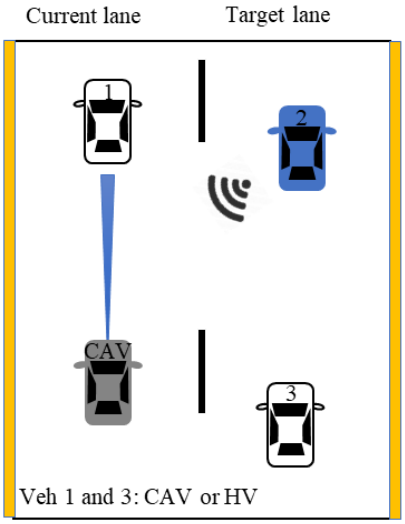

Source: FHWA.
Veh = vehicle.

A. Uncooperative CAV.

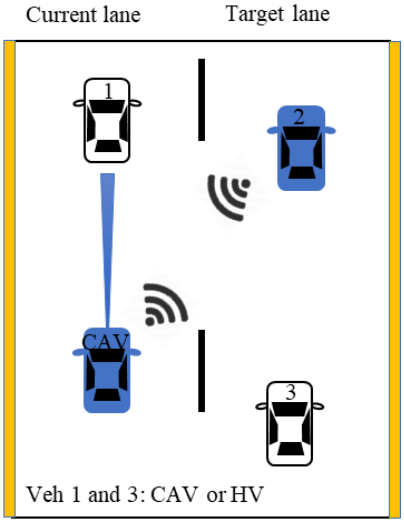

Source: FHWA.
Veh = vehicle.

B. Cooperative CAV.

Figure 40. Illustration. Uncooperative/cooperative CAV.

The CAV cooperative states are defined as follows:

- CAV *n* uncooperative: CAV *n* only follows the preceding vehicle in the current lane regardless of the LC signals(s) of the preceding CAV(s) in the neighboring lane(s), shown in figure 40-A.

- CAV *n* cooperative: CAV *n* follows not only the preceding vehicle in the current lane but also the preceding CAV(s) in the neighboring lane(s) with the LC signal(s) on, shown in figure 40-B.

CAV LC

At simulation time *t*, CAV *n*'s LC behavior contains two components: LC decisionmaking and LC/LC abortion path generation and following.

LC Decisionmaking

LCs are divided into two categories: discretionary LCs and mandatory LCs. Discretionary LCs are optional and take place when vehicles want to make an LC to improve mobility (e.g., pass a slower-moving preceding vehicle). Mandatory LCs are implemented when vehicles make an LC to reach their desired destinations. The involved LC decision criteria are defined as follows:

- Lane marking criterion: Before any LC behavior, CAV *n* checks the current lane marking. The following criteria are checked only when the lane marking is dashed, communicating that LC behavior is permitted. Otherwise, CAV *n* is not allowed to make an LC now.

- Incentive criterion: Defined only for discretionary LCs. It asks whether CAV *n* can travel faster by conducting an LC to follow a vehicle in the target lane—i.e., vehicle 2 in figure 41-A. If yes, the incentive criterion is met.

- Safety criterion: Defined for both discretionary LCs and mandatory LCs. It asks whether or not CAV *n*'s deceleration induced by following the preceding vehicle in the target lane—i.e., vehicle 2 in figure 41-B—is greater than a safety/comfort deceleration threshold and whether or not the deceleration of the following vehicle in the target lane—i.e., vehicle 3 in figure 41-B—induced by CAV *n*'s LC is greater than a safety/comfort deceleration threshold. If both are yes, the safety criterion is met.

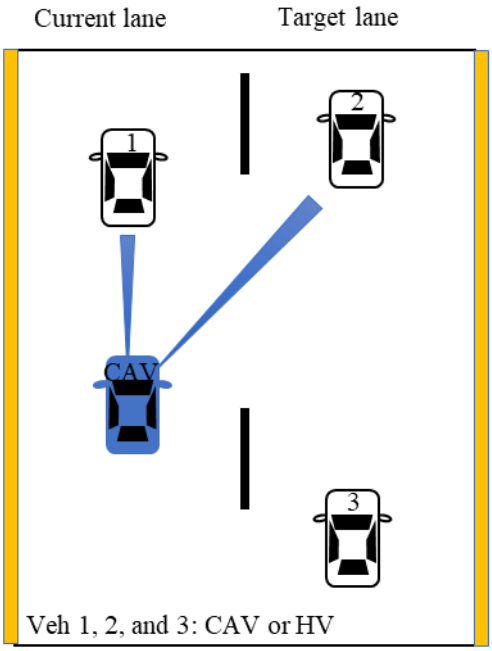

Source: FHWA.
Veh = vehicle.

A. Incentive criterion.

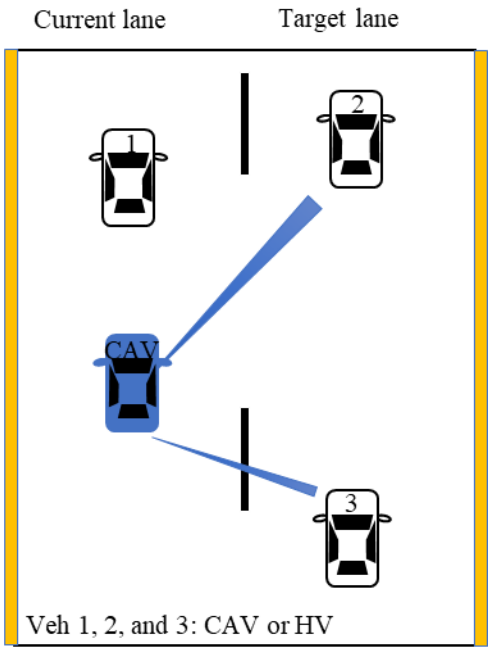

Source: FHWA.
Veh = vehicle.

B. Safety criterion.

Figure 41. Illustration. Incentive and safety criteria.

LC/LC Abortion Path Generation and Following

For a discretionary LC, an LC path is generated and followed if both the incentive and safety criteria are met for CAV *n*. For a mandatory LC, an LC path is generated and followed if the safety criterion is met for CAV *n*. The safety criterion is continuously checked before the CAV crosses the lane marking. An LC abortion path is generated and followed if the safety criterion fails to be met before the CAV crosses the lane marking. This means CAV *n* goes back to its original lane to guarantee safety.

Model Development

CAV CF Model

A linear ACC model (Milanés and Shladover 2014) is used to control CAVs longitudinal movements, formulated in figure 42:

$$\tilde{a}_{\mathrm{CAV}}(t) = K_1(x_l(t) - x_{\mathrm{CAV}}(t) - C - v_{\mathrm{CAV}}(t)g_{\mathrm{CAV}}) + K_2\big(v_l(t) - v_{\mathrm{CAV}}(t)\big), \forall t \in \mathcal{T}$$

Figure 42. Equation. Linear ACC model.

e-CAV LC Model

e-LC Decisionmaking Model

First, the lane marking type between the current and target lanes is checked to verify whether or not the CAV is permitted to make an LC. According to the *Manual of Uniform Traffic Control Devices*, dashed lane marking indicates drivers are permitted to make LCs; drivers are not permitted to change lanes when lane marking is solid (MUTCD 2006). If the marking type is dashed, the marking criterion is met. Otherwise, the CAV maintains its current lane.

Second, the incentive criterion checking is necessary for CAV discretionary LCs, formulated in figure 43. The incentive criterion is only met when the target acceleration of the CAV following preceding vehicle in the target lane is greater than that in the current lane by a certain value, i.e., Δa plus a_{bias}.

$$\hat{a}_{\mathrm{CAV}}(t) - \tilde{a}_{\mathrm{CAV}}(t) > \Delta a + a_{bias}$$

Figure 43. Equation. Incentive criterion.

Third, the safety criterion checking is necessary for both CAV discretionary and mandatory LCs. The safety criterion consists of two criteria with respect to the preceding and following vehicles in the target lane, respectively, as demonstrated in figure 41-B.

First, the CAV checks the distance between the CAV longitudinal position and the preceding vehicle longitudinal position in the target lane when the LC is finished. *S(t)* is the expected minimum safety distance calculated by Gipps' safe distance algorithm (Gipps 1981), shown in figure 44.

$$S(t) = v_{\mathrm{CAV}}(t)\tau_{\mathrm{CAV}} + \frac{\left(v_{\mathrm{CAV}}(t)\right)^2}{2b_{\mathrm{CAV}}} - \frac{\left(\hat{v}_l(t)\right)^2}{2\hat{b}_l}, \forall t \in \mathcal{T}$$

Figure 44. Equation. Gipps' safe distance.

If $\hat{x}_l(t) - x_{\mathrm{CAV}}(t) - C \geq S(t)$, the CAV LC does not cause a deceleration to the CAV that is too dramatic (Wang et al. 2020). Hence, the safety criterion with respect to the preceding vehicle in the target lane is met. $\hat{x}_l(t)$ is the longitudinal position of the preceding vehicle at time *t* in the target lane with unit feet, $x_{\mathrm{CAV}}(t)$ is the longitudinal position of CAV *n* at time *t* with unit feet, and *C* is the uniform vehicle length for CAVs and HVs with unit feet.

The second criterion is for the following vehicle in the target lane, formulated in figure 45. The intelligent driver model (IDM) is used to calculate the target acceleration of the following vehicle in the target lane $\hat{a}_f(t)$ (Treiber 2013; Wang et al. 2020).

$$\hat{a}_f(t) = \hat{w}_f \left[1 - \left(\frac{\hat{v}_f(t)}{v_{\mathrm{CAV}}(t)}\right)^{\delta} - \left(\frac{S^*(\hat{v}_f(t), \Delta v(t))}{\hat{S}(t)}\right)^2\right], \forall t \in \mathcal{T}$$

$$S^*(\hat{v}_f(t), \Delta v(t)) = s_0 + \max\left(0, \hat{v}_f(t)\Delta \mathrm{T} + \frac{\hat{v}_f(t)\left(v_{\mathrm{CAV}}(t) - \hat{v}_f(t)\right)}{2\sqrt{-\hat{w}_f \hat{b}_f}}\right), \forall t \in \mathcal{T}$$

$$\hat{S}(t) = x_{\mathrm{CAV}}(t) - \hat{x}_f(t) - C, \forall t \in \mathcal{T}$$

Figure 45. Equation. Target acceleration calculated by IDM.

If $\hat{a}_f(t) \geq \hat{b}_f(t)$, the CAV LC maneuver does not cause deceleration to the following vehicle in the target lane that is too dramatic. Hence, the safety criterion concerning the following vehicle in the target lane is met.

LC/e-LC Abortion Path Generation and Following Model

After all criteria are met, a smooth two-dimensional (2D) spatial LC path is generated and updated at each timestep for the CAV to follow and complete the LC, reaching its final target position—obtained with the equation in figure 46—safely and comfortably. A sine-function-based LC path (i.e., the black dotted curve in figure 48) is applied to generate a smooth trajectory at time *t* composed of discrete points $(x'_{\mathrm{CAV}}, y'_{\mathrm{CAV}})$ in the local coordinate system, formulated in figure 46 (Wang et al. 2020):

$$y'_{\mathrm{CAV}}(t) = \frac{R^{\mathrm{Y}}(t)}{2\pi}[\Delta \mathrm{X} - \sin(\Delta \mathrm{X})] + y_{\mathrm{CAV}}(t), x'_{\mathrm{CAV}} \in [x_{\mathrm{CAV}}(t), x_2(t) - S(t) - C], \forall t \in \mathcal{T}$$

$$\Delta \mathrm{X} = \frac{2\pi}{R^{\mathrm{X}}(t)}\left(x'_{\mathrm{CAV}}(t) - x_{\mathrm{CAV}}(t)\right)$$

$$R^{\mathrm{X}}(t) = x_2(t) - S(t) - x_{\mathrm{CAV}}(t) - C, \forall t \in \mathcal{T}$$

$$R^{\mathrm{Y}}(t) = y_{\mathrm{CAV}}(t) - y_2(t), \forall t \in \mathcal{T}$$

Figure 46. Equation. A sin-function-based LC path.

In the large-scale simulation, a linear function LC path (i.e., the solid red line in figure 48) was used to replace the sine-function-based LC path (i.e., the black dotted curve in figure 48) for simplicity, formulated in figure 47:

$$y'_{\mathrm{CAV}}(t) = y_{\mathrm{CAV}}(t) + \frac{R^{\mathrm{Y}}(t)}{R^{X}(t)}\left(x'_{\mathrm{CAV}}(t) - x_{\mathrm{CAV}}(t)\right), x'_{\mathrm{CAV}} \in [x_{\mathrm{CAV}}(t), x_2(t) - S(t) - C], \forall t \in \mathcal{T}$$

Figure 47. Equation. A linear function LC path.

The safety criterion is continuously checked before the CAV crosses the lane marking. The CAV LC is aborted if it fails to meet the safety criterion. In this scenario, the LC abortion path (i.e., the green dashed line in figure 48) is generated and followed. The CAV goes back to its original lane following the LC abortion path. With the LC abortion mechanism, CAV LC safety can be guaranteed.

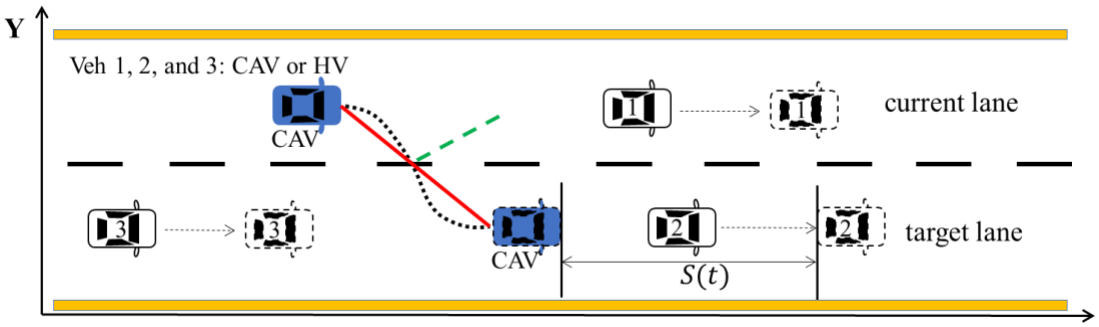

Source: FHWA.
Veh = vehicle.

Figure 48. Illustration. CAV LC/LC abortion path.

During the LC process, the CAV uses the ACC model to follow the preceding vehicles in the current and target lanes (i.e., vehicles 1 and 2 in figure 49-A) before it passes the lane marking. After the CAV passes the lane marking, it only follows the current preceding vehicle—i.e., vehicle 2 in figure 49-B—using the ACC model.

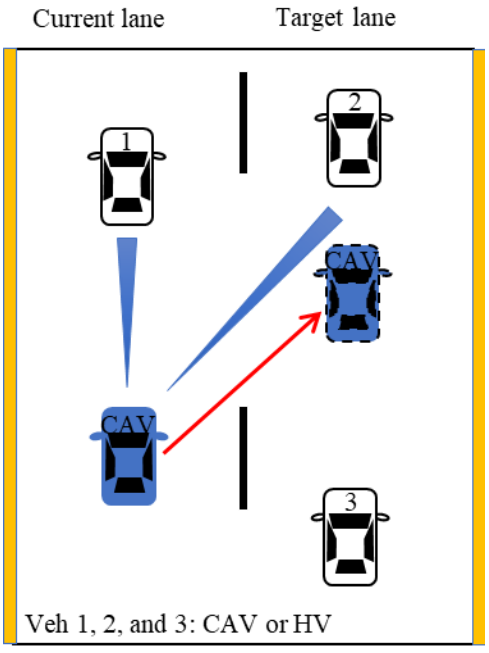

Source: FHWA.
Veh = vehicle.

A. CF before the lane marking.

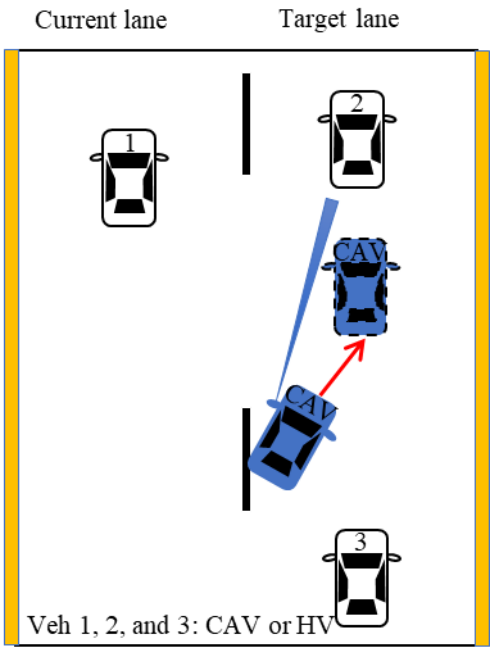

Source: FHWA.
Veh = vehicle.

B. CF after the lane marking.

Figure 49. Illustration. CF of LC.

During the LC abortion process, the CAV uses the ACC model to follow the preceding vehicles in the current lane (i.e., vehicle 1 in figure 50) and goes back to the center line of the lane.

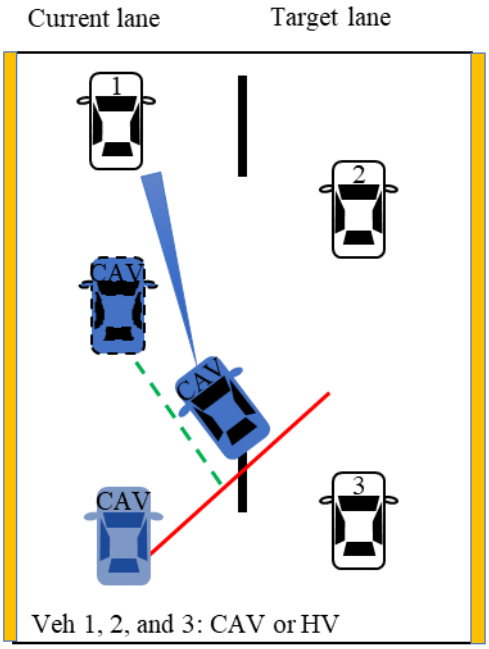

Source: FHWA.
Veh = vehicle.

Figure 50. Illustration. CF of LC abortion.

MODEL CALIBRATION AND VALIDATION

Model Calibration

To demonstrate how to calibrate the proposed CAV LC model, the researchers used field data collected from small-scale field experiments of a CAV mandatory LC model with three surrounding HVs collected during a previous study (Wang et al. 2020). The CAV mandatory LC model flow chart is presented in figure 51. This chart is just a simplification of the proposed CAV LC model in the mandatory LC context in figure 37. In the field experiments, the CAV used the ACC model to follow HVs 1 and 2, and continuously checked the safety criterion considering HV 2 and HV 3. Once the safety criterion was met, a sine-function-based LC path (i.e., figure 48) was generated for the CAV to follow. The safety criterion was continuously checked in the LC path-following process, and the LC maneuver was aborted if the safety criterion failed to be met before the CAV crossed the lane marking. When the CAV reached the target position (i.e., the center line of the target lane) it successfully made an automated LC.

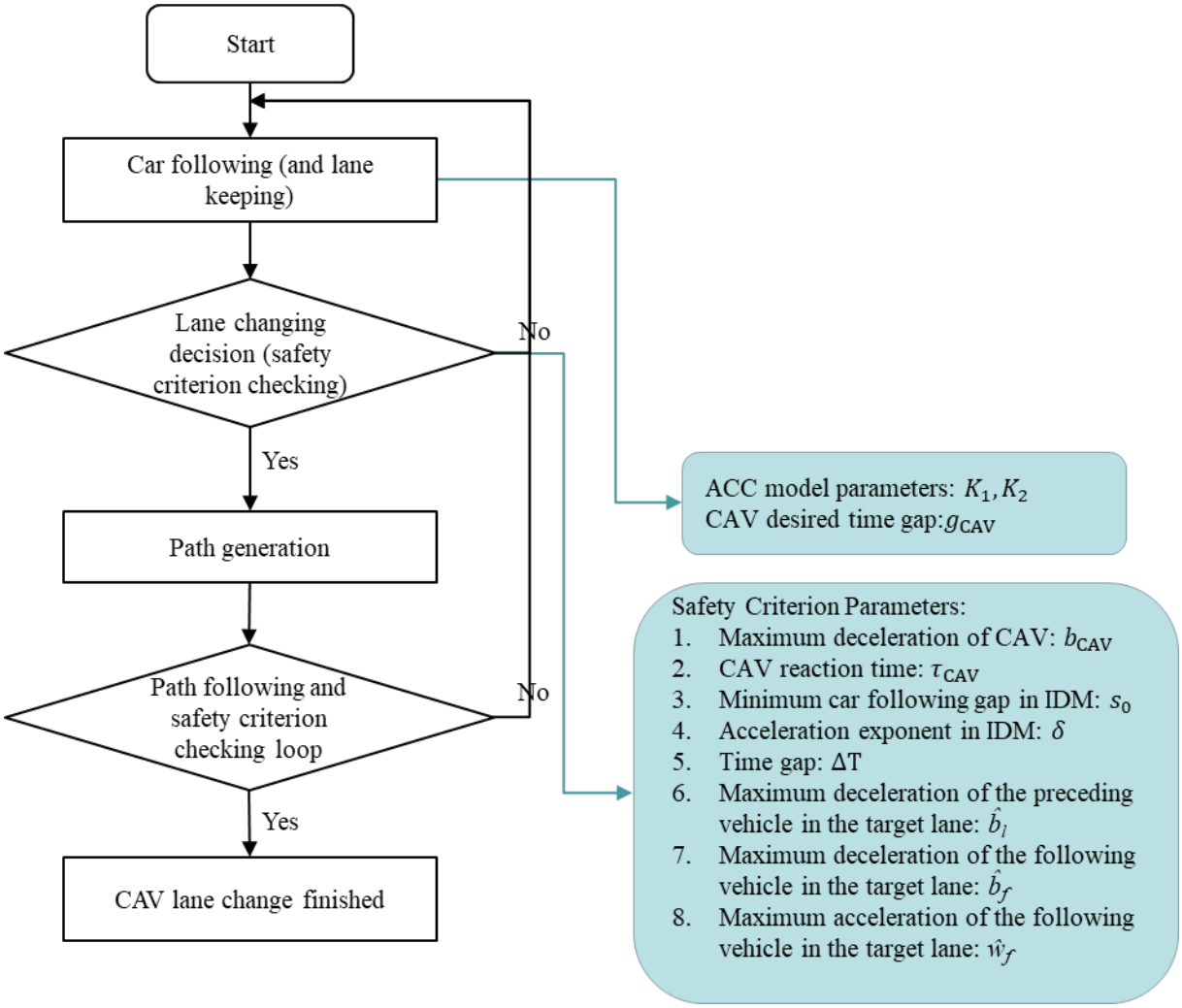

Source: FHWA.

Figure 51. Flowchart. CAV mandatory LC logic with key parameters.

The test track segment for the small-scale field experiment was a straight, two-lane road with length (L) of 0.5 mi and lane width (D) of 11.5 feet. All vehicles' lengths (C) were 15 ft. The sine-function-based LC path was implemented during the field experiments.

The project team conducted the following four case-study ($c \in \{1, 2, 3, 4\}$) experiments representing four different traffic situations:

- In the first case ($c = 1$), the preceding vehicle in the current lane (i.e., HV 1 in figure 48) was asked to decelerate, creating a shock wave. The preceding vehicle in the target lane (i.e., HV 2 in figure 48) kept a relatively constant speed and the following vehicle in the target lane (i.e., HV 3 in figure 48) was not aggressive, yielding to the CAV LC.

- In the second case ($c = 2$), HV 2 was asked to decelerate, creating a shock wave. HV 1 kept relatively constant speed and HV 3 was not aggressive, yielding to the CAV LC.

- In the third case (c = 3), HVs 1 and 2 in figure 48 both kept relatively constant speed and HV 3 was not aggressive, yielding to the CAV LC.

- In the final case (c = 4), HVs 1 and 2 in figure 48 both kept relatively constant speed, but HV 3 was accelerating instead of yielding to the CAV LC, which represented aggressive driving; this forced the CAV to abort the LC maneuver.

The speeds of HV 1 and HV 2 were kept within 9-41 ft/s during the experiments (Wang et al. 2020). Note that two runs of the experiments with the same settings were conducted for each case. The data from the first run of four cases were used for simulation model calibration; the second run data were used for simulation model validation. Small-scale simulation with the same setting as the field experiments was conducted to calibrate the CAV mandatory LC model parameters (listed in figure 51), a component of the mixed-traffic simulation model. HVs 1, 2, and 3 trajectories were controlled to replicate the field experiment trajectories and the CAV trajectory was generated using the proposed CAV LC model. Root mean square error (RMSE) of the CAV longitudinal positions was formulated as shown in figure 52:

$$RMSE_c^x(\beta) = \sqrt{\frac{1}{Q_c}\sum_{q=1}^{Q_c}\left(x_{c,q}^{obs} - x_{c,q}^{cal}(\beta)\right)^2}$$

Figure 52. Equation. RMSE of the CAV longitudinal positions in model calibration.

The error between the calibrated LC time point and field-observed LC time point was formulated as shown in figure 53:

$$E_c^t(\beta) = |t_c^{LCobs} - t_c^{LCcal}(\beta)|$$

Figure 53. Equation. The error between the calibrated LC time point and field-observed LC time point in model calibration.

Thus, the calibration optimization objective was formulated as shown in figure 54:

$$\min_{\beta} \frac{1}{4}\sum_{c=1}^{4}\left(RMSE_c^x(\beta) + E_c^t(\beta)\right)$$

Figure 54. Equation. The calibration optimization objective.

RMSE of the CAV speeds was also calculated to measure the calibration results, formulated as shown in figure 55:

$$RMSE_c^v(\beta) = \sqrt{\frac{1}{Q_c}\sum_{q=1}^{Q_c}\left(v_{c,q}^{obs} - v_{c,q}^{cal}(\beta)\right)^2}$$

Figure 55. Equation. RMSE of the CAV speeds in model calibration.

The interior-point method was used to find the optimal parameter values. As shown in figure 56, the objective function value was stable at 6.19 after iteration 7 with an average $RMSE_c^x(\beta)$ of 4.79 ft and an average $E_c^l(\beta)$ of 1.4 s, indicating a good calibration result (shown in table 14). The parameters β calibration results are provided in table 15. The detailed CAV longitudinal positions, speeds, and LC time calibration results of four cases are provided in figure 57, figure 58, figure 59, and figure 60. The calibrated CAV trajectories (i.e., the dashed curves) were almost consistent with the field-observed trajectories (i.e., the solid curves) with minor differences with an average $RMSE_c^x(\beta)$ value of 4.79 ft and an average $E_c^l(\beta)$ value of 1.18 ft/s. The difference between the calibrated and field-observed LC time point was less than 3 s across all cases.

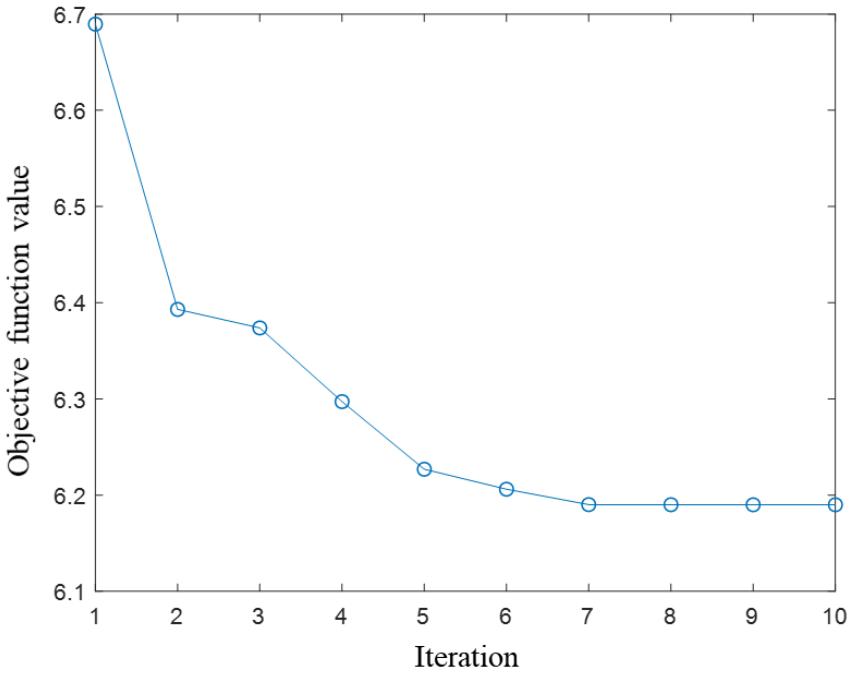

Source: FHWA.

Figure 56. Graph. Calibration objective function convergence.

Table 14. Calibration results summary.

Case	t_c^{LCobs} (s)	t_c^{LCcal} (s)	E_c^t (s)	$RMSE_c^x$ (ft)	$RMSE_c^v$ (ft/s)
$c = 1$	36.2	39.0	2.8	6.10	1.80
$c = 2$	11.5	13.4	1.9	3.48	1.28
$c = 3$	30.2	31.1	0.9	3.02	0.66
$c = 4$	inf	inf	0.0	6.53	0.98
Average	—	—	1.4	4.79	1.18

— = not applicable.
inf = no LC behavior.

Table 15. Parameter calibration results.

Parameters β	Calibration Results
$K_1(s^{-2})$	0.1997
$K_2(s^{-1})$	0.6820
$g_{CAV}(s)$	1.5265
$b_{CAV}(ft/s^2)$	−14.7600
$\tau_{CAV}(s)$	0.9000
$s_0(ft)$	13.1324
δ	2.0000
$\Delta T(s)$	1.3000
$\hat{b}_l / \hat{b}_f(ft/s^2)$	−13.7795
$\hat{w}_f(ft/s^2)$	13.1234

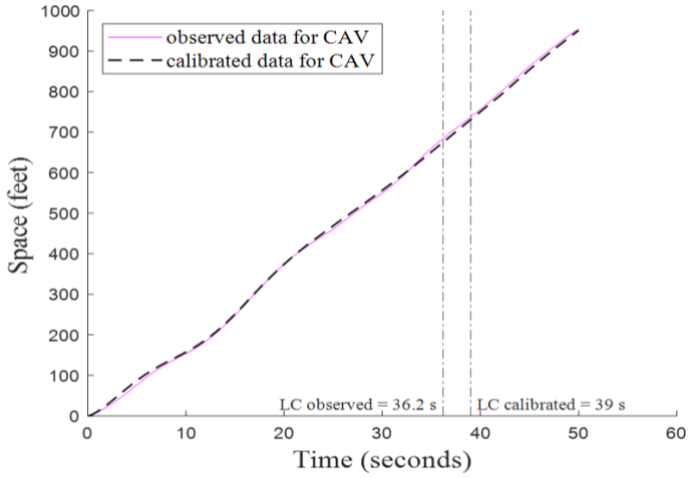

Source: FHWA.

A. Vehicle trajectories in case one.

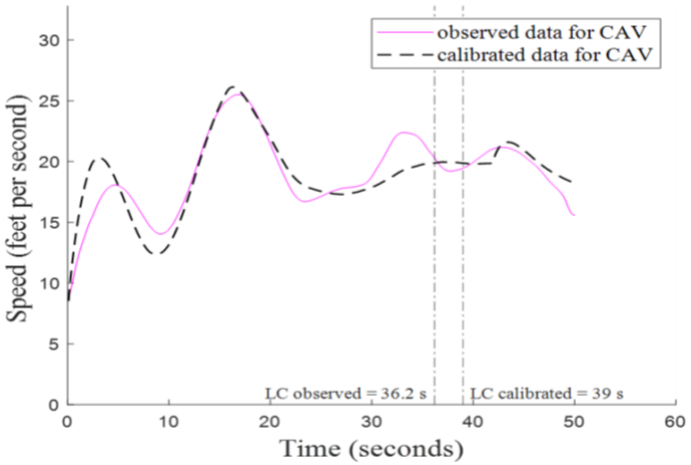

Source: FHWA.

B. Vehicle speeds in case one.

Figure 57. Graph. Calibration results of case one.

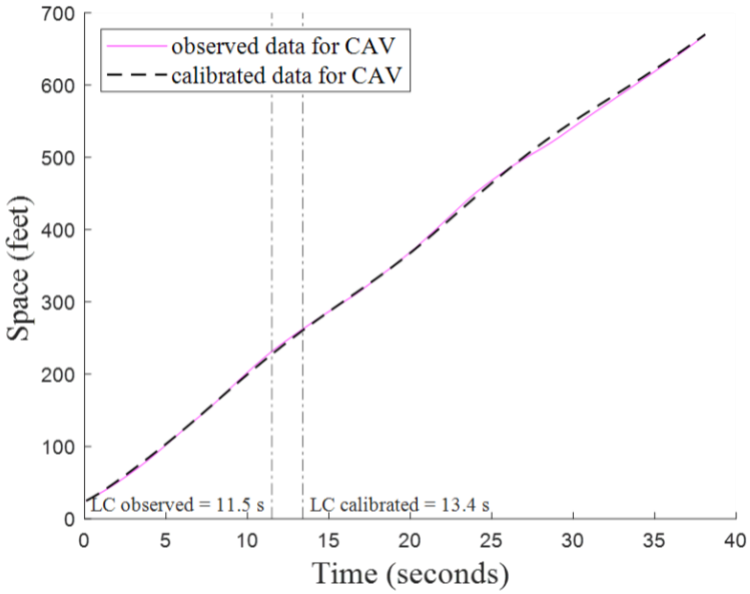

Source: FHWA.

A. Vehicle trajectories in case two.

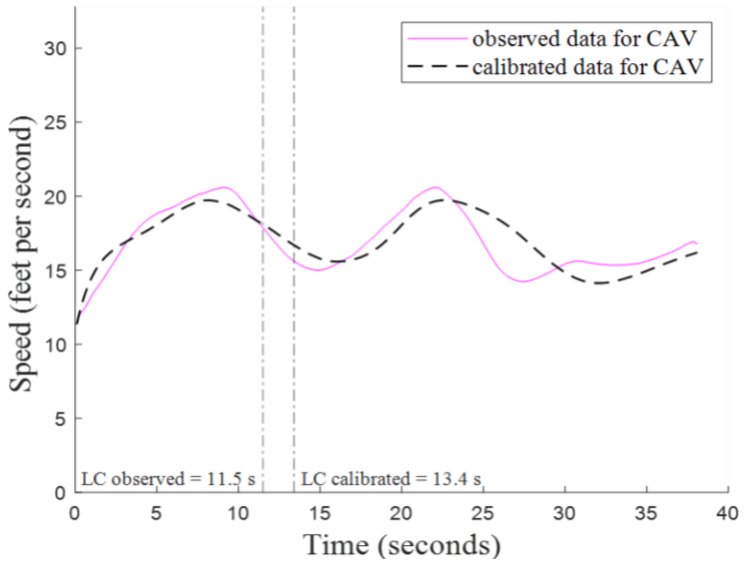

Source: FHWA.

B. Vehicle speeds in case two.

Figure 58. Graph. Calibration results of case two.

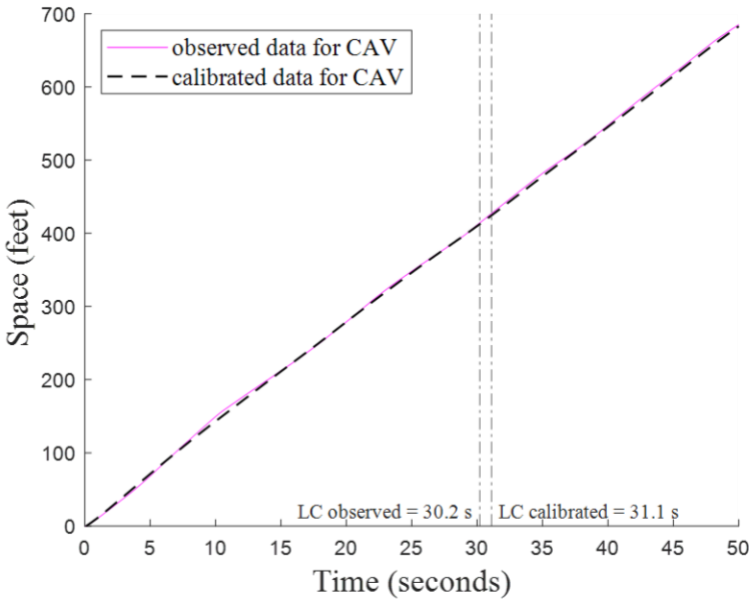

Source: FHWA.

A. Vehicle trajectories in case three.

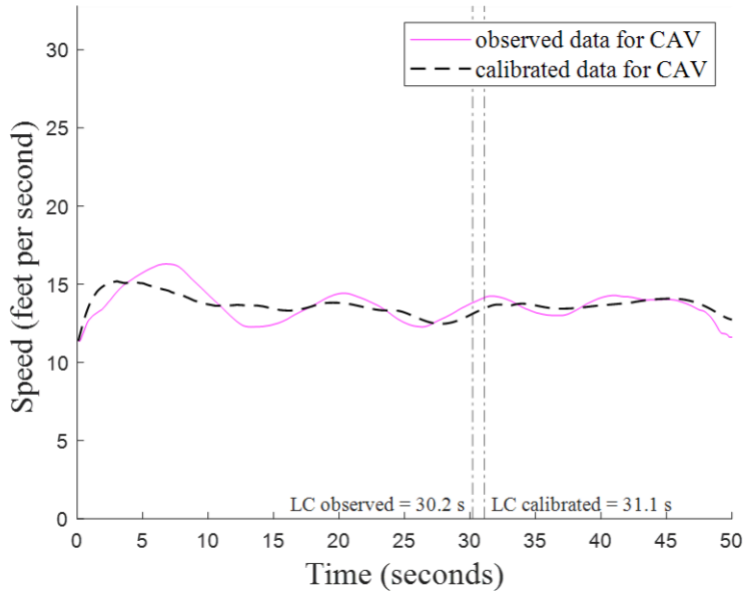

Source: FHWA.

B. Vehicle speeds in case three.

Figure 59. Graph. Calibration results of case three.

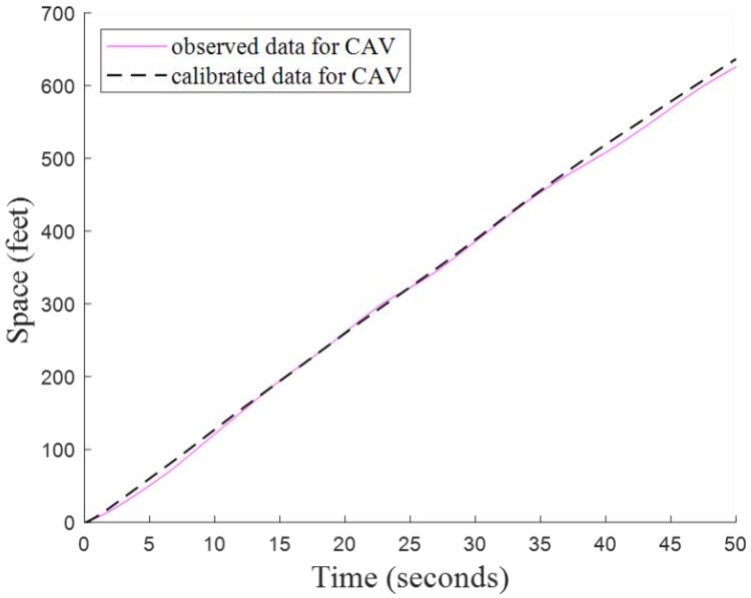

Source: FHWA.

A. Vehicle trajectories in case four.

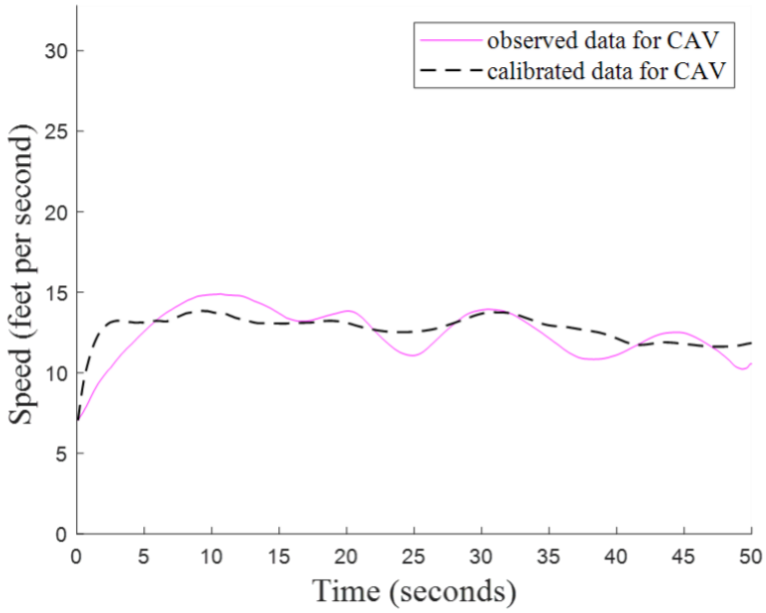

Source: FHWA.

B. Vehicle speeds in case four.

Figure 60. Graph. Calibration results of case four.

Model Validation

The second run data of the four cases were used for model validation. RMSE of CAV longitudinal positions $RMSE_c^x$ and speeds $RMSE_c^v$ were calculated as shown in figure 61 for four cases using the calibrated parameters from the first run.

$$RMSE_c^x(\beta) = \sqrt{\frac{1}{Q_c}\sum_{q=1}^{Q_c}\left(x_{c,q}^{obs} - x_{c,q}^{val}(\beta)\right)^2}$$

$$RMSE_c^v(\beta) = \sqrt{\frac{1}{Q_c}\sum_{q=1}^{Q_c}\left(v_{c,q}^{obs} - v_{c,q}^{val}(\beta)\right)^2}$$

Figure 61. Equation. RMSE of the CAV longitudinal positions and speeds in model validation.

The validation results are summarized in table 16. The error between the validated LC time and field observed LC time was only 0.53 s on average. $RMSE_c^x$ had an average value of 6.89 ft. Compared with the calibration results (i.e., the LC time error with an average value of 1.4 s and $RMSE_c^x$ with an average value of 4.79 ft), the validation results showed less difference, which suggested a valid calibration. Detailed validation results are provided in figure 62 through figure 65.

Table 16. Validation results summary.

Case	t_c^{LCobs}(s)	t_c^{LCval} (s)	E_c^t (s)	$RMSE_c^x$ (ft)	$RMSE_c^v$ (ft/s)
$c = 1$	53.6	53.8	0.2	5.09	0.82
$c = 2$	26.0	26.2	0.6	6.14	1.44
$c = 3$	21.3	22.6	1.3	6.14	1.05
$c = 4$	inf	inf	0.0	10.24	1.25
Average	—	—	0.53	6.89	1.15

— = not applicable.
inf = no LC behavior.

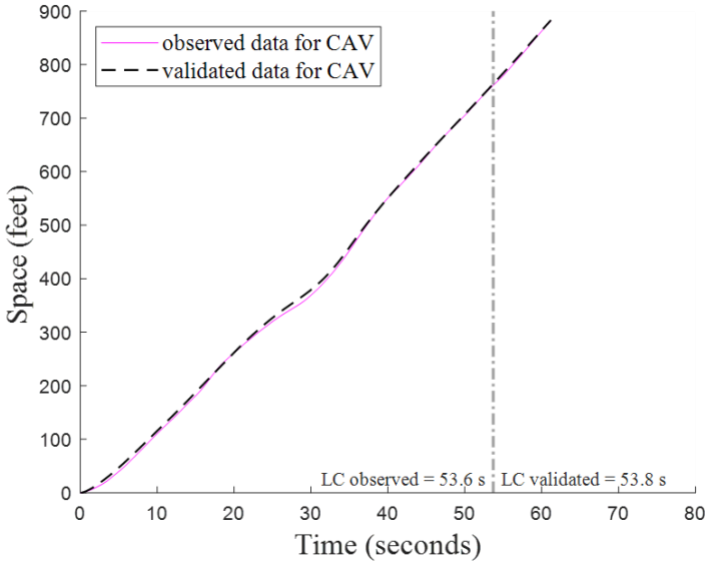

Source: FHWA.

A. Vehicle trajectories in case one.

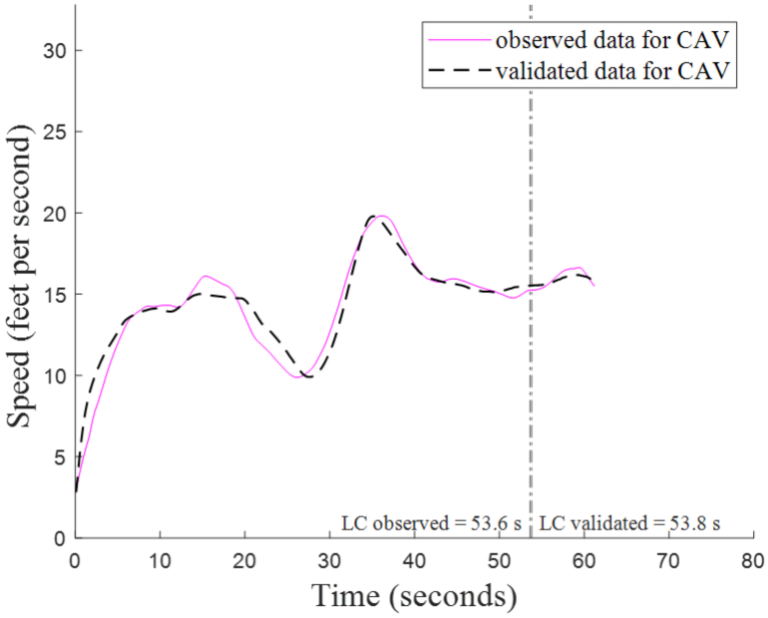

Source: FHWA.

B. Vehicle speeds in case one.

Figure 62. Graph. Validation results of case one.

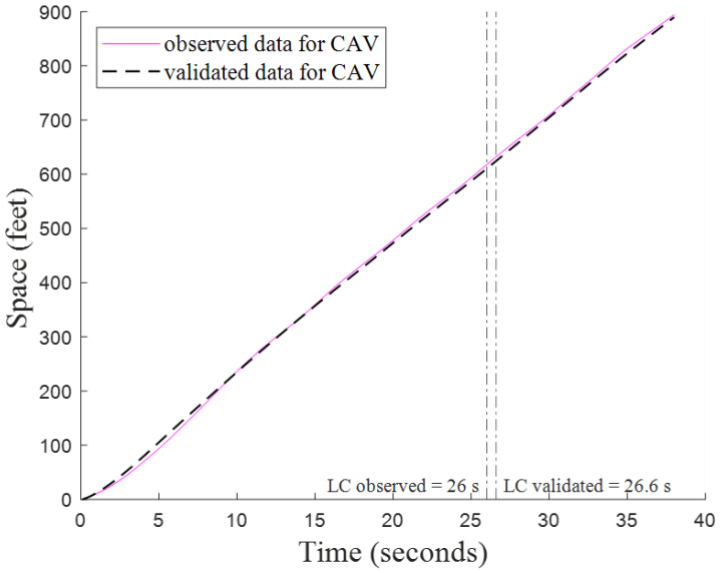

Source: FHWA.

A. Vehicle trajectories in case two.

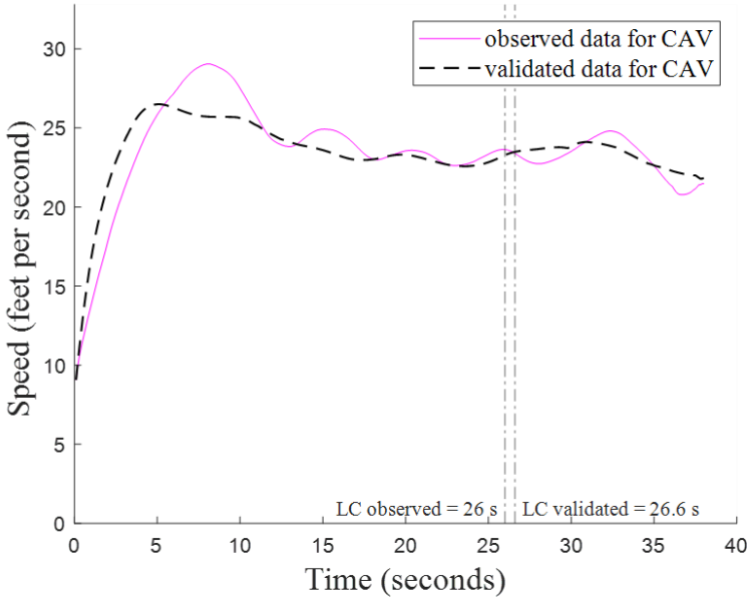

Source: FHWA.

B. Vehicle speeds in case two.

Figure 63. Graph. Validation results of case two.

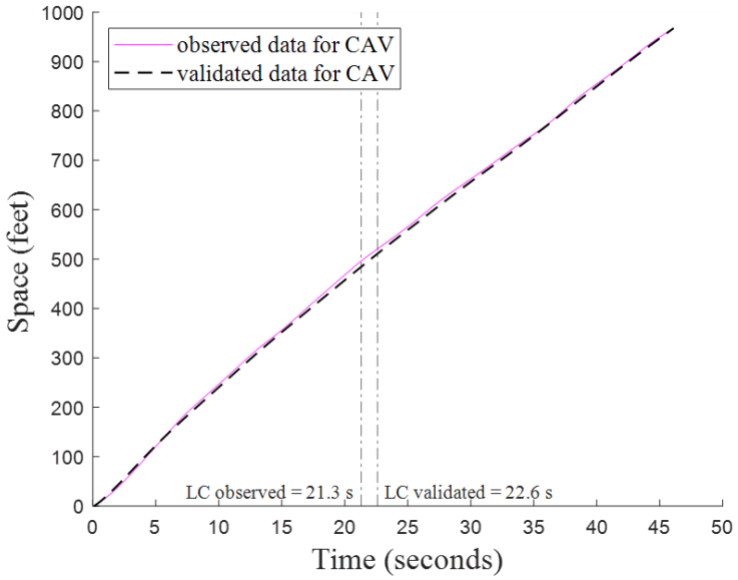

Source: FHWA.

A. Vehicle trajectories in case three.

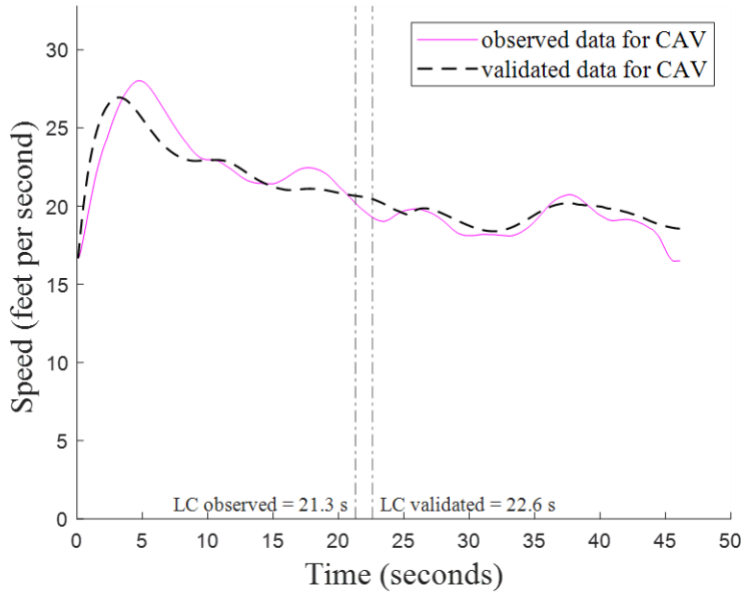

Source: FHWA.

B. Vehicle speeds in case three.

Figure 64. Graph. Validation results of case three.

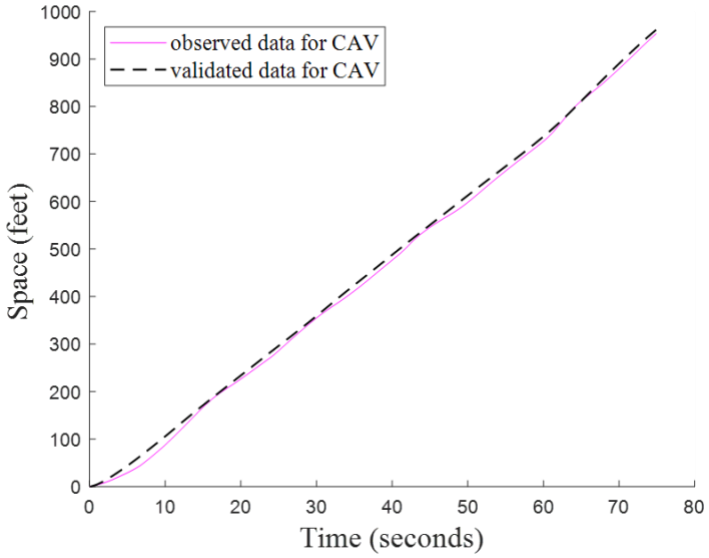

Source: FHWA.

A. Vehicle trajectories in case four.

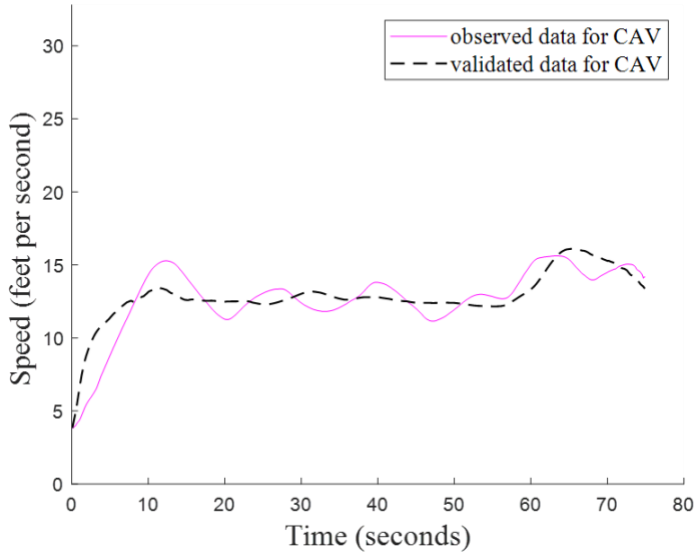

Source: FHWA.

B. Vehicle speeds in case four.

Figure 65. Graph. Validation results of case four.

BASIC INFORMATION ON MODEL IMPLEMENTATION

The following steps are important to implement the proposed model into existing microsimulation platforms:

- Create a customized roadway network according to the application requirements.

- Set roadway throughput, assign vehicle types (e.g., HV, CAV) when populating them, define CAV cooperation rate, initialize CAV and HV routes (i.e., origins and destinations), and define desired speeds in the demand-loading module.

- Replace the simulator's default vehicle CF and LC rules with the proposed CAV CF and LC rules for CAV control in the vehicle dynamic module.

Note that the simulator's default vehicle control rules can still be used for HV control. Figure 66 provides an illustration. There is a three-lane main road, a single-lane onramp, and a single-lane off-ramp. The traffic stream moves from left to right with mainline throughput q_1 and onramp throughput q_2. CAV penetration rates r_1^{CAV} and r_2^{CAV}, CAV diverging rates (i.e., right-exiting rates) r_1^{CAVdiv} and r_2^{CAVdiv}, and HV diverging rates r_1^{HVdiv} and r_2^{HVdiv} are defined for mainline and onramp, respectively. CAV cooperative rate is defined as φ, denoting the probability of a CAV being cooperative. Vehicles are randomly generated based on these predefined parameters.

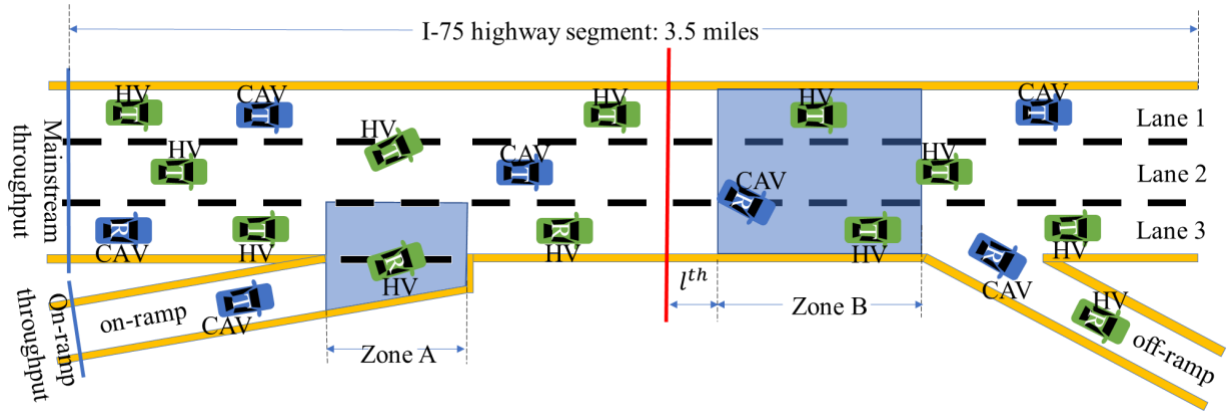

Source: FHWA.
l^{th} = throughput measurement location.
R = right-exiting vehicle.
T = through vehicle.

Figure 66. Illustration. The mixed-traffic simulation model implementation.

Two mandatory LC zones (i.e., zone A and zone B), shaded in figure 66, were defined for this illustration segment because of the requirements of onramp merging and off-ramp diverging. Zone A, with a length of L_A, defined the mandatory LC area where onramp CAVs had to merge into the main lanes. Zone B, with a length of L_B, defined the mandatory LC area that right-exiting CAVs had to reach the right-most lane to exit the freeway through the off-ramp. The other areas were the CAV discretionary LC area. Note that existence of the mandatory LC zones would vary per geometric scenario. If there is no onramp, zone A does not exist. If there is no off-ramp, zone B does not exist. If there is no ramp at all, neither zone exists.

USE CASE AND SENSITIVITY STUDY

To illustrate how to apply the entire simulation framework (including the proposed CAV LC model and the HV model in a mixed-traffic environment), this section presents a large-scale case study with a commercial traffic simulator. Note that emerging CAV technology has experienced

and will experience rapid change and diversification from the prototypes to commercial vehicles. The associated parameter settings in the LC model may change and diversify over the developments. Since these changes cannot be observed or accurately predicted, it is important to conduct sensitivity analyses to show how different values of the key parameters impact the traffic performance.

Implementation of the Developed Model into a Traffic-Simulation Tool

PTV Vissim was used to implement the mixed-traffic simulation framework on the I-75 highway segment, located in Tampa, FL, as shown in figure 67. The program was coded in C++ programming language in Microsoft® Visual Studio® integrated development environment to generate the external DriverModel.DLL, which was used for CAV control in the microsimulation software (Microsoft Visual Studio 2019). The following calibration parameters (table 15) were used in the simulation:

- The selected roadway segment created in the microsimulation software was about 3.27 mi with three main lanes, a single-lane onramp, and a single-lane off-ramp, shown in figure 67. Zone A and Zone B were set as 0.19 mi and 0.87 mi in length, respectively.

- The congested traffic-simulation default case used mainline and onramp throughputs q_1 and q_2 set as 4,500 vehicles per h (vehicle/h) and 1,200 vehicle/h. In the uncongested traffic-simulation default case, mainline and onramp throughputs q_1 and q_2 were set as 3,000 vehicle/h and 1,200 vehicles/h. All other parameters were identical for both default cases. CAV diverging rates r_1^{CAVdiv} and r_2^{CAVdiv} were set as 20 percent for the mainline and onramp traffic, HV diverging rates r_1^{HVdiv} and r_2^{IIVdiv} were set as 20 percent for the mainline and onramp traffic, CAV penetration rates r_1^{CAV} and r_2^{CAV} were set as 50 percent for the mainline and onramp traffic, CAV cooperation rate φ was set as 50 percent, and incentive criterion threshold Δa and bias a_{bias} were set as 0.3 ft/s^2 and 0.9 ft/s^2, respectively. Vehicles were randomly generated based on these parameters, with their desired speeds around 100 ft/s in the mainline and 80 ft/s in the onramp. The simulation duration was set as 5 min in default with 0.1 s as the timestep.

- The CAVs were controlled through an external DriverModel.dll that implements the proposed model, and HVs were controlled using the simulator default CF/LC rules (PTV Group 2018).

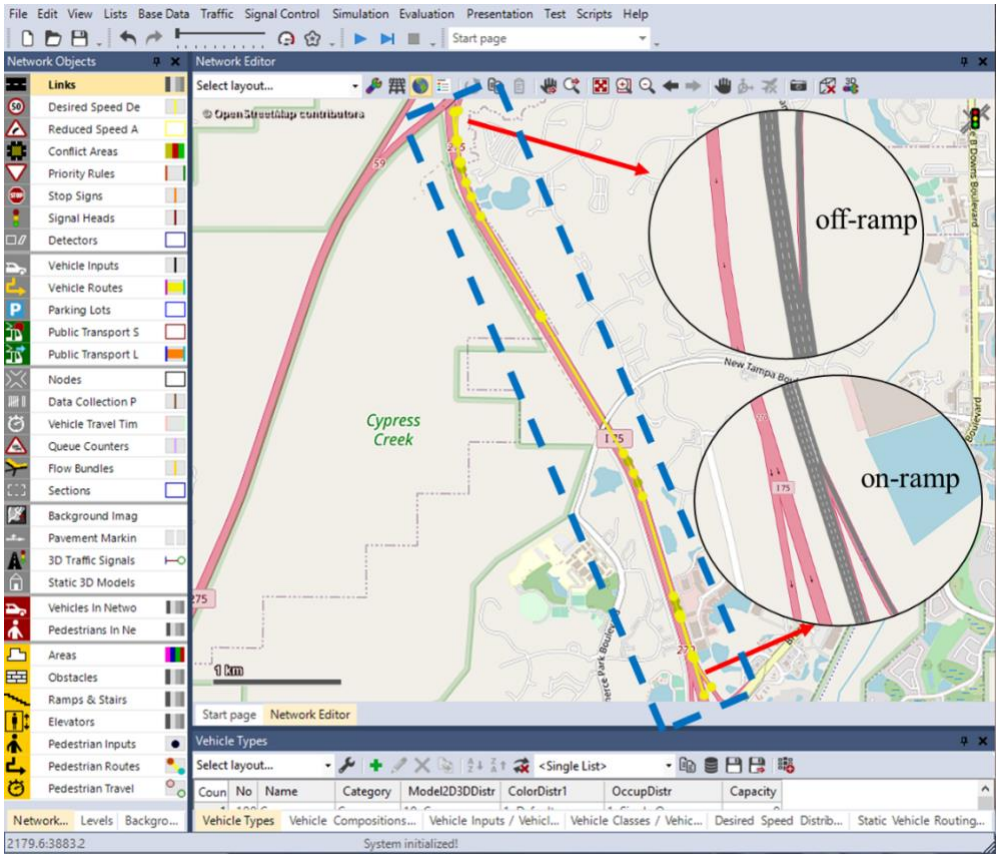

Created with PTV Vissim. Source: FHWA.

Figure 67. Screenshot. Study road segment.

Design of Simulation Experiments

To investigate the impacts of CAV LC maneuvers on traffic system performance, sensitivity analyses were conducted on key parameters r_1^{CAV}, r_2^{CAV}, φ, Δa, and a_{bias} with one of the key parameters changed and other parameters kept the same. Vehicle average speed and speed standard deviation along the study roadway segment were used to measure traffic mobility and stability performance, respectively.

Vehicle set $\mathcal{N}$ was separated into CAV set $j \in \mathcal{J} := \{1, 2, \ldots, J\}$ and HV set $k \in \mathcal{K} := \{1, 2, \ldots, K\}$. The CAV average speed $\bar{v}_{CAV}$ in the simulation period was formulated as shown in figure 68:

$$\bar{v}_{\text{CAV}} = \frac{\sum_{j=1}^{j=J} \frac{\sum_{t=0}^{t=T_j} v_j(t)}{T_j}}{J}$$

Figure 68. Equation. The CAV vehicle average speed.

The CAV speed standard deviation $\text{STD}v_{\text{CAV}}$ in the simulation period was formulated as shown in figure 69:

$$\mathrm{STD}_{v_{\mathrm{CAV}}} = \frac{\sum_{j=1}^{j=J} \sqrt{\frac{\sum_{t=0}^{t=T_j} (v_j(t) - \hat{v}_j)^2}{T_j}}}{J}$$

Figure 69. Equation. The CAV speed standard deviation.

The HV average speed $\bar{v}_{HV}$ in the simulation period was formulated as shown in figure 70:

$$\overline{v}_{\mathrm{HV}} = \frac{\sum_{k=1}^{k=K} \frac{\sum_{t=0}^{t=T_k} v_k(t)}{T_k}}{K}$$

Figure 70. Equation. The HV average speed.

The HV speed standard deviation $\mathrm{STD}v_{\mathrm{HV}}$ in the simulation period was formulated as shown in figure 71:

$$\mathrm{STD}_{v_{\mathrm{HV}}} = \frac{\sum_{k=1}^{k=K} \sqrt{\frac{\sum_{t=0}^{t=T_k} (v_k(t) - \hat{v}_k)^2}{T_k}}}{K}$$

Figure 71. Equation. The HV speed standard deviation.

The average speed across all vehicles $\bar{v}_{all}$ in the simulation period is formulated as shown in figure 72:

$$\overline{v}_{\mathrm{all}} = \frac{\sum_{j=1}^{j=J} \frac{\sum_{t=0}^{t=T_j} v_j(t)}{T_j} + \sum_{k=1}^{k=K} \frac{\sum_{t=0}^{t=T_k} v_k(t)}{T_k}}{J + K}$$

Figure 72. Equation. The average speed across all vehicles.

The speed standard deviation across all vehicles $\mathrm{STD}v_{\mathrm{all}}$ in the simulation period was formulated as shown in figure 73:

$$\mathrm{STD}_{v_{\mathrm{all}}} = \frac{\sum_{j=1}^{j=J} \sqrt{\frac{\sum_{t=0}^{t=T_j} (v_j(t) - \hat{v}_j)^2}{T_j}} + \sum_{k=1}^{k=K} \sqrt{\frac{\sum_{t=0}^{t=T_k} (v_k(t) - \hat{v}_k)^2}{T_k}}}{J + K}$$

Figure 73. Equation. The speed standard deviation across all vehicles.

CAV, HV, and total traffic throughput (q_{CAV}, q_{HV}, and q_{all}) during a 5-min simulation period were also measured at the location where the red line is located in figure 66, and l^{th} is set as

1,640 ft. Note that researchers assumed $r_1^{CAV} = r_2^{CAV} = r^{CAV}$ in the simulation, indicating that CAV penetration rates were the same in the mainline and onramp traffic.

Simulation Results

Figure 74 shows a CAV discretionary LC process. Sensitivity analyses results of congested traffic simulation are provided in figure 75 through figure 78. Sensitivity analyses results of uncongested traffic simulation are provided in figure 79 through figure 82. These results provide insight into understanding mixed traffic and provide basic suggestions for engineering practice.

LC Process Demonstration

In figure 74-A, the CAV met both the incentive criterion and the safety criterion with respect to vehicles 2 and 3; thus, the CAV initiated the discretionary LC. In figure 74-B, the CAV was crossing the lane marking. By figure 74-C, the CAV finished the discretionary LC, as it had arrived at the center line of the target lane. The mandatory LC process is not presented because it is a similar movement, albeit under different circumstances.

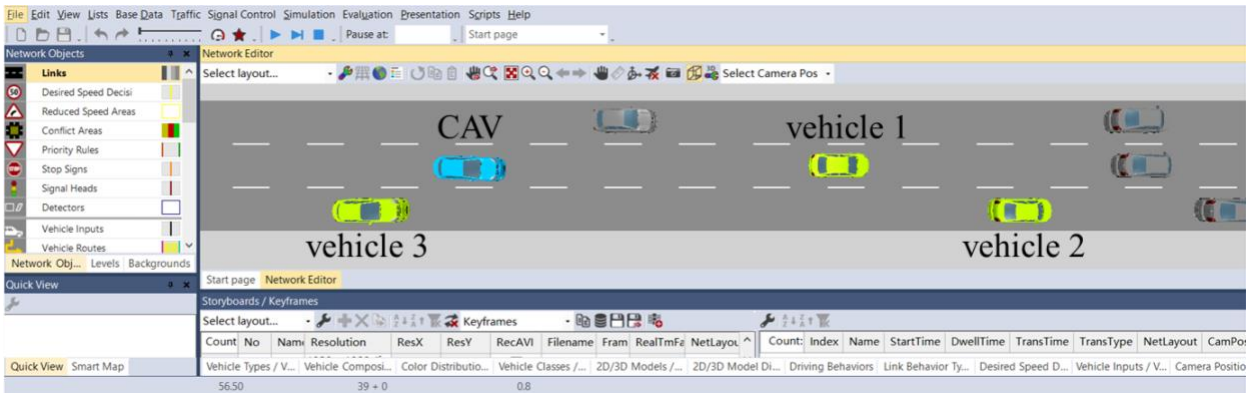

Created with PTV Vissim. Source: FHWA.

A. Discretionary LC initiated.

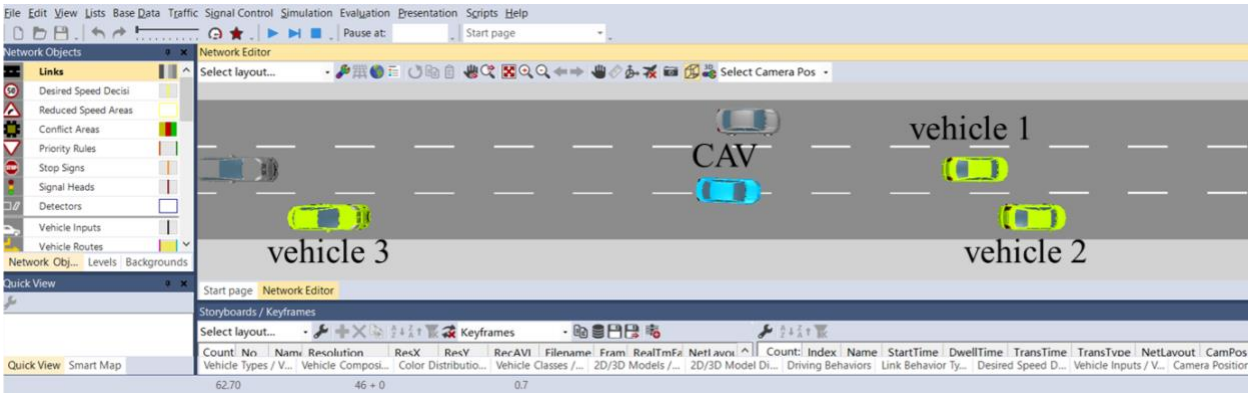

Created with PTV Vissim. Source: FHWA.

B. Discretionary LC in process.

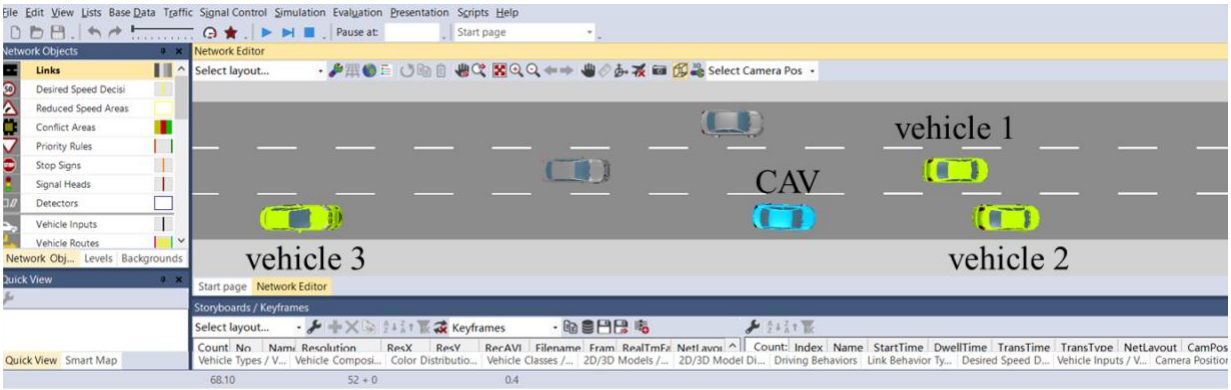

Created with PTV Vissim. Source: FHWA.

C. Discretionary LC finished.

Figure 74. Screenshots. CAV LC process.

Sensitivity Analysis Results of Congested Traffic

The researchers used average speed as a surrogate for mobility performance: the greater the average speed, the better the mobility. The speed standard deviation was used to measure stability performance: the greater the speed standard deviation, the worse the stability. Vehicle throughput was another measurement of mobility performance.

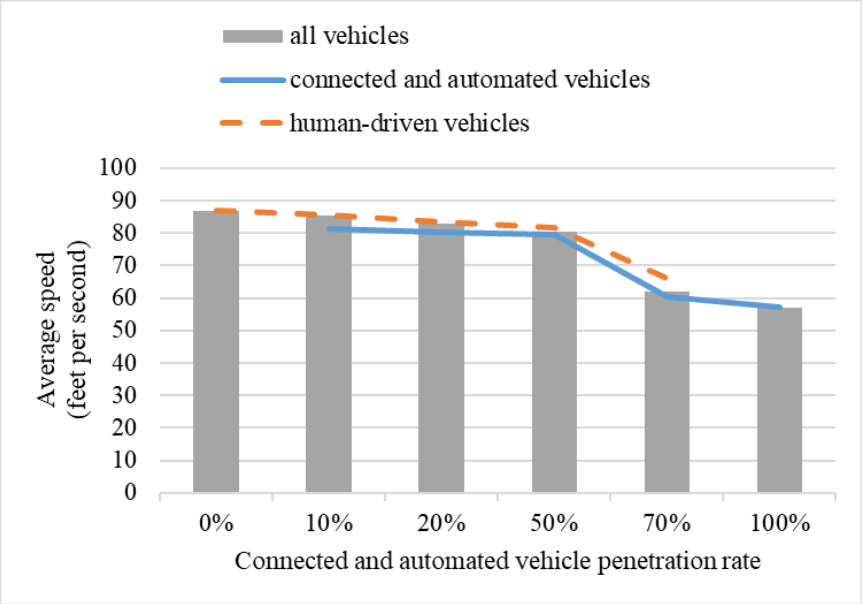

Source: FHWA.

A. Average speed versus CAV penetration rate.

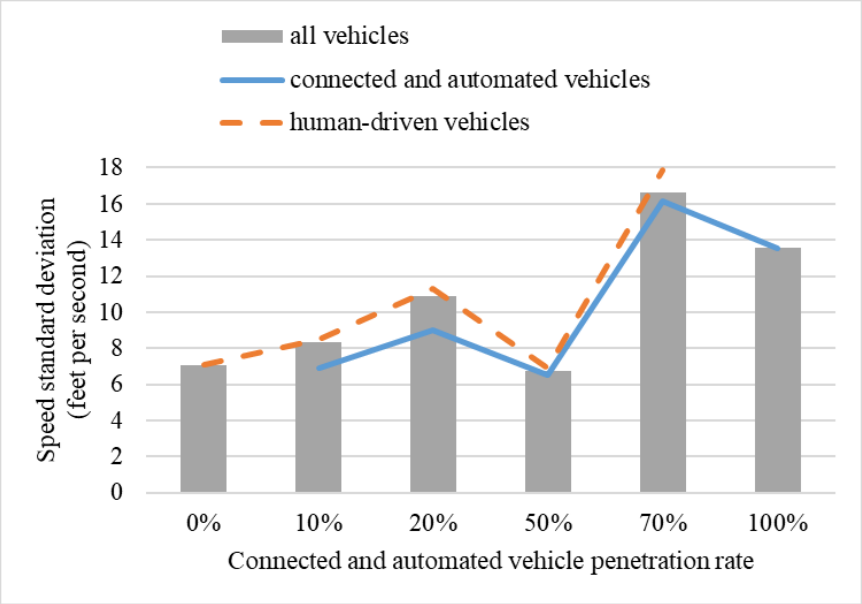

Source: FHWA.

B. Speed standard deviation versus CAV penetration rate.

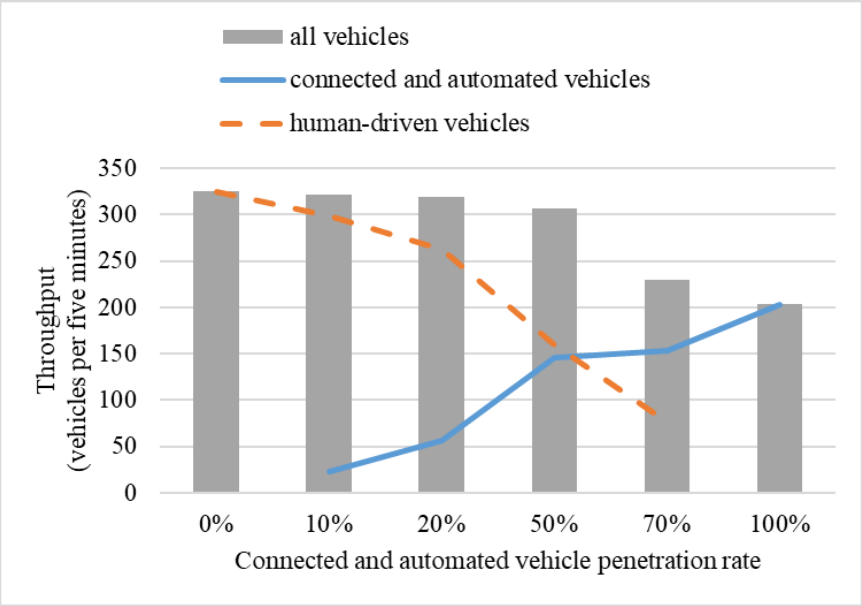

Source: FHWA.

C. Throughput versus CAV penetration rate.

Figure 75. Graph. Sensitivity analysis on CAV penetration rate under congested traffic.

The results in figure 75 showed that as the CAV penetration rate r^{CAV} increased, mobility performance degraded. This is primarily because the CAV CF and LC models used here were calibrated with data from a lab vehicle with more conservative driving rules than an average human driver for safety concerns (see the previous section for related calibration and verification). As a result, CAVs produced a longer average headway than HVs. Thus, as the CAV penetration rate increased, the average headway increased in the mixed traffic and thus the mobility measures degraded. These results are not completely out of context, since CAV technologies are expected to have conservative settings in the initial deployment stage for safety concerns as well.

As r^{CAV} increased, the stability performance fluctuated. Increases in r^{CAV} resulted in more CAV LCs that caused more traffic oscillation and led to worse stability performance. Yet r^{CAV} kept increasing, probably because more cooperative CAVs were present and their cooperation behavior improved the stability performance. Note that the best stability performance was observed when r^{CAV} equaled 50 percent. If the calibrated CAV model had a shorter time headway, it would be expected that both the mobility and stability performance would have improved with increasing r^{CAV}. Future studies would be needed to verify whether that expectation is correct.

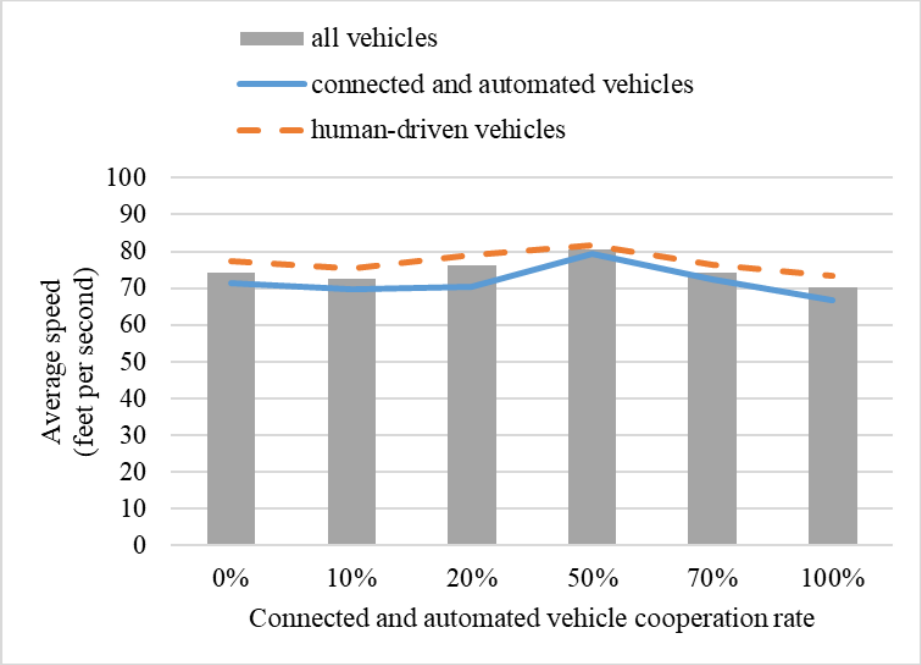

Source: FHWA.

A. Average speed versus CAV cooperation rate.

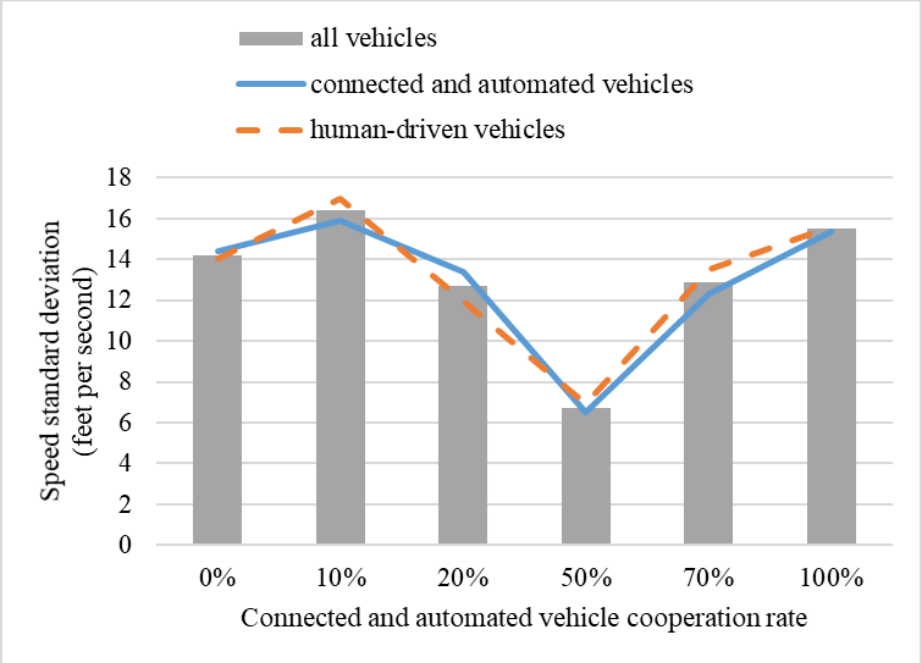

Source: FHWA.

B. Speed standard deviation versus CAV cooperation rate.

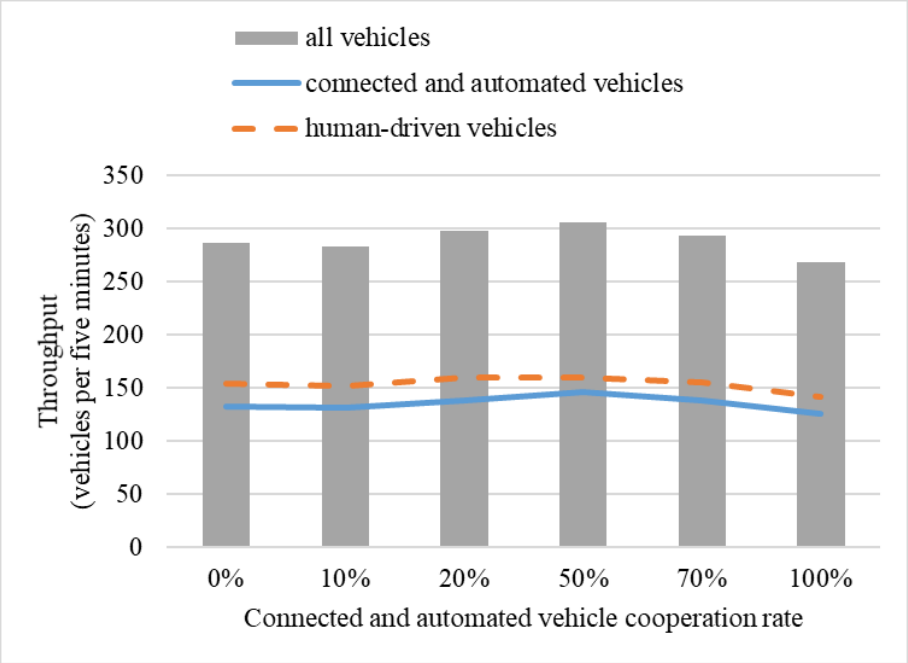

Source: FHWA.

C. Throughput versus CAV cooperation rate.

Figure 76. Graph. Sensitivity analysis on CAV cooperation rate under congested traffic.

As shown in figure 76, as CAV cooperation rate φ increased, the mobility and stability performance improved initially ($\varphi < 50$ percent). This was probably because as φ initially increased, the traffic stream was more cooperative (i.e., this increased the chance of CAVs completing LCs quickly). This reduced the impedance from downstream LCs to upstream vehicle movements. However, the traffic performance degraded as φ further increased ($\varphi > 50$ percent). This is probably because many LCs are incentivized by a high cooperation rate. Overly frequent LCs consequentially increase the average gaps between vehicles and create more oscillatory vehicle speeds, which lead to slower and less stable traffic.

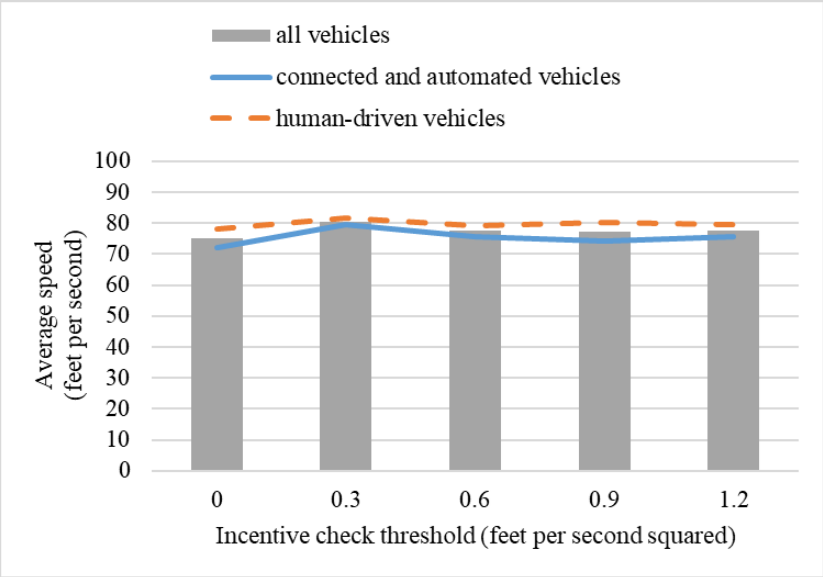

Source: FHWA.

A. Average speed versus incentive criterion threshold.

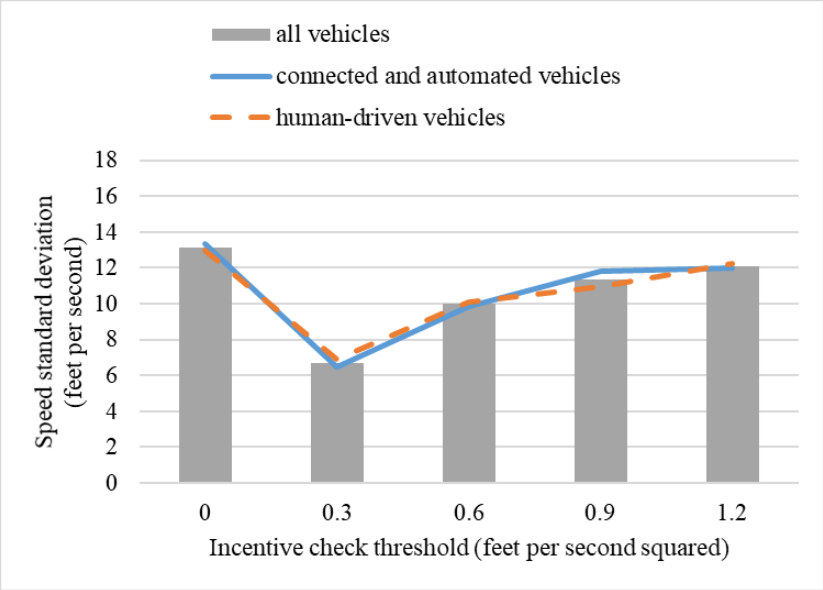

Source: FHWA.

B. Speed standard deviation versus incentive criterion threshold.

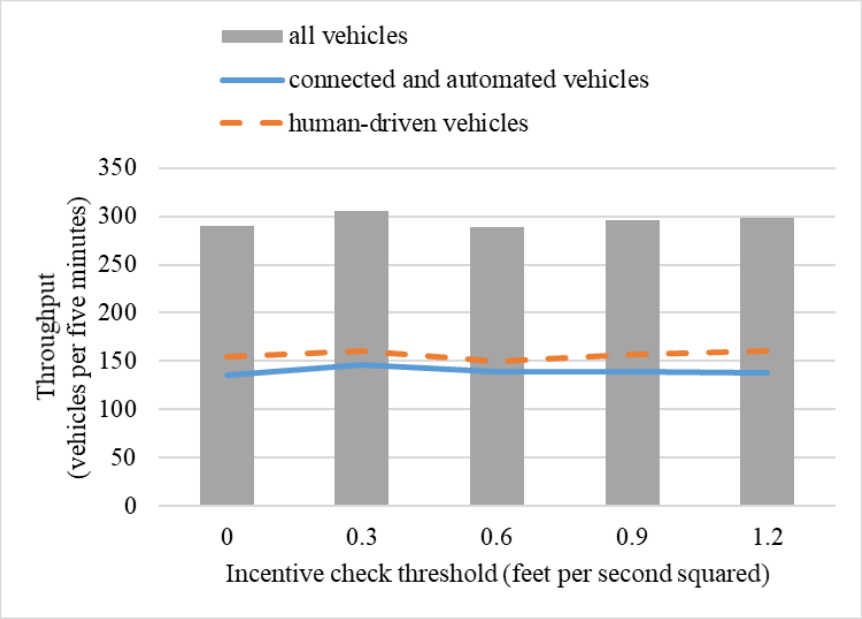

Source: FHWA.

C. Throughput versus incentive criterion threshold.

Figure 77. Graph. Sensitivity analysis on incentive criterion threshold under congested traffic.

As the incentive criterion threshold Δa increased, both mobility and stability initially improved and then worsened. The pivot point was observed at Δa = 0.3 ft/s^2. Interestingly, this pivot Δa value was consistent with the typical value for the HV LC model suggested in the existing study (Treiber and Kesting 2013), indicating that human drivers might have subconsciously learned the optimal LC behavior through extensive driving experience. As Δa increased, the CAV discretionary lane change (DLC) incentive criterion became more difficult to meet, leading to fewer DLC behaviors. At first, fewer DLC behaviors led to less traffic oscillation and thus contributed to better traffic performance. However, as Δa increased, DLCs became quite rare and many CAVs stuck to a slower speed rather than attempting to change to a faster lane. This held vehicles moving slower overall and thus deteriorated traffic performance (Li et al. 2006).

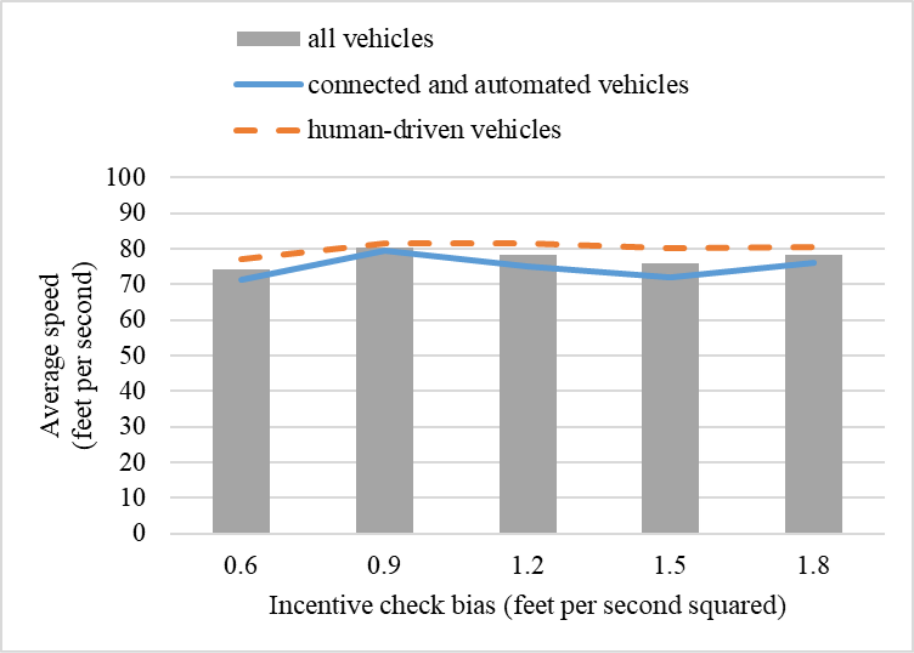

Source: FHWA.

A. Average speed versus incentive criterion bias.

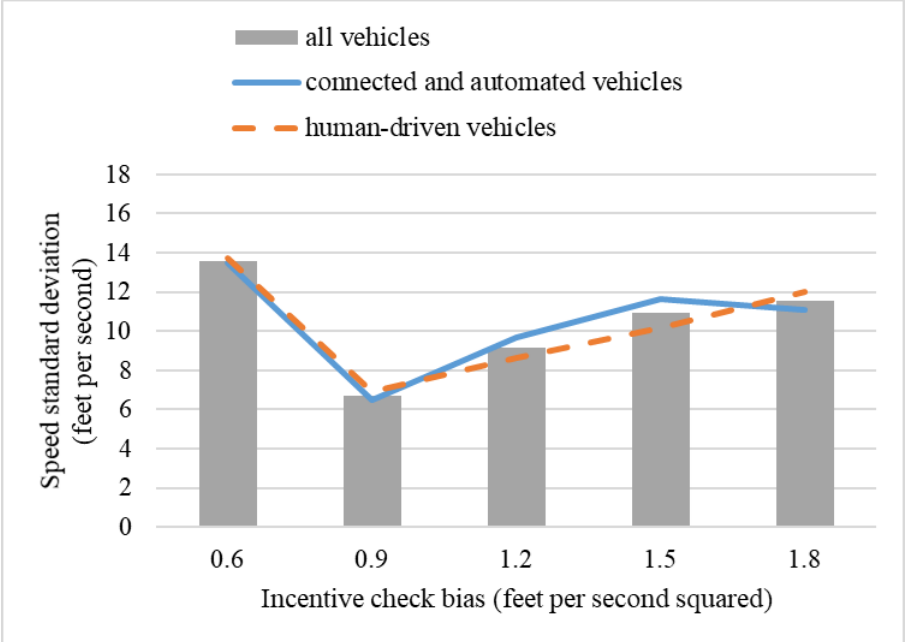

Source: FHWA.

B. Speed standard deviation versus incentive criterion bias.

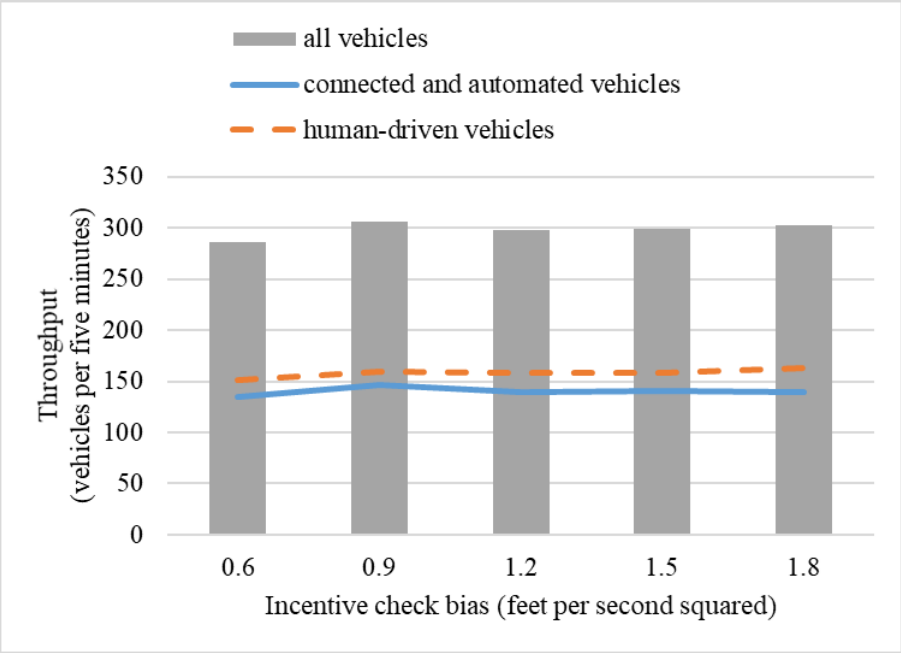

Source: FHWA.

C. Throughput versus incentive criterion bias.

Figure 78. Graph. Sensitivity analysis on incentive criterion bias under congested traffic.

Again, as the incentive criterion bias a_{bias} (the tendency for a vehicle to stay in a right lane) increased, both mobility and stability performance first improved and then worsened. The best system performance was observed when a_{bias} = 0.9 ft/s^2. Interestingly, this value is again consistent with the typical value for HVs suggested in the existing study (i.e., Treiber and Kesting 2013), suggesting the optimal human driver learning capability. The reasons to observe this trend were probably because as a_{bias} initially increased, congestion in the left lanes decreased, allowing more vehicles to overtake at faster speeds in the left lanes. However, as a_{bias} further increased, vehicles disproportionally concentrated in the right lanes, which impeded onramp traffic and aggravated overall congestion.

Sensitivity Analysis Results of Uncongested Traffic

As shown in figure 79 through figure 82, mobility and stability performance under uncongested traffic were better than those under congested traffic in general. This is intuitive, because traffic congestion degrades the traffic performance. Overall, the trends of the impacts were consistent with those in the congested traffic. However, a closer look reveals that the traffic performance (i.e., the average speed, the speed standard deviation, or the throughput) varies in a smaller range compared with that in figure 75 though figure 78. This indicates that the influence of the parameters' values on traffic became marginal as the traffic volume decreased (i.e., uncongested traffic). This is probably because in uncongested traffic, vehicles have more room to maneuver to mitigate impacts from surrounding LC vehicles. From another angle, these findings indicate that the impacts will be amplified in more congested traffic, and thus more efforts are necessary to manage congested mixed traffic.

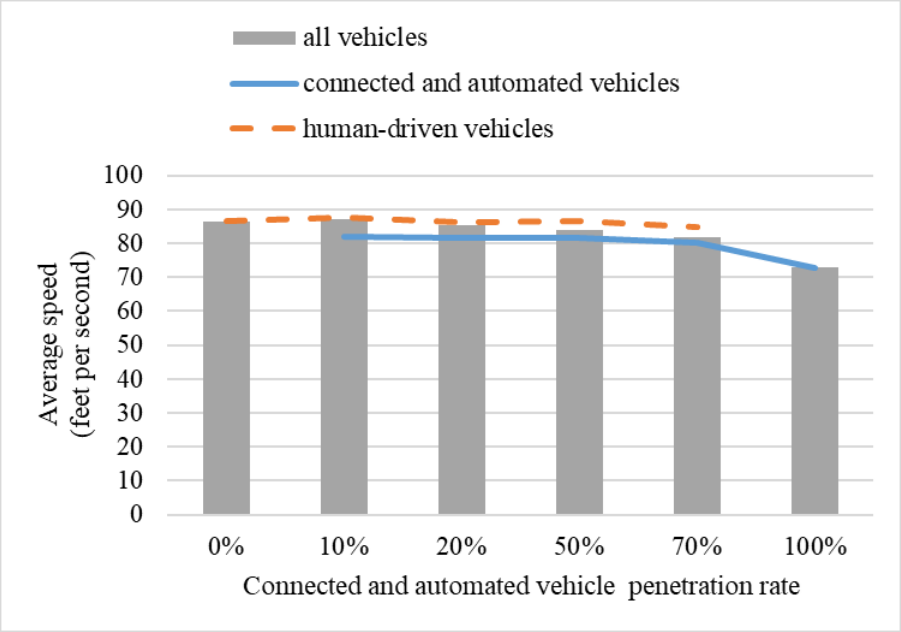

Source: FHWA.

A. Average speed versus CAV penetration rate.

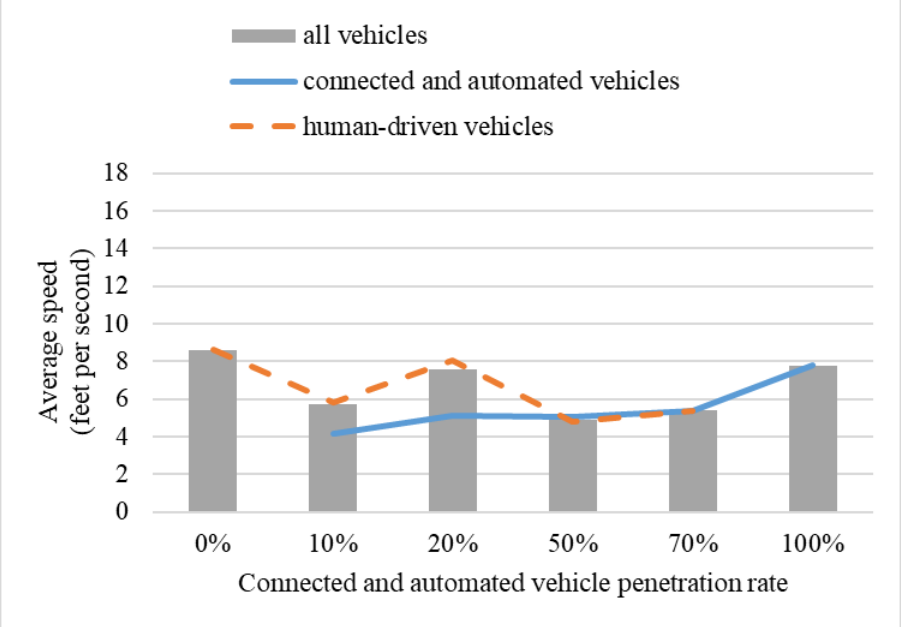

Source: FHWA.

B. Speed standard deviation versus CAV penetration rate.

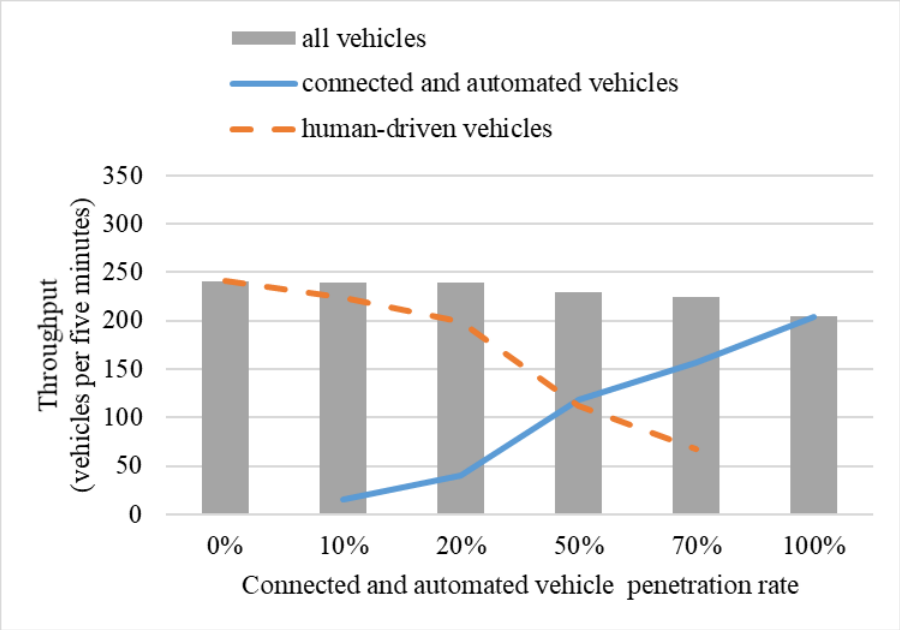

Source: FHWA.

C. Throughput versus CAV penetration rate.

Figure 79. Graph. Sensitivity analysis on CAV penetration rate under uncongested traffic.

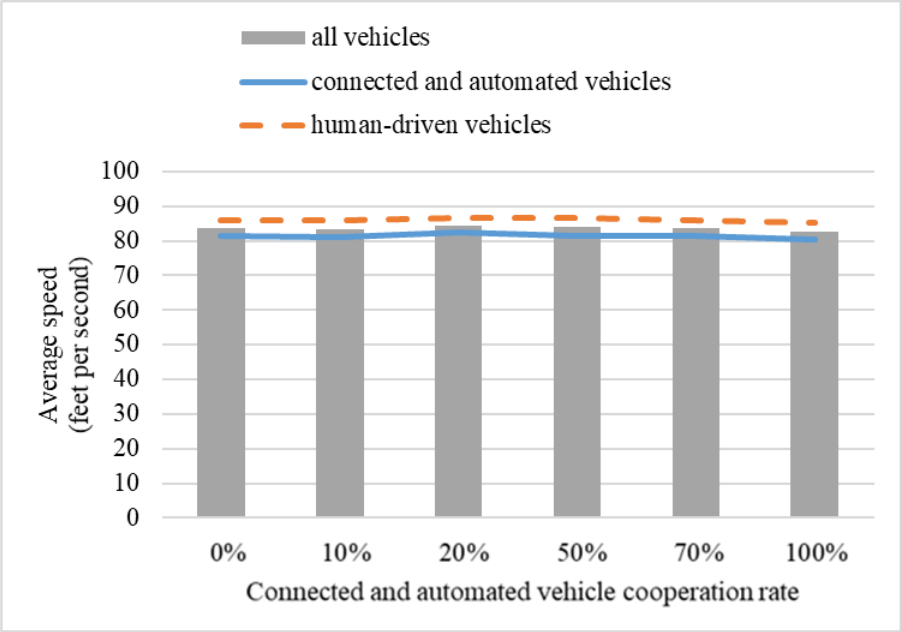

Source: FHWA.

A. Average speed versus CAV cooperation rate.

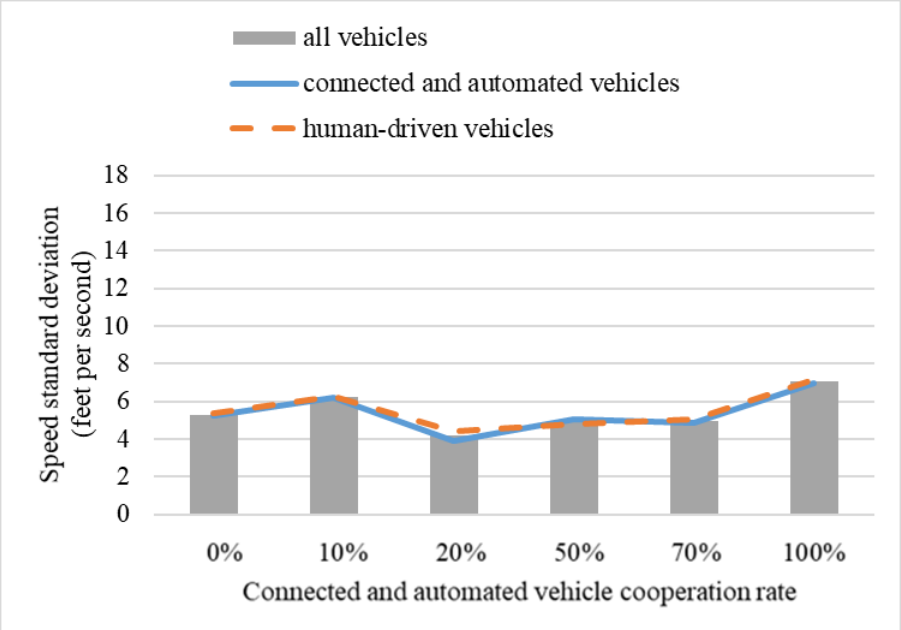

Source: FHWA.

B. Speed standard deviation versus CAV cooperation rate.

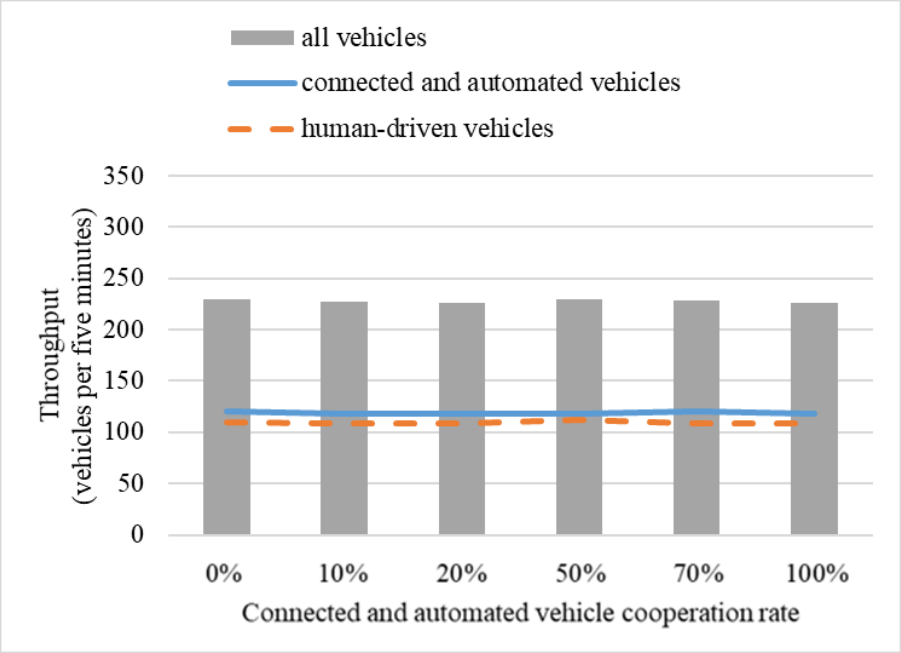

Source: FHWA.

C. Throughput versus CAV cooperation rate.

Figure 80. Graph. Sensitivity analysis on CAV cooperation rate under uncongested traffic.

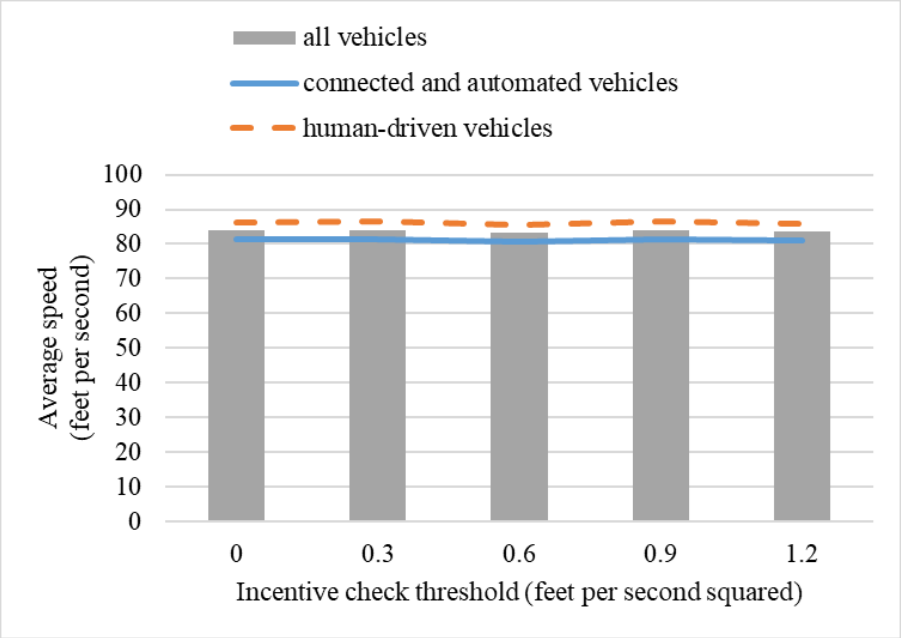

Source: FHWA.

A. Average speed versus incentive criterion threshold.

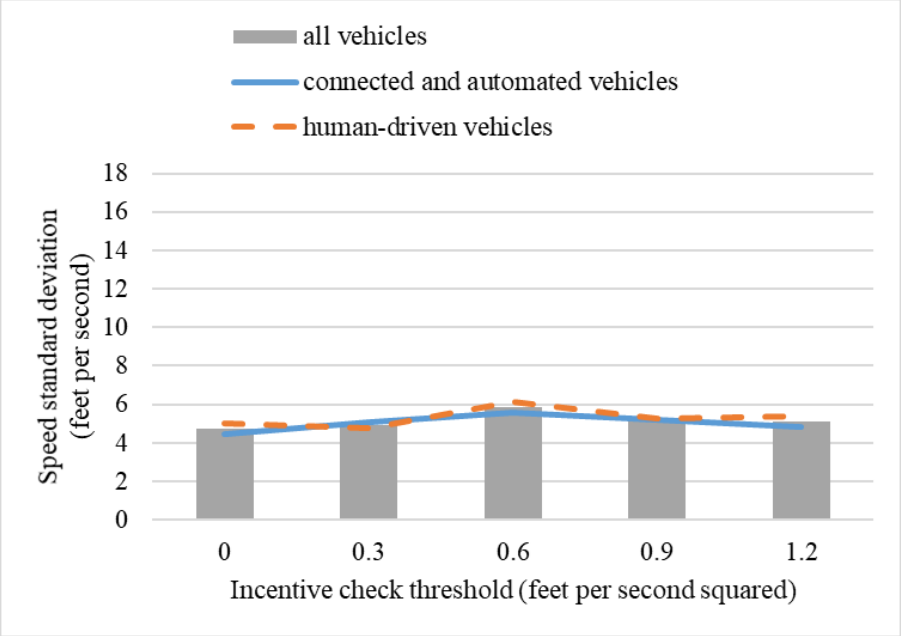

Source: FHWA.

B. Speed standard deviation versus incentive criterion threshold.

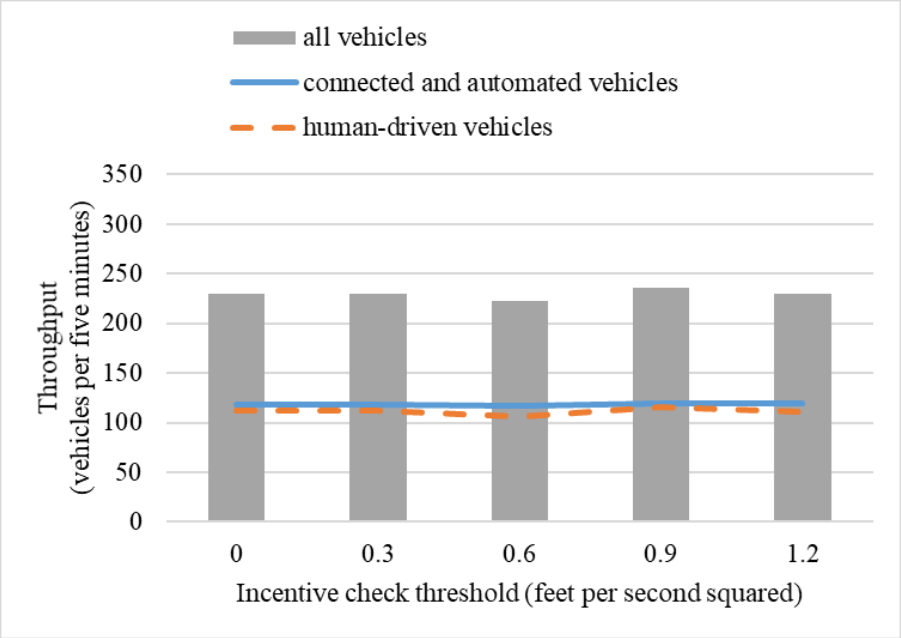

Source: FHWA.

C. Throughput versus incentive criterion threshold.

Figure 81. Graph. Sensitivity analysis on incentive criterion threshold under uncongested traffic.

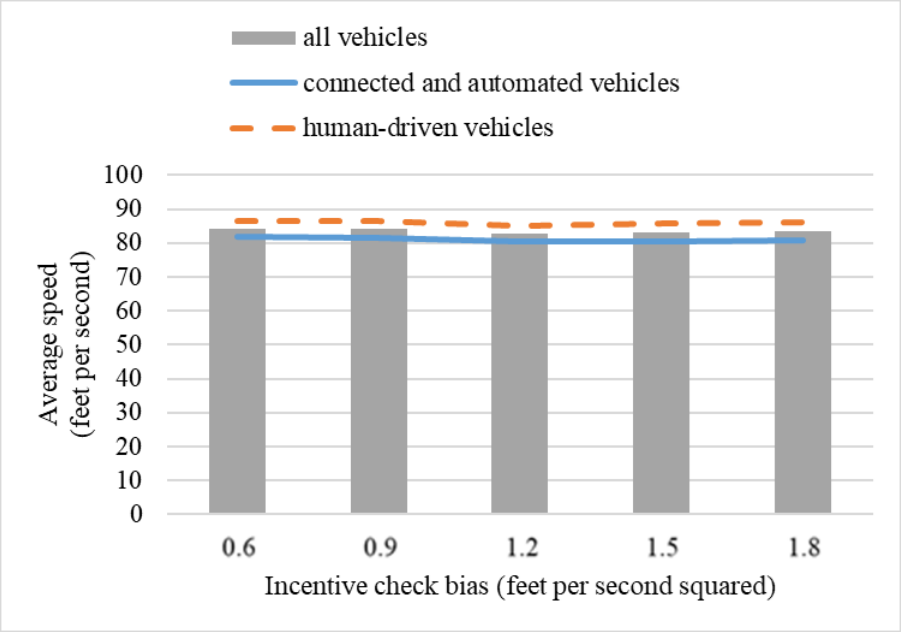

Source: FHWA.

A. Average speed versus incentive criterion bias.

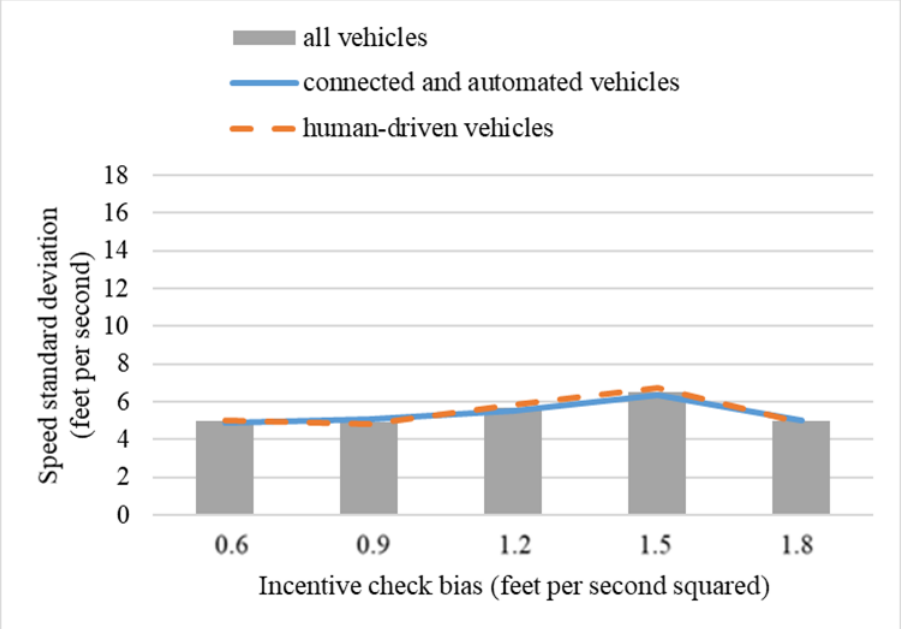

Source: FHWA.

B. Speed standard deviation versus incentive criterion bias.

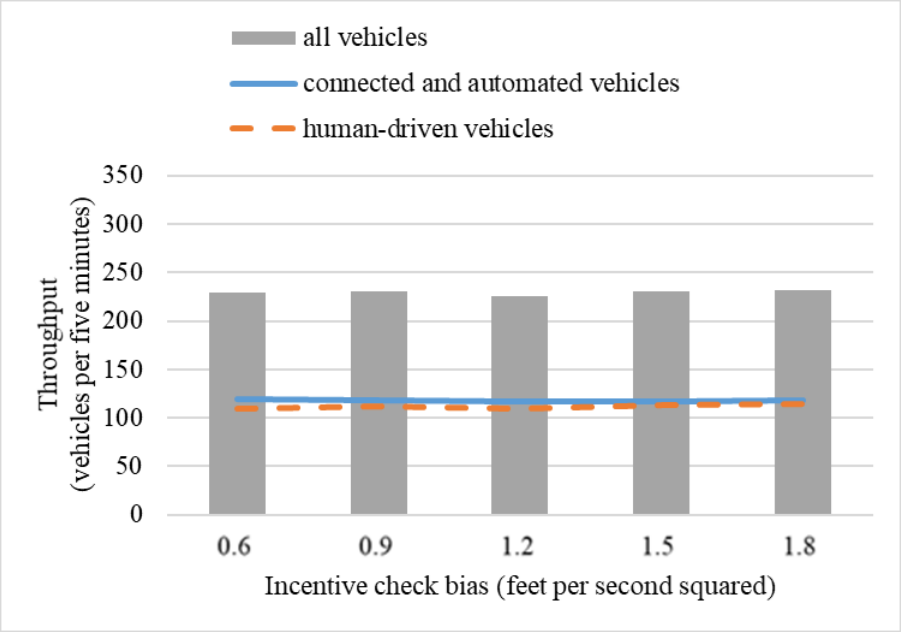

Source: FHWA.

C. Throughput versus incentive criterion bias.

Figure 82. Graph. Sensitivity analysis on incentive criterion bias under uncongested traffic.

Overall, note that the impacts of several key parameters (e.g., CAV cooperation rate) LC incentive criterion threshold and bias on traffic performance are nonlinear (e.g., first improving and then degrading). These findings indicate that thoughts on optimization may be taken when designing these parameters from the perspective of transportation operators (e.g., facilities and policies to promote vehicle cooperation) and automakers (e.g., tuning parameters in their LC models) to achieve the best traffic performance. These insights may help stakeholders better understand and prepare for near-future mixed-CAV traffic with different LC behaviors and suggests the optimal LC configurations for automakers to achieve the best overall traffic performance.

SUMMARY

This chapter described a mixed-traffic simulation framework that is centered at the CAV LC model and fully considers the dynamics of surrounding vehicles under different mixed-traffic scenarios. The model was calibrated and validated using data collected from a small-scale field experiment. The model is open source and can be customized and implemented into existing microscopic simulators to meet different application requirements in the future. For the purposes of this project, PTV Vissim was adopted as an example to implement the model, and a case study was conducted on the I–75 highway segment. The results from sensitivity analyses on key parameters revealed:

- The mobility performance was affected by the CAV headway in relation to the HV headway. In the case that the CAV headway was longer (which is possible in the initial stage of CAV deployment), the mobility performance degraded when the CAV penetration rate increased.

- The overall traffic performance initially improved and then degraded as the cooperation rate increased. This is probably because too-low cooperation rates would have decreased the chances for CAVs to complete LCs, and thus the CAVs remained at a slower speed for longer. On the other hand, too-high cooperation rates would have resulted in greater vehicle gaps and more speed oscillation due to overly frequent LC activities.

- The traffic performance initially improved and then degraded as incentive criterion threshold Δa increased. This result was probably because too low Δa values would have encouraged overly frequent DLCs that, again, would have increased vehicle gaps and speed oscillation. On the other hand, too high Δa values would have decreased the chances of DLCs, and thus caused vehicles to be stuck at slower speeds.

- The traffic performance initially improved and then degraded as incentive criterion bias a_{bias} increased. This result was probably because too-low a_{bias} values would have resulted in more vehicles in the left lanes, thus blocking fast-overtaking vehicles. On the other hand, too high a_{bias} would have led to disproportionally heavy traffic concentration in the right lanes, which would have impeded onramp traffic and aggravate overall congestion.

- The optimal Δa and a_{bias} values for the best performance were consistent with those observed in the existing HV traffic. This indicated that human drivers, to some extent, might have learned the optimal driving behavior. Thus, the design of CAV driving models might benefit from learning HV driving behavior.

- The impacts were amplified as the traffic congestion level increased, probably because vehicles in more congested traffic would have had less room to maneuver through downstream LC activities.

The proposed model is limited in the following aspects: First, the calibration and validation approaches were performed with the field data from relatively small-scale experiments with a specific lab-designed automated vehicle. These approaches may be tested with larger-scale data with more diverse CAV technologies. Second, platooning for longitudinal CAV control is not considered in the study. Third, various HV behaviors in response to surrounding CAVs as indicated from previous studies (e.g., Zhao et al. 2020) are not yet incorporated.

CHAPTER 5. JOINT APPLICATION: SPDHRM AND MERGE COORDINATION

LIST OF VARIABLES

This section lists all variables used in this chapter along with their definitions. Those variables only apply to models described in this chapter. The same notation might represent different variables in other chapters of the report.

a = acceleration.
$|A|$= area covered by section A.
a_0 = factor used to normalize the acceleration.
a_l = acceleration of the leader.
a_n = maximum acceleration.
a_n^d = acceleration of vehicle n.
a_n^{decc} = maximum deceleration of vehicle n.
a_s = acceleration of the follower.
a_x^{max} = maximum longitudinal acceleration.
a_y^{max} = maximum lateral acceleration.
b_n = desired deceleration.
d = candidate broadcasting distance.
D = set of broadcasting distance values.
$d(A)$ = total distance traveled by all vehicles in section A.
$DT_{tv}(u_v^{m5})$ = distance traveled by all vehicles in the vehicle set (V^{us}) over an optimization horizon (t_{oh}).
k = timestep.
$k(A)$ = density for observed vehicles in section A.
L = vehicle length.
l = vehicle length.
l_n = length of vehicle n.
N = number of vehicles.
N_p= prediction horizon.
$P(C)$ = probability of driving in a congested traffic condition.
$P(UC)$ = probability of driving in a uncongested traffic condition.
$p_{n,i}$ = crash probability.
$q(A)$ = flow for observed vehicles in section A.
S = total deceleration effort of SV.
s_0^n = jam distance.
s^{data} = spacing between vehicles based on data.
s_{min} = minimum distance.
s_n = spacing for vehicle n.
s_{ref} = maximum between the minimum distance (s_{min}), following distance based on the reaction time (s_{system}), and safe following distance (s_{safe}).
s_{safe} = safe following distance.
s^{sim} = spacing between vehicles based on simulation.
s_{system} = following distance based on the reaction time.
t = timestep.

$t(A)$ = total time spent by all vehicles in section A.
t_{oh} = optimization horizon.
t_{LC} = lane-changing duration.
T = desired time headway.
T_0 = original time headway.
$T_{current}$ = current time headway.
T_n = desired time headway for vehicle n.
$t_{sampling}$ = sampling duration.
TTI = travel time index.
u = candidate speed.
U = set of speed values.
u_{min} = minimum speed.
u_{max} = maximum speed.
U_{PT} = expected value function.
U_{PT}^{C} = value function for the congested traffic conditions.
U_{PT}^{UC} = value function for the uncongested traffic conditions.
v = speed.
v_l = predecessor velocity.
v_0^n = desired speed for vehicle n.
v_n = speed of vehicle n.
$v(A)$ = mean speed for observed vehicles in section A.
v_0 = the desired speed.
V^{us} = vehicle set.
v_s = follower velocity.
γ = *prospect theory-based model parameter*
w_m = *prospect theory-based model parameter*
w_c = crash weighing factor
x = position.
x^{data} = vehicle location based on data.
x_l = predecessor location.
x_l^{data} = leader location based on data.
x_n = position of vehicle n.
x^{sim} = vehicle location based on simulation.
x_s = follower location.
β_{PT} = sensitivity of choice to the utility.
δ_n = free acceleration exponent.
τ_n = reaction time of vehicle n.
λ = string stability parameter.

PURPOSE OF THE MODELS

Technologies related to advanced driving assistance systems (ADAS) and AVs have gained significant interest recently. The focus of the transportation community has been on investigating the implications of widespread adoption of these technologies on safety, congestion, energy consumption, and emissions. Relatively limited research has focused on designing AVs to improve the aggregate traffic-flow dynamics by considering both the longitudinal and lateral

vehicular movements. To address this shortcoming, the researchers focused on combining SPDHRM (as a longitudinal vehicular movement control logic) and merge coordination (as lateral vehicle movement control logic).

SPDHRM

As a traffic control strategy, SPDHRM adjusts the speed limit of a freeway section based on prevailing traffic conditions (Talebpour et al. 2013). The strategy helps mitigate shock-wave formation, dampen shock-wave propagation, improve traffic homogeneity by minimizing the spatial variance of speed, and accelerate the recovery from a traffic breakdown (Mahmassani 2016; Mahmassani et al. 2012). Benefits of implementing such a strategy include (Mahmassani et al. 2018):

- Improved traffic safety by effectively delaying or eliminating traffic breakdown (Talebpour 2013).
- Reduced emissions and higher fuel consumption efficiency as a result of effectively suppressing the development of vehicle-speed oscillation (Wang et al. 2015; Yang 2014).
- Improved traffic efficiency by reducing the total time spent in the network (Wang et al. 2015).

Shock-wave detection and speed-limit broadcasting to upstream vehicles constitute the major components of the SPDHRM strategy. Traditionally, this strategy was conducted using sensors embedded in the infrastructure for the shock-wave detection component and VSL signs at prespecified locations for the speed-limit broadcasting component. This setup faces three main challenges. First, fixed-infrastructure sensors provide an incomplete representation of traffic-flow dynamics, which can significantly diminish the effectiveness of the strategy. Second, relying on fixed-road sensors and signs significantly affects the strategy performance. Finally, it is difficult to develop accurate models that are capable of predicting the future traffic state utilizing data from fixed-traffic sensors (Elfar et al. 2019; Elfar et al. 2020).

CVs as probe vehicles can monitor their surrounding traffic conditions and communicate that information to the infrastructure and to other connected vehicles. Capabilities of CVs enable more accurate shock-wave detection and a greater range of effectiveness in speed-limit broadcasting compared to conventional methods. Besides the benefits of CVs, AVs can help to dampen the effect of shock waves in the traffic flow.

Merge Coordination

To explore the impact of both lateral and longitudinal movements on traffic-flow dynamics and shock-wave formation, the researchers focused on developing a CM application. LC maneuvers are considered a major source of disturbance in the traffic stream, and their impact is more prominent at the merging points. The shock-wave magnitude and duration resulting from an LC depends on the LC trajectory, traffic conditions in the origin and target lanes, and the response of the vehicles in the target lane to the LC vehicle. The focus of this model development effort was to illustrate that, with careful coordination between the LC vehicle and other vehicles in the target lane, one can significantly reduce the shock-wave magnitude and duration (and even completely prevent it in some cases).

Accordingly, the researchers proposed a combined optimization approach for both lateral and longitudinal movements of the vehicles involved in the LC maneuver (both the LC vehicle and vehicles in the target lane). The proposed approach consisted of: designing a model predictive control (MPC) for the CF behavior of vehicles in the target lane and optimizing the LC trajectory to minimize the total deceleration effort in the target lane (i.e., the amount of deceleration that occurs in the target lane to accommodate the LC vehicle). Note that the LC maneuver could have a reasonable duration.

Joint Application

While each of the aforementioned models can significantly improve congestion and prevent shock-wave formation or propagation, the benefit of combining them into one joint application can significantly surpass the benefits of individual applications. Particularly, merge coordination can eliminate or reduce the shock-wave formation at merge locations (and eliminate or reduce the shock-wave formation from any LC maneuver if extended to the coordinated LC application), which can significantly benefit SPDHRM in the following ways:

- The merging vehicle can provide an accurate prediction of the magnitude and duration of the created shock wave to the SPDHRM system. Combined with the utilized machine-learning approach, the SPDHRM system can accurately predict the flow dynamics and adjust the speed limit accordingly.

- The merge-coordination system can significantly reduce the magnitude and duration of the shock waves at the merge coordination, thus reducing the load on the SPDHRM system. Accordingly, the SPDHRM system will be activated only in cases that it provides the most benefit.

Similarly, the SPDHRM system can significantly benefit the merge-coordination system by:

- Adjusting the inflow to the merge location to assist the merging vehicle in finding the right gap.

- Reducing the negative impacts of merging on traffic-flow dynamics by controlling the shock-wave propagation at the merge location.

Supporting CAV Simulation/Community

Combining multiple applications can provide the opportunity to achieve a much greater positive impact on the transportation system. However, the majority of the existing CAV applications have been developed in isolation without considering the complications that can arise from operating multiple applications simultaneously. By combining two applications into one joint application, this demonstrates: how combining two applications can outperform both applications in terms of impacts on congestion mitigation and how one can address the complications that can arise from combining and operating two applications simultaneously. The development of this joint application can provide some insight into the challenges and benefits of combining and operating multiple applications simultaneously.

MODEL DEVELOPMENT AND LOGIC

SPDHRM

This section discusses the model development procedure and provides details about the overall design of the SPDHRM model.

Descriptions of SPDHRM Logic

A set of novel SPDHRM algorithms were developed that utilize machine learning to predict the onset of congestion and to activate the SPDHRM in a highway segment. These algorithms also utilize various methods of communicating the updated speed limits to the CVs (automated or human-driven) and non-CVs (automated or human-driven). The overall framework is shown in figure 83.

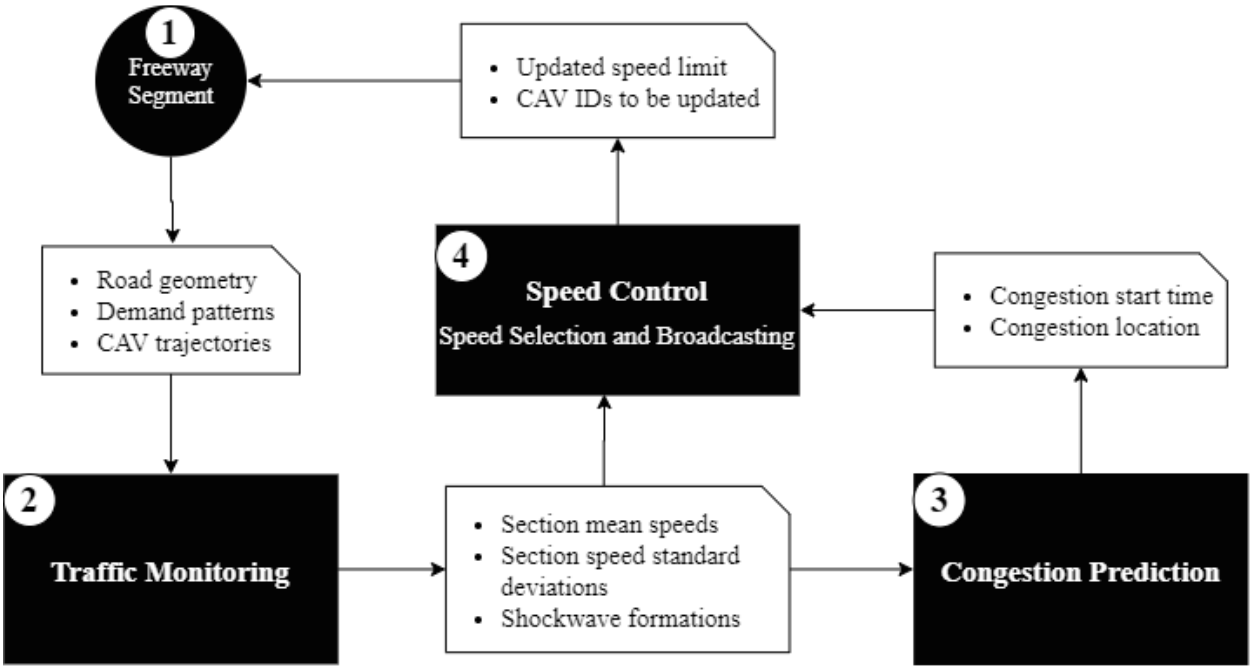

Figure 83. Diagram. SPDHRM overall framework.

The main algorithm of the simulation tool is shown in figure 84. The first component corresponds to the freeway segment element of the framework. It includes the inputs, outputs, and the driving logic of the tool. The driving logic contains the CF and LC models that specify the interaction among vehicles. The traffic monitoring module of the framework relates to the second element of the algorithm. Then, as the congestion-prediction module (third element of the algorithm), the model predicts the congestion characteristics and evaluates the SPDHRM strategy selected by the user (decentralized, centralized, or optimization-based). The fourth element in the algorithm is related to the speed-control module of the framework. This part of the algorithm implements the SPDHRM strategy by determining the advisory speed for each vehicle.

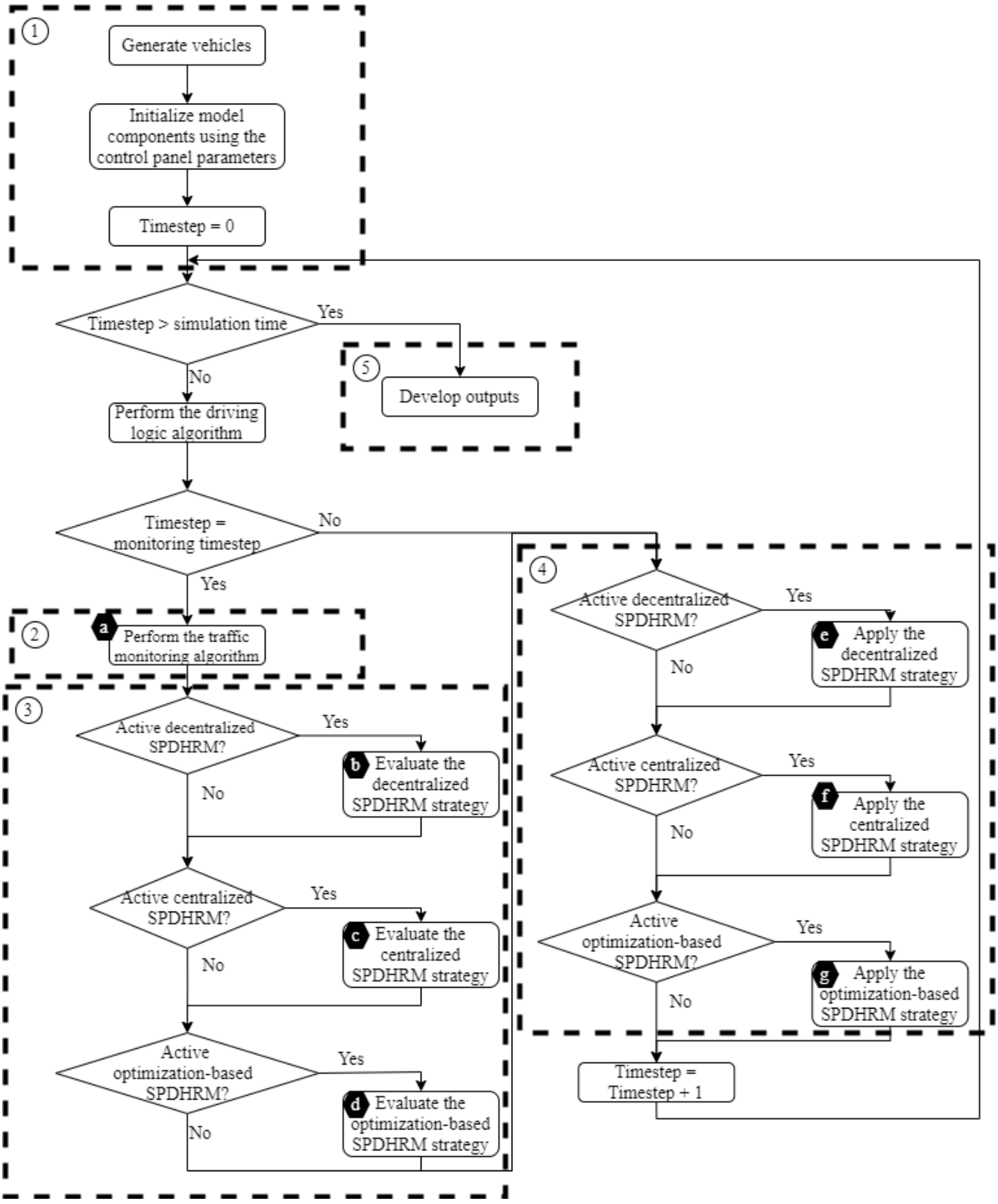

Source: FHWA.

Figure 84. Flowchart. Main algorithm.

The traffic monitoring module, as shown in figure 85, calculates the performance metrics for all sections of the road segment at each monitoring time step. The performance metrics are calculated using the CVs and CAVs in order to be used in the congestion prediction and speed-control modules. Simultaneously, the performance metrics are calculated for all vehicles in the system to evaluate the accuracy of the prediction models. As a result, to evaluate and implement the SPDHRM strategies, only the CAV information is analyzed.

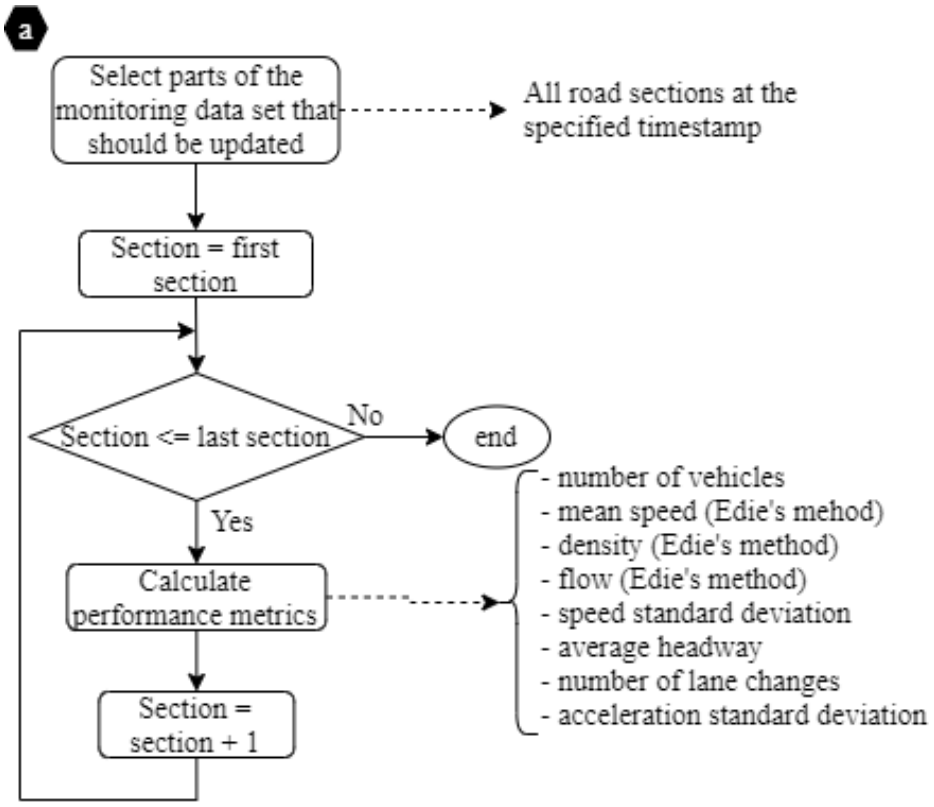

Source: FHWA.
*Edie's generalized definitions of fundamental traffic flow variables are shown in figure 92.

Figure 85. Flowchart. Traffic-monitoring algorithm.

Figure 86, figure 87, and figure 88 show the algorithms in the congestion-prediction module. Based on the settings defined in the control panel, one of the algorithms is performed: centralized, decentralized, or optimization based. This module determines the location and time of the congestion along with the advisory speed limit. The training part of the algorithms could be performed in an online or offline manner. The training part could be skipped if a predefined congestion-prediction model is utilized.

In the centralized strategy, the system evaluates the state of the transport facility through information received from CAVs and detectors. Then, it predicts future states using machine-learning algorithms. Finally, the advisory messages are prepared to be broadcast to CAVs in order to minimize disturbance (speed standard deviation). On the other hand, in the decentralized strategy, each CAV receives information from a cluster or fleet of CAVs within a detection/connection range. Then, each vehicle utilizes individualized or group-based machine-learning algorithms to predict the future state of clusters. Finally, the vehicles adjust

their longitudinal and lateral driving behavior to minimize disruption in a cluster or fleet of vehicles, i.e., self-homogenize. The advisory speed limit in the optimization-based strategy is determined by solving an optimization problem that seeks to maximize the distance traveled by the vehicles in a specified period (prediction time horizon). Based on the available computational resources, the complexity of the optimization problem could be adjusted ranging from jointly determining the advisory speed for each vehicle and the broadcasting distance (high complexity) to selecting the advisory speed limit and the broadcasting distance from a limited set (low complexity).

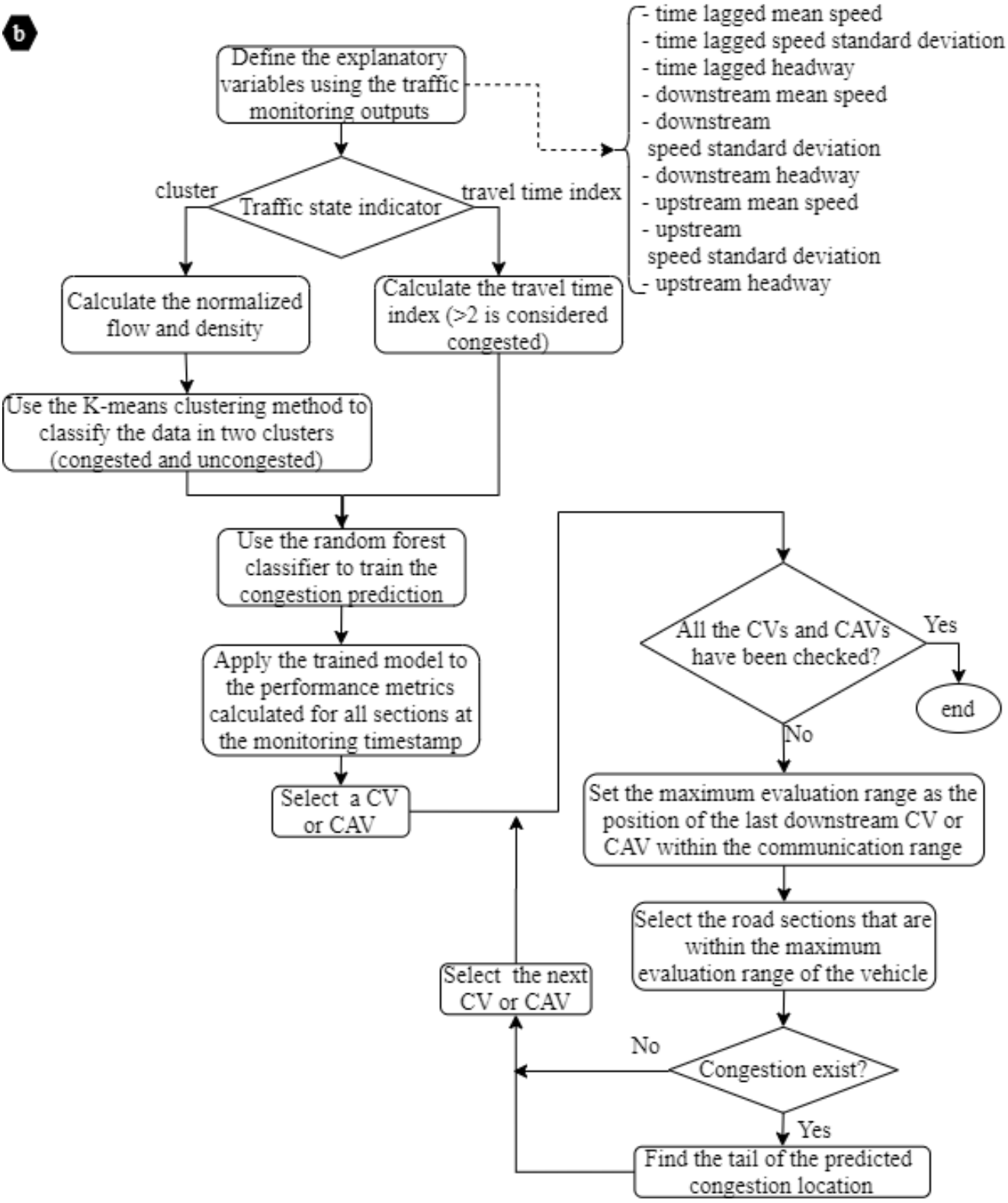

Source: FHWA.

Figure 86. Flowchart. Decentralized SPDHRM strategy evaluation algorithm.

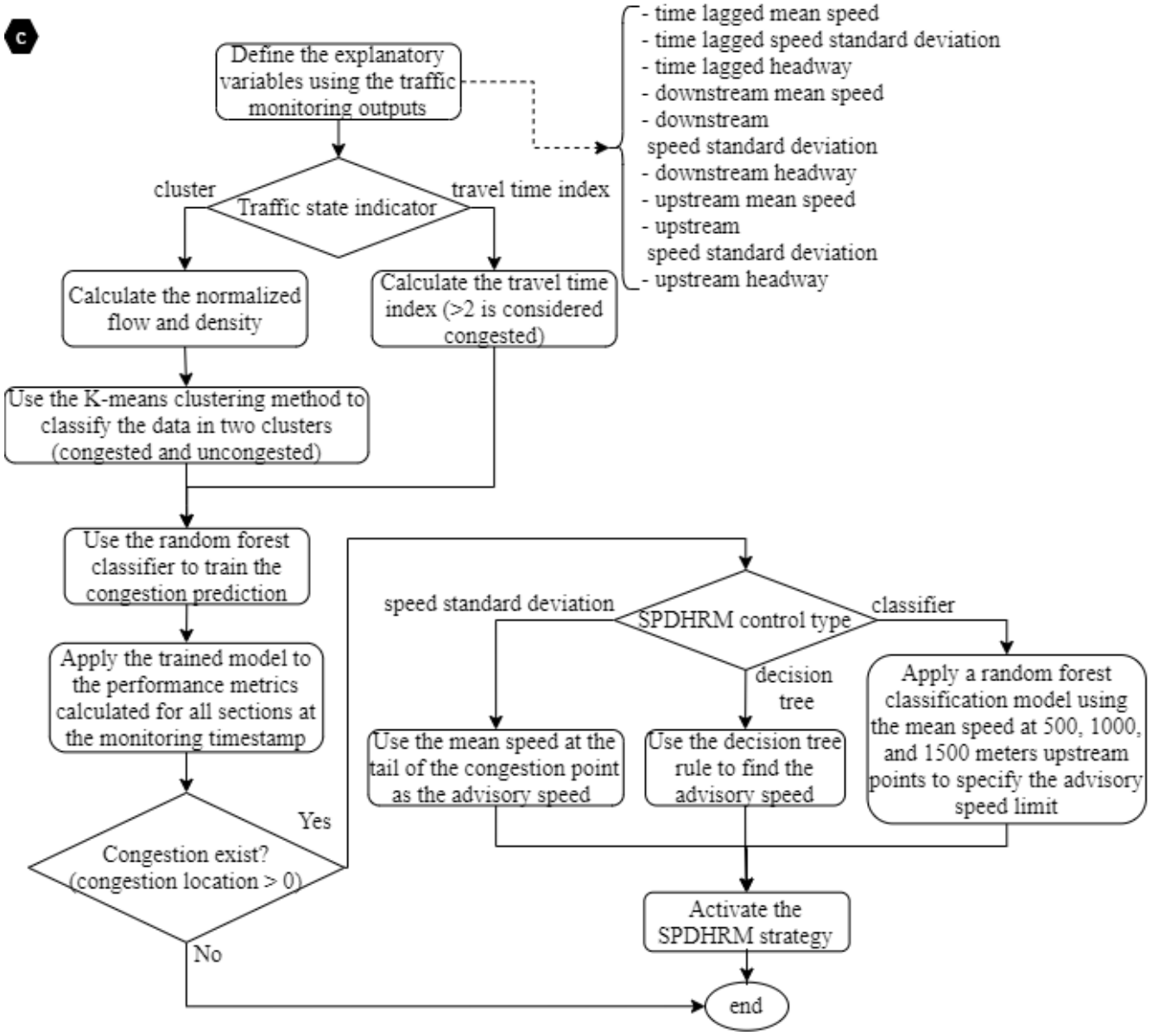

Source: FHWA.

Figure 87. Flowchart. Centralized SPDHRM strategy evaluation algorithm.

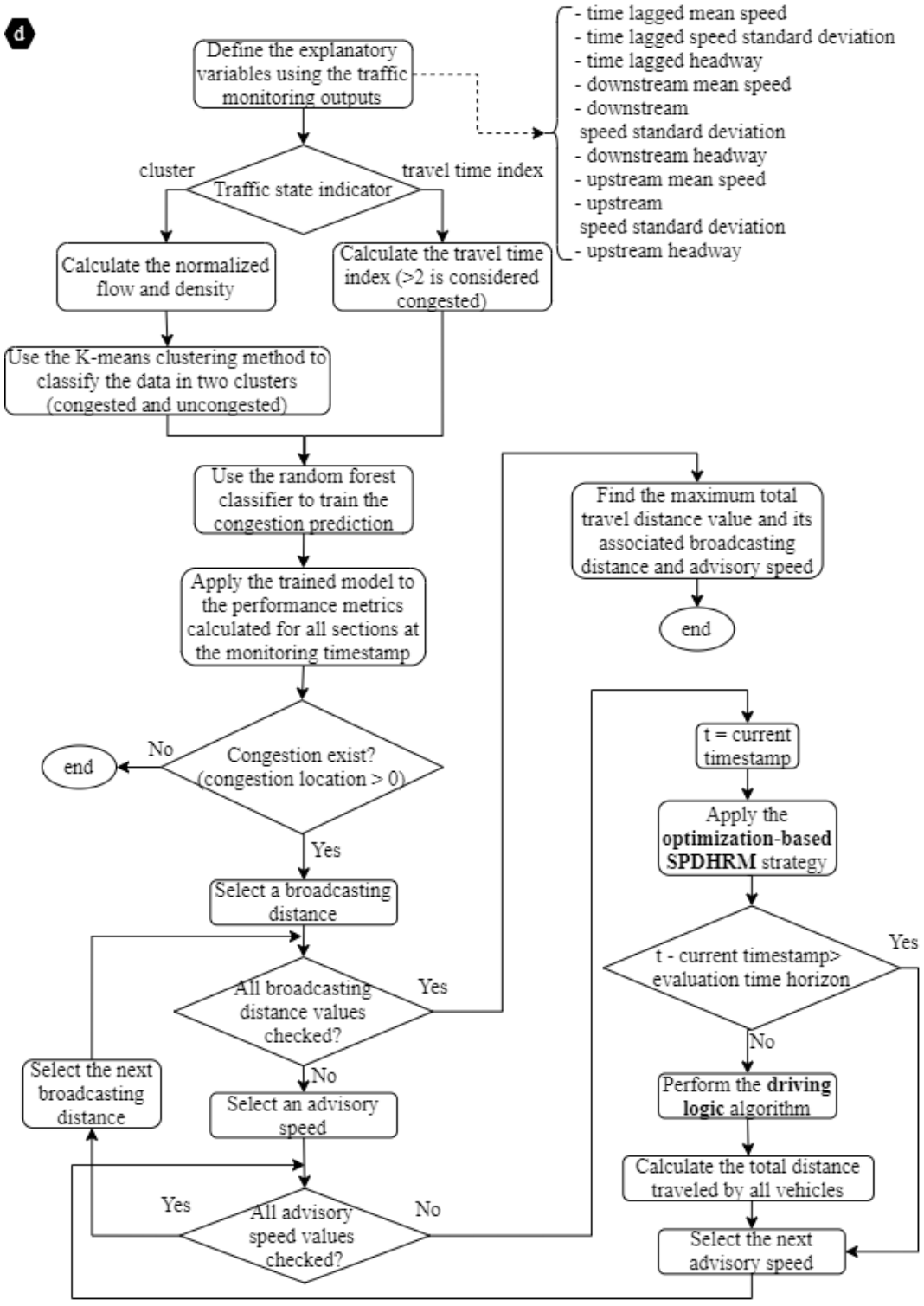

Source: FHWA.

Figure 88. Flowchart. Optimization-based SPDHRM strategy evaluation algorithm.

Figure 89 through figure 91 show the algorithms of the speed-control module. A step-by-step procedure is performed to communicate an advisory speed limit to CVs and AVs. Extra precautions are taken to prevent artificial slowdowns in the simulation by applying a gradual transition in the advisory speed limit communicated to the vehicles.

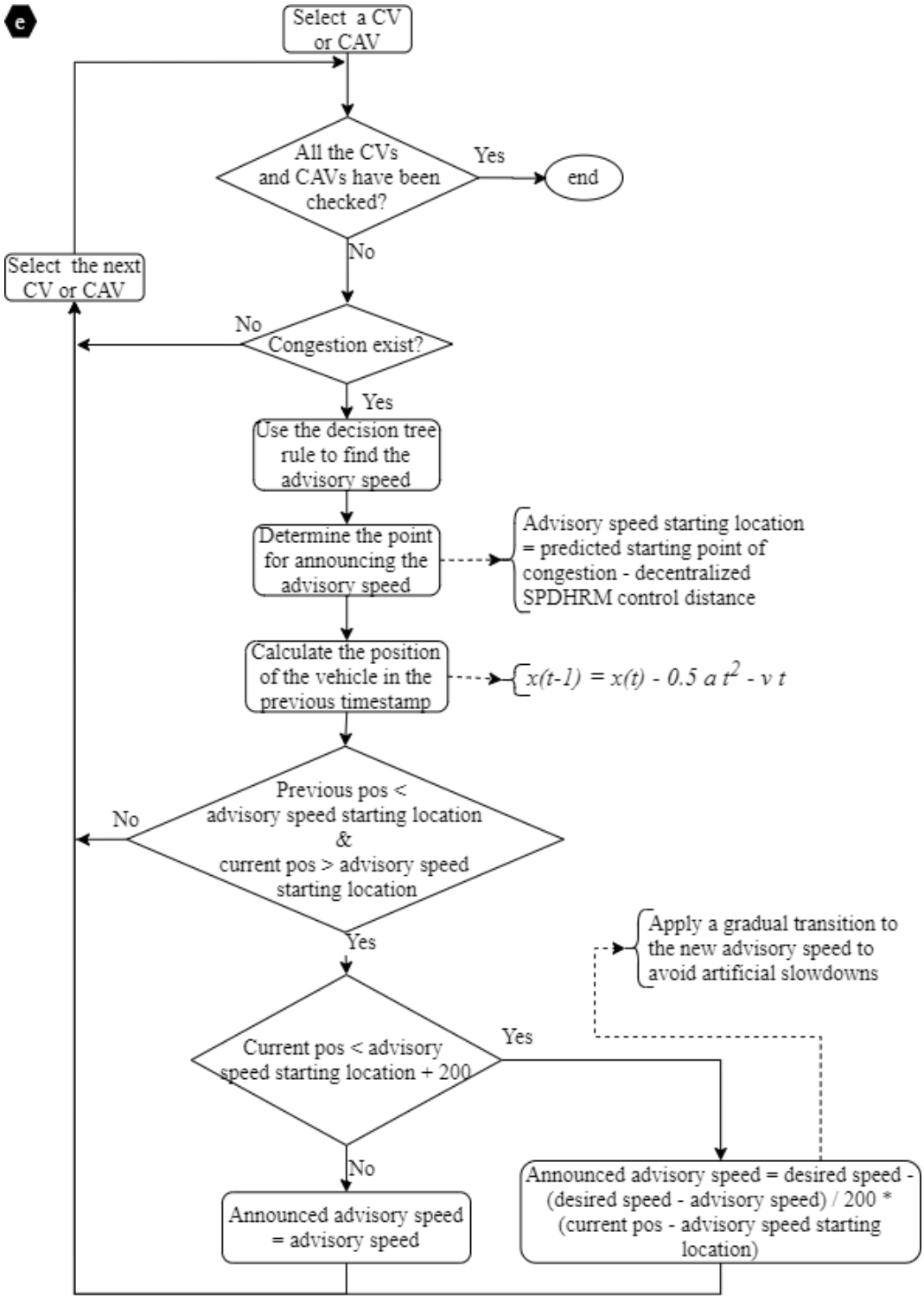

Source: FHWA.

Figure 89. Flowchart. Decentralized SPDHRM strategy implementation algorithm.

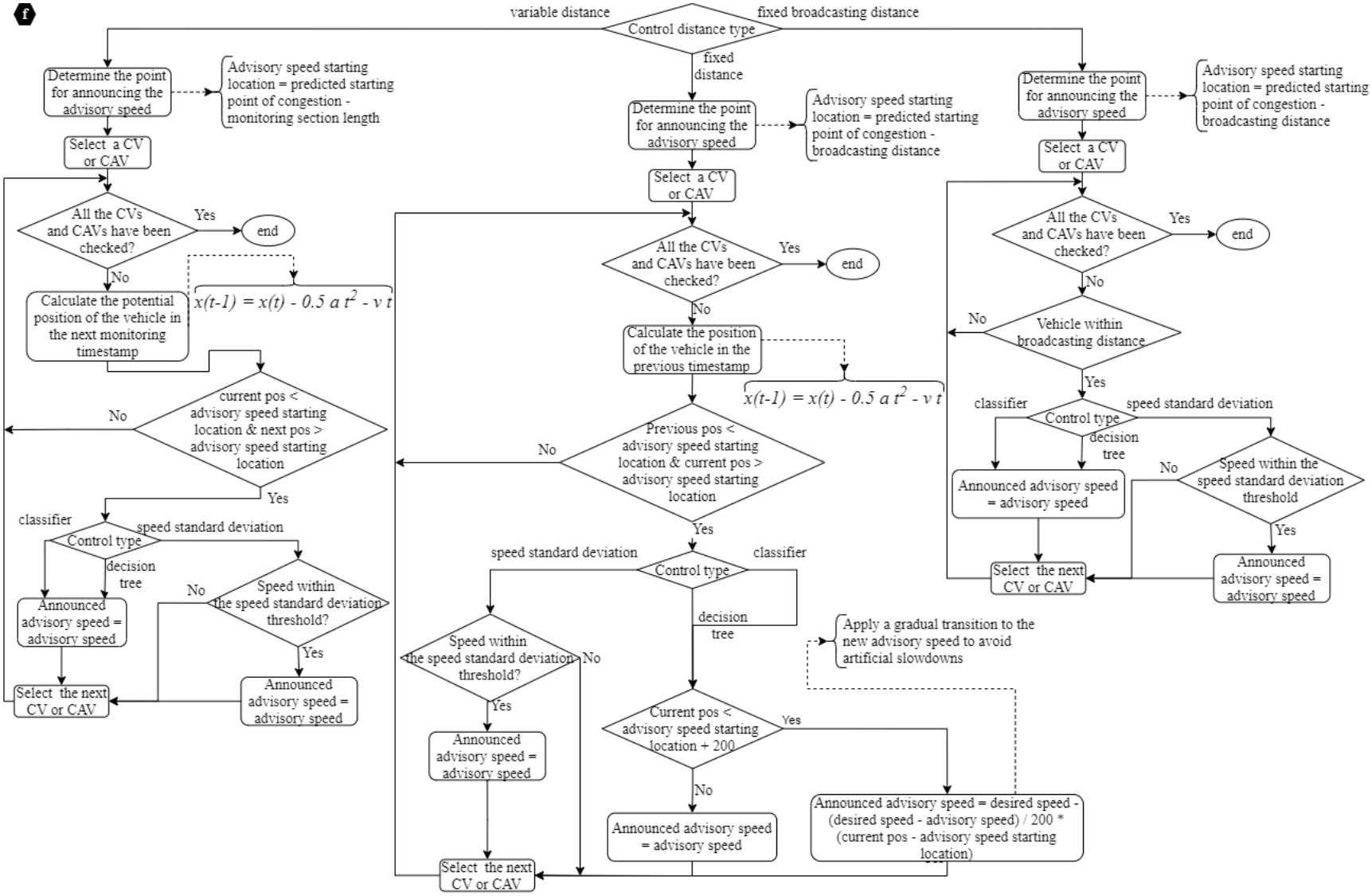

Source: FHWA.

Figure 90. Flowchart. Centralized SPDHRM strategy implementation algorithm.

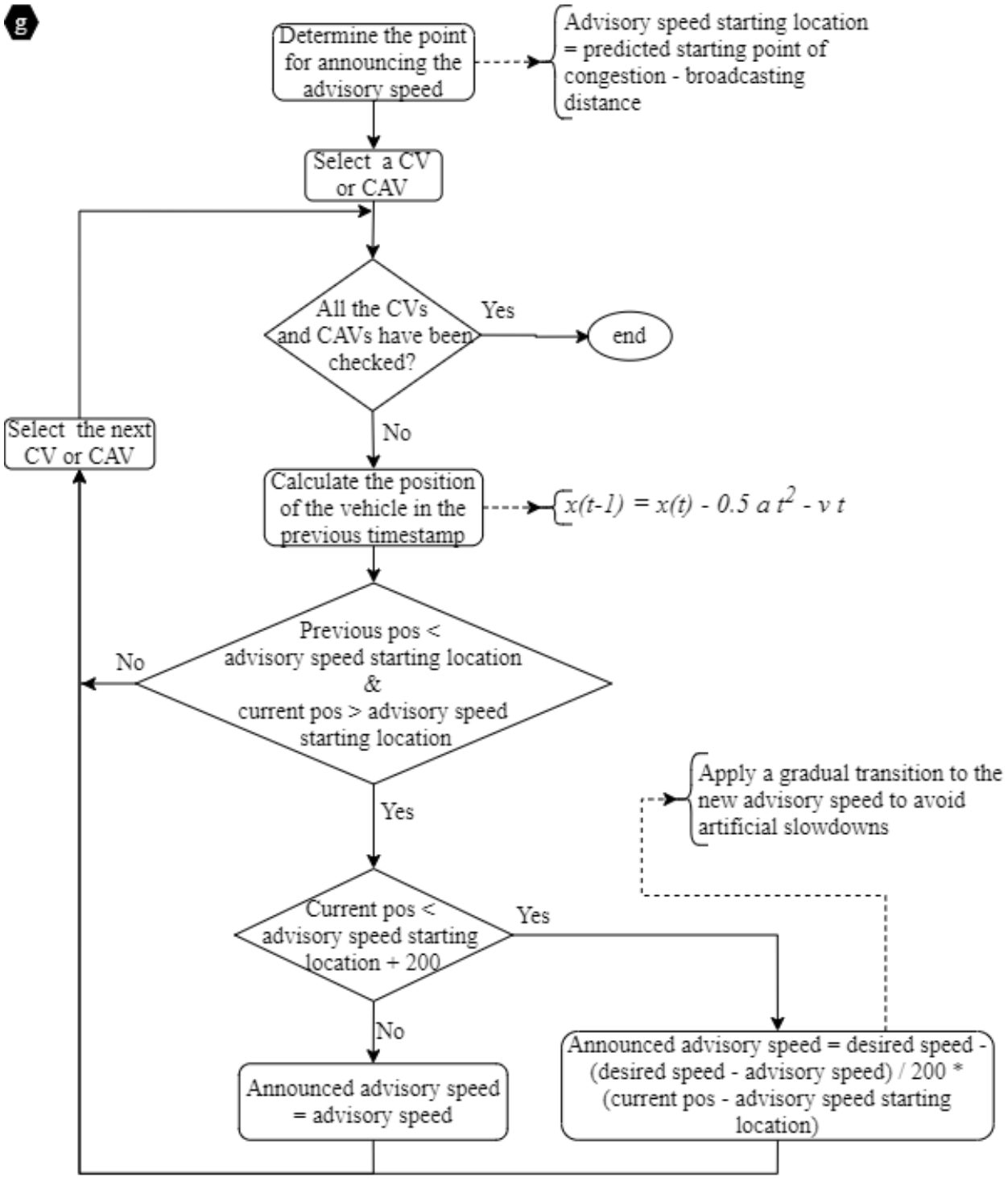

Source: FHWA.

Figure 91. Flowchart. Optimization-based SPDHRM strategy implementation algorithm.

SPDHRM Model Development

In the traffic monitoring module, the study area is divided into sections with a specified monitoring length determined by the user. Flow, mean speed, and density for each section at each timestep were calculated using Edie's generalized definitions for individual facilities (Edie 1963), shown in figure 92:

$$q(A) = \frac{d(A)}{|A|}$$

A. Edie's definition of flow.

$$k(A) = \frac{t(A)}{|A|}$$

B. Edie's definition of density.

$$v(A) = \frac{d(A)}{t(A)}$$

C. Edie's definition of speed.

Figure 92. Formulas. Edie's generalized definition of the traffic-flow characteristics.

Other statistics of the traffic such as the standard deviation of the speed could be calculated for each road section at the monitoring timestep.

Different methodologies could be used to predict the state of the traffic and the location and time of congestion points. Machine learning is one way to take advantage of a large amount of information that can be generated by CVs. Some studies investigated congestion prediction with machine learning using various data sources. For example, Thianniwet (2009) developed a congestion classifier by applying a decision tree algorithm on the movement patterns of vehicles collected through phone global positioning systems. In another study by Pattara-Atikom (2007), neural networks were used as a machine-learning algorithm to estimate traffic congestion from cell dwell time. Some studies utilized a hybrid of multiple techniques, such as a study by Vlahogianni et al. (2008) that identified traffic patterns using clustering and then forecasted flow using neural networks.

The first step for building predictive models is to identify the traffic state from vehicle trajectories. The traffic state is used as the dependent variable in the machine learning-based classification model. Travel time index (TTI) (Texas Transportation Institute 2005) and K-means clustering (Hartigan 1975) are the two methods implemented in the tool that would enable the traffic state to be classified in one of the two classes used in this study: congested or uncongested. The K-means clustering algorithm segments data points into clusters (groups) where the total distances calculated from each point to its respective cluster center is minimized. As density and flow values are significantly different, the values were scaled to be between 0 and one before running the algorithm. Then, the density values were multiplied by a factor of five (arbitrarily chosen) to give density values a higher weight and force the algorithm to split the clusters based on density and define the critical density at which traffic breaks down. The *TTI* defined in figure 93 has been suggested as a way of identifying traffic congestion (Dong and Mahmassani 2009). The *TTI* could be calculated for each section of the study area.

$$TTI = \frac{Mean\ Speed^{-1}}{Free\ Flow\ Speed^{-1}}$$

Figure 93. Formula. TTI.

The congestion-prediction module utilizes the traffic characteristics and performance metrics calculated for each road section to predict the location and time of congestion formation within a short time horizon (10–30 s). Besides the traffic-flow characteristics calculated using Edie's generalized formulation, Elfar et al. (2018) showed that the speed standard deviation could be used as an indicator of shock-wave formation and propagation. They found that a 30-percent connectivity level is necessary to identify the shock wave accurately.

For the prediction model that utilizes machine-learning algorithms, temporally lagged and spatially distributed variables are developed for the traffic characteristics and performance metrics. As a result, the developed congestion models have temporally lagged models, which are a type of time-series model trained to predict current and future values of the dependent variable using explanatory variable values observed in previous timesteps. Therefore, by plugging in the current values of independent variables, the model predicts the future values of the dependent variable. Elfar (2019) showed that for an accurate prediction of the congestion state of a road section, the following three statistics calculated in the previous monitoring timestep could be considered as the explanatory variables: the mean speed in the specified section, the mean speed in the downstream section, and the speed standard deviation in the downstream section.
Elfar et al. (2018) tested three types of machine-learning techniques for the prediction model: binary logistic regression, random forests, and artificial neural networks. They found that the models with the binary logistic regression and random forests algorithms performed slightly better than the model with the neural network algorithm. In this simulation tool, the random forest technique was implemented. Table 17 summarizes the nature of variables used in the predictive model.

Table 17. Variables used in the predictive model.

Variable Type	Variable Name	Description
Dependent variable	Traffic state	Binary: the state of traffic whether congested or uncongested as identified using the travel time index with a threshold above 2 or the K-means clustering algorithm
Explanatory variable 1	Lagged mean speed in current section	Continuous: the average speed of individual vehicles in the current section, lagged 10, 20, or 30 s
Explanatory variable 2	Lagged mean speed in downstream section	Continuous: the average speed of individual vehicles in the next downstream section, lagged 10, 20, or 30 s
Explanatory variable 3	Lagged speed standard deviation in downstream section	Continuous: the speed standard deviation of individual vehicles in the next downstream section, lagged 10, 20, or 30 s

In the speed-control module, the optimization-based SPDHRM strategy evaluates a wide set of potential speed limits. It selects the limit that maximizes traffic speed and mitigates congestion. The formulation proposed in figure 94 enables the possibility of assigning a speed limit for each CV in the system.

$$\max \sum_{t=t_\circ}^{t_\circ+t_{oh}} \sum_{v\in V} DT_{tv}(u_v^{m5})$$

$$u_{min} \le u_v^{m5} \le u_{max}, \quad \forall v \in V^{us}$$
$$u_v^{m5} = 5 * u_v, \quad \forall v \in V^{us}$$
$$u_v \text{ integer}, \quad \forall v \in V^{us}$$

Figure 94. Formulas. Mathematical formulation of the optimization-based SPDHRM strategy.

The optimal speed of each vehicle as the decision variable varies between a set of minimum (u_{min}) and maximum (u_{max}) values. The second condition in the formulation limits the speed selected for each vehicle to multiples of five. This would ensure that the drivers could practically adhere to the new speed limits. Maximizing the distance traveled over a fixed period is equivalent to maximizing the traffic speed.

A simulation-based optimization approach can be adopted in order to find the advisory speed for each vehicle that would collectively result in maximizing the distance traveled by all vehicles because of the interactions of the vehicles captured by the CF, LC behavior, vehicle classes, and traffic control. The primary limitation of simulation-based optimization problems is the computationally intensive and time-consuming simulations that are associated with finding the optimal solution. The number of decision variables could be reduced significantly to practically solve the optimization problem. A simplified version of the problem is shown in figure 95 where the speed and the broadcasting distance are selected from sets. Furthermore, instead of solving for a unique speed limit per vehicle, the problem is reformulated to solve for one speed limit for all vehicles upstream of the predicted congestion location.

$$\max \sum_{t=t_\circ}^{t_\circ+t_{oh}} \sum_{v\in V} DT_{tv}(u,d)$$
$$u \in U = \{u_{min}, (u_{min} + 5), \ \dots, u_{max}\}$$
$$d \in D$$

Figure 95. Formulas. Simplified mathematical formulation of the optimization-based SPDHRM strategy.

Merge Coordination

This section discusses the model development procedure and provides details about the overall design of the merge-coordination model.

Descriptions of Merge-Coordination Logic

The merge-coordination model consists of two core modules: CF and LC. In the following, the logic behind both modules is presented.

CF Behavior

Interest in vehicle automation started several decades ago. From the CF behavior perspective, vehicle automation studies have mainly focused on vehicle platooning and its various derivations. Vehicle platooning and platoon-control design are considered necessary to achieve connected automated transportation systems. Moreover, the role of communications (V2V and vehicle-to-infrastructure (V2I)) on the performance of the platooning/CF behavior have been investigated extensively.

Several platooning strategies have been proposed in the literature. These strategies can be categorized into three distinct categories: constant spacing, where the platoon controller is focused on keeping a fixed spacing between vehicles, constant-time headway (CTH), where the platoon controller is focused on keeping a fixed-time headway between vehicles, and variable-time headway, where fluctuations in time headway are allowed to dampen the disturbances in the platoon. In general, the effectiveness of a platooning strategy and its associated controller have been investigated based on the concept of string stability. String stability is concerned with how the disturbance propagates through the string (Swaroop 1997). In a string-stable platoon, any disturbance has to attenuate along the platoon and cannot stay for a long time. Several studies investigated string stability in ACC and CACC systems. Seiler et al. (2004), by thinking of a platoon of vehicles as a system, describes how the disturbance caused by a vehicle propagates in the platoon. This type of research framework is mostly based on dealing with transfer functions between an initial disturbance and other states affected by the disturbance, such as position error or the acceleration of followers. Many studies have adopted a similar approach to investigate string stability. For example, Maschuw et al. (2008) and Kianfar et al. investigated how a disturbance affects the acceleration of followers. These studies proposed a methodology to reduce the overshoot in followers' velocity and acceleration caused by the disturbance.

In addition to the platooning strategies that only rely on onboard sensors, several studies have explored the impact of V2V and V2I communications and the information from other vehicles and infrastructure on the string stability. In Swaroop (1997), information about the platoon leader and the predecessor were found important for string stability in CACC. Swaroop showed that communication with the platoon leader is the necessary condition to ensure string stability in a platoon controlled by the constant spacing policy. Seiler et al. (2004) showed that the availability of the leader information is key to ensure string stability. They also compared the platooning results with the case without leader information. Wang and Rajamani (2004) compared CTH and constant-spacing strategies. Recently, Talebpour and Mahmassani (2016) investigated string stability in a platoon of CAVs and showed that both connectivity and automation increase the speed above which instabilities start to occur. In Talebpour et al. (2017), important concepts have been tackled to ensure connectivity in a mixed driving environment with CAVs. The authors showed how the correlation between communication range and connected vehicle density affects the connectivity level and the string stability of the traffic flow. Arefizadeh and Talebpour (2018) proposed a new CTH strategy for AV platoons to prevent shock-wave formation caused by speed drops.

LC Maneuver

Many approaches have been suggested to generate LC trajectories in a safe and reliable way. Typically, adopting a function that describes the geometric representations of trajectory has been a dominant approach. Various functions have been used in the literature (table 18). To compare several LC-trajectory functions, the project team considered continuity and smoothness.

Circular arcs: This is a simple approach to describe an LC trajectory. By putting circular arcs together, a simple trajectory can be obtained, and the radius of curvature is determined by lateral and longitudinal displacement after an LC maneuver. Based on the constant curvature, the lateral position can be determined depending on the velocity and the corresponding longitudinal position. However, this method has certain disadvantages; for instance, additional consideration is involved when dealing with the discontinuity issue that happens from connecting two arcs. More importantly, speed adjustment during the LC maneuver can become very complicated.

Polynomial: This is the most common approach to represent an LC trajectory. The trajectory can be generated by considering position constraints that the vehicle has to pass through. The key advantages of this approach are that these curves are easy to compute and can always generate a continuous curvature. Moreover, the polynomial can be of any order, and being able to consider higher order polynomials (polynomials higher than 4 degrees) gives more flexibility in terms of designing the trajectory. Normally, using a higher order increases flexibility in terms of trajectory shaping. In Cong et al. (2010), a fourth-order polynomial was used and constraints like maximum acceleration and maximum driving force were considered. In another study, Nelson (1989) used a fifth-order polynomial to describe the lateral position of the vehicle.

Bezier curves: Originally, Bezier curves were used in the field of computer graphics to obtain the curves. A Bezier curve is based on a concept called control points. Rastelli et al. (2014) showed that it is possible to shape the trajectory curve depending on the convex hull based on the control points. Therefore, this approach is a very intuitive way to manipulate the trajectory, and it has low computational cost to generate. González et al. (2014) obtained the LC trajectory using a Bezier curve considering the roadway constraints.

Spline curves: In a nutshell, this method is a piecewise polynomial curve. After generating points, each sub-interval between points can be described using any type of curve, including polynomial and circular (Piazzi et al. 2002; Bacha et al. 2008).

Occupancy grid: By discretizing the search space into a grid—as shown in figure 96—and checking the possibility that a grid is occupied by an obstacle, a feasible trajectory can be generated. Out of many graph-based approaches, this method is relatively straightforward to implement and computationally efficient. In Schroder et al. (2008) and Kolski et al. (2006), for each cell, the possibility of being occupied by an obstacle and the corresponding risk were calculated to check the feasibility of a trajectory.

State lattice: This approach also starts from the reconstruction of the environment but into a different search space, called state lattice, as shown in figure 96. Pivtoraiko and Kelly (2005) and Pivtoraiko et al. (2009) generated the trajectory based on state lattices that guarantee the feasibility of the path.

Table 18 summarizes the LC trajectory-generation methods. This project adopted the polynomial-based LC trajectory-generation method. Several factors contributed to this selection. First, the approach has a low-computation overhead and can use the boundary conditions to generate the polynomial that best describes the optimal trajectory. Second, by adding the sixth-order term, the method can optimize trajectory curvature to minimize impacts on the target lane. These features provide the trajectory optimization process with the opportunity to predict the behavior of the MPC and to minimize the disturbance caused by the LC maneuver.

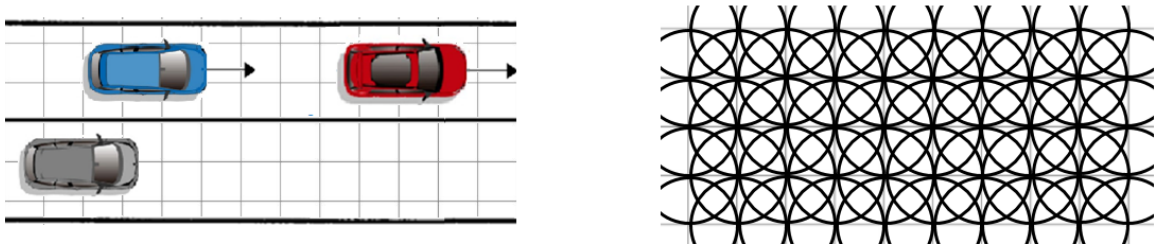

Source: FHWA.

Figure 96. Illustration. Trajectory-generation approaches: occupancy grid (left) and state lattice (right).

Table 18. LC trajectory-generation methods.

Methods	Description
Circular arc	Interpolation of waypoints using a circle
Polynomial	Interpolation of waypoints using polynomial curves
Bezier curve	Generating curves based on selected Bezier control points
Spline	Generating a piecewise trajectory
Occupancy grid	Generating a feasible trajectory based on the obstacle locations in a grid
State lattice	Generating a feasible trajectory based on the obstacle locations in a state lattice

Formal Problem Statement

The main focus of this study was to develop a merge-coordination application to minimize the negative impacts of the merging process on the target lane. During the merge-coordination process, the LC vehicle (LV) identifies the appropriate gap to initiate the merge process. The merge-coordination process ends with LV joining the platoon with SV as the new follower. SV is the key vehicle in the proposed merge-coordination application and will often be referenced as the platoon head (since a backward-moving shock wave starts from SV and moves backward in traffic). However, this reference does not mean that the platoon is divided into two separate platoons. On the contrary, both vehicles in front of LV and behind LV will be involved in the developed merge-coordination application to ensure a smooth LC maneuver.

Merge-Coordination Model Development

CF Controller

The goal here was to capture the full impact of LV on the target lane. Accordingly, SV was controlled based on the MPC and the remaining vehicles in the target lane could either be HVs, controlled by IDM (Treiber et al. 2000), or AVs, controlled based on a well-established fix-time headway car-following policy (Swaroop 1997). The overview of these modeling frameworks follows. More details can be found in An and Talebpour (2019).

Platoon Members: CTH Policy

The CTH policy of Swaroop (1997) was adopted in this section to represent the CF behavior of AVs. This model ensures a safe distance between vehicles by adjusting the vehicle speed/acceleration. As the first step, the spacing error between vehicles can be calculated in figure 97 as follows:

$$\delta(t) = (x_s - x_l) + Tv_l + l$$

Figure 97. Equation. Spacing error between the predecessor and its follower.

Once the spacing error is calculated, the equation in figure 98 can be utilized to calculate the acceleration:

$$a(t) = \frac{1}{T}[v_s(t) - v_l(t) + \lambda\delta(t)]$$

Figure 98. Equation. Acceleration of a string-stable platoon.

As indicated by An and Talebpour (2019), Swaroop's model (1997) can be extremely inefficient dealing with sudden changes in time headway (e.g., the case of the LC into a platoon). More details on the behavior of this model when dealing with sudden changes in time headway is presented in the next section.

Platoon Head: MPC Approach

To address the issues associated with CTH policy, this study utilizes an MPC-based control for SV. Following the information provided by An and Talebpour (2019), the CF dynamics can be formulated in figure 99 as follows:

$$\dot{v}_s = a_s$$

A. Relationship between acceleration and speed for the follower.

$$\dot{v}_l = a_l$$

B. Relationship between acceleration and speed for the leader.

$$\dot{x} = (v_l - v_s) + \frac{1}{2}(a_l - a_s)t_{sampling}$$

C. Relationship between follower location, follower speed, leader speed, follower acceleration, and leader acceleration.

Figure 99. Equations. Longitudinal dynamics equations.

The equation in figure 100 can be discretized using the Euler method for simulation purposes.

$$v_s(k+1) = v_s(k) + a_s(k)t_{sampling}$$

A. Relationship between acceleration and speed for the follower.

$$v_l(k+1) = v_l(k) + a_l(k)t_{sampling}$$

B. Relationship between acceleration and speed for the leader.

$$x(k+1) = x(k) + (v_l(k) - v_s(k))t_{sampling} + \frac{1}{2}(a_l(k) - a_s(k))t_{sampling}{}^2$$

C. Relationship between follower location, follower speed, leader speed, follower acceleration, and leader acceleration.

Figure 100. Equations. Discretized longitudinal dynamics equations.

The key difference between the CTH policy and the MPC design is the fact that MPC works based on the projected trajectory of LV to calculate the acceleration for SV. Assuming that LV can share its movement profile (i.e., trajectory and speed), MPC can use actual a_l to predict v_l. Accordingly, MPC can accurately predict T based on a_l and a_s. This opens up the opportunity to utilize a cost function to ensure the optimal T by generating an optimal control sequence based on a_s, i.e., $a_s(k)$- a_s $(k-1)$, where k is the timestep. Two cost functions are defined to address SV's safety requirement to slow down to prevent a collision with LV and SV's desired speed requirement. The details of these cost functions are discussed in the following section.

First Cost Function: Keeping a Safety Distance

The first cost function is concerned with creating the safe distance between SV and LV. This is the key, as sudden slow down (similar to the CTH policy) can result in a significant shock wave. The cost function is formulated in figure 101 as follows (An and Talebpour 2019):

$$\left\|\hat{\boldsymbol{T}}_{current(k+i/s)} - \hat{\boldsymbol{T}}_{(k+i/s)}\right\|_{R_1}^2 + \left\|\hat{\boldsymbol{a}}_{s(k+i/s)} - \hat{\boldsymbol{a}}_{l(k+i/s)}\right\|_{R_2}^2 + \left\|\Delta \boldsymbol{a}_{(k+i/k)}\right\|_{R_3}^2$$

Figure 101. Equation. Cost function for making the safe distance.

The first part of the equation tries to capture the deviation from the desired time headway. The second part of the equation ensures consistency between the acceleration behavior of SV and LV. In other words, SV tries to mimic the acceleration/deceleration behavior of SV while maintaining a desired time headway. The last part of the equation ensures comfort and prevents sudden changes in acceleration values.

Second Cost Function: Speed Recovery

The second cost function is concerned with recovering the speed after slowing down to accommodate the LC vehicle. The cost function is formulated in figure 102 as follows (An and Talebpour 2019):

$$\left\|\hat{\boldsymbol{v}}_{s(k+i/s)} - \hat{\boldsymbol{v}}_{0(k+i/s)}\right\|_{\boldsymbol{Q_1}}^{\boldsymbol{2}} + \left\|\hat{\boldsymbol{a}}_{s(k+i/s)} - \hat{\boldsymbol{a}}_{l(k+i/s)}\right\|_{\boldsymbol{Q_2}}^{\boldsymbol{2}} + \left\|\Delta \boldsymbol{a}_{(k+i/k)}\right\|_{\boldsymbol{Q_3}}^{\boldsymbol{2}} + \left\|\boldsymbol{a}_{(k+i/k)}\right\|_{\boldsymbol{Q_3}}^{\boldsymbol{2}}$$

Figure 102. Equation. Cost function for speed recovery.

The first term in this equation captures the deviation from the desired speed. The second and third terms are similar to the first cost function. The fourth term is included to capture the preference to zero acceleration (i.e., minimum possible response to LV).

Combined with the following constraints, the above cost functions can result in the optimal acceleration choice, shown in figure 103 (An and Talebpour 2019):

$$\begin{aligned} \text{Subject to:} \quad & s_{k+1} = f(s_k, \Delta a_s(k)) && k = t, \dots, t + N_p \\ & \Delta a_{min} \leq \Delta a_{s(k)} \leq \Delta a_{max} && k = t, \dots, t + N_p \\ & a_{s(k)} = a_{s(k-1)} + \Delta a_{s(k)} && k = t, \dots, t + N_p \end{aligned}$$

Figure 103. Equation. Constraints for the safe recovery problem.

The prediction horizon is shorter for the first cost function compared to the second cost function. This ensures a quick adaptation to the LC vehicle. The first constraint in figure 103 models the longitudinal dynamics, predicted based on control input. The second constraint limits the control input, and the third constraint illustrates how acceleration value can be calculated over the prediction horizon based on the control input.

Choosing the correct model weights is the key to a successful implementation of the aforementioned MPC design. Consideration and use of different weight values depends on the scenario. R_1 captures the sensitivity to the deviation from the time headway. High values of R_1 mean that the vehicle would be sensitive to small changes in the time headway. R_2 determines how fast SV could adjust to the changes in LV's acceleration choices. The combination of R_1 and R_2 ensures naturalistic CF behavior by determining how quickly the algorithm can react to the reduction in the time headway and how aggressively it can respond to it. Accordingly, by adjusting these weights, the desired MPC design can be reached. Note that a similar argument can be made for Q_1 and Q_2.

Considering the above discussion, the following parameter values were selected in this study (An and Talebpour 2019):

- Sampling time ($t_{sampling}$): 0.2 s.
- Prediction horizon (N_p): 2 for safe distance (figure 101) and 10 for speed recovery (figure 102).
- Constraints on acceleration change per $t_{sampling}$: -8.20 ft/s^2 ≤ $\Delta a_{s(k)}$ ≤ 8.20 ft/s^2.

LC Trajectory

As discussed previously, there are several methods to model the LC trajectory. This study utilizes a higher-order polynomial approach.

Sixth-Order Polynomial

Building on the findings of Papadimitriou and Tomizuka (2003), this study introduced a sixth-order polynomial for the movement in the *x*-axis and a fifth-order polynomial for the movement in the *y*-axis. Since, unlike Papadimitriou and Tomizuka (2003), the object was not to avoid objects but to minimize the negative impacts of the LC maneuver on the target lane, this study utilized a fixed-LC duration, t_{LC}. The following equations in figure 104 can be formulated (An and Talebpour 2019):

$$x(t) = \alpha_6 t^6 + \alpha_5 t^5 + \alpha_4 t^4 + \alpha_3 t^3 + \alpha_2 t^2 + \alpha_1 t$$

A. Trajectory along the x-axis.

$$y(t) = \beta_5 t^5 + \beta_4 t^4 + \beta_3 t^3 + \beta_2 t^2 + \beta_1$$

B. Trajectory along the y-axis.

Figure 104. Formulas. Trajectory curve for the LC maneuver.

By fixing the LC duration, one can fix the initial and final boundary conditions (i.e., location, speed, and acceleration values before the start of the LC maneuver and at the end of it). Therefore, changing a_6 results in a change in the curvature of the LC trajectory; thus, a different impact on the SV is expected for different values of a_6.

Trajectory Optimization

The overall schematic for identifying the optimum trajectory is depicted in figure 105. For the two vehicles in the target lane, the LC vehicle in the current lane evaluates two sets of possible trajectories for final boundary conditions considering a desired-time headway after the LC maneuver and the desired maximum lateral acceleration. The time headway can be chosen for individual vehicles or in accordance with the platooning strategy. Since t_{LC} can directly impact the outcome of the LC maneuver, a carefully selected value is suggested. Large values of t_{LC} can make LC infeasible/unrealistic, and small values of it can result in significant shock-wave formation. Accordingly, this study utilizes the maximum acceleration values (in both *x* and *y* directions) to calculate the minimum t_{LC}. The largest value of t_{LC} is selected among all possible candidates to ensure both feasibility of the LC maneuver and the minimum impact on the target lane.

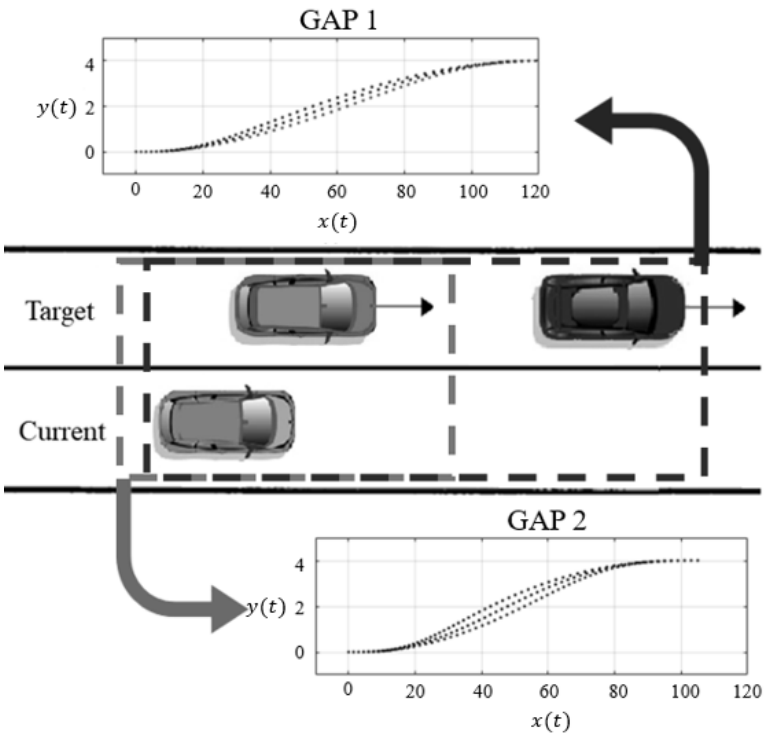

Source: FHWA.

Figure 105. Illustration. Sets of feasible trajectories depending on the gap choice.

In this research, based on the findings of Toledo and Zohar (2007), the LC duration was fixed to 6 s. The following optimization system is formulated in figure 106 to identify the best LC trajectory (An and Talebpour 2019):

$$
\begin{aligned}
& Z = Min(S) \\
\text{Subject to:} \quad & a_x(t) = a_x^{max} && t = 0, \dots, T \\
& a_y(t) = a_y^{max} && t = 0, \dots, T \\
& a_x(t) = \frac{d^2x(t)}{dt^2} && t = 0, \dots, T \\
& a_y(t) = \frac{d^2y(t)}{dt^2} && t = 0, \dots, T
\end{aligned}
$$

Figure 106. Formulas. Optimization problem for finding the best LC trajectory.

The equation shown in figure 107 is based on An and Talebpour (2019):

$$S = \sum_{k=1}^{K} a_k$$

Figure 107. Equation. Total control effort.

Calculating *S* is the core of this optimization process.

Assuming that SV shares the MPC design with LV through V2V communications, LV can predict the SV acceleration profile for any given LC trajectory. Accordingly, the total deceleration effort can be evaluated for different values of a_6, as shown in figure 108. Note that in this research, the constraint on the maximum longitudinal acceleration can only affect the range of feasible a_6. Then, multiple sets of possible trajectories are obtained by considering each vehicle in the target lane as the future leader. From there, LV chooses the optimal trajectory based on the effect of each trajectory on the target lane calculated using the objective function.

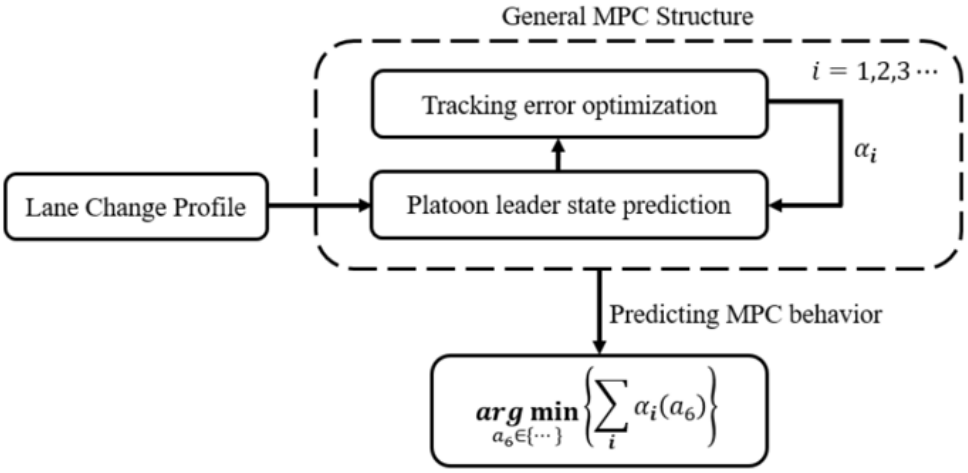

Source: FHWA.

Figure 108. Flowchart. Strategy for the accurate prediction of MPC behavior.

The key element in this optimization system is the methodology to predict the states of each vehicle since each LC trajectory has a different impact on the target lane and imposes a unique disturbance to the system. A methodology was developed to evaluate the impact of each trajectory on the changes in vehicles' speed in the target lane, thus capturing the impact of LC on total travel time. After generating a trajectory for a given set of available gaps, the model predicts the acceleration profile of the platoon head according to the designed MPC. Note that it is assumed that the LC vehicle has information about the MPC design.

Gap Generation

In addition to designing an MPC controller to mitigate the negative impacts of LC at the merge locations, one can generate enough gap for the LC vehicle by introducing a forward-moving shock wave. Prior to controlling cars ahead of an LV, a set of time-headway (h) values could be determined for the vehicles. Time-headway values will be smaller than or equal to the original time headway (h_0) that platoon members follow before the system starts to work. The change of relative position of platoon members in the platoon is illustrated in figure 109. In this figure, circles represent vehicles, and two platoons are compared. The platoon above is when platoon members keep their constant h_0, and the one below is when some of the platoon members (green rectangles) reduce their h. In other words, the system makes vehicles move forward relative to their original position in a platoon. Green rectangles are cars controlled to achieve their new h, which is smaller than or equal to h_0, and we can see that their resulting positions are relatively ahead of their assumed positions with the CTH, h_0. Consequently, LV is assigned a space to join

in the target lane as a new member of the platoon. Automatically, LV will have less impact on the vehicle following it.

In this project, two formulations were considered to generate the *h* distribution: one approach is to maximize the generated gap, and the other approach is to provide LV the necessary gap based on the final position of the LV at the end of the LC maneuver. Note that it is assumed that the final position of the LV will be communicated to the vehicles.

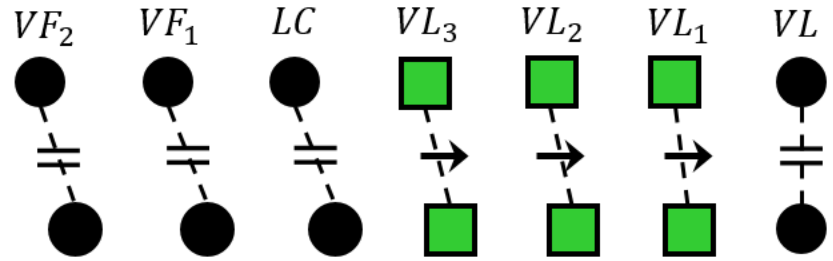

Source: FHWA.

Figure 109. Illustration. Time headway adjustment: relative position comparison: no dynamic MPC (up) versus dynamic MPC (down).

Case One: Maximizing Distance

This case maximizes a new space given the particular number of vehicles, *N*, to control and the constraint on their *h* distribution. The strategy was to distribute time headways of all *N* vehicles based on the time headway variances. The following optimization in figure 110 is developed:

$$Z = Max\left(\sum_{i=1}^{N}(T_0 - T_{current,i})\right)$$

A. Object function.

Subject to:

$$Var(T_{current,1}, T_{current,2}, \dots, T_{current,N}) \leq \max\_var_1$$

B. Constraint 1: Maximum variance considering all time headways.

$$Var(T_{current,i-1} - T_{current,i}) \leq \max\_var_2 \qquad \forall i = 0, 1, \dots, N$$

C. Constraint 2: Maximum variance between consecutive time headways.

$$T_{current,i} \geq T_{safety} \qquad \forall i = 0, 1, \dots, N$$

D. Constraint 3: minimum safe time headway.

$$T_{current,i} \geq T_{current,i+1} \qquad \forall i = 0, 1, \dots, N$$

E. Constraint 4: relationship between consecutive time headways.

Figure 110. Formulas. Optimization problem for case one: maximizing distance.

Checking the $Var(T_{current,1}, T_{current,2}, \ldots, T_{current,N})$ is based on the idea that large variance of vehicles' speed can result in shock-wave formation and unsafe driving instances. Therefore, by having a constraint on the variance of $T_{current,i}$, the set of $T_{current,i}$s is obtained that does not cause a variance larger than a particular number. As long as the variance of a set does not exceed the safe limit, $T_{current,i}$s are acceptable.

Case Two: Determining What Size to Make a New Gap

This case assumes that LV defines the size of the necessary gap in advance. In such a case, all the *N* vehicles can be controlled focusing on making the gap just larger than a particular size instead of maximizing it. Here, it is assumed that the platoon can receive the information on the expected gap from LV before the execution of the LC maneuver. The following optimization in figure 111 is formulated:

$$Z = Min\left(\sum_{i=1}^{N}(T_0 - T_{current,i})\right)$$

A. Objective function.

Subject to:

$$Var(T_{current,1}, T_{current,2}, \ldots, T_{current,N}) \leq \max\_var_1$$

B. Constraint 1: Maximum variance considering all time headways.

$$Var(T_{current,i-1} - T_{current,i}) \leq \max\_var_2 \qquad \forall i = 0, 1, \ldots, N$$

C. Constraint 2: Maximum variance between consecutive time headways.

$$T_{current,i} \geq T_{safety} \qquad \forall i = 0, 1, \ldots, N$$

D. Constraint 3: Minimum safe time headway.

$$T_{current,i} \geq T_{current,i+1} \qquad \forall i = 0, 1, \ldots, N$$

E. Constraint 4: Relationship between consecutive time headways.

$$\sum_{i=1}^{N}(T_0 - T_{current,i}) \geq Required\ Gap\ by\ LV$$

F. Constraint 5: Relationship between time headways and required gap for lane changing.

Figure 111. Formulas. Optimization problem for case two: new gap to make is determined.

Interaction of SPDHRM and Merge Coordination

The interoperation of the SPDHRM and the merge-coordination systems can happen at two levels:

1. Both systems are active but independent. Accordingly, the SPDHRM system can have an improved performance due to less severe shock waves at the merge location due to implementation of the merge-coordination system.

2. Both systems are exchanging information. Accordingly, in addition to the benefits that the SPDHRM can have from an active merge-coordination system, the merge coordination can benefit from an active SPDHRM. The SPDHRM system can create the right gap for the merging vehicles by reducing/eliminating shock waves.

MODEL CALIBRATION AND VALIDATION

To calibrate and validate the joint application calibration, the project team developed and integrated two key features into an open-source microscopic simulation platform developed by researchers previously:

- SPDHRM—a set of novel SPDHRM algorithms were developed that utilize machine learning to predict the onset of congestion and to activate the SPDHRM in a highway segment. These algorithms also utilize various methods of communicating the updated speed limits to the CVs (automated or human-driven) and non-CVs (automated or human-driven).

- Merge coordination—a couple of algorithms were developed to enable merge coordination in connected and nonconnected driving environments. These algorithms aim to prevent shock-wave formation in the target lane, even at very small time headways.

In addition to these models, the simulation platform utilizes several already calibrated and validated CF and LC models for nonconnected HVs, connected HVs, CAVs, and nonconnected AVs (Talebpour and Mahmassani 2016).

Since most of the models used were already calibrated and validated based on the NGSIM US 101 dataset (FHWA 2007), the focus of this calibration and validation effort was on the calibration of CF models of HVs to capture the effects of interacting with AVs on driver behavior. The validation effort ensures the accuracy of the calibration process.

Dataset

Vehicle trajectories are a cornerstone of modern traffic-flow theory, with applications in driver behavior studies and AV research. Unfortunately, the existing vehicle trajectory datasets are limited, mostly due to the high cost of data collection and preparation. Moreover, with the arrival of ADAS and AVs, there is a potential to see changes in human-driving behavior when interacting with these technologies. As a result, there is a desire for new vehicle trajectory datasets that cover various levels of automation. Aerial imagery using small unmanned aerial vehicles (UAV) is an economical and effective solution to collect trajectory data.

The project team collected a new trajectory dataset on I–35 in Austin, TX, (figure 112) to address the shortcomings of the existing vehicle trajectory datasets. A platoon of three SAE Level 1 AVs with ACC technology was circulating in the traffic stream during the data collection. Two UAVs (e.g., drones) were used for the aerial videography of the traffic stream. The trajectories of the vehicles were extracted from the video frames recorded in bird's-eye view from a segment of the roadway (figure 113). In every video frame, the location of the vehicles was estimated for a fixed-coordinate system and reference point on the ground. Every video recording was converted to a sequence of images (i.e., frames) separated at a constant rate over time (e.g., 25 frames per s). Tracking the location of any vehicle over the sequence of images enabled extracting the vehicle's trajectory over time.

The vehicle trajectory extraction was performed in four steps: image stabilization, vehicle detection, vehicle tracking, and trajectory construction. In the image stabilization step, all the images were transformed to match a reference field of view. Then the vehicles were detected in every frame and tracked over the sequence of images. Finally, the vehicles' location and trajectories were constructed by converting the image coordinates to the adopted reference coordinates on the ground. Figure 114 shows a sample of collected vehicle trajectory data.

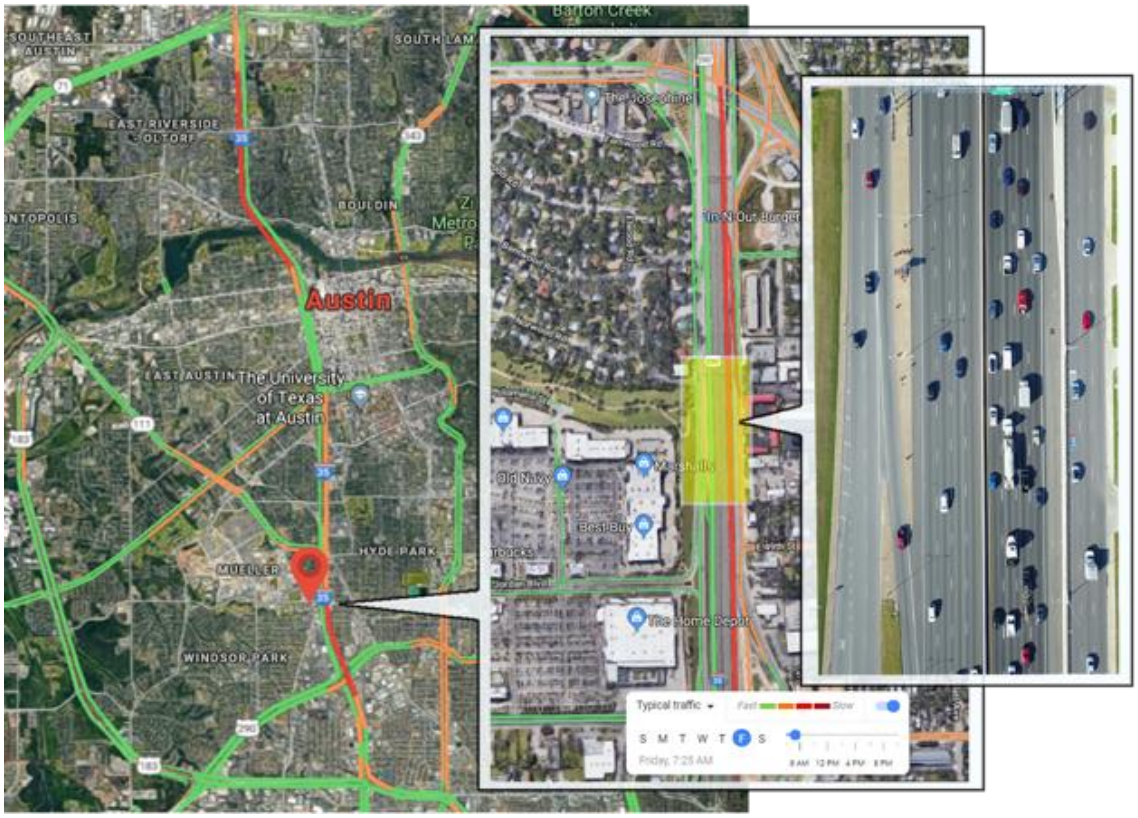

© 2019 Google® Earth™. Modifications by FHWA to show traffic congestion.

Figure 112. Photo. Data collection location on I–35 near Austin, TX.

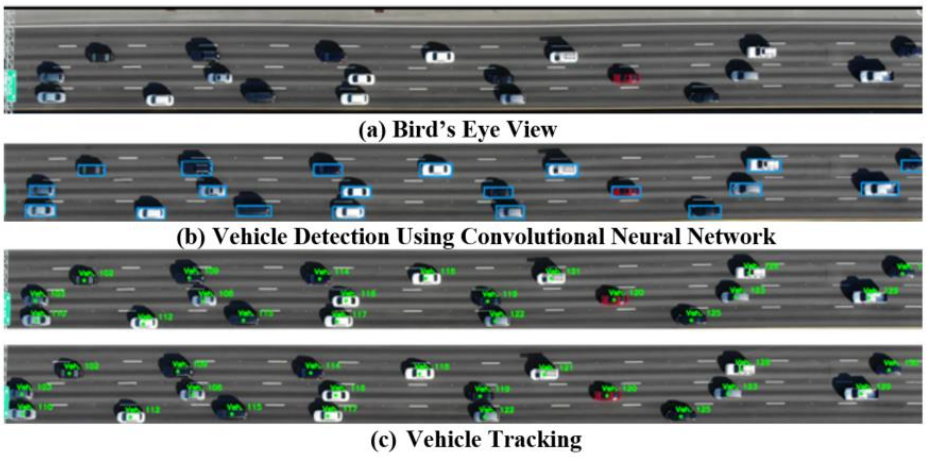

Source: FHWA.

Figure 113. Photo. Vehicle detection and tracking in aerial images.

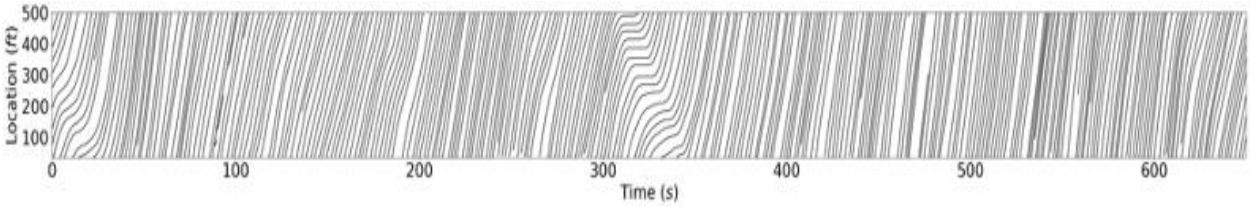

Source: FHWA.

Figure 114. Illustration. Sample trajectory data collected on I–35 near Austin, TX.

Calibration Approach

This study adopted the genetic algorithm calibration approach introduced by Hamdar et al. (2009). The approach relies on comparing the driving behavior in the dataset with the simulated behavior based on a set of model parameters. For CF models, the error is calculated based on the error in the gap between the lead vehicle and the target vehicle, as shown in figure 115 and figure 116:

$$F_{mix}[s^{sim}] = \sqrt{\frac{1}{|s^{data}|}\left\langle \frac{(s^{sim} - s^{data})^2}{|s^{data}|} \right\rangle}$$

Figure 115. Equation. Error in the gap between the lead vehicle and the target vehicle.

$$\langle z \rangle = \frac{1}{\Delta T}\int_0^{\Delta T} z(t)dt$$

Figure 116. Equation. Definition of ‹ ›.

For LC models, the same process is followed with one key difference: the error in the gap between the LC vehicle and both the new leader and new follower is considered.

Once the error function is defined, the genetic algorithm heuristic can be implemented as follows:

- The parameters of a CF/LC model are initialized to random numbers. Each set of these parameters is called a chromosome and the total of N_{GA} chromosomes will be created.
- The fitness of each chromosome is determined using the aforementioned error function.
- The chromosomes, except for the chromosome with the lowest error value, will be evolved through crossover and mutation (see Hamdar 2009 for the definition of crossover and mutation in genetic algorithm).
- The process is terminated once a minimum error threshold is achieved by the best chromosome. The parameters of that chromosome will form the calibration results.

Following the procedure outlined above, an initial set of 100 parents will be initiated. These parents will produce 900 children at each iteration, and the top 99 children will join the best of the parents to move to the next iteration. The calibration process stops once the error is below 5 percent or less than 0.1-percent improvement in error is observed for more than 20 consecutive iterations.

Calibration and Validation Process

The behavioral parameters of drivers in microscopic simulation models are expected to be correlated. Kim and Mahmassani (2011) presented a methodology to capture this correlation across the parameters of each driver. They showed that sampling from the empirical data while accounting for the correlation between the parameters of each sample (e.g., individual drivers) is the best method for capturing heterogeneity in microscopic simulation models. The same method was utilized in this study for the calibration of CF and LC models.

To calibrate and validate the model, each vehicle trajectory in the dataset was divided into calibration and validation sets. The calibration set had about four times more data points than the validation set, with all selected randomly from the data points in the vehicle trajectory dataset. The model was first calibrated using the data in the calibration set that utilized the same error function presented in the previous section. The calibrated model parameters were then used to simulate the data in the validation set and the results (i.e., gap between vehicles) were compared. The outcome of this calibration and validation process is a set of CF/LC parameters for each individual vehicle trajectory in the dataset.

As discussed previously, the models utilized in the adopted simulation platform have gone through a similar calibration and validation process based on NGSIM US 101 dataset (FHWA 2007). Accordingly, this study only focuses on the cases when a human driver interacts with an AV in the dataset. The focus was on a human driver following an AV. Note that Rahmati et al. (2019) showed that there is potential to see significant changes in driver behavior in this case.

A Note on Calibrating and Validating CF and LC Models for AVs

Regarding CF models of AVs, the adopted simulation framework utilizes the ACC/CACC models that were calibrated based on empirical data (Van Arem et al. 2006). Accordingly, the CF behavior of AVs will not be calibrated again in this study.

Regarding LC models of AVs, these models are designed based on the capabilities and characteristics of an automated vehicle. Accordingly, any LC trajectory generated by the models can be followed in the real world.

Calibration and Validation Results

This section presents the calibration results for the CF model of human drivers. The selected CF model is the Prospect theory model developed by Hamdar et al. (2008) and extended by Talebpour et al. (2011).

Table 19 and table 20 show the calibration results for the Austin data along with the data collected by Rahmati et al. (2019). The details of the model are presented in the next section. The model consists of three core parameters that were calibrated in this study. w_m and γ capture drivers' different preferences when dealing with acceleration and deceleration. In other words, drivers put more negative weight on deceleration. w_c is the crash weighting factor and higher values of this parameter represent more cautious drivers.

Conducting an analysis of variance test (Wilcox 1996) between values in table 19 and table 20 showed that two of the key model parameters show no statistically significant difference (i.e., w_m and γ), indicating that drivers' utility in response to acceleration and deceleration were the same for both cases of following an AV and following another human driver.

Table 19. CF model calibration results for human following.

Parameters	Mean	Std Dev
w_m	0.268	0.443
w_c	115200.00	21432.52
γ	0.71	0.62

Std Dev = standard deviation.

Table 20. CF model calibration results for AV following.

Parameters	Mean	Std Dev
w_m	0.271	0.365
w_c	81432.83	2870.79
γ	0.69	0.61

Std Dev = standard deviation.

Unlike w_m and γ parameters, the crash weighing factor w_c showed a statistically significant difference between the two cases. Following an AV, human drivers' behavior resulted in much less w_c compared with the case of following another human driver (w_c is 36 percent less for the

AV-following case than the human-following case). Such a significant difference shows that human drivers are more comfortable following the AV compared with another human driver, and they feel safer. Such an observation on w_c can also be interpreted from the risk-taking perspective. The smooth behavior of the AV encourages more risk-taking behaviors by the following human driver, resulting in lower values of w_c.

BASIC INFORMATION ON MODEL IMPLEMENTATION

SPDHRM

The three modules of the framework can be incorporated in a simulation tool. The information that is transferred to the traffic monitoring at each monitoring timestep is as follows: vehicle position (lane and location in the lane), speed, acceleration, gap and speed difference between the vehicle and the leader, desired speed, relative position of the vehicle in the traffic (leader's identity (ID), follower's ID, potential left-lane leader's ID, potential left-lane follower's ID, potential right-lane leader's ID, potential right-lane follower's ID), maximum deceleration, target exit location, and vehicle class (regular, connected, or automated). Once the input is analyzed by the three modules, the desired speed of each vehicle is updated. The new desired speed would be used in the CF and LC models in the next simulation steps. The modules are called repetitively at each monitoring timestep.

Besides the input from the simulation tool, each module involves a set of parameters. The traffic monitoring module has two major parameters that would be useful in determining the spatiotemporal area used in the Edie's (1963) generalized definitions of the traffic flow characteristics:

- Monitoring section length.
- Monitoring timesteps.

The predictive model settings depend on the type of SPDHRM strategy selected by the user. If the centralized method is used, the user can determine:

- Control type—two control types are incorporated in the model, namely decision tree and speed standard deviation. The logic of the decision tree is to select suitable speed limits, according to average speed of road section. For example, the decision tree logic could flow such that speed limits are either 56 mph, when average speed of the road section is larger than 46.6 mph; 43.5 mph, when average speed of the road section is larger than 34 mph and is smaller than 46.6 mph; or 34 mph, when average speed of the road section is less than 34 mph (Talebpour et al. 2013; Mittal et al. 2018). The speed standard deviation approach adjusts the advisory speed of a vehicle if the vehicle speed falls within a certain range of the average speed in the road section. The range is defined as the speed standard deviation in the road section multiplied by a threshold defined by the user.

- Control distance type—three types of control distance could be specified: fixed-broadcasting distance, variable distance depending on vehicle speed, or fixed-broadcasting point. The fixed-broadcasting distance allows the new advisory speed to be communicated to the CVs that are within a specified distance upstream of the

predicted congestion location. The variable distance control distance type extends the previous approach. Compared to the fixed-broadcasting distance control type, this approach allows dissemination of the new speed limit to vehicles that are farther from the congestion location but possess a higher speed. The third approach sends the new advisory speed limit to the connected vehicles at a prespecified location on the roadway. This approach is similar to the conventional method with the exception that the advisory speed limit is sent to the CVs through a V2I communication platform.

- Compliance error—This parameter controls the level of compliance of CVs with the updated speed limit. It is assumed that the CAVs would fully comply with the advisory speed limit.

Under the decentralized SPDHRM strategy settings, the evaluation distance to be used in the congestion-prediction module and the CV communication range can be specified. A control distance similar to the one defined for the centralized SPDHRM strategy is incorporated in the model.

The optimization-based SPDHRM strategy requires the user to determine three parameters: the optimization horizon, a list of potential values for advisory speed, and a list of potential values for broadcasting distance.

Merge Coordination

Figure 117 illustrates the flowchart for the implementation of the merge-coordination algorithm. The integration with any microscopic traffic simulation is possible. The model input is vehicle location, speed, and acceleration (both merging vehicle and other vehicles in the target lane). The output, however, can be different based on the capabilities of the microscopic simulation tool. Since the model operates in a 2D environment (i.e., both lateral and longitudinal movements are considered), the implementation in most commercially available microscopic simulation tools involves an adjustment to the model outcome. In other words, instead of outputting both lateral and longitudinal movements, the model could be adjusted to output longitudinal location and lane number.

In addition to the implementation of the LC maneuver, the existing implementation is capable of outputting the impact on shock-wave formation. This part can be removed, if found to be unnecessary for the purpose of the study, without impacting the merging/LC algorithm.

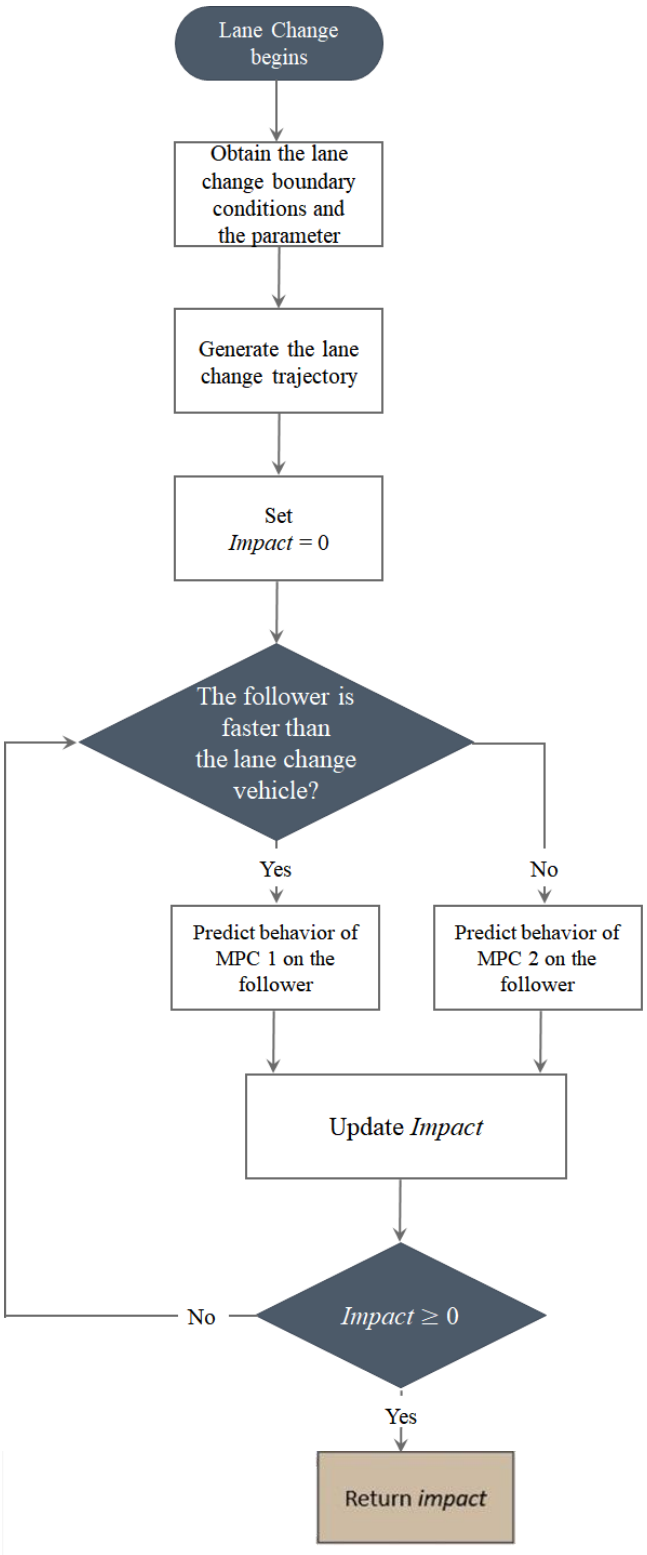

Source: FHWA.

Figure 117. Flowchart. Implementation of merge-coordination system.

USE CASE AND SENSITIVITY STUDY

Implementation of SPDHRM

The objective of this case study was to conduct a proof-of-concept test of the proposed framework. The focus was on the implementation of the major components of the SPDHRM framework. The framework was incorporated into a microsimulation tool developed in Python (Python Software Foundation, n.d.). The microsimulation tool is a special-purpose platform for simulating mixed-traffic conditions on freeways with the possibility of including CVs and AVs in the system. In the current case study, the testbed used a 3.1-mi section of a two-lane highway with an onramp that starts at the 1.67 mi marker of the segment and has a length of 0.19 mi.

In the simulation platform, distinct CF models were defined to specify the behavior of each agent: manually driven vehicles (i.e., regular vehicles), CVs, and AVs.

In the microsimulation platform, manually driven vehicles used the acceleration model first developed by Hamdar et al. (2008) and extended by Talebpour et al. (2011). The model was formulated based on Kahneman and Tversky's prospect theory (Kahneman and Tversky, 1979). Two value functions were introduced—one for modeling driver behavior in congested regimes and the other for modeling driver behavior in uncongested regimes. The formula in figure 118 shows the value function for the uncongested regime:

$$U_{PT}^{UC}(a_n) = \frac{\left[w_m + (1 - w_m)\left(\tanh\left(\frac{a_n}{a_0} \right) + 1 \right) \right]}{2} \left[\frac{\left(\frac{a_n}{a_0} \right)}{\left(1 + \left(\frac{a_n}{a_0} \right) \right)^{\left(\frac{\gamma - 1}{2} \right)}} \right]$$

Figure 118. Formula. Value function for the uncongested regime.

The following formula in figure 119 shows the value function for the congested regime:

$$U_{PT}^{C}(a_n) = \frac{\left[w'_m + (1 - w'_m)\left(\tanh\left(\frac{a_n}{a_0} \right) + 1 \right) \right]}{2} \left(\frac{a_n}{a_0} \right)^{\gamma'}$$

Figure 119. Formula. Value function for the congested regime.

At each evaluation timestep, the driver evaluates the gain from a candidate acceleration selected from a feasible set of values. The surrounding traffic condition is taken into consideration by the driver throughout the acceleration evaluation process. The driver utilizes the following binary probabilistic regime selection model, shown in figure 120, to evaluate each acceleration value:

$$U_{PT}(a_n) = P(C).U_{PT}^{C} + P(UC).U_{PT}^{UC}$$

Figure 120. Formula. Binary probabilistic regime selection model.

After calculating the expected value function, the total utility function for acceleration could be written as shown in figure 121:

$$U(a_n) = (1 - p_{n,i})U_{PT}(a_n) - p_{n,i} w_c k(v, \Delta v)$$

Figure 121. Formula. Total utility function for the choice of acceleration.

Finally, figure 122 shows: the probability density function used to evaluate the stochastic response of the drivers:

$$f(a_n) = \begin{cases} \dfrac{e^{\beta_{PT} U(a_n)}}{\int_{a_{\min}}^{a_{\max}} e^{\beta_{PT} U(a')}\, da'} & a_{\min} < a_n < a_{\max} \\ 0 & Otherwise \end{cases}$$

Figure 122. Formula. Probability density function for the evaluation of drivers' stochastic response.

CVs are capable of exchanging information with other vehicles and infrastructure-based equipment. The information is exchanged through the V2V and V2I communications networks. As a result, the driver receives information about other CVs as well as updated information containing TMC decisions (e.g., real-time changes in speed limit). The drivers' behavior may change based on the information conveyed to the driver. The reliability and the frequency of the information received by the driver plays a significant role in the drivers' behavior and on the overall performance of the traffic network.

An active V2V communication network allows the drivers to be aware of other drivers' behavior and the driving environment, road condition, and weather condition. As a result, the driving behavior could be modeled using a deterministic acceleration modeling framework. The simulation tool utilizes the IDM to model this connected environment, because the IDM is able to capture various congestion dynamics and provides greater realism than most of the deterministic acceleration modeling frameworks.

The acceleration model specified by the IDM (figure 123) entails the vehicle's current speed; the ratio of the current spacing to the desired spacing; the difference between the leading and the following vehicles' velocities; and subjective parameters such as desired acceleration, desired gap size, and comfortable deceleration.

$$a_{IDM}^{n}(s_n, v_n, \Delta v_n) = \bar{a}_n \left[1 - \left(\frac{v_n}{v_0^n}\right)^{\delta_n} - \left(\frac{s^*(v_n, \Delta v_n)}{s_n}\right)^2\right]$$

A. The acceleration in the intelligent driver acceleration model.

$$s^*(v_n, \Delta v_n) = s_0^n + T_n v_n + \frac{v_n \Delta v_n}{2\sqrt{\bar{a}_n \bar{b}_n}}$$

B. The effective safe gap in the intelligent driver acceleration model.

Figure 123. Formula. The intelligent driver acceleration model.

These parameters could be calibrated to better capture the behavior of CVs.

If the V2V communication network is inactive, the driving behavior of CVs would be similar to that of isolated manually driven vehicles. In the presence of V2I communications, the TMC decisions, such as the speed limits in the case of SPDHRM, could be transferred to the drivers. However, their reaction times would still be similar to human drivers.

AVs can continuously monitor other vehicles in their vicinity, which results in a deterministic behavior when interacting with other drivers. Furthermore, they can quickly react to any perturbations in the driving environment. Therefore, the CF behavior of AVs could be specified by a deterministic modeling framework. Talebpour and Mahmassani (2016) developed a CF model for AVs based on the previous simulation studies by Van Arem et al. (2006) and Reece et al. (1993). They simulated similar individual sensors installed on the AVs in order to generate the input data for the acceleration model.

Considering the sensor range and limitations in accuracy, AVs can be ready to react to any situation outside of their sensing range once it is detected (e.g., a vehicle at a complete stop right outside of the sensors' detection range). Furthermore, if an AV spots a leader, the speed of the AV could be adjusted in a way that allows it to stop if the leader decides to decelerate with its maximum deceleration rate and reach a full stop. Considering different situations that involve immediate reaction of the AV, the maximum safe speed can be calculated using the equations in figure 124:

$$\Delta x_n = (x_{n-1} - x_n - l_{n-1}) + v_n \tau_n + \frac{v_{n-1}^2}{2a_{n-1}^{decc}}$$

A. relative position of vehicle *n* (with respect to the leader).

$$\Delta x = min(SensorDetectionRange, \Delta x)$$

B. relative position of vehicle *n* (with respect to the leader and the sensor detection range).

$$v_{max} = \sqrt{-2a_i^{decc}\,\Delta x}$$

C. Maximum safe speed for autonomous vehicles.

Figure 124. Formulas. Maximum speed of AVs.

Besides the safety constraint, the formula in figure 125, adopted from the model proposed by Van Arem et al. (2006), updates the acceleration of the AV at every decision point:

$$a_n^d(t) = k_a a_{n-1}(t-\tau) + k_v(v_{n-1}(t-\tau) - v_n(t-\tau)) + k_d(s_n(t-\tau) - s_{ref})$$

Figure 125. Formula. Acceleration model for AVs.

In this study, the minimum distance was set at 6.56 ft and s_{safe} was calculated according to the following formula in figure 126:

$$s_{safe} = \frac{v_{n-1}^2}{2}\left(\frac{1}{a_n^{decc}} - \frac{1}{a_{n-1}^{de\,cc}}\right)$$

Figure 126. Formula. Safe following distance formula.

Finally, the acceleration of the AV can be calculated using the equation in figure 127:

$$a_n(t) = min\left(a_n^d(t), k\left(v_{max} - v_n(t)\right)\right)$$

Figure 127. Formula. Acceleration of AVs.

Van Arem et al. (2006) suggested using the following values for the model parameters: $k=1$, $k_a = 1$, $k_y = 0.58$, and $k_a = 0.1$.

Implementation of Merge Coordination

The merge-coordination system was implemented in the adopted microscopic simulation tool. The description of this tool was provided in the previous section.

SPDHRM: Design of Experiments and Simulation Results

The project team defined two sets of scenarios for the sensitivity analysis. Various MPRs of CVs and CAVs were considered in the scenarios. The researchers assumed that all vehicles were equipped with communication features and, as a result, would be able to interact with the traffic monitoring, congestion prediction, and speed-control modules of the simulation tool. The first set of scenarios was used to evaluate the accuracy of the congestion-prediction model. The second set of scenarios was used to compare the effectiveness of various SPDHRM strategies with different parameters. The scenarios are shown in table 21 and table 22. Each scenario was simulated 10 times to incorporate the randomness in the input data, such as the lane assigned to a vehicle at the entry point, the time at which the vehicle entered the simulated environment, the vehicle's initial speed, the vehicle class (CV or CAV), and so on.

Table 21. Scenarios for evaluating accuracy of congestion-prediction models.

Scenario ID	MPR of CV (%)	MPR of CAV (%)	Monitoring Timestep (s)	Section Length (ft)
A1	100	0	10	330
A2	70	30	10	330
A3	30	70	10	330
A4	0	100	10	330
A5	100	0	10	660
A6	70	30	10	660
A7	30	70	10	660
A8	0	100	10	660
A9	100	0	10	1,640
A10	70	30	10	1,640
A11	30	70	10	1,640
A12	0	100	10	1,640
A13	100	0	20	330
A14	70	30	20	330
A15	30	70	20	330
A16	0	100	20	330
A17	100	0	20	660
A18	70	30	20	660
A19	30	70	20	660
A20	0	100	20	660
A21	100	0	20	1,640
A22	70	30	20	1,640
A23	30	70	20	1,640
A24	0	100	20	1,640
A25	100	0	30	330
A26	70	30	30	330
A27	30	70	30	330
A28	0	100	30	330
A29	100	0	30	660
A30	70	30	30	660
A31	30	70	30	660
A32	0	100	30	660
A33	100	0	30	1,640
A34	70	30	30	1,640
A35	30	70	30	1,640
A36	0	100	30	1,640

Table 22. Scenarios for evaluating effectiveness of the SPDHRM strategies.

Scenario ID	MPR of CV (%)	MPR of CAV (%)	Speed Control Strategy	Broadcasting Distance (ft)
B0*	0	0	N/A	N/A
B1	100	0	Centralized	3,280
B2	70	30	Centralized	3,280
B3	30	70	Centralized	3,280
B4	0	100	Centralized	3,280
B5	100	0	Centralized	1,640
B6	70	30	Centralized	1,640
B7	30	70	Centralized	1,640
B8	0	100	Centralized	1,640
B9	100	0	Decentralized	Sensor range**
B10	70	30	Decentralized	Sensor range
B11	30	70	Decentralized	Sensor range
B12	0	100	Decentralized	Sensor range
B13	100	0	Optimization based	VA
B14	70	30	Optimization based	VA
B15	30	70	Optimization based	VA
B16	0	100	Optimization based	VA

*Base case scenario where the SPDHRM algorithm was deactivated and there are only manually driven vehicles (without connectivity features) in the system.
**Sensor range is assumed to be 500 ft.
VA = variable; N/A = not applicable.

In order to train and test the congestion-prediction model, the project team determined the status of each section of the highway based on the TTI. Then, the random forest-based model was developed by training the model with 80 percent of the simulation data. The model performance was evaluated by comparing the status predicted by the model and the status determined by TTI on the remaining 20 percent of the data. Table 23 shows the result of analyzing the first set of scenarios. The average and standard deviation of the prediction model accuracy was calculated for each pair of monitoring timestep and section length. The accuracy is reported for the entire flow, the congested instances, and the uncongested instances. As the goal of the first sensitivity analysis was to determine the best pair of monitoring timestep and section length, the average accuracy was calculated for the four different scenario types created by changing the MPR of CVs and CAVs. The researchers assumed that all the vehicles were equipped with connectivity features. Therefore, there were minor differences between the accuracy values among various monitoring timestep and section length pairs. The source of difference was the CF model used for each vehicle class. Among the analyzed scenarios, the scenario with a monitoring timestep of 20 s and section length of 660 ft has a slightly better performance (higher accuracy and lower standard deviation in accuracy) compared to the other scenarios. Analyzing a more comprehensive set of scenarios with manually driven vehicles that do not possess connectivity features could determine the most suitable parameter combination that accurately predicts the traffic status.

Table 23. Accuracy result of the congestion-prediction model under different monitoring timestep and section length scenarios.

Monitoring Timestep (s)	Section Length (ft)	Average Overall Accuracy (%)	Average Congested Accuracy (%)	Average Uncongested Accuracy (%)	Std Dev Overall Accuracy (%)	Std Dev Congested Accuracy (%)	Std Dev Uncongested Accuracy (%)
10	330	97.14	89.56	98.96	0.11	0.40	0.08
10	660	97.15	89.80	98.93	0.15	0.51	0.10
10	1,640	97.14	89.63	98.94	0.09	0.50	0.09
20	330	97.15	89.71	98.93	0.11	0.57	0.08
20	660	97.19	89.94	98.94	0.09	0.38	0.07
20	1,640	97.14	89.75	98.93	0.10	0.43	0.10
30	330	97.19	89.85	98.95	0.10	0.49	0.09
30	660	97.12	89.60	98.93	0.11	0.49	0.12
30	1,640	97.17	89.88	98.91	0.09	0.42	0.07

Std Dev = standard deviation.

The selected pair from the previous sensitivity analysis was incorporated into the speed-control module to compare the effectiveness of various SPDHRM strategies.

Table 24 shows the result of scenarios involving different speed-control strategies and various MPRs of CVs and CAVs. The scenarios where no SPDHRM strategy had been applied were used as a reference to assess the effectiveness of the examined speed-control strategies. As can be seen in the table, the effect of CAVs in the full-automation scenario dominated the effect of the speed-control strategies. As a result, applying the speed-control module did not change the performance metrics of the vehicles on the road. As expected, the optimization-based control system was more successful than the centralized and decentralized control systems due to the decreased speed variation and the increased reliability in travel time (lower travel time standard deviation). Although these cases show a slight decrease in the average speed and a marginal increase in the average travel time, the strategies prevented or postponed formation of shock waves in the system.

Table 24. Performance metrics of different speed-control strategies along with various market shares of CVs and AVs.

Speed Control Strategy	Broadcasting Distance (ft)	MPR of CV (%)	MPR of CAV (%)	Average Speed (mph)	Speed Std Dev (mph)	Average Travel Time (s)	Travel Time Standard Deviation (s)
No SPDHRM	N/A	0	0	44.36	13.21	251.88	31.52
No SPDHRM	N/A	0	100	62.08 (39.93)*	1.19 (−90.98)	179.07 (−28.91)	5.46 (−82.67)
No SPDHRM	N/A	30	70	57.99 (30.70)	9.22 (−30.22)	176.05 (−30.11)	50.66 (60.73)
No SPDHRM	N/A	70	30	40.60 (−8.48)	16.80 (27.17)	182.72 (−27.46)	136.24 (332.24)
No SPDHRM	N/A	100	0	41.13 (−7.30)	15.59 (17.99)	263.20 (4.49)	42.65 (35.32)

Speed Control Strategy	Broadcasting Distance (ft)	MPR of CV (%)	MPR of CAV (%)	Average Speed (mph)	Speed Std Dev (mph)	Average Travel Time (s)	Travel Time Standard Deviation (s)
Centralized	3,280	0	100	62.08 (39.93)	1.19 (−90.98)	179.07 (−28.91)	5.46 (−82.67)
Centralized	3,280	30	70	57.59 (29.81)	9.51 (−28.04)	177.46 (−29.55)	50.19 (59.24)
Centralized	3,280	70	30	40.66 (−8.35)	16.96 (28.41)	180.89 (−28.19)	135.24 (329.07)
Centralized	3,280	100	0	40.46 (−8.80)	16.20 (22.67)	252.48 (.24)	47.90 (51.98)
Centralized	1,640	0	100	62.08 (39.93)	1.19 (−90.98)	179.07 (−28.91)	5.46 (−82.67)
Centralized	1,640	30	70	58.13 (31.03)	8.84 (−33.08)	176.86 (−29.79)	46.78 (48.42)
Centralized	1,640	70	30	41.51 (−6.44)	16.80 (27.14)	176.48 (−29.93)	132.21 (319.45)
Centralized	1,640	100	0	43.38 (−2.21)	13.34 (.95)	254.44 (1.02)	31.52 (.01)
Decentralized	Sensor Range**	0	100	62.08 (39.93)	1.19 (−90.98)	179.07 (−28.91)	5.46 (−82.67)
Decentralized	Sensor Range	30	70	56.83 (28.10)	10.65 (−19.41)	177.72 (−29.44)	53.71 (70.40)
Decentralized	Sensor Range	70	30	41.74 (−5.91)	14.71 (11.36)	176.97 (−29.74)	133.16 (322.46)
Decentralized	Sensor Range	100	0	41.59 (−6.25)	14.81 (12.14)	267.07 (6.03)	33.63 (6.68)
Optimization-based	VA	0	100	62.08 (39.93)	1.19 (−90.98)	179.07 (−28.91)	5.46 (−82.67)
Optimization-based	VA	30	70	57.94 (30.59)	9.14 (−30.80)	172.11 (−31.67)	56.88 (80.46)
Optimization-based	VA	70	30	41.79 (−5.81)	16.35 (23.80)	178.44 (−29.16)	132.72 (321.06)
Optimization-based	VA	100	0	39.99 (−9.86)	16.66 (26.13)	245.80 (−2.41)	69.26 (119.73)

*Numbers in parentheses represent percent changes in the performance metric of a scenario compared to the base case scenario where the SPDHRM algorithm is deactivated and there are only manually driven vehicles (without connectivity features) in the system.
**Sensor range is assumed to be 500 ft.
Std Dev = standard deviation; N/A = not applicable; VA = variable.

Figure 128 through figure 132 show the fundamental diagrams for the base case (manually driven vehicles without connectivity features) and for different SPDHRM strategies when CVs constitute 70 percent of the traffic and 30 percent of the vehicles are CAVs. Comparing the maximum *y*-axis values of the diagrams shows that applying any of the SPDHRM strategies would improve the system capacity. Although activating the centralized SPDHRM strategy benefited the system based on the performance metrics represented in table 24, a higher number of points was observed in high-density values. Due to the higher number of traffic slowdowns and the higher spread in the data points, the centralized SPDHRM was not as efficient as the

other SPDHRM strategies. The decentralized and optimization-based SPDHRM strategies were able to improve the system performance while decreasing the maximum density. Furthermore, the traffic under these two cases experienced higher stability due to the smoother transition from the uncongested state to the congested states.

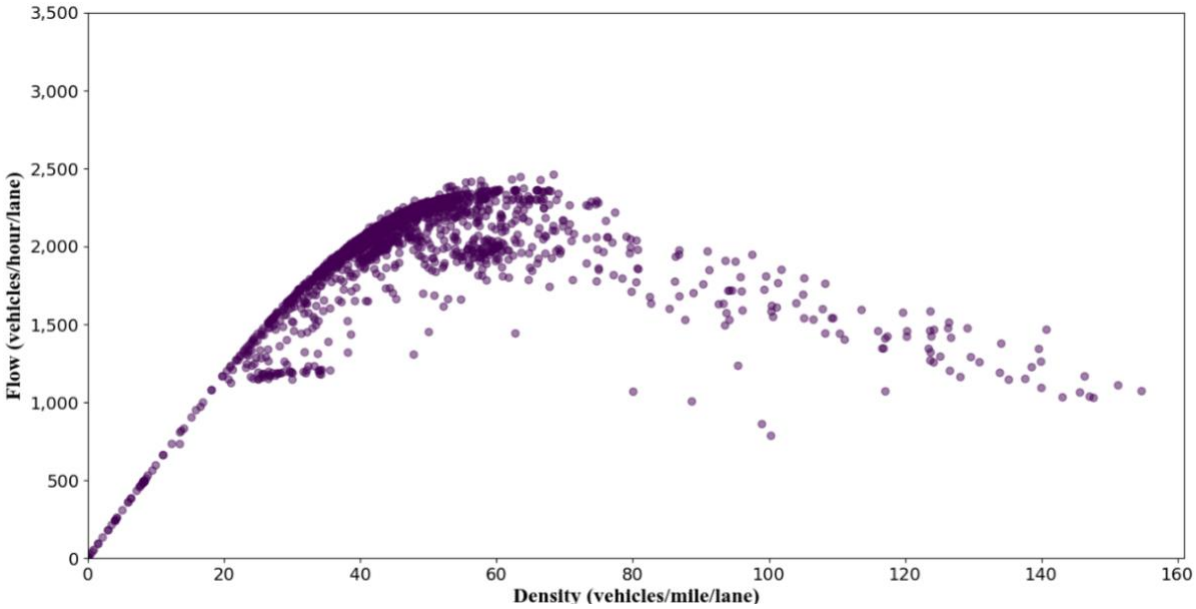

Source: FHWA.

Figure 128. Diagram. Fundamental diagram of the base case (100-percent MPR of manually driven vehicles).

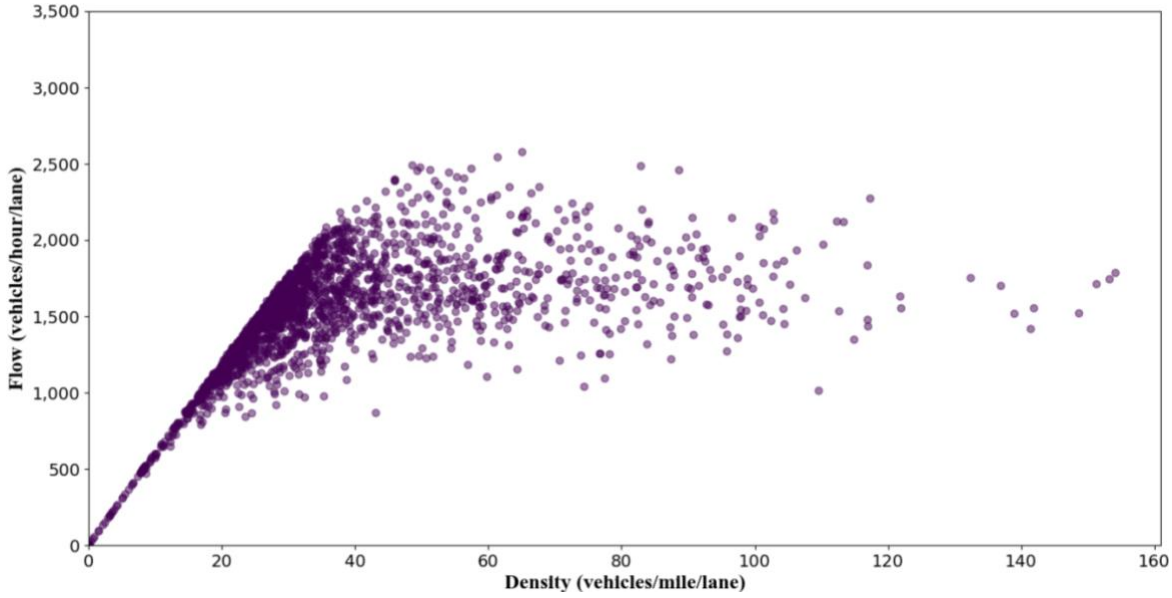

Source: FHWA.

Figure 129. Diagram. Fundamental diagram of the use case without any SPDHRM strategy (70-percent MPR of CVs and 30-percent MPR of CAVs).

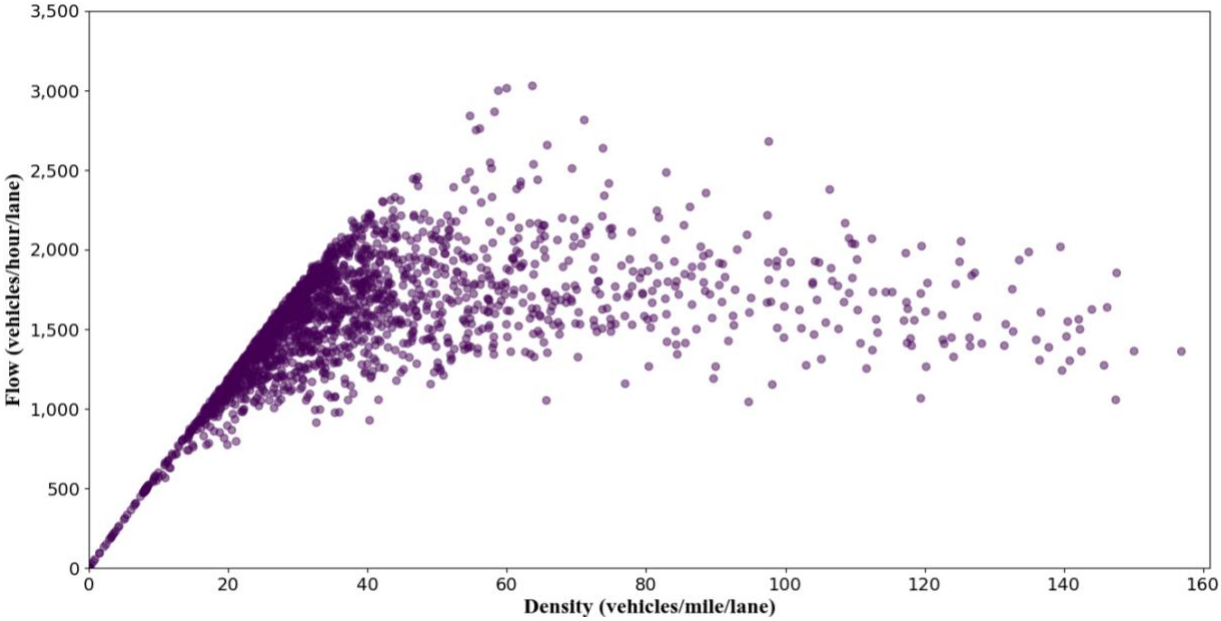

Source: FHWA.

Figure 130. Diagram. Fundamental diagram of the use case with the centralized SPDHRM strategy (broadcasting distance = 3,280 ft) (70-percent MPR of CVs and 30-percent MPR of CAVs).

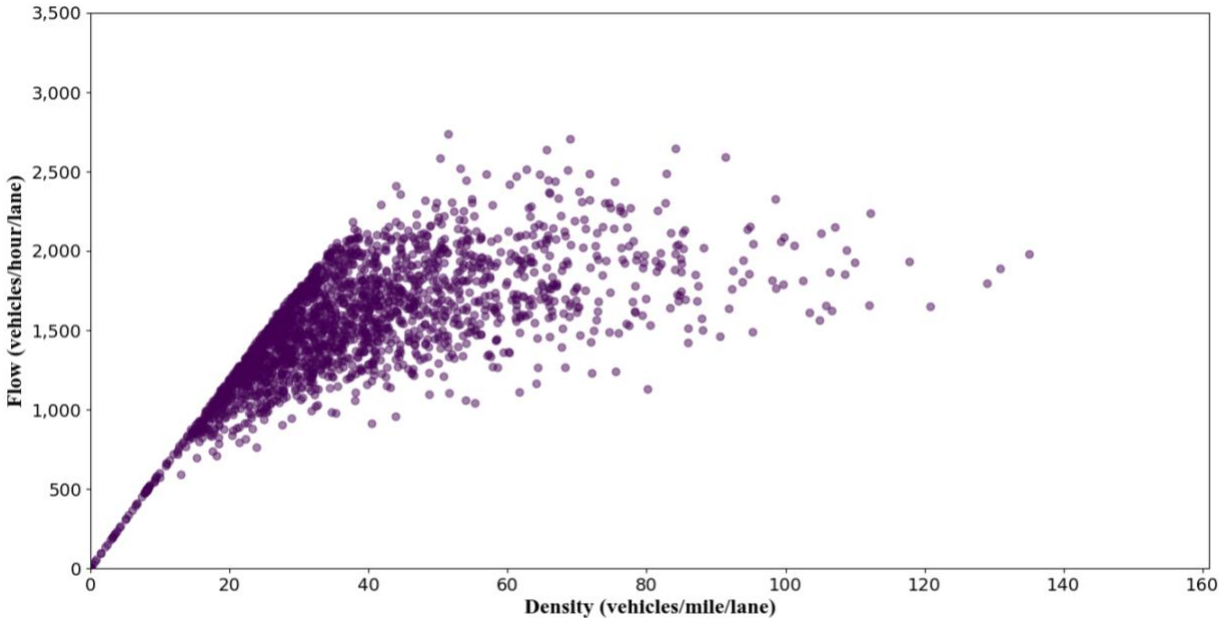

Source: FHWA.

Figure 131. Diagram. Fundamental diagram of the use case with the decentralized SPDHRM strategy (70-percent MPR of CVs and 30-percent MPR of CAVs).

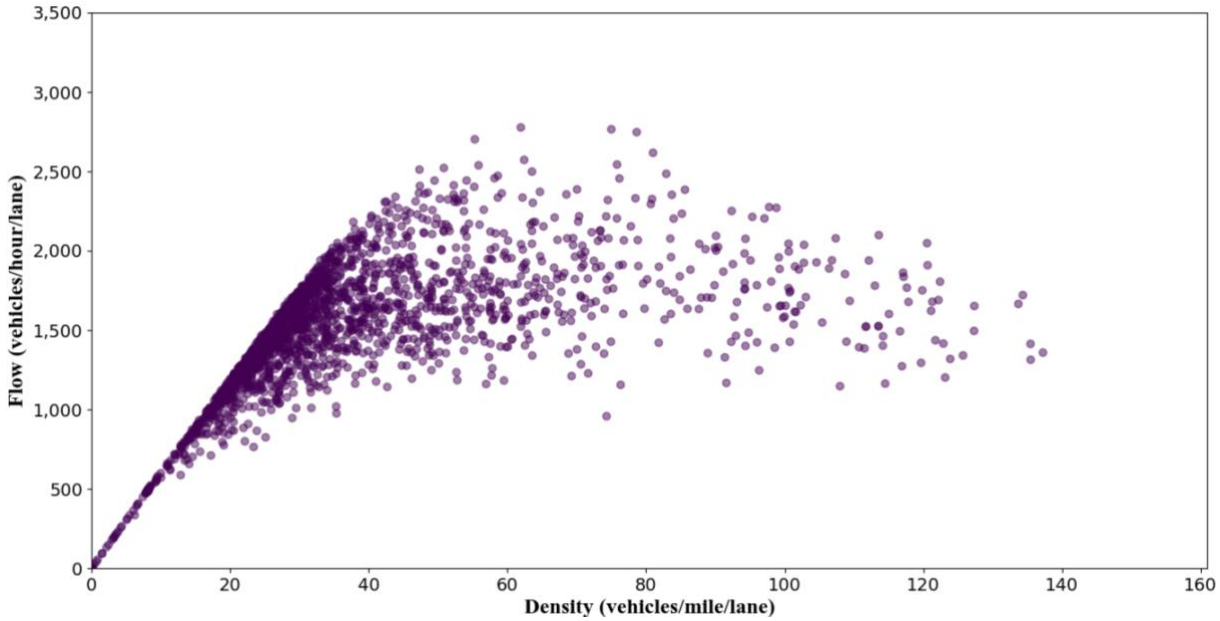

Source: FHWA.

Figure 132. Diagram. Fundamental diagram of the use case with the optimization-based SPDHRM strategy (70-percent MPR of CVs and 30-percent MPR of CAVs).

Since the congestion prediction model was independent of the speed-control module, performing a bi-level sensitivity analysis, such as the one described, could significantly decrease the number of scenarios that could be analyzed to reach a comprehensive conclusion. As a next step, scenarios with manually driven vehicles will be incorporated to accommodate different scenarios with partial connectivity.

Merge Coordination: Design of Experiments and Simulation Results

In the following sections, the performance of the proposed joint optimization of LC trajectory, CF controller, and gap-generation mechanisms are evaluated.

CF Control

The project team simulated several cases of highway driving. The team analyzed the behavior of a platoon that consisted of a combination of AVs and HVs. The focus of this study was on merge coordination; thus, a form of mandatory LC was used. The merge process started with the SV accepting the LV as the new predecessor. Accordingly, the SV started to slow down to accommodate the LV. Once the LV had safely entered the target lane, the SV started to speed up to the desired speed. It was assumed that the vehicles on the ramp had a lower or equal speed limit (different scenarios were tested).

The first set of experiments was focused on evaluating the impact of different weights in the cost functions (figure 101 and figure 102) on the performance of the merge-coordination application. Note that the weights used in this set of experiments were not optimized weights, and they were selected to illustrate the impact of weight selection on the merge-coordination process. In fact,

the performance of the model was expected to significantly improve by selecting optimized values.

For a general description of how the weight values were selected for simulation in this study, R_2 was related to the initial conditions, such as the velocity difference between SV and LV and the headway between SV and the old leader in the target lane. Considering how polynomial-based trajectory is generated, those two factors were related to the condition used to generate the LC trajectory and velocity profile. To find the proper value for R_2 in a scenario, some values for R_2 based on several generic simulations were found first. Afterward, they were interpolated to obtain an estimated proper R_2 depending on the initial conditions (i.e., $v_s - v_l$ and d). This does not reveal accurate values for the weight, but it can still be an appropriate estimate depending on $v_s - v_l$.

In the remainder of this section, different values of R_2 were selected for each experiment. The remaining weights used for the simulations were:

- Cost function of figure 101: $R_1 = 100$, $R_3 = 500$.
- Cost function of figure 102: $Q_1 = 70$, $Q_2 = 50$, $Q_3 = 800$, and $Q_4 = 200$.

In order to fully investigate the performance of the proposed model, the project team plotted speed and acceleration profiles of all vehicles in the simulation. The model performance was assessed against the performance of Swaroop's (1997) control logic. Two generic scenarios were tested:

- Maintaining speed: both lanes have the same speed (v_s and $v_t = 82$ ft/s).
- Increasing speed: current lane speed ($v_s = 65$ ft/s) and target lane speed ($v_t = 82$ ft/s).

Two key factors were considered in the assessment: driver/passenger comfort (i.e., changes in the acceleration value) and safety. Figure 133 illustrates the simulation results for the maintaining speed scenario. The red line (also indicated by x) represents LV, and the blue line (also indicated by square) represents SV hereafter in all figures. This figure indicates that Swaroop's (1997) model results in significant and rapid change in the acceleration value due to the LC maneuver. However, in figure 134, with the same simulation setup, the proposed MPC resulted in a smooth change in acceleration and velocity.

The improvement in the performance of the merging process was even more evident in the increasing speed scenario. While Swaroop's (1997) model resulted in an even more significant deceleration and reduction in speed (this happened because SV was dealing with a much slower LV), the proposed MPC resulted in behavior similar to the maintaining speed scenario. This was mainly due to the fact the LV had information about SV's decision logic and could optimize its trajectory.

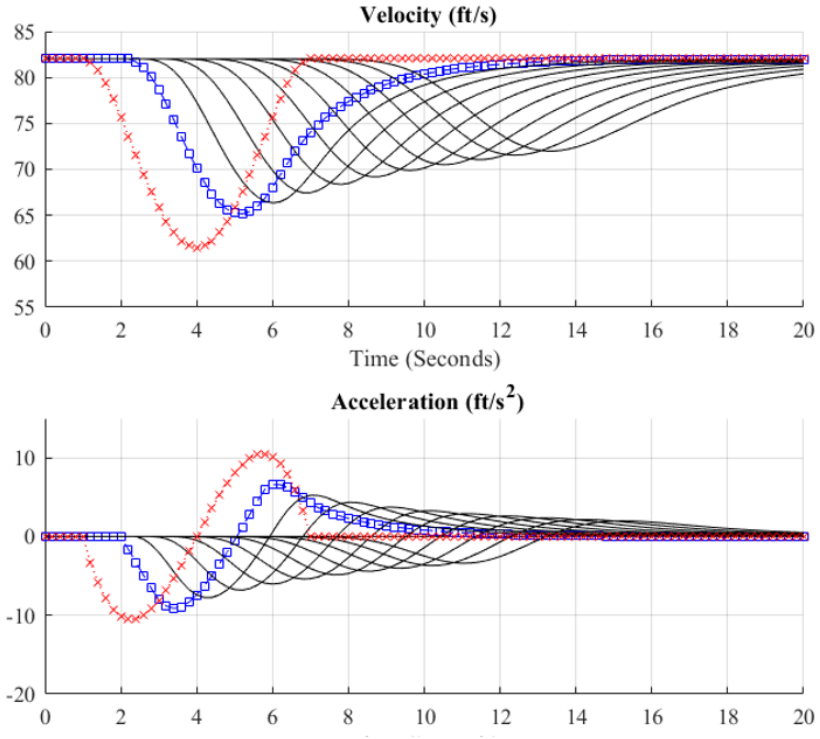

Source: FHWA.

Note: Swaroop's controller results in unrealistic jerk; and x marks, squares, and solid lines in the figure illustrate the LV, immediate follower in the target lane, and upstream vehicles, respectively.

A. MPC-based platoon.

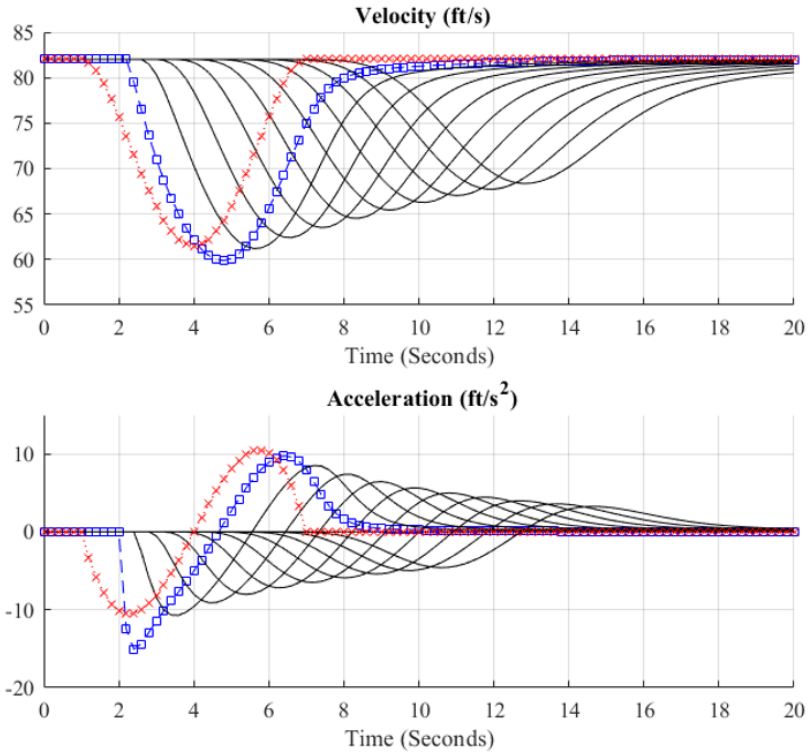

Source: FHWA.
Note: Swaroop's controller results in unrealistic jerk; and x marks, squares, and solid lines in the figure illustrate the LV, immediate follower in the target lane, and upstream vehicles, respectively.

B. Swaroop's controller-based platoon.

Figure 133. Diagrams. Maintaining speed: both lanes speed = 82 ft/s; A. MPC-based platoon and B. Swaroop's controller-based platoon.

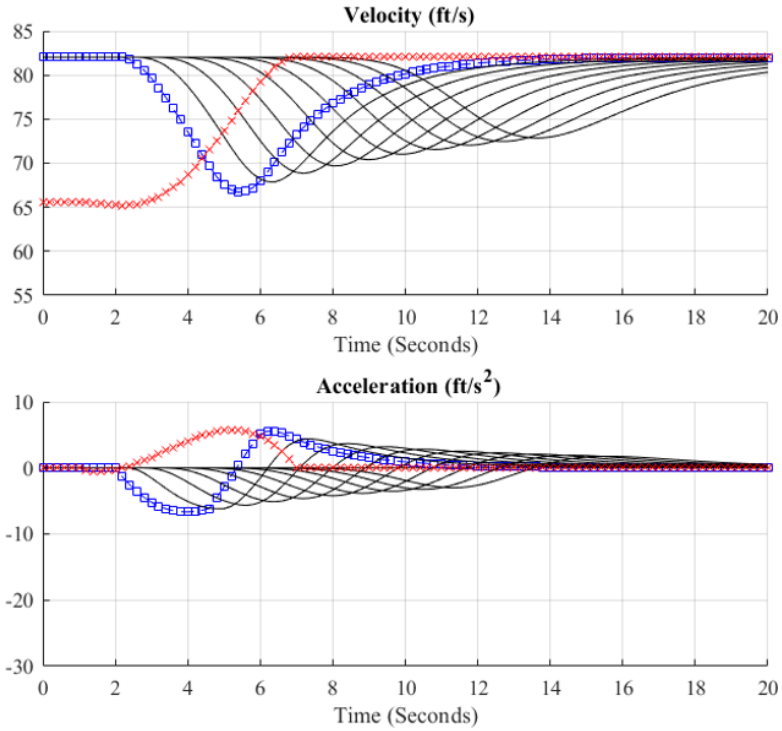

Source: FHWA.
Note: Swaroop's controller results in unrealistic jerk; and x marks, squares, and solid lines in the figure illustrate the LV, immediate follower in the target lane, and upstream vehicles, respectively.

A. MPC-based platoon.

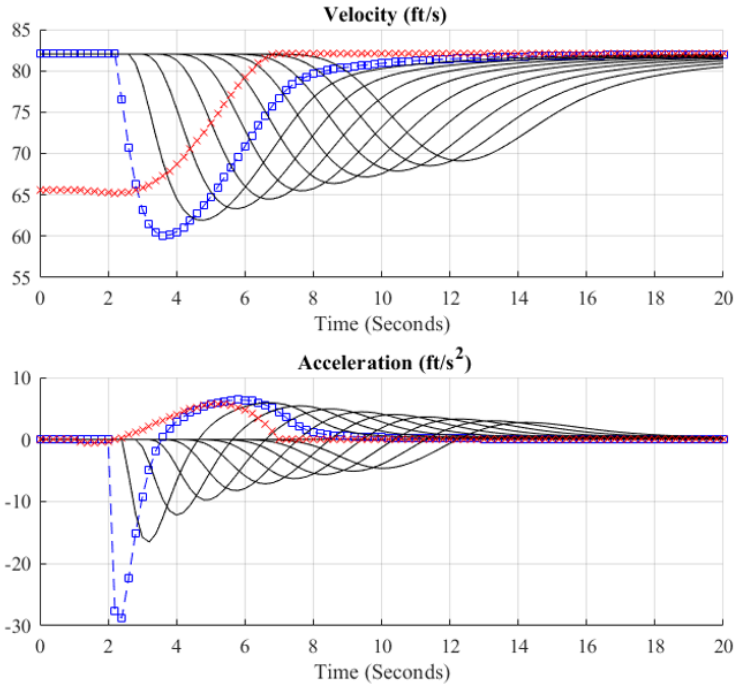

Source: FHWA.
Note: Swaroop's controller results in unrealistic jerk; and x marks, squares, and solid lines in the figure illustrate the LV, immediate follower in the target lane, and upstream vehicles, respectively.

B. Swaroop's controller-based platoon.

Figure 134. Diagrams. Increasing speed: current lane speed = 65 ft/s, target lane speed = 82 ft/s.

Performance

The previous section showed that the proposed MPC can easily outperform a typical CTH AV model. In this section, we further explore the impact of trajectory selection on the outcome of the proposed merge-coordination model. The following simulation parameters were selected:

- LC duration: $T = 6$ s.
- Current lane speed (v_s) = 65 ft/s, target lane speed (v_l) = 74 ft/s.
- Distance between LV and the target leader: $d = 0.2$, $v_l \times d = 14.8$ ft.

Note that these parameters were chosen carefully to show the impact of adding the sixth-order term to the LC trajectory. In order to conduct the trajectory optimization, first a range of feasible a_6 was obtained based on the physical constraints. Note that since a_6 only impacts the movement along the x-axis, the constraints along the y-axis were not considered in this simulation. In a real-world setting, such an assumption can result in infeasible trajectories to follow, even by fixing the initial and final conditions as well as the LC duration. However, for simplicity, this section assumes that only longitudinal location of LV impacts the behavior of SV.

Figure 135 shows the feasible values of a_6 during the LC. Accordingly, as long as a_6 remains between the two dotted lines, the trajectory will be feasible to execute. Note that in this

simulation setup, the longitudinal acceleration values were confined between 8.2 ft/s^2 and −13.0 ft/s^2. Accordingly, the optimization process searches for the optimal a_6 between −0.0058 and 0.0034.

As discussed previously, the optimization approach focuses on minimizing the total control/deceleration effort. Figure 136 illustrates how the optimization results in less deviation from the desired speed in the target lane. Based on this figure, even with $a_6 = 0.0$, the proposed MPC design works well and can significantly limit the shock-wave magnitude. However, by adding a nonzero a_6 ($a_6 = 0.0034$), the model is capable of even further improving the merge process and reducing its impact on the target lane.

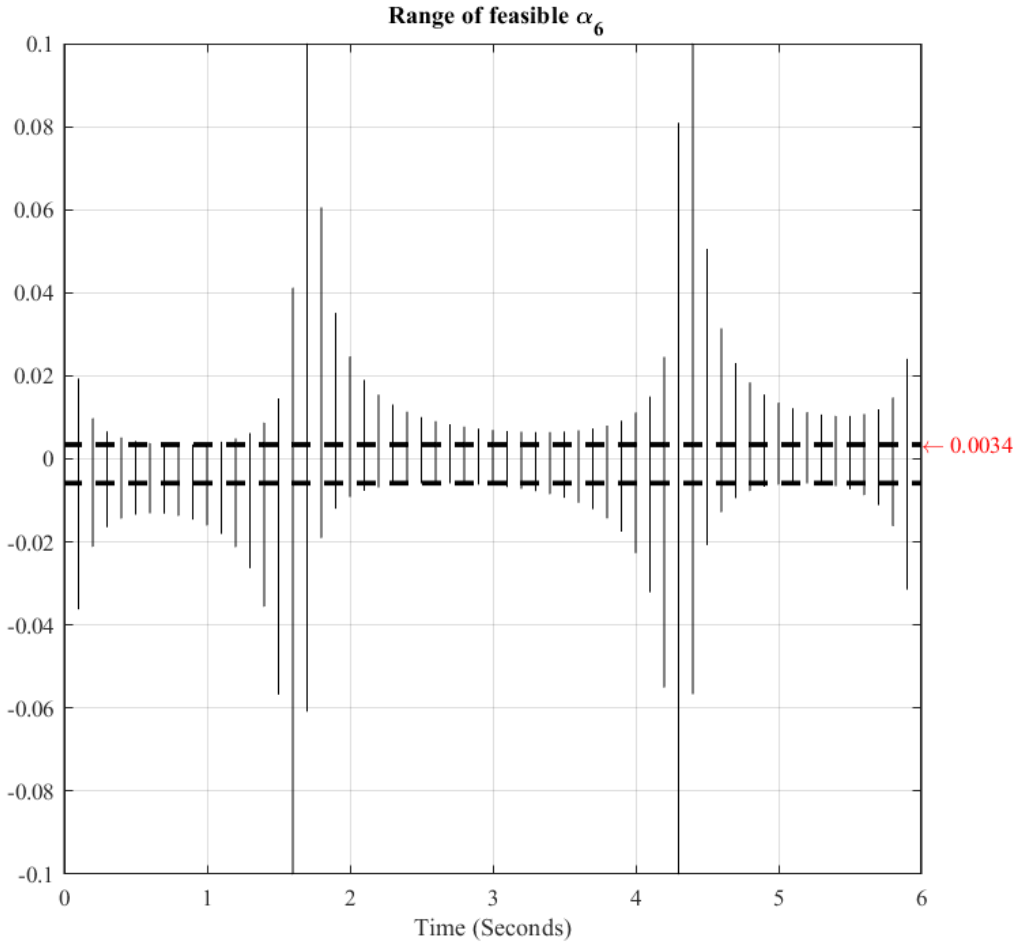

Source: FHWA.

Figure 135. Diagram. Range of feasible value of a_6: constrained by maximum longitudinal acceleration.

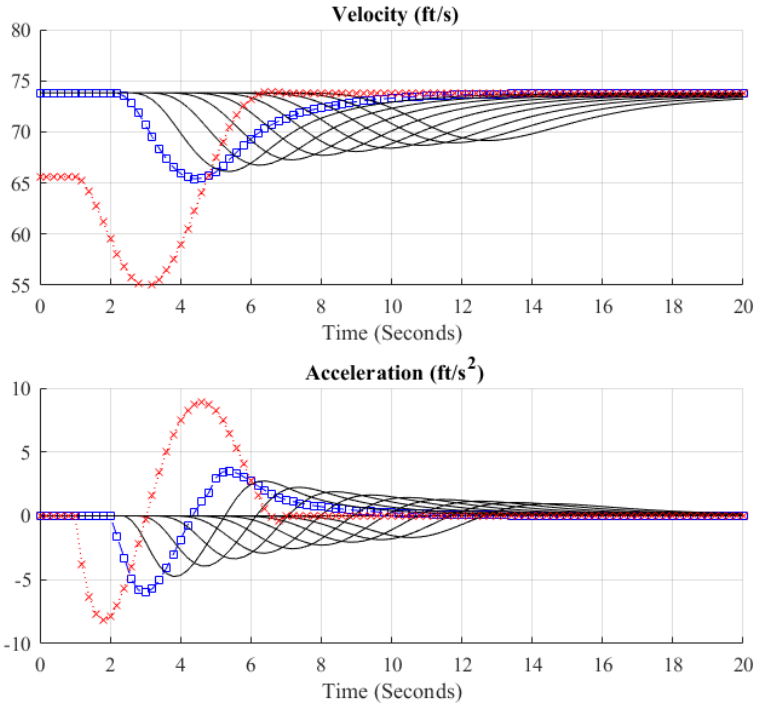

Source: FHWA.

Note: x marks, squares, and solid lines in the figure illustrate the LV, immediate follower in the target lane, and upstream vehicles, respectively.

A. $\alpha_6 = 0$ (lower order polynomial).

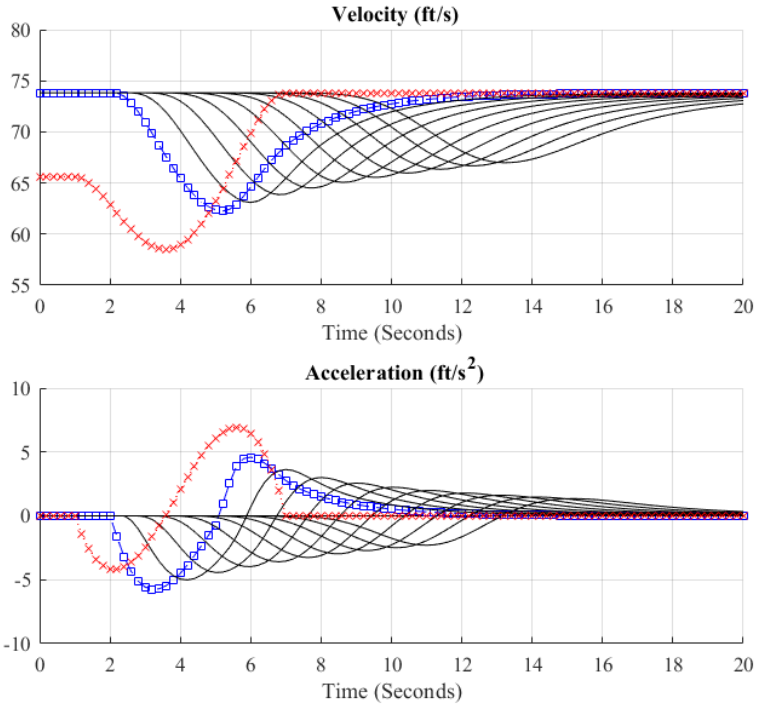

Source: FHWA.
Note: x marks, squares, and solid lines in the figure illustrate the LV, immediate follower in the target lane, and upstream vehicles, respectively.

B. $\alpha_6 = 0.0034$ (optimal).

Figure 136. Diagrams. LC maneuver profiles (ACC-based platoon).

Note that the existence of V2V communications is necessary in the performance of the proposed model. Without V2V communications, LV cannot accurately predict the movements of SV and can only be reactive (based on the onboard sensor inputs). Finally, in order to investigate if minimizing total control effort can reduce shock-wave magnitude in a mixed-driving environment, the same set of simulation scenarios were performed for a platoon of AVs and HVs. Platoon members were considered based on IDM only, ACC only, and ACC and IDM combined. Figure 137 illustrates the simulation results for various market penetration rates of AVs (i.e., 30 percent and 70 percent). The results indicate the capability of the presented approach in containing the shock wave due to the LC maneuver in the mixed-driving environment. However, as the MPR of AV increases, the shock-wave magnitude and duration decreases.

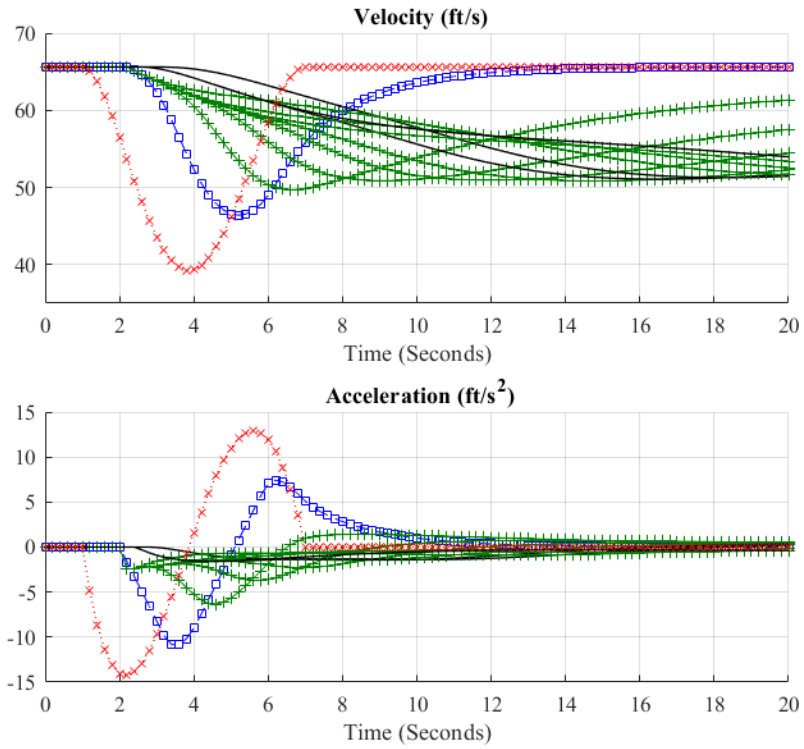

Source: FHWA.
Note: x marks, squares, plus marks, and solid lines illustrate the LV, immediate follower in the target lane, and human-driven upstream vehicles, and ACC upstream vehicles, respectively.

A. 30 percent of ACC-based cars in the platoon: maintaining speed.

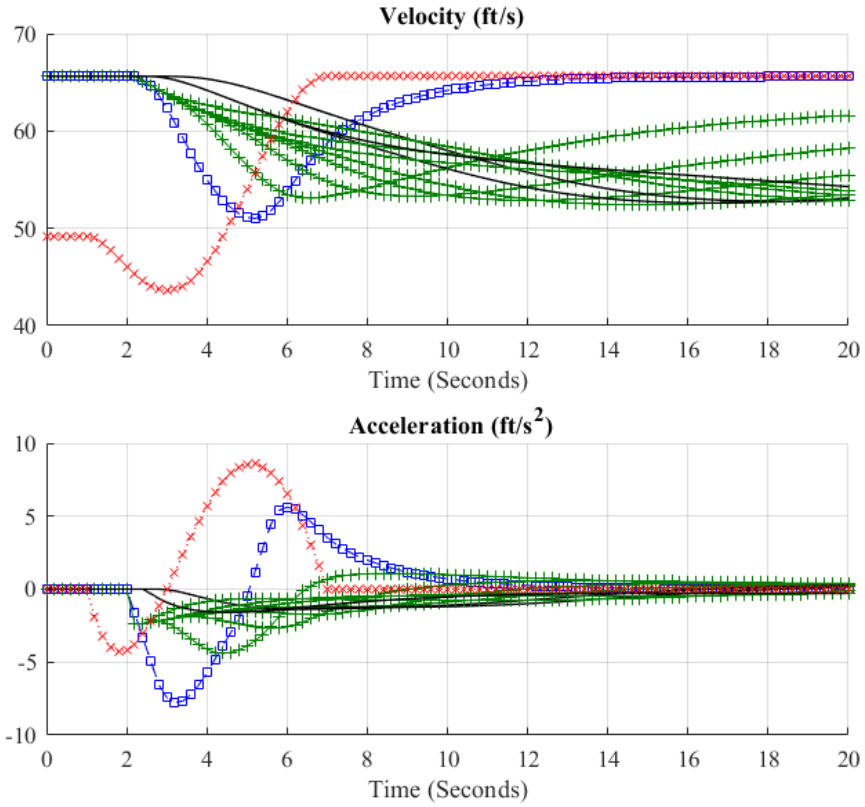

Source: FHWA.
Note: x marks, squares, plus marks, and solid lines illustrate the LV, immediate follower in the target lane, and human-driven upstream vehicles, and ACC upstream vehicles, respectively.

B. 30 percent of ACC-based cars in the platoon: increasing speed.

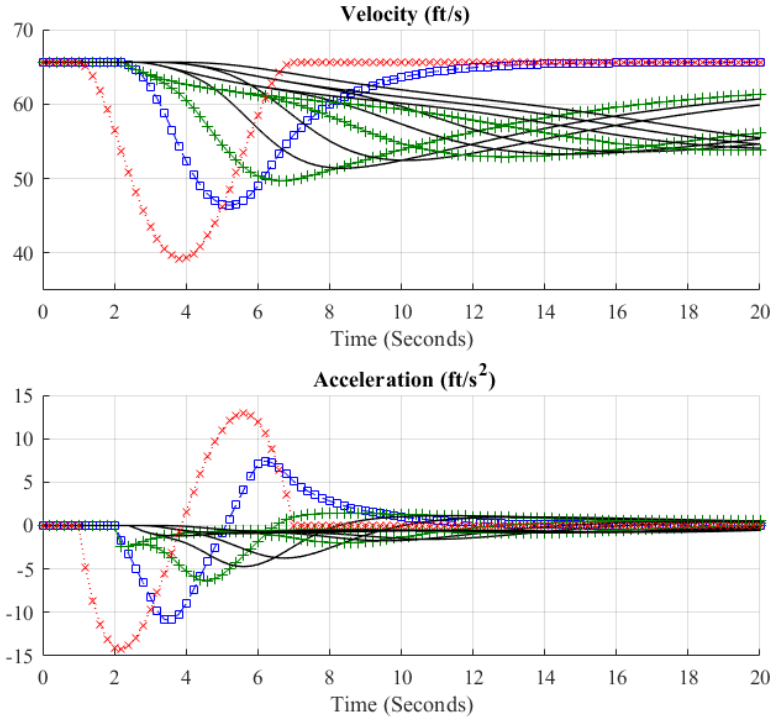

Source: FHWA.
Note: x marks, squares, plus marks, and solid lines illustrate the LV, immediate follower in the target lane, and human-driven upstream vehicles, and ACC upstream vehicles, respectively.

C. 70 percent of ACC-based cars in the platoon: maintaining speed.

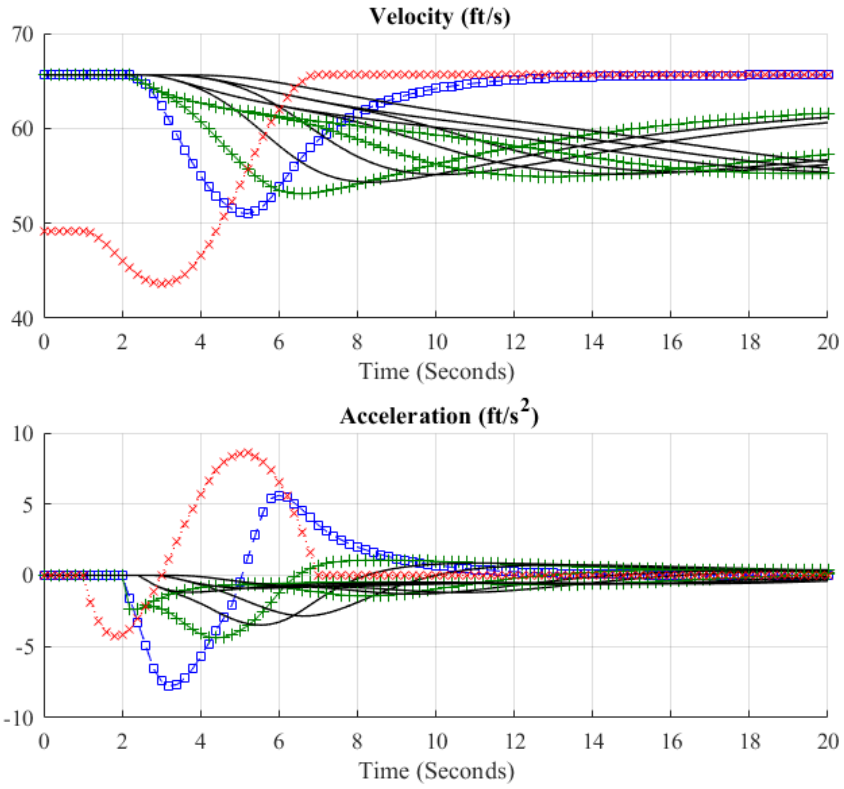

Source: FHWA.
Note: x marks, squares, plus marks, and solid lines illustrate the LV, immediate follower in the target lane, and human-driven upstream vehicles, and ACC upstream vehicles, respectively.

D. 70 percent of ACC-based cars in the platoon: increasing speed.

Figure 137. Diagrams. Percent of ACC-based cars in the platoon.

Gap Generation

Figure 138 through figure 140 show how the value of variance constraints can change the platoon behavior. Three constraint sets were utilized for this purpose:

- Constraint set 1: $max\_var_1 = 0.02$ and $max\_var_2 = 0.007$.
- Constraint set 2: $max\_var_1 = 0.0018$ and $max\_var_2 = 0.0065$.
- Constraint set 3: $max\_var_1 = 0.0015$ and $max\_var_2 = 0.0063$.

These figures indicate that a more restrictive set of constraints results in lower overall variance as well as lower maximum variance. Considering that having smaller speed variance is more desirable for safety, this observation indicates that the desired safety level can be achieved by setting up the correct set of constraints. Moreover, stricter constraints result in closer time headways to the original time headway, which results in a smaller gap overall. Accordingly, choosing the right set of constraints is key to ensure both safety and efficiency of the LC maneuver.

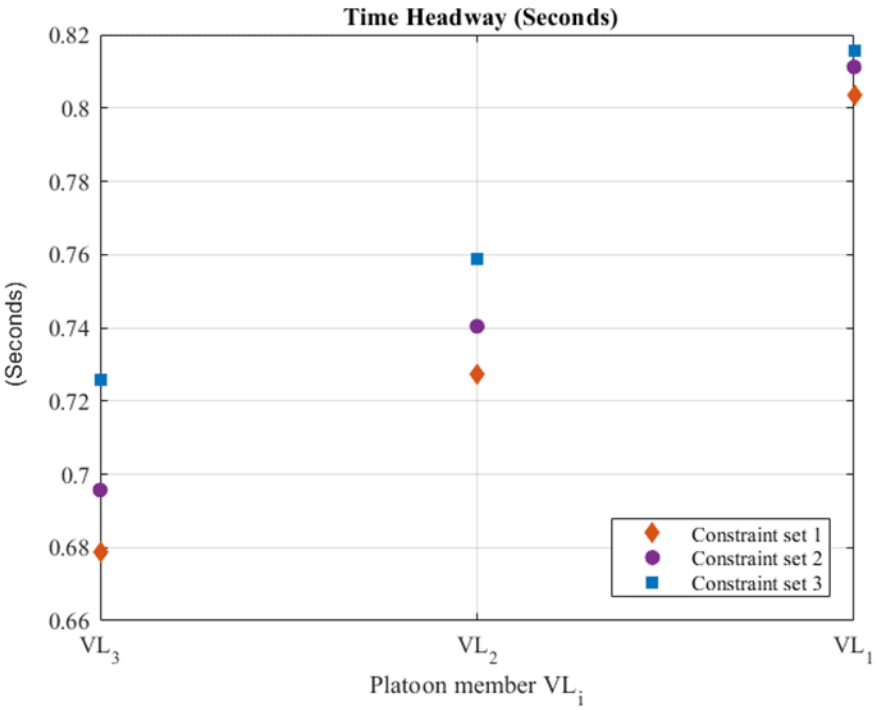

Source: FHWA.
VL = leading vehicle.

Figure 138. Graph. Effects of different variance constraints on the time headway of three vehicles ahead of the LVs in the target lane for $h_{desired}$ = 1.0 s, h_{safety} = 0.6 s, and sum of change of h = 1.0 s.

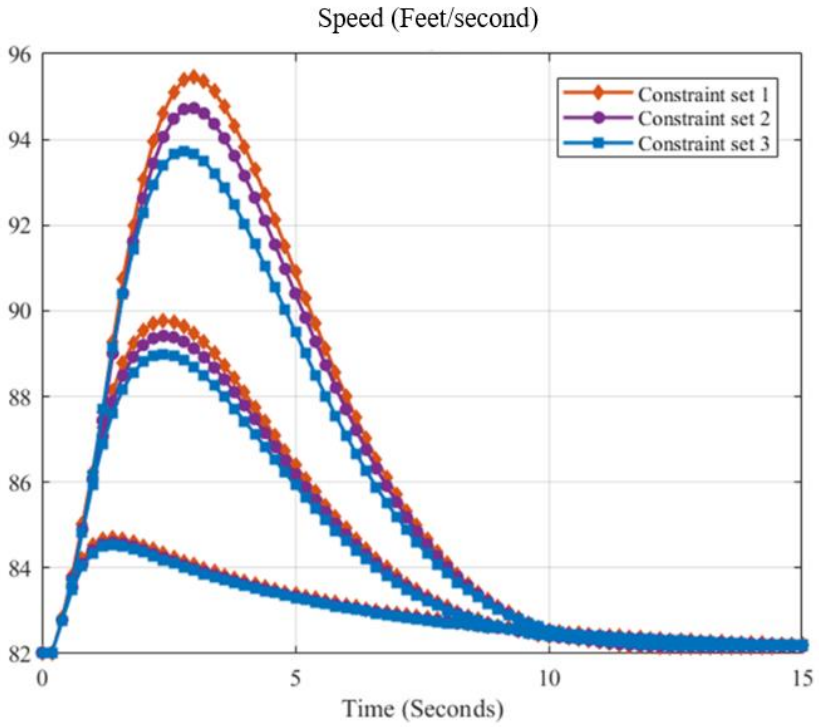

Source: FHWA.

Figure 139. Graph. Impact.

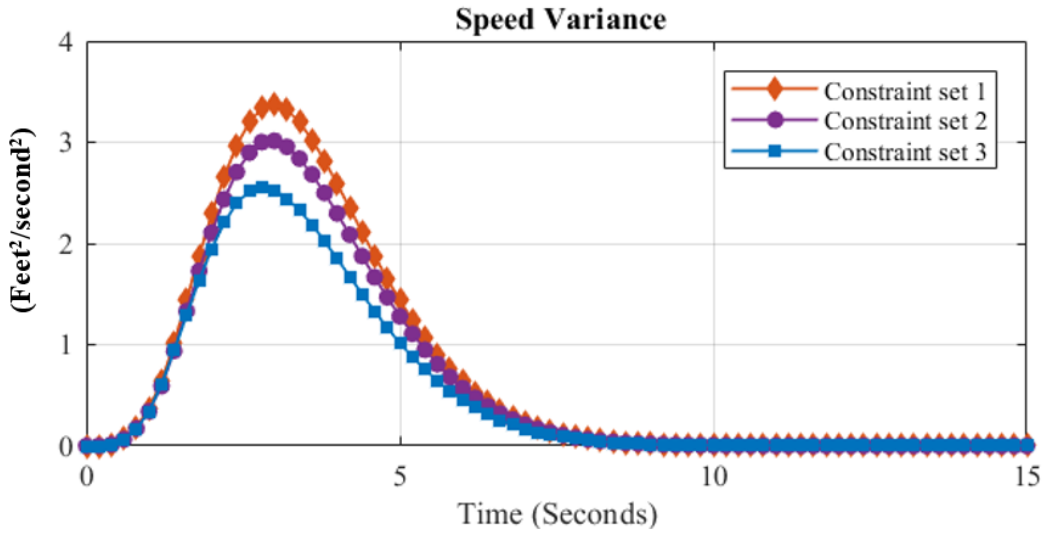

Source: FHWA.

Figure 140. Graph. Effects of different variance constraints on speed variance of three vehicles ahead of the LVs in the target lane for $h_{desired}$ = 1.0 s, h_{safety} = 0.6 s, and sum of change of h = 1.0 s.

Joint Application: Design of Experiments and Simulation Results

The optimization-based SPDHRM and merge-coordination strategies were applied jointly on the road segment defined in the SPDHRM use-case section. As can be seen in figure 141, applying both strategies simultaneously improved the system performance by increasing the capacity of the road segment. Furthermore, applying both strategies reduced the scatter in the fundamental diagram, resulting in more stability in the traffic flow during the transitioning phase. Based on table 25, the application of both strategies increased the average speed while decreasing the average travel time, the speed standard deviation, and the travel time standard deviation. Another benefit of applying the applications jointly was the reduction in the number and intensity of the shock waves that occurred at the merging point of the road segment (figure 142). In this case, the merge coordination was applied at the speed-control module stage of the SPDHRM strategy. One way to improve the joint application would be to incorporate the joint application in the congestion prediction module of the SPDHRM strategy.

Table 25. Performance metrics of the joint application use case at 80-percent MPR of CVs and 20-percent MPR of CAVs.

SPDHRM	Merge Coordination	Average Speed (mph)	Speed Standard Deviation (mph)	Average Travel Time (s)	Travel Time Std Dev (s)
N/A*	N/A	44.36	13.21	251.88	31.52
Inactive	Inactive	45.57 (2.71)**	15.06 (14.00)	198.23 (-21.30)	91.91 (191.59)
Inactive	Active	45.92 (3.50)	14.96 (13.24)	197.48 (-21.60)	91.05 (188.86)
Active	Inactive	46.94 (5.80)	13.31 (.75)	194.55 (-22.76)	85.80 (172.21)
Active	Active	46.89 (5.69)	13.07 (-1.06)	193.32 (-23.25)	86.18 (173.41)

*The first row shows the base-case scenario, where there are only manually driven vehicles (i.e., without connectivity features) in the system. As a result, the SPDHRM and merge coordination would not be applicable to this case due to the absence of CVs and CAVs.
**Numbers in parentheses represent percent changes in the performance metric of a scenario compared to the base case scenario where the SPDHRM and merge-coordination algorithms are deactivated and there are only manually driven vehicles (i.e., without connectivity features) in the system.
Std Dev = standard deviation.

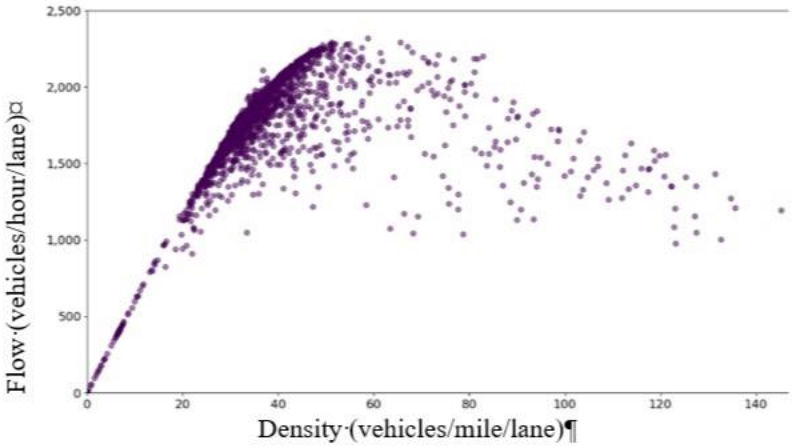

A. Fundamental diagram for the case where the SPDHRM and merge-coordination strategies are both inactive.

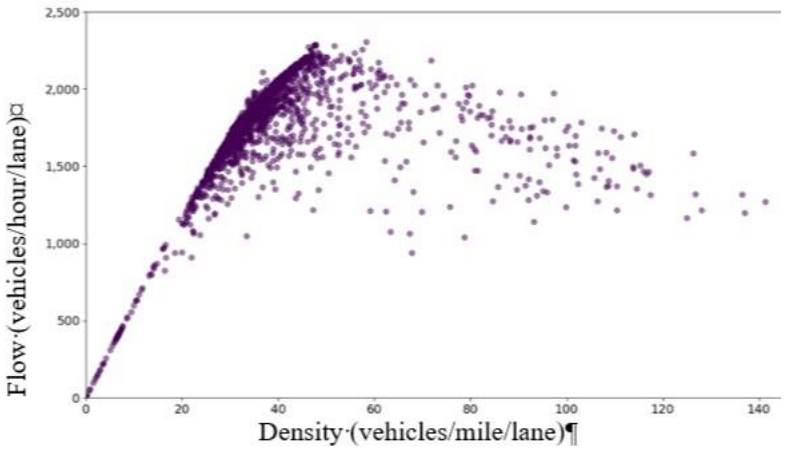

C. Fundamental diagram for the case where SPDHRM is inactive but merge coordination is active.

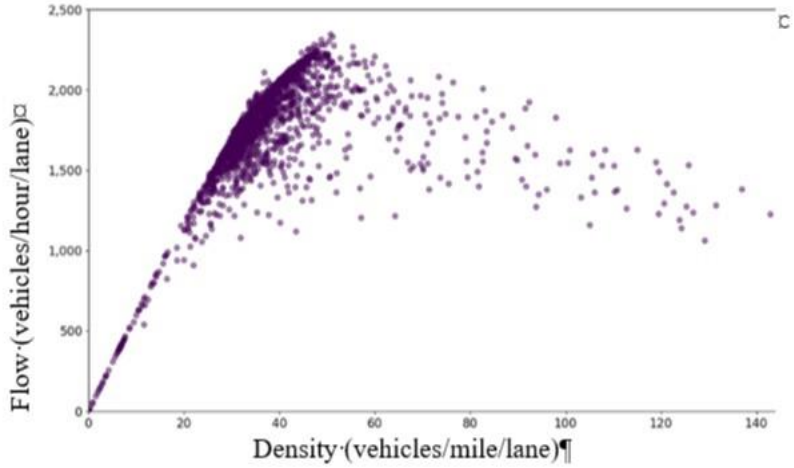

B. Fundamental diagram for the case where SPDHRM is active but merge coordination is inactive

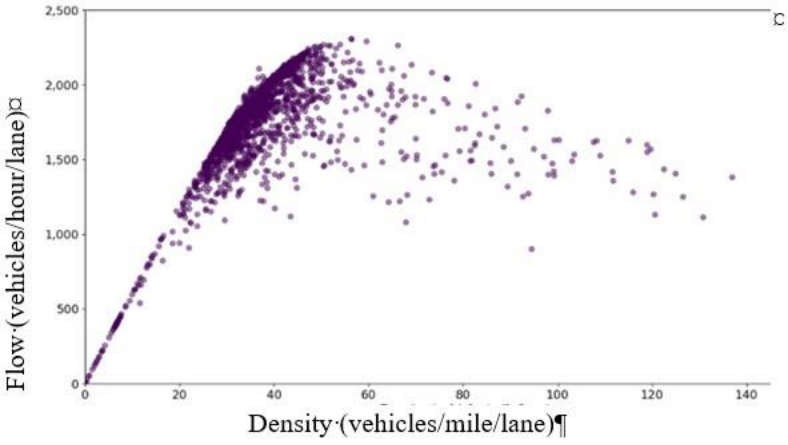

D. Fundamental diagram for the case where SPDHRM and merge-coordination strategies are both active.

Source: FHWA.

Figure 141. Diagrams. Fundamental diagrams (flow versus density) at 80-percent MPR of CVs and 20-percent MPR of CAVs for the joint application use case.

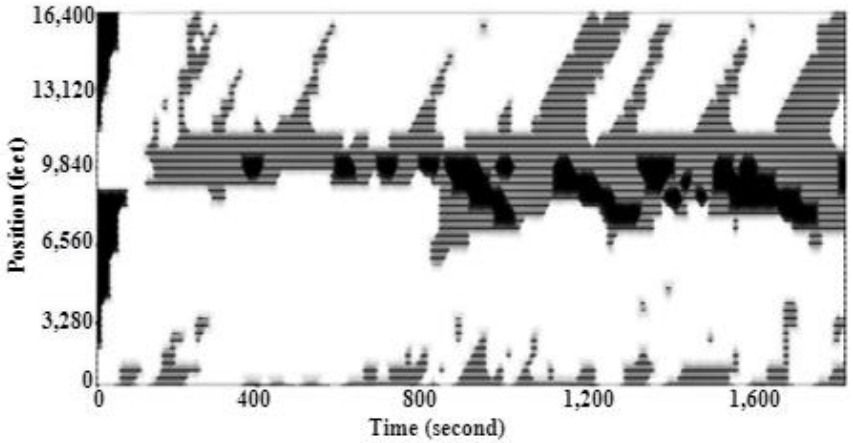

A. Spatiotemporal distribution of speed for the case where the SPDHRM and merge coordination strategies are both inactive.

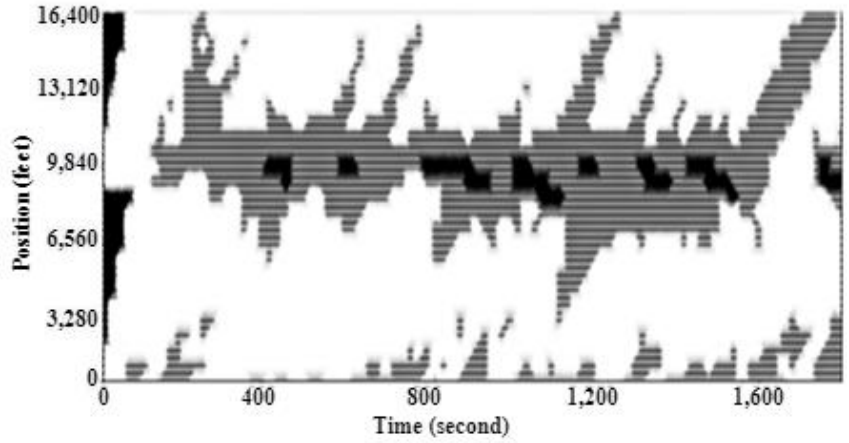

B. Spatiotemporal distribution of speed for the case where SPDHRM is active but merge coordination is inactive.

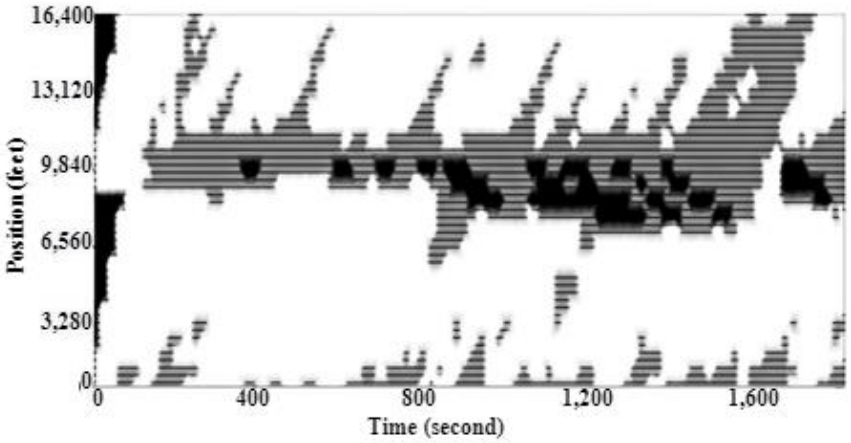

C. Spatiotemporal distribution of speed for the case where SPDHRM is inactive but merge coordination is active.

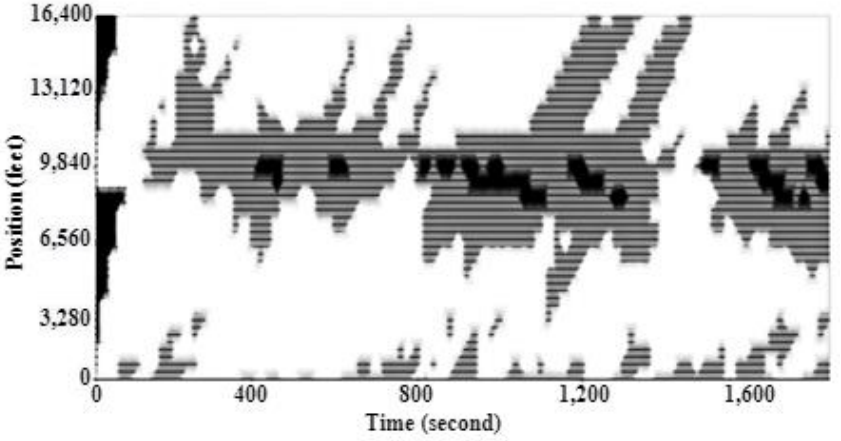

D. Spatiotemporal distribution of speed for the case where SPDHRM and merge-coordination strategies are both active.

Source: FHWA.

*Speed values of less than 20 miles per hour (mph) are solid black, speed values of greater than 50 mph are solid white, and speed values between 20 and 50 mph are striped gray.

Figure 142. Diagrams. Spatiotemporal distribution of speed at 80-percent MPR of CVs and 20-percent MPR of CAVs for the joint application use case.

SUMMARY

SPDHRM is an active traffic-management strategy that is used to delay traffic-flow breakdown and mitigate congestion by changing speed limits based on prevailing traffic, weather, and road conditions. Traditional implementations utilize fixed-roadway sensors to collect traffic information and variable-speed signs at fixed locations to display updated speeds. Most implementations use simple models, such as a reactive rule-based decision tree, to activate the control strategy. Due to the incomplete picture of the traffic-flow dynamics provided by the fixed-infrastructure sensors, the effectiveness of these strategies is impaired. Furthermore, since the road sensors and the advisory speed signs are in fixed locations, the performance is reduced due to the limited set of scenarios that this type of implementation can accommodate. Reactive SPDHRM strategies are generally less effective than predictive ones.

To overcome the aforementioned challenges, the researchers developed a predictive SPDHRM system that utilizes the detailed vehicle trajectories of CVs, the communication capabilities of CVs, and machine-learning algorithms. This innovative system collects detailed information from the CVs within a road segment of interest, predicts locations of traffic congestion, and updates the speed limits for the CVs in order to mitigate congestion. To leverage the opportunities created by the V2I and V2V communication systems, the researchers developed a simulation tool that incorporates a variety of SPDHRM strategies: centralized, decentralized, and optimization based. Case studies of multiple operational scenarios show that the proposed SPDHRM system can reduce the severity and length of traffic shock waves and improve the overall traffic stability.

This chapter also presented a novel merge-coordination system based on controlling both the LC trajectory and CF behavior of the vehicles in the target lane. The researchers implemented the model in the adopted microscopic traffic-simulation tool. The simulation results indicated the effectiveness of the proposed methodology in reducing the shock-wave magnitude and duration. Multiple sensitivity analysis experiments were also conducted for both fully autonomous and mixed-driving environments. The model was successful in mitigating shock-wave formation and propagation in almost all cases.

The proposed merge-coordination methodology, however, depends significantly on reliable communications. Vehicle-to-everything communications do not necessarily exist at all times due to signal interference and information loss. An updated model can be developed to consider this lack of information. Such a model would be helpful for a reliable merge-coordination system in the real world.

While each of the aforementioned models can significantly improve congestion and prevent shock-wave formation or propagation, the benefit of combining them into one joint application can surpass the benefits of individual applications. Particularly, merge coordination can eliminate or reduce the shock-wave formation at merge locations (and eliminate or reduce the shock-wave formation from any LC maneuver if extended to the coordinated LC application), which can significantly benefit SPDHRM in the following ways:

- The merging vehicle can provide an accurate prediction of the magnitude and duration of the created shock wave to the SPDHRM system. Combined with the utilized

machine-learning approach, the SPDHRM system can accurately predict the flow dynamics and adjust the speed limit accordingly.

- The merge-coordination system can significantly reduce the magnitude and duration of the shock waves at the merge coordination, thus reducing the load on the SPDHRM system. Accordingly, the SPDHRM system will only be activated in cases where it provides the most benefit.

Similarly, the SPDHRM system can significantly benefit the merge-coordination system by:

- Adjusting the inflow to the merge location to assist the merging vehicle in finding the right gap.

- Reducing the negative impacts of merging on traffic-flow dynamics by controlling the shock-wave propagation at the merge location.

Simulation results indicate that utilizing both strategies increase the average speed while decreasing the average travel time, the speed standard deviation, and the travel time standard deviation. Moreover, applying the applications jointly can reduce the number and intensity of the shock waves that occur at the merging point of the road segment.

CHAPTER 6. CONCLUSION

Current AMS tools are not well-suited for evaluating CAV applications due to their inability to represent vehicle connectivity and automated driving features. Many independent researchers have been working on models of CAV systems and have published widely divergent findings from models based on widely divergent assumptions. In order to produce realistic and believable predictions of CAV impacts, it is desirable to have a consistent set of models based on the best available data and the most accurate possible representations of the behaviors of drivers of conventional vehicles and CAVs.

FHWA sponsored this project to: develop AMS models for the most prominent CAV applications, incorporate these models into existing AMS simulation tools, and conduct real-world case studies (i.e., practical implementation scenarios and real-world transportation networks) for the most prominent CAV applications to better understand their impacts and deployment strategies and methods. This report focused on the first two objectives. Case-study reports were published separately (Ma et al. 2021; Huang et al. [forthcoming]; Liu et al. 2021).

MAIN OUTCOMES

One application developed for this project was an improved CACC model, in which CMDV drivers responded to I2V-based VSAs in mixed traffic (i.e., HVs, CVs, AVs, and CAVs). A sensitivity analysis study indicated that the I2V-based VSA control could increase fuel efficiency by 2–5 percent when the CMDV market penetration is 10–40 percent. As the CMDV market penetration further increased, the reduction in speed variation and the improvement in fuel efficiency approached 5–6 percent. When the CMDV drivers fully complied with the VSA, this helped to ensure a 5–6-percent benefit. When the VSA was implemented with CACC, the CACC controller could perfectly adopt the advisory speed as the reference speed. Nonetheless, adding the VSA algorithm to the CACC vehicles did not improve fuel efficiency beyond 5–6 percent because the VSA controller tended to underuse the bottleneck capacity due to its delayed response to the traffic variations.

Another model developed for this project was the light-duty CAV LC model. This model fully considered the dynamics of surrounding vehicles under different mixed-traffic scenarios. It included three crucial components: CF, incentive-based and mandatory LC decisionmaking, LC/LC abort path generation and following. The model was calibrated and validated using data collected from a small-scale field experiment. Sensitivity analyses revealed that the parameter values producing optimal mobility performance were consistent with those observed in the existing HV traffic. This indicated that human drivers, to some extent, might have learned optimal LC behaviors. Thus, the design of CAV-driving models might benefit from learning HV-driving behavior.

A third application developed for this project was the joint application of CM and SPDHRM. A set of novel algorithms was developed that utilized machine learning to predict the onset of congestion and to activate the SPDHRM in a highway segment. The predictive SPDHRM system exploited both the collected trajectories and the communication capabilities of CVs. The CM model jointly optimized the lateral trajectory of an LV and the longitudinal CF control of

vehicle(s) in the target lane. While each of the SPDHRM and CM can significantly relieve congestion and prevent shock-wave formation or propagation, the benefit of combining them into one joint application can surpass the benefits of the individual models.

In addition, the researchers calibrated and/or validated the three applications developed under this project according to the best available CAV field data to improve the fidelity of these applications. All of these applications are open source and can be customized according to future users' needs. To help the CAV stakeholder community easily implement these models within their preferred simulation tools, the research team provided information for the above applications, including model development and logic, model calibration and validation, and examples of how to implement developed models into a simulation tool.

MODEL LIMITATIONS AND SUGGESTED IMPROVEMENTS

The CACC (or CAV) CF model in this report was based on field-test data from four research product CAVs in public freeway traffic. This model may have captured the dynamic interactions of CAVs with other public traffic, but since the data were collected for speeds above 35 mph, the CACC CF did not behave well when traffic speeds were lower than 35 mph in microscopic simulation of mixed traffic. In particular, this CF model could not be used for microsimulation of low-speed surface arterials or even for stop-and-go traffic. It would therefore be helpful to extend this CACC CF model for the whole speed profile (e.g., 0–70 mph) based on some available field-test data covering the whole speed profile.

The proposed light-duty CAV LC model was limited in the following aspects: First, the proposed LC model was developed only with field data from relatively small-scale experiments with a specific lab-designed AV. Second, platooning for longitudinal CAV control was not considered in the study. Third, possible heterogeneous HV behaviors in response to surrounding CAVs were not yet incorporated. It would be beneficial to collect CAV LC data on public roads to investigate how human drivers interact with CAVs to improve this CAV LC model in the future.

In the algorithm development for SPDHRM or VSL/VSA, it was preferable to target systemwide optimization. To achieve this objective, the researchers took several factors into account:

1. Estimating the traffic state—considering the practical data available and CV and CAV as mobile sensors.
2. Predicting traffic in space and time (in a future time horizon)—what model or prediction approach is realistically available.
3. Formulating the problem—this can consider dynamic characteristics of the traffic pattern in both space and time.
4. Addressing uncertainties—the main uncertainties are the driver (local) behavior, plus the demands from the further upstream mainline and from onramps (sectionwide and systemwide).
5. Evaluating the objective function—how can the objective function be evaluated if an optimal control (MPC is a simplified version) approach is adopted.

The congestion-prediction model defined in the SPDHRM application considered a binary traffic state: congested and uncongested. A possible limitation of the current application is that a

transition state between the congested and uncongested states is not defined as a possible output for the prediction model. A possible improvement would be to take advantage of machine-learning techniques that could be combined with approaches based on fundamental traffic concepts and theories to develop models that are capable of predicting multiple states of the traffic. A multistate traffic-prediction model could be coupled with a revised framework of SPDHRM strategies to test whether such refinement might improve the performance of the application and provide a smoother transition in the traffic flow.

The proposed merge-coordination model requires at least two CAVs to coordinate the maneuvers. The possibility of coordinating maneuvers between a merging CAV and connected HVs has not been explored in this study. This is particularly critical at low MPRs of CAVs where the chances of encountering another CAV in the target lane are rather low. The proposed algorithm also relies heavily on V2V communications to share controller design along with vehicle position and velocity. It is, however, important to consider utilizing onboard sensors and V2I communications for applicability of the proposed algorithm in the real world.

RECOMMENDATIONS FOR FUTURE RESEARCH

During this project, a key challenge was insufficient CAV field data for CAV application development, calibration, or validation. This is also a major difficulty facing the CAV simulation and modeling community. As a result, assessments and predictions provided by CAV simulation for various CAV applications may not be realistic. To improve the fidelity of CAV simulation and modeling results, the project team recommends collecting more CAV field data from different perspectives (e.g., how different human drivers interact with AVs/CAVs and how AVs/CAVs interact with different HVs on public roads) while acknowledging that AV/CAV behavior in traffic continues to evolve as does human-driver behavior around AVs/CAVs.

The project team also recommends conducting additional case studies to evaluate other prominent CAV applications to help State and local agencies understand how to prepare and deploy their preferred CAV technologies.

REFERENCES

Aimsun. 2020. “Aimsun Editions.” (web page). https://www.aimsun.com/aimsun-next/editions/, last accessed April 28, 2020.

An, G., and A. Talebpour. 2019. “Lane-Changing Trajectory Optimization to Minimize Traffic Flow Disturbance in a Connected Automated Driving Environment.” *2019 IEEE Intelligent Transportation Systems Conference*. Auckland, New Zealand: Institute of Electrical and Electronics Engineers.

Arefizadeh, S., and A. Talebpour. 2018. “A Platooning Strategy for Automated Vehicles in the Presence of Speed Limit Fluctuations.” *Transportation Research Record* 2672, no. 20: 154–161.

Bacha, A. et al. 2008. “Odin: Team VictorTango’s Entry in the DARPA Urban Challenge.” *Journal of Field Robotics* 25, no. 8: 467–492.

Ciuffo, B., V. Punzo, and M. Montanino. 2012. “Thirty Years of Gipps’ Car-Following Model: Applications, Developments, and New Features.” *Transportation Research Record* 2315, no. 1: 89–99.

Cong, Y., O. Sawodny, H. Chen, J. Zimmermann, and A. Lutz. 2010. “Motion Planning for an Autonomous Vehicle Driving on Motorways by Using Flatness Properties.” *2010 IEEE International Conference on Control Applications*. Yokohama, Japan: Institute of Electrical and Electronics Engineers.

Dong, J., and H. S. Mahmassani. 2009. “Flow Breakdown and Travel Time Reliability.” *Transportation Research Record* 2124, no. 1: 203–212.

Edie, L. C. 1963. “Discussion of Traffic Stream Measurements and Definitions”. *Proceedings of the Second International Symposium on the Theory of Traffic Flow.* London, UK.

Elfar, A. 2019. “Predictive Traffic Operations and Control of Connected and Automated Vehicle Systems.” Doctoral dissertation, Northwestern University.

Elfar, A. et al. 2018. “Traffic Shockwave Detection in a Connected Environment Using the Speed Distribution of Individual Vehicles.” *Transportation Research Record* 2672, no. 20: 203–214.

Elfar, A., A. Talebpour, and H. S. Mahmassani. 2018. “Machine Learning Approach to Short-Term Traffic Congestion Prediction in a Connected Environment.” *Transportation Research Record* 2672, no. 45: 185–195.

Elfar, A., A. Talebpour, and H. S. Mahmassani. 2019. “Predictive Speed Harmonization in a Connected Environment: A Machine Learning Approach.” *Transportation Research Board Annual Meeting.* Washington, DC: Transportation Research Board.

Elfar, A., A. Talebpour, and H. S. Mahmassani. 2020. “Predictive Speed Harmonization in Traffic Flow with Connected and Automated Vehicles: Machine Learning Application.” *Transportation Research Board Annual Meeting*. Washington, DC: Transportation Research Board.

Farah, H., H. N. Koutsopoulos, M. Saifuzzaman, R. Kölbl, S. Fuchs, and D. Bankosegger. 2012. “Evaluation of the Effect of Cooperative Infrastructure-to-Vehicle Systems on Driver Behavior.” *Transportation Research Part C: Emerging Technologies* 21, no. 1: 42–56.

FHWA. 2007. *Next Generation Simulation (NGSIM) US–101 Dataset*. Washington, DC: U.S. Department of Transportation.

Gipps, P. G. 1981. “A Behavioural Car-Following Model for Computer Simulation.” *Transportation Research Part B: Methodological* 15, no. 2: 105–11.

González, D., J. Pérez, R. Lattarulo, V. Milanés, and F. Nashashibi. 2014. “Continuous Curvature Planning with Obstacle Avoidance Capabilities in Urban Scenarios”. *17th International IEEE Conference on Intelligent Transportation Systems*. Institute of Electrical and Electronics Engineers.

Gunter, G., C. Janssen, W. Barbour, R. Stern, and D. Work. 2019. “Model Based String Stability of Adaptive Cruise Control Systems Using Field Data.” *IEEE Transactions on Intelligent Vehicles* 5, no. 1: 90–99.

Hamdar, S. H. et al. 2008. “Modeling Driver Behavior as Sequential Risk-Taking Task.” *Transportation Research Record* 2088, no. 1: 208–217.

Hamdar, S. H., M. Treiber, and H. S. Mahmassani. 2009. “Calibration of a Stochastic Car-Following Model Using Trajectory Data: Exploration and Model Properties.” *Transportation Research Board Annual Meeting*. Washington, DC: Transportation Research Board.

Hamdar, S. H., V. V. Dixit, A. Talebpour, and M. Treiber. 2019. “A Behavioral Microeconomic Foundation for Car-Following Models.” *Transportation Research Part C: Emerging Technologies* 113: 228–244.

Hartigan, J. A. 1975. *Clustering Algorithms*. New York, NY: John Wiley & Sons Inc.

Huang, Z., J. Ma, Y. Guo, and N. Matout. [forthcoming]. *Developing Analysis, Modeling, and Simulation Tools for Connected Automated Vehicle Applications: Traffic Optimization for Signalized Corridors—Case Studies in Ann Arbor, Michigan, and Conroe, Texas*. Washington, DC: Federal Highway Administration.

Kahneman, D., and A. Tversky. 1979. “Prospect Theory: An Analysis of Decision Under Risk.” *Econometrica* 47, no. 2: 263–291.

Kan, X. D., L. Xiao, H. Liu, M. Wang, W. J. Schakel, X. Y. Lu, and R. A. Ferlis. 2019. “Cross-Comparison and Calibration of Two Microscopic Traffic Simulation Models for Complex

Freeway Corridors with Dedicated Lanes." *Journal of Advanced Transportation* 2019: Article ID 8618476, 14 pp.

Kianfar, R. et al. 2014. "Combined Longitudinal and Lateral Control Design for String Stable Vehicle Platooning within a Designated Lane." *17th International IEEE Conference on Intelligent Transportation Systems*. Qingdao, China: Institute of Electrical and Electronics Engineers.

Kiefer, R. J., M. T. Cassar, C. A. Flannagan, D. J. LeBlanc, M. D. Palmer, R. K. Deering, M. A. Shulman. 2003. *Forward Collision Warning Requirements Project: Refining the CAMP Crash Alert Timing Approach by Examining "Last-Second" Braking and Lane Change Maneuvers Under Various Kinematic Conditions*. Report No. HS-809 574. Washington, DC: National Highway Traffic Safety Administration.

Kim, J., and H. S. Mahmassani. 2011. "Correlated Parameters in Driving Behavior Models: Car-Following Example and Implications for Traffic Microsimulation." *Transportation Research Record* 2249, no. 1: 62–77.

Kolski, S., D. Ferguson, M. Bellino, and R. Siegwart. 2006. "Autonomous Driving in Structured and Unstructured Environments," *2006 IEEE Intelligent Vehicles Symposium*. Meguro-Ku, Japan: Institute of Eletrical and Electronics Engineers.

Li, B., Y. Zhang, Y. Feng, Y. Zhang, Y. Ge, and Z. Shao. 2018. "Balancing Computation Speed and Quality: A Decentralized Motion Planning Method for Cooperative Lane Changes of Connected and Automated Vehicles." *IEEE Transactions on Intelligent Vehicles* 3, no. 3: 340–350.

Li, X. G., B. Jia, Z. Y. Gao, and R. Jiang. 2006. "A Realistic Two-Lane Cellular Automata Traffic Model Considering Aggressive Lane-Changing Behavior of Fast Vehicle." *Physica A: Statistical Mechanics and its Applications* 367: 479–486.

Liu, H., X. D. Kan, S. E. Shladover, X. Y. Lu, and R. A. Ferlis. 2018. "Modeling Impacts of Cooperative Adaptive Cruise Control on Mixed Traffic Flow in Multi-Lane Freeway Facilities." *Transportation Research Part C: Emerging Technologies* 95: 261–279.

Liu, H., X. Y. Lu, S. E. Shladover, and Z. Huang. 2021. *Developing Analysis, Modeling, and Simulation Tools for Connected Automated Vehicle Applications: A Case Study for SR 99 in California*. Report No. FHWA-HRT-21-039. Washington, DC: Federal Highway Administration.

Lu, X. Y., J. Spring, C. J. Wu, D. Nelson, and Y. Kan. 2019. *Field Experiment of Variable Speed Advisory Final Report*. Berkeley, CA: University of California, Berkeley: California Partners for Advanced Transportation Technology.

Ma, J., Y. Guo, and Z. Huang. 2021. *Developing Analysis, Modeling, and Simulation Tools for Connected Automated Vehicle Applications: A Case Study for Interstate 66 in Virginia*. Report No. FHWA-HRT-21-050. Washington, DC: Federal Highway Administration.

Mahmassani, H. S. 2016. “50th Anniversary Invited Article—Autonomous Vehicles and Connected Vehicle Systems: Flow and Operations Considerations.” *Transportation Science* 50, no. 4: 1140–1162.

Mahmassani, H. S. et al. 2012. *Concept Development and Needs Identification for Intelligent Network Flow Optimization: Assessment of Relevant Prior and Ongoing Research*. Washington, DC: U.S. Department of Transportation.

Mahmassani, H. S., A. Elfar, S. E. Shladover, and Z. Huang. 2018. *Development of an Analysis/Modeling/Simulation (AMS) Framework for V2I and Connected/Automated Vehicle Environment*. Washington, DC: U.S. Department of Transportation.

Maschuw, J. P., G. C. Kebler, and D. Abel. 2008. “LMI-Based Control of Vehicle Platoons for Robust Longitudinal Guidance.” *IFAC Proceedings* 41, no. 2: 12111–12116.

Massey Jr, F. J. 1951. “The Kolmogorov-Smirnov Test for Goodness of Fit.” *Journal of the American Statistical Association.* 46, no. 253: 68–78.

Microsoft Visual Studio. 2019. https://visualstudio.microsoft.com/, last accessed May 6, 2021.

Milanés, V., and S. E. Shladover. 2014. “Modeling Cooperative and Autonomous Adaptive Cruise Control Dynamic Responses Using Experimental Data.” *Transportation Research Part C: Emerging Technologies* 48: 285–300.

Mittal, A. et al. 2018. “Predictive Dynamic Speed Limit in a Connected Environment for a Weather Affected Traffic Network: A Case Study of Chicago.” *Transportation Research Record* 2672, no. 19: 13–24.

MUTCD. 2006. *Manual on Uniform Traffic Control Devices*. Austin, TX: Texas Department of Transportation.

Nelson, W. 1989. “Continuous-Curvature Paths for Autonomous Vehicles.” *Proceedings of the 1989 International Conference on Robotics and Automation*. Scottsdale, AZ: Institute of Electrical and Electronics Engineers.

Newell, G. F. 2002. “A Simplified Car-Following Theory: A Lower Order Model.” *Transportation Research Part B: Methodological* 36, no. 3: 195–205.

Papadimitriou, I., and M. Tomizuka. 2003. “Fast Lane Changing Computations Using Polynomials.” *Proceedings of the 2003 American Control Conference*. Denver, CO: Institute of Electrical and Electronics Engineers.

Pattara-Atikom, W., and R. Peachavanish. 2007. “Estimating Road Traffic Congestion from Cell Dwell Time Using Neural Network.” *2007 7th International Conference on ITS Telecommunications.* Sophia Antipolis, France: Institute of Electrical and Electronics Engineers.

Piazzi, A. et al. 2002. “Quintic G/sup 2/-splines for the Iterative Steering of Vision-Based Autonomous Vehicles.” *IEEE Transactions on Intelligent Transportation Systems* 3, no. 1: 27–36.

Pivtoraiko, M., and A. Kelly. 2005. “Efficient Constrained Path Planning via Search in State Lattices.” *International Symposium on Artificial Intelligence, Robotics, and Automation in Space.* Munich, Germany.

Pivtoraiko, M., R. A. Knepper, and A. Kelly. 2009. “Differentially Constrained Mobile Robot Motion Planning in State Lattices.” *Journal of Field Robotics* 26, no. 3: 308–333.

PTV Group. 2018. PTV Vissim. https://www.ptvgroup.com/en/solutions/products/ptv-vissim/, last accessed May 3, 2020.

Python Software Foundation. n.d. *Python*. https://www.python.org/, last accessed July 20, 2020.

Rahmati, Y., M. Khajeh Hosseini, A. Talebpour, B. Swain, and C. Nelson, 2019. “Influence of Autonomous Vehicles on Car-Following Behavior of Human Drivers.” *Transportation Research Record* 2673, no. 12: 367–379.

Rakha, H. A., K. Ahn, K. Moran, B. Saerens, and E. Van den Bulck. 2011. “Virginia Tech Comprehensive Power-Based Fuel Consumption Model: Model Development and Testing.” *Transportation Research Part D: Transport and Environment* 16, no. 7: 492-503.

Ramezani, H., X. Y. Lu, and S. E. Shladover. 2019. “Calibration of Motor Vehicle Emission Simulator (MOVES) to Incorporate Effect of Truck Platooning.” *Transportation Research Board Annual Meeting*. Washington, DC: Transportation Research Board.

Rastelli, J. P., R. Lattarulo, and F. Nashashibi. 2014. “Dynamic Trajectory Generation Using Continuous-Curvature Algorithms for Door to Door Assistance Vehicles.” *2014 IEEE Intelligent Vehicles Symposium Proceedings*. Ypsilanti, MI: Institute of Electrical and Electronics Engineers.

Reece, D. A., and S. A. Shafer. 1993. “A computational model of driving for autonomous vehicles.” *Transportation Research Part A: Policy and Practice* 27, no. 1: 23–50.

Schroder, J., T. Gindele, D. Jagszent, and R. Dillmann. 2008. “Path Planning for Cognitive Vehicles Using Risk Maps.” *2008 IEEE Intelligent Vehicles Symposium*. Eindhoven, Netherlands: Institute of Electrical and Electronics Engineers.

Seabold, S., and J. Perktold. 2010. “Statsmodels: Econometric and Statistical Modeling with Python.” *Proceedings of the 9th Python in Science Conference.* Vol. 57. Austin, TX: SciPy.

Seiler, P., A. Pant, and K. Hedrick. 2004. “Disturbance Propagation in Vehicle Strings.” *IEEE Transactions on Automatic Control* 49, no. 10: 1835–1842.

Smith, B. W. 2013. *SAE Levels of Driving Automation*. Center for Internet and Society. Stanford Law School. http://cyberlaw.stanford.edu/blog/2013/12/sae-levels-driving-automation, last accessed May 7, 2021.

Spyropoulou, I. K., M. G. Karlaftis, and N. Reed. 2014. "Intelligent Speed Adaptation and Driving Speed: Effects of Different System HMI Functionalities." *Transportation Research Part F: Traffic Psychology and Behaviour* 24: 39–49.

Swaroop, D. 1997. *String Stability of Interconnected Systems: An Application to Platooning in Automated Highway Systems*. Berkeley, CA: University of California, Berkeley: California Partners for Advanced Transportation Technology.

Talebpour, A., and H. S. Mahmassani. 2016. "Influence of Connected and Autonomous Vehicles on Traffic Flow Stability and Throughput." *Transportation Research Part C: Emerging Technologies* 71: 143–163.

Talebpour, A., H. S. Mahmassani, and S. H. Hamdar. 2011. "Multiregime Sequential Risk-Taking Model of Car-Following Behavior: Specification, Calibration, and Sensitivity Analysis." *Transportation Research Record* 2260, no. 1: 60–66.

Talebpour, A., H. S. Mahmassani, and S. H. Hamdar. 2013. "Speed Harmonization: Evaluation of Effectiveness under Congested Conditions." *Transportation Research Record* 2391, no. 1: 69–79.

Talebpour, A., H. S. Mahmassani, and S. H. Hamdar. 2017. "Effect of Information Availability on Stability of Traffic Flow: Percolation Theory Approach." *Transportation Research Procedia* 23: 81–100.

Texas Transportation Institute. 2005. *Travel Time Reliability: Making It There on Time, All the Time*. Report No. HOP-06-070. Washington, DC: Federal Highway Administration.

Thianniwet, T., S. Phosaard, and W. Pattara-Atikom. 2009. "Classification of Road Traffic Congestion Levels from GPS Data Using a Decision Tree Algorithm and Sliding Windows." *Proceedings of the World Congress on Engineering*. London, UK: International Association of Engineers.

Toledo, T., and D. Zohar. 2007. "Modeling Duration of Lane Changes." *Transportation Research Record* 1999, no. 1: 71–78.

Treiber, M., A. Hennecke, and D. Helbing. 2000. "Congested Traffic States in Empirical Observations and Microscopic Simulations." *Physical Review E* 62, no. 2: 1805.

Treiber, M., and A. Kesting. 2013. *Traffic Flow Dynamics: Data, Models and Simulation*. Berlin, Germany: Springer.

Van Arem, B., C. J. Van Driel, and R. Visser. 2006. "The Impact of Cooperative Adaptive Cruise Control on Traffic-Flow Characteristics." *IEEE Transactions on Intelligent Transportation Systems* 7, no. 4: 429–436.

Vlahogianni, E. I. et al. 2008. “Temporal Evolution of Short-Term Urban Traffic Flow: A Nonlinear Dynamics Approach.” *Computer-Aided Civil and Infrastructure Engineering* 23, no. 7: 536–548.

Wang, J., and R. Rajamani. 2004. “Should Adaptive Cruise-Control Systems Be Designed to Maintain a Constant Time Gap Between Vehicles?” *IEEE Transactions on Vehicular Technology* 53, no. 5: 1480–1490.

Wang, M. et al. 2015. “Connected Variable Speed Limits Control and Vehicle Acceleration Control to Resolve Moving Jams” (authors’ version). *Transportation Research Board 94th Annual Meeting*. Washington, DC: Transportation Research Board.

Wang, Z., X. Zhao, Z. Xu, X. Li, and X. Qu. 2020. “Modeling and Field Experiments on Autonomous Vehicle Lane Changing of an Autonomous Vehicle in Mixed Traffic.” *Computer-Aided Civil and Infrastructure Engineering*.

Wilcox, R. R. 1996. *Statistics for the Social Sciences*. Academic Press.

Xiao, L., and F. Gao. 2010. “A Comprehensive Review of the Development of Adaptive Cruise Control Systems.” *Vehicle System Dynamics* 48, no. 10: 1167–1192.

Xu, G., L. Liu, Y. Ou, and Z. Song. 2012. “Dynamic Modeling of Driver Control Strategy of Lane-Change Behavior and Trajectory Planning for Collision Prediction.” *IEEE Transactions on Intelligent Transportation Systems* 13, no. 3: 1138–1155.

Yang, H., and W-L Jin. 2014. “A Control Theoretic Formulation of Green Driving Strategies Based on Inter-Vehicle Communications.” *Transportation Research Part C: Emerging Technologies* 41: 48–60.

Yeo, H., A. Skabardonis, J. Halkias, J. Colyar, and V. Alexiadis. 2008. “Oversaturated Freeway Flow Algorithm for Use in Next Generation Simulation.” *Transportation Research Record* 2088, no. 1: 68–79.

Zhao, X., Z. Wang, Z. Xu, Y. Wang, X. Li, and X. Qu. 2020. “Field Experiments on Longitudinal Characteristics of Human Driver Behavior Following an Autonomous Vehicle.” *Transportation Research Part C: Emerging Technologies* 114: 205–224.

HRDO-20/09-21(WEB)E